



**HAL**  
open science

# Study of Deeply Virtual Compton Scattering at COMPASS at CERN

Brian Ventura

► **To cite this version:**

Brian Ventura. Study of Deeply Virtual Compton Scattering at COMPASS at CERN. High Energy Physics - Experiment [hep-ex]. Université Paris-Saclay, 2021. English. NNT : 2021UPASP125 . tel-03612938

**HAL Id: tel-03612938**

**<https://theses.hal.science/tel-03612938>**

Submitted on 18 Mar 2022

**HAL** is a multi-disciplinary open access archive for the deposit and dissemination of scientific research documents, whether they are published or not. The documents may come from teaching and research institutions in France or abroad, or from public or private research centers.

L'archive ouverte pluridisciplinaire **HAL**, est destinée au dépôt et à la diffusion de documents scientifiques de niveau recherche, publiés ou non, émanant des établissements d'enseignement et de recherche français ou étrangers, des laboratoires publics ou privés.

Study of Deeply Virtual Compton  
Scattering at COMPASS at CERN  
*Etude de la diffusion Compton profondément virtuelle  
dans l'expérience COMPASS au CERN*

**Thèse de doctorat de l'université Paris-Saclay**

École doctorale n° 576: Particules, Hadrons, Energie, Noyau, Instrumentation,  
Imagerie, Cosmos et Simulation (PHENIICS)  
Spécialité de doctorat: Physique Hadronique  
Graduate School : Physique, Référent : Faculté des sciences d'Orsay

Thèse préparée dans l'unité de recherche **Département de Physique Nucléaire**  
(Université Paris-Saclay, CEA), sous la direction de **Nicole D'HOSE**, directrice de recherche

**Thèse soutenue à Paris-Saclay, le 2 décembre 2021, par**

**Brian VENTURA**

**Composition du jury**

<b>Franck SABATIÉ</b> Directeur de recherche, Université Paris-Saclay - CEA/IRFU/DPhN	Président
<b>Laurent FAVART</b> Directeur de recherche, Université Libre de Bruxelles - IIHE	Rapporteur & Examineur
<b>Charles Earl HYDE</b> Eminent Scholar and University Professor of Physics (Professeur éminent), Old Dominion University	Rapporteur & Examineur
<b>Eva-Maria KABUSS</b> Prof. Dr., Johannes Gutenberg Universität Mainz - KPH	Examinatrice
<b>Pawel SZNAJDER</b> Assistant Professor (Professeur assistant), National Centre for Nuclear Research	Examineur
<b>Nicole D'HOSE</b> Directrice de recherche, Université Paris-Saclay - CEA/IRFU/DPhN	Directrice de thèse



---

## ACKNOWLEDGEMENTS

---

First of all, I would like to mention the institutions in which I have spent 3 years and met so many interesting persons. Thanks to the CEA/IRFU and particularly the DPhN, the University Paris Saclay and the COMPASS collaboration.

I would like to express all my gratitude to the members of my jury: Franck Sabatié, Pawel Sznajder, Eva Maria Kabuś and my two referees Charles Earl Hyde and Laurent Favart. Their careful reading and pertinent questions improved the manuscript and led to very thoughtful and interesting discussions.

Je remercie Danielle et Isabelle pour leur aide inestimable tout au long de ces trois années. Nos nombreuses discussions étaient vraiment agréables et m'ont donné un vrai moyen de décompresser surtout en fin de thèse où mes visites se sont faites plus fréquentes. Je tiens à remercier les personnes qui m'ont aidé à m'orienter vers cette thèse, et plus particulièrement Hervé Moutarde. Grâce à ses cours donnés à Centrale, j'ai découvert certains pans de la physique que je ne soupçonnais pas et qui ont donné un aspect plus concret à toutes ces années de mathématiques. Au-delà du cours, nos discussions plus générales concernant la recherche en physique m'ont donné envie de me lancer dans le domaine, et c'est aussi grâce à lui que j'ai trouvé mon sujet de thèse au sein du DPhN. Ton soutien et ta bienveillance m'ont été inestimables et tu es une des personnes à qui je dois le plus. Je souhaite bien sûr remercier Andrea et Nicole qui ont su me me donner envie de me lancer dans cette aventure en physique expérimentale. Je souhaite aussi adresser mes plus sincères remerciements à Franck pour son écoute attentive et pour tout le suivi des étudiants durant ces trois années. Tu as donné des solutions concrètes à des amis en difficulté autour de moi, et cela m'a été particulièrement rassurant.

Mon stage de fin d'études a aussi beaucoup aidé à valider mon choix pour ce domaine. C'est grâce à Matthieu Vivier que j'ai découvert une des très nombreuses facettes du métier qui m'a été essentielle pour mieux comprendre ce qu'on demandait aujourd'hui dans la recherche en physique expérimentale. Je tiens donc à remercier Matthieu, Guillaume Mention et Claudia Nones pour leur accompagnement pendant ce stage ainsi que pour tous les conseils que vous m'avez donnés pour la suite.

As part of the COMPASS collaboration during 3 years, I had the opportunity to work with very interesting smart and various persons. I would like to thank particularly all the people from the DVCS/SIDIS analysis group, whose questions and inputs were always very fruitful and have made this analysis more and more rigorous with time. Thanks to Marcin, Jan, Yann, Bakur, Andrzej, Andrea B., Eva, Anna, Horst and all the others. Thanks to Sergei G. for your tremendous work on the calorimeters, and of course Renat for the so delicate alignment procedure. I would also like to thank the students who accompanied me among the collaboration: Andrea M., Karolina, Marketa, Sandro, Anatolii and Johannes. We spent crazy times together either at CERN, Freiburg, Aveiro and Saclay, and I regret that we could not have seen each other more often due to the pandemic situation. In particular, I have never worked as closely as we did with Johannes during the last months and I would like to thank him for his intense reactivity and for keeping his humor even at

3am. In addition, nothing could have been possible in time without the huge implication of Vincent. As analysis coordinator, he worked night and days in order to help us towards the results (especially for the last minute Monte Carlo) and I definitely cannot thank him enough for this. His phone calls were always a pleasure and a good reason for a break between two lines of code. I also would like to thank Bakur for his dedication and help especially during my first year among the collaboration. I still have a picture of him sleeping in the COMPASS room, which summarises well the mood after a "release night" (or was it due to grappa ?).

I would also like to express all my gratitude to Po-Ju Lin. We shared the same office for more than 3 years and he always knew how to set a pleasant mood in the room, even though I am definitely not a very chatty person. Even during stressful moments he was wonderfully calm, zen, patient and rigorous. In addition he always had some nice stories to tell either from the United States, Japan or Taiwan. I often asked for his help either correcting my English or discussing complicated points from the analysis on which he was always rigorous and pertinent. He taught me so many things, humanly and scientifically, and I thank him for these 3 years. I wish you the best for you and your family back in Taiwan. Je ne peux pas non plus oublier de mentionner mes autres collègues de Saclay avec qui nous formions en partie la "Saclay team" de COMPASS. Nous avons beaucoup vécu ensemble et je tiens à vous en remercier tous. Je remercie Nicolas pour tout son travail qui m'a bien aidé et tous nos moments de discussions (notamment sur nos références communes comme la fameuse "boule magique"), Charles pour sa passion de la physique et son humour, Marco pour son aide inestimable sur TGeant et nos moments de détente en salle café ou dans ton bureau (toujours prêt pour dégainer une capsule !). L'ambiance COMPASS à Saclay n'était plus la même après chacune de vos soutenances. Je tiens aussi à remercier Antoine avec qui j'ai été très proche pendant ma première année. Outre les pauses thés/brioche dans son petit salon de thé nous avons beaucoup voyagé ensemble, depuis Aveiro avec Charles sur des plages entièrement vides à la sublime ville de Freiburg en passant par le CERN. Je garde des souvenirs mémorables lorsque nous errions dans les rues de Freiburg avec Antoine et Johannes, verre de vin de la Weinfest à la main, ou encore quand nous avons marché au Col de la Faucille dans une neige épaisse avec Antoine et Sandro (et il y a eu plusieurs glissades). Je remercie aussi tous les stagiaires et doctorants du DPhN, et en particulier Christopher, Zoé, Benjamen, Vladimir, Robin, Hervé et Aurore, ainsi que tous les autres étudiants que je n'ai pu prendre le temps de connaître. Je remercie aussi les chercheurs du DPhN avec qui j'ai pu discuter notamment en salle café : merci à Loïc pour nos discussions motivantes (tu as été un bon tuteur !) à Maxime pour ton aide, ton énergie et ta bienveillance, à Thomas, Eric, Marine, Francesco, David, et tous les autres. J'aimerais remercier plus particulièrement ma directrice de thèse, Nicole sans qui rien n'aurait été possible. Son soutien et son aide ont été constantes depuis le début, même avant le commencement de ma thèse. Après le départ de Nicolas et Antoine, elle a su rester parfaitement à l'écoute de la situation lorsque j'avais des problèmes (techniques ou non), et elle a toujours su répondre à tous mes doutes et questions. En plus de cela, lorsque j'étais concentré sur des détails de l'analyse, elle m'a appris à prendre du recul et m'a aidé sur les très nombreuses présentations à la collaboration. Même si elle est toujours débordée de travail, elle a consacré un temps incommensurable sur chacune des releases de notre analyse. Je la remercie en particulier pour sa relecture très détaillée de mon manuscrit de thèse. En plus de cela, sa gentillesse et sa bienveillance sont légendaires dans le laboratoire et j'ai toujours admiré son implication et son côté humain. Je ne te souhaite que des vacances ! Je remercie aussi Fabienne pour n'avoir cessé de m'encourager, Damien pour ses anecdotes improbables (notamment dans une villa aux alentours du JLab), Yann pour son savoir encyclopédique et son humour, et Stéphane pour sa bonne humeur. Je voudrais

---

aussi remercier Pierre Guichon pour son humour et les moments agréables à l'heure du déjeuner ou en salle café avec Nicole et Po-Ju avant ses sessions de golf.

I would like also to thank Philipp Jörg for all his help during my first year. I have been very glad to work with him for few months. I wish you the best for you and your family ! Thanks to Matthias Gorzelli for his availability at Freiburg and all the work he did on CAMERA with Philipp, as well as all the other students from Freiburg.

I also would like to thank the CERN and especially the IT department who thoroughly helped me. Thanks to Enric Tejedor Saavedra, Prasanth Kothuri, Piotr Mrowczynski, Javier Cervantes Villanueva, Vincenzo Eduardo Padulano and all the team for the help you provided me with SWAN and Spark. I really enjoyed our meeting at CERN and with more time and travels I would have been glad to know all of you more, and try to help more than as a simple user (and offer you some beers for everything you did). Special thanks to Enric and Vincenzo for their availability and all the meetings and discussions we had trying to debug PyRDF. I would also like to thank Enrico Guiraud for everything he did to ROOT. I wish you all a great future among the ROOT team or elsewhere !

Je tiens à remercier le petit groupe qui m'accompagne depuis le collège ainsi que les personnes que j'ai rencontrées depuis. Constant, Inès, Gautier, Laure, Alexandre, Marine, Raphaël, vous êtes les meilleurs ! Entre escalade, cinémas, jeux, randonnées et soirées, on arrive toujours à trouver du temps pour se détendre. Merci à Judith, Adão, Charles-Albert et Thuy-Hang pour tous ces excellents dîners et ces bons moments passés depuis le collège. Je remercie Noëlie pour sa patience, son soutien de tous les jours, ainsi que pour l'organisation de nombreuses randonnées, picnics, cinémas et voyages. Je ne ferai pas grand chose sans vous tous ! Enfin, merci à mes parents, à Alexis, Kevin, Corinne, Jean-Louis, Emmanuel, Gwenola, Gildas, Rozenn, Alexandre, Caroline, Gaëlle et Gilles pour tous les moments de détente.



# Contents

<b>Acknowledgements</b>	<b>iii</b>
<b>Acronyms</b>	<b>xi</b>
<b>Introduction</b>	<b>1</b>
<b>I THE NUCLEON STRUCTURE</b>	<b>3</b>
<b>1 Probing the structure of hadrons</b>	<b>4</b>
1.1 Wigner distributions	4
1.2 GTMDs and projections	5
<b>2 Elastic scattering and Form Factors</b>	<b>7</b>
<b>3 Deep inelastic scattering and Parton Distribution Functions</b>	<b>10</b>
<b>4 Generalised Partons Distributions</b>	<b>14</b>
4.1 QCD factorisation and twist	15
4.2 Support and partonic interpretations	15
4.3 Properties and impact parameter	17
4.4 Double distributions and D-term	19
<b>5 Accessing GPDs through DVCS experiments</b>	<b>20</b>
5.1 Compton Form Factors	20
5.2 Interferences and cross section	22
5.3 Beam charge and helicity measurements at COMPASS	23
5.4 Overview on other experiments	25
<b>II THE COMPASS EXPERIMENT</b>	<b>31</b>
<b>1 The polarised muon beam</b>	<b>32</b>
1.1 Spill structure and intensity	32
1.2 Beam momentum reconstruction	33
<b>2 The target</b>	<b>34</b>
<b>3 The spectrometer and trackers</b>	<b>35</b>

<b>4</b>	<b>Particle identification</b>	<b>37</b>
4.1	Muon filters	37
4.2	RICH detector	37
4.3	Electromagnetic and hadronic calorimeters	38
<b>5</b>	<b>The CAMERA detector</b>	<b>40</b>
5.1	Proton identification in CAMERA	42
5.2	CAMERA characterisation and improvements	43
5.3	Readout electronics and data acquisition framework	44
5.4	Reconstruction principle	44
<b>6</b>	<b>The trigger system</b>	<b>45</b>
6.1	The muon trigger	45
6.2	The random trigger	46
<b>7</b>	<b>Data acquisition</b>	<b>46</b>
<b>8</b>	<b>Event reconstruction</b>	<b>48</b>
<b>III PREPARATORY WORK ON THE 2016-2017 DATA</b>		<b>51</b>
<b>1</b>	<b>Target position evaluation and vertex selection</b>	<b>52</b>
<b>2</b>	<b>Muon beam and spill selection</b>	<b>54</b>
2.1	The muon beam quality	54
2.2	Time in spill and bad spills determination	54
<b>3</b>	<b>Luminosity determination</b>	<b>55</b>
<b>4</b>	<b>Scattered muon selection and trigger efficiencies</b>	<b>57</b>
4.1	Scattered muon selection	57
4.2	Trigger efficiencies	57
<b>5</b>	<b>Monte Carlo simulation and validation using the structure function <math>F_2</math></b>	<b>59</b>
5.1	The physics generators	59
5.2	Particle propagation and reconstruction	59
5.3	Comparison and extraction of the structure function $F_2$	60
<b>6</b>	<b>ECALs calibrations and quality</b>	<b>62</b>
6.1	Time calibration and bad cells determination	62
6.2	Energy calibration	66
6.3	Monte Carlo simulation	76
<b>IV EXCLUSIVE REACTIONS AND CAMERA CALIBRATIONS</b>		<b>79</b>
<b>1</b>	<b>Exclusive processes and multivariate analysis</b>	<b>80</b>
1.1	The mathematical framework	80
1.2	Application to the exclusive $\rho^0$ events	87
<b>2</b>	<b>CAMERA calibrations</b>	<b>90</b>
2.1	Exclusive $\rho^0$ event selection	90
2.2	Azimuthal calibration	90
2.3	Radial tomography	92

2.4	Longitudinal calibration . . . . .	95
2.5	Time of flight calibration and momentum adjustment . . . . .	96
2.6	Monte Carlo simulation . . . . .	97
<b>V THE EXCLUSIVE SINGLE PHOTO-PRODUCTION EVENT SELECTION</b>		<b>105</b>
1	The 2016 data and luminosity per period . . . . .	106
2	Monte Carlo simulations for Bethe-Heitler, DVCS and $\pi^0$ . . . . .	107
3	The exclusive single photon event selection . . . . .	109
3.1	Overview of the different cuts . . . . .	109
3.2	Vertex and muons selection . . . . .	109
3.3	Photon selection . . . . .	110
3.4	Proton selection . . . . .	112
3.5	Exclusivity cuts . . . . .	112
3.6	Kinematical fit . . . . .	116
4	Strategy of the DVCS analysis with a 160 GeV muon beam . . . . .	124
5	Comparison of the data with the Bethe-Heitler prediction at large $\nu$ . . .	124
5.1	Quality of the Monte Carlo description . . . . .	124
5.2	Quality of the agreement between the data and the Monte Carlo Bethe-Heitler prediction . . . . .	129
6	The $\pi^0$ contamination at small $\nu$ . . . . .	130
6.1	The visible $\pi^0$ background . . . . .	130
6.2	The invisible $\pi^0$ contamination . . . . .	130
6.3	Evaluation of the sharing ratio between exclusive and semi-inclusive productions . . . . .	131
7	The DVCS contribution at small $\nu$ . . . . .	134
8	Summary and $\phi_{\gamma^*\gamma}$ azimuthal distributions . . . . .	137
<b>VI DVCS CROSS SECTION EVALUATION</b>		<b>139</b>
1	Method of the analysis . . . . .	140
2	Acceptance determination . . . . .	141
3	The DVCS cross section evaluation . . . . .	145
4	Study of the $ t $ -dependence of the DVCS cross section . . . . .	147
4.1	Fitting procedure to extract the B slope . . . . .	147
4.2	Systematic studies . . . . .	149
5	Study of the $\phi_{\gamma^*\gamma}$ azimuthal dependence of the DVCS cross section . .	154
6	Interpretation, comparison to other results and prospects . . . . .	156
<b>A CAMERA description and calibrations</b>		<b>161</b>

<b>B Additional content: Bethe-Heitler comparison per period and beam charge</b>	<b>171</b>
<b>C Optimized kinematical generation</b>	<b>175</b>
<b>Synthèse en français</b>	<b>177</b>

---

## Acronyms

---

**CFF** Compton Form Factor

**ES** Elastic Scattering

**FF** Form Factor

**GPD** Generalised Parton Distribution

**HEMP** Hard Exclusive Meson Production

**PDF** Parton Distribution Function

**QCD** Quantum Chromo Dynamics

**TCS** Time-like Compton Scattering



---

## INTRODUCTION

---

About a century ago, the picture of the atom was completed by J.J. Thomson, E. Rutherford and J. Chadwick with experimental proofs of the existence of electrons, and the nucleons (protons and neutrons). Nevertheless, the proton and neutron, the supposedly building blocks of what composes more than 99% of the mass of the visible universe, remain still flabbergastingly mysterious, and the question persists: what is a proton ?

At the end of the 60s, the SLAC collaboration shed light on the complex nature of nucleons and provided the root of our understanding. Following this, the Parton model was developed, where the nucleon is considered as a composite particle made out of partons (quarks and gluons). The success of the model led to the construction of the Quantum Chromo Dynamics (QCD), which is nowadays part of the Standard Model. Nevertheless some parts of QCD are not yet fully understood. The field of hadronic physics consists in the study of confined states of QCD, such as nucleons (under the denomination of hadrons), and especially how they are made up out of quarks and gluons. Even if we are able to write the proper QCD equations for the partons, it is presently impossible to formally or analytically derive the properties of the hadrons. However, in response of this gridlock, a numerical implementation of QCD rule called Lattice QCD, is possible and reproduces successfully most of the hadron properties. One explanation of the difficulty to solve QCD equations is displayed in **Fig. (1)**, which shows the evolution of the strong coupling constant  $\alpha_S$  as a function of the energy scale. In the high energy domain, the coupling constant is small and shows a property called *asymptotic freedom*. In this domain, perturbative treatments can be employed (through the Feynman diagram formalism). On the contrary, these tools cannot be used in the low energy domain, where  $\alpha_S$  becomes larger, and other solutions need to be studied.

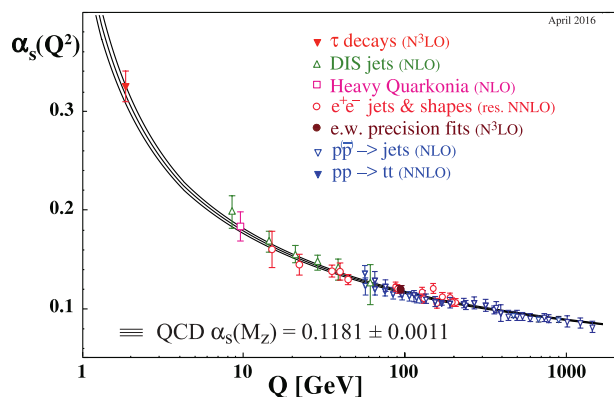


**Figure 1:** Evolution of the QCD coupling constant as function of the energy scale.

Nevertheless the Parton Model suggested also a remarkable property which is called *QCD factorization*. It says that a large class of cross sections on the nucleon can be

factorized into a short-distance (hard) part calculable and a long-distance (soft) part which accounts for the structure of the nucleon.

- The short distance (hard) part describes how the probe interacts with almost free constituents of the nucleon due to the asymptotic freedom property. As short distances mean high-energies, such interaction is perturbative by nature and therefore calculable.
- The large distance (soft) part contains the information of the structure of the nucleons, and how the constituents behave within it. This contribution can be parametrised by intrinsically non-perturbative objects to account for the phase space distributions of the components of the nucleon. These objects are universal and independent of the probe.

Examples of these objects are Form Factors measured in elastic scattering and Parton Distribution Functions measured in Deep Inelastic Scattering. These essential but incomplete descriptions of the hadron structure are now unified under more general objects as the Generalised Partons Distributions which can be accessed through Deeply Virtual Compton Scattering (DVCS) experiments.

The first part of this thesis will introduce some interpretations of GPDs and their link to the DVCS process. The DVCS process is associated with the well known Bethe-Heitler process, so we have to deal with their interferences and consider the global process, called exclusive single photon production. The potential of a DVCS experiment realized at COMPASS using the polarized positive and negative muon beams will be discussed and a selection of similar experiments made around the world will be presented.

The COMPASS experiment will be further developed in the second part, showing the experimental apparatus and detection techniques involved. After a pilot run in 2012 with promising results produced, a dedicated data-taking was performed in 2016-2017. The third part will show the data quality and different tools needed to measure the absolute cross section for the DVCS process, such as the flux calculation and the electromagnetic calorimeter qualification. In the fourth part, the focus will be put on exclusive reactions by studying the recoiled proton detector. In addition, a multidimensional analysis tool will be presented to be further used.

The fifth part will explain the single exclusive photon event selection with a comparison to a dedicated Monte carlo simulation. Results will be highlighted regarding the Bethe-Heitler prediction and the inherent  $\pi^0$  contamination within the data, which are essential to extract the DVCS contributions. Finally the sixth part will present the results on the DVCS cross section measurement and its  $t$ -slope dependency, which is related to the transverse extension of partons in the proton.

# CHAPTER I

---

## THE NUCLEON STRUCTURE

---

### Contents

---

<b>1</b>	<b>Probing the structure of hadrons</b> . . . . .	<b>4</b>
1.1	Wigner distributions . . . . .	4
1.2	GTMDs and projections . . . . .	5
<b>2</b>	<b>Elastic scattering and Form Factors</b> . . . . .	<b>7</b>
<b>3</b>	<b>Deep inelastic scattering and Parton Distribution Functions</b> . . . . .	<b>10</b>
<b>4</b>	<b>Generalised Partons Distributions</b> . . . . .	<b>14</b>
4.1	QCD factorisation and twist . . . . .	15
4.2	Support and partonic interpretations . . . . .	15
4.3	Properties and impact parameter . . . . .	17
4.4	Double distributions and D-term . . . . .	19
<b>5</b>	<b>Accessing GPDs through DVCS experiments</b> . . . . .	<b>20</b>
5.1	Compton Form Factors . . . . .	20
5.2	Interferences and cross section . . . . .	22
5.3	Beam charge and helicity measurements at COMPASS . . . . .	23
5.4	Overview on other experiments . . . . .	25

---

This chapter gives an overview of the theoretical concepts and the experimental knowledge on the study of nucleon structure. This non-exhaustive review is inspired from the work of Markus Diehl [1], Cédric Mezrag [2] and Nabil Chouika [3] for the theoretical parts, while the introduction is inspired from the very comprehensive "CEA highlight" written by Hervé Moutarde [4]. The nucleon is made out of quarks, antiquarks and gluons gathered under the denomination of partons, and their interaction is governed by quantum chromodynamics (QCD). The Wigner distributions are first introduced as the most general objects encompassing the phase space information of the partons, which are nowadays only accessible through their projections. The zoology of these projections and the links between them will be depicted. Furthermore, the experimental access to some of them will be developed, such as through elastic scattering or deep inelastic processes. Finally, the emphasis will be put on a 3-dimensional projection of the Wigner distributions called Generalised Partons Distributions. They are accessible in suitable exclusive processes such as deeply virtual Compton scattering, which is the subject of this thesis.

## 1 Probing the structure of hadrons

*Can one hear the shape of a drum ?* This question was raised by M. Kac in 1966 as a leisure exercise within the very active fields of functional analysis and integral equations [5]. It has been proven that a drum obeys the wave equation, so that one can calculate its frequencies if the shape is known. However the inverse problem is much more complicated, and it is fair to ask whether one can retrieve the shape of a drum based on the analysis of its harmonics. In the general case, a negative response was raised first in 16 dimensions, and in a more elegant way in 2 dimensions in 1992 [6]. Nevertheless one can still extract relevant information such as the perimeter, the number of holes, the area, the convexity, and research is still ongoing to understand what more can be extracted from the harmonic analysis.

The harmonic or spectral analysis has been thoroughly developed and used in various applications from mathematics to physics under the more general notion of signal processing. This field of study is based on the concept of distribution introduced by Laurent Schwartz in 1950 [7], and concerns the interpretation of signals, and also the underlying inverse problems. In a similar way, in the case of hadronic physics and the study of the proton structure, one can ask how much information we can recover from experimentally accessible observables. Quaint correspondences can be found between signal processing and quantum physics, such as the well-known concept of auto-correlation of a signal, leading us to the notion of Wigner distributions.

### 1.1 Wigner distributions

Before introducing the physics, it is useful to define the mathematical framework for the objects we will consider. Classical mechanics obeys the rules of symplectic geometry [8], at the interface of differential geometry and dynamic systems. It consists in the study of closed nondegenerated 2-forms within a so-called phase space (a differentiable manifold) of even dimension  $2n$ . The phase space is decomposed into a position and a momentum space, each of dimension  $n$ , and these two subspaces are conjugated one from the other through the Fourier transform.

As mentioned before, Wigner introduced in 1932 a fundamental function called the Wigner-Ville distribution [9], defined as a generalisation of the auto-correlation concept to quantum mechanics defined as follow. Let  $q$  be a generalised position, and  $p$  a generalised momentum, and taking a wave function  $\psi(q)$  in the position space, we define

$$W(q, p) = \int_{-\infty}^{+\infty} dz e^{ipz} \psi^*(q - z) \psi(q + z) \quad (\text{I.1})$$

In signal processing, this function is used to provide a time-frequency representation of a signal (replacing  $q$  by the time and  $p$  by the frequency). It is interpreted as the power spectral density of the signal in the classical limit. In the general case of quantum physics this interpretation does not stand due to the fact that the Wigner distribution encompasses information on the interference and is therefore not positive-definite on the quantum scale[10]. However it is still possible to compute the expectation value of an operator  $\mathcal{O}(q, p)$  by evaluating the following convolution product [10]:

$$\langle \mathcal{O} \rangle = \int d^3q d^3p \mathcal{O}(q, p) W(q, p) \quad (\text{I.2})$$

The Wigner distribution has the remarkable property of being equivalently defined in the momentum space through the Fourier transform  $\hat{\psi}(p)$  of  $\psi(q)$ . In addition the associated spatial distribution can be retrieved by integrating over the generalised momentum.

In the same way, the momentum distribution is also computed by integrating on the generalised position.

This formalism can be extended in the case of quantum field theory, or in other words in the relativistic case. Considering the field  $\Psi^f$  of a quark of flavour  $f$ , we define the Wigner operators:

$$\mathcal{W}_\Gamma^f(q, p) = \int d^4z e^{ipz} \bar{\Psi}^f(q-z) \Gamma \mathcal{L} \Psi^f(q+z) \quad (\text{I.3})$$

where  $q$  is the space-time position of the quark and  $p$  its 4-momentum.  $\Gamma$  is a Dirac operator and  $\mathcal{L}$  is a Wilson line ensuring gauge invariance. By construction, and similarly to their non-relativistic counterparts, the Wigner operator encompasses all information on the momentum and space distributions of a quark, as their correlations. As in signal processing, they can be understood as the auto-correlation of the wave function  $\Psi^f$ .

As the parton is part of a hadronic system (we will consider the proton in this case), we can define the Wigner distributions by sandwiching the Wigner operator  $\mathcal{W}_\Gamma^f$  between an initial and final proton state  $|P\rangle$  and  $|P'\rangle$  of respective momentum  $p$  and  $p'$ :

$$W_\Gamma^f(q, p) = \int \frac{d^4\Delta}{(2\pi)^4} \langle P' | \mathcal{W}_\Gamma^f(q, p) | P \rangle \quad (\text{I.4})$$

where  $\Delta = p - p'$  the momentum difference between the initial and final proton.

This distribution represents the auto-correlation (or convolution) of the proton in the initial state with the proton in the final state. As the proton momentum is in general not the same in the initial and final state, such operator probes the *interference* between different quantum fluctuations of the proton [1].

## 1.2 GTMDs and projections

The Wigner distributions introduced in the previous section are used in the field of quantum tomography to provide a phase space image of the proton. However these distributions do not have any straightforward physical interpretation due to relativistic corrections. Nevertheless, Lorcé and Pasquini [11] have introduced 5-dimensional objects allowing direct interpretation in the frame where the hadron under consideration moves fast in a certain direction. Such object encompasses the phase space distribution of partons within hadrons. For illustrative purposes and definiteness, **Fig. (I.1)** displays a general diagram where it is symbolised by a blob. The double lines stand for the hadron, while the simple lines represent a single parton within the hadron. We introduce  $P$  the hadron's average 4-momentum,  $\Delta$  the 4-momentum transfer and  $k$  the probed parton's average 4-momentum.

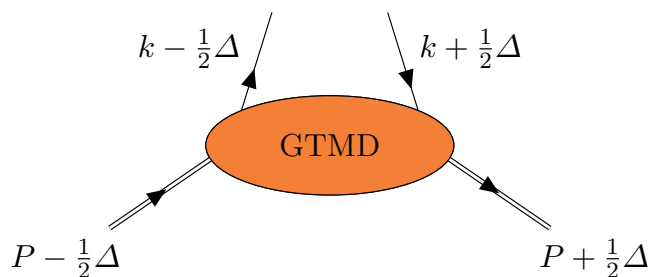


**Figure I.1:** GTMD diagram and momentum assignments.

We consider the infinite momentum frame (IMF) as the reference frame where the hadron moves fast in the positive  $z$ -direction, or in other words where  $P^+$  is large. This choice naturally promotes the  $z$ -direction as *longitudinal* in opposition to the *transverse* directions indexed by the symbol  $\perp$ .

For convenience we introduce the light-cone coordinates for a Minkowski space, defined by the Sudakov 4-vectors  $\tilde{p}$ ,  $\tilde{n}$ , such that:

$$\tilde{p} = \frac{1}{\sqrt{2}} \begin{pmatrix} 1 & 0 & 0 & 1 \end{pmatrix}^T \quad \tilde{n} = \frac{1}{\sqrt{2}} \begin{pmatrix} 1 & 0 & 0 & -1 \end{pmatrix}^T \quad (\text{I.5})$$

We also define  $v^\pm = v^0 \pm v^3$  and  $v_\perp = \begin{pmatrix} 0 & v^1 & v^2 & 0 \end{pmatrix}^T$ ; therefore any 4-vector  $v$  can be written as:

$$v = v^+ \cdot \tilde{p} + v^- \cdot \tilde{n} + q_\perp \quad (\text{I.6})$$

Using these notations, the above-mentioned 5-dimensional Wigner distributions are parametrised by  $(x, k_\perp, b_\perp)$ , where  $b_\perp$  and  $k_\perp$  are respectively the average transverse position and momentum of the parton, and  $x = \frac{k^+}{P^+}$  its average longitudinal momentum fraction with respect to the hadron, as illustrated in **Fig. (I.2a)**. At this step, one should note that *average* positions (resp. momentum) are Fourier conjugate of *differences* of momenta (resp. positions). Particularly,  $b_\perp$  and  $\Delta_\perp$  are Fourier conjugate variables. That being said, the previous 5-dimensional Wigner distributions are related through a Fourier transform over  $b_\perp$  to objects called Generalised Transverse Momentum Distributions (GTMDs). These distributions are thus functions of  $(x, k_\perp, \Delta_\perp)$ . The GTMDs allow simpler interpretations and are considered as mother distributions among the zoology of existing objects as shown in **Fig. (I.2b)**.

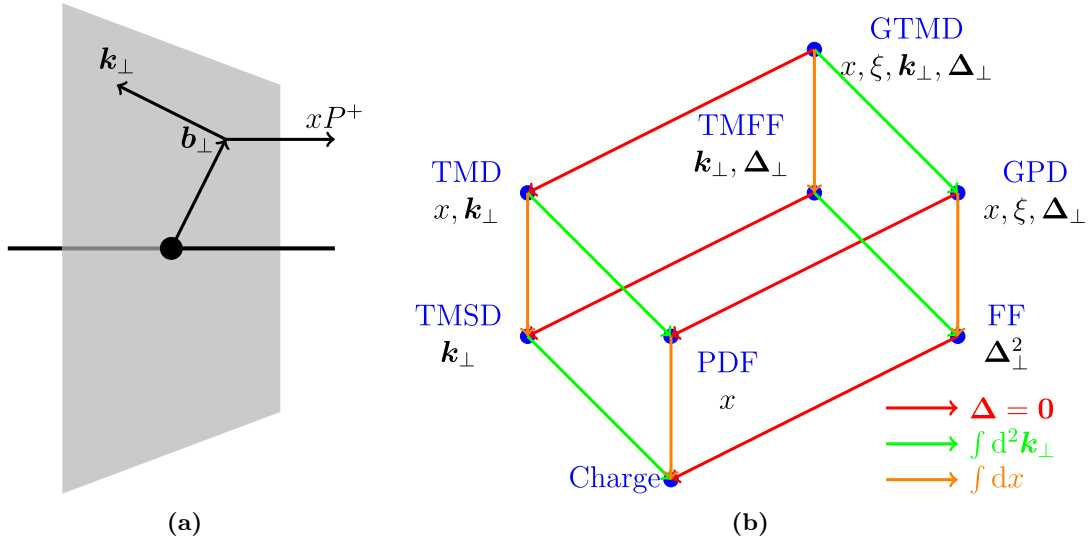


**Figure I.2:** (a) Transverse plane representation of the GTMDs variables. (b) Relationship between different projections of GTMDs (or equivalently 5-dimensional Wigner distributions). Taken from [3].

From the previous paragraph, we also note that the parameters  $b_\perp$  and  $\Delta_\perp$  are Fourier conjugates. Thus, integrating over  $b_\perp$  is strictly equivalent as setting  $\Delta_\perp = 0$ . Moreover, **Fig. (I.2b)** also introduces the additional variable  $\xi = -\frac{\Delta^+}{2p^+}$ , called the skewness parameter; it corresponds to the longitudinal momentum transfer of the active quark. This additional parameter stands for phenomenological reasons: a vanishing skewness corresponds to a purely transversely probed hadron, and is crucial for theoretical interpretations. However this condition is hardly reachable for experimental reasons, and phenomenological tools have been developed to extrapolate the data to  $\xi = 0$ .

Nowadays research is ongoing in order to retrieve information on the Wigner distributions from physics processes. Since more than 50 years, a lot of information on the nucleon

structure has been given by Form Factors (FFs) measured in Elastic Scattering experiments (ES) and by Parton Distributions Functions (PDFs) measured in Deep Inelastic Scattering experiments (DIS). Both of these objects are 1-dimensional projections of the Wigner distributions. Generalised Partons Distributions (GPDs) introduced at the end of the 90's [12, 13, 14, 15, 16] will finally provide the bridge between these two fundamental quantities. These objects describe the correlations between the longitudinal momentum information held by PDFs and the transverse position distribution given by FFs, and are the subjects of this thesis.

In addition, other projections have to be mentioned such as Transverse Momentum Distributions (TMDs). They give complementary information through the correlations between longitudinal and transverse momentum, and can be reached by the means of processes such as Semi-Inclusive DIS (SIDIS) or Drell-Yan (DY).

## 2 Elastic scattering and Form Factors

Elastic scattering was at the basis of historical experiments to determine the structure of the nuclei and nucleon. In 1911, Rutherford used this technique with an  $\alpha$  particle beam impinging on a gold foil to reveal the structure of atom [17]. In 1956, Hofstadter [18, 19] used the 600 MeV electron beam available at the HEP Laboratory of Stanford to measure the radius of the proton. **Fig. (I.4)** shows the Feynman diagram at lowest order of elastic scattering of a lepton  $l$  off a proton  $P$  with the hypothesis of a single photon exchange. The kinematic variables involved are defined by:

- $k = (E, \mathbf{k})$  the 4-momentum of the incoming lepton of mass  $M_l$
- $k' = (E', \mathbf{k}')$  the 4-momentum of the outgoing lepton
- $\theta_l$  the scattering angle between the two leptons in the laboratory frame
- $q = (k - k')$  the 4-momentum of the virtual photon exchanged
- $Q^2 = -q^2$  the virtuality of the exchanged photon. In the laboratory frame and if  $M_l \ll |\mathbf{k}|$  we can write  $Q^2 = 4EE' \sin^2(\theta_l/2)$

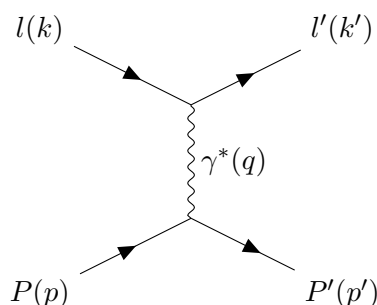


**Figure I.3:** Elastic scattering of a lepton off a point-like particle

If we do not consider the spins of the probe and the target, and if we assume a massless lepton  $M_l \ll |\mathbf{k}|$  and an infinite proton mass  $M_p \gg |\mathbf{k}|$

$$\left(\frac{d\sigma}{d\Omega}\right)_{\text{Rutherford}} = \frac{\alpha_{\text{em}}^2}{16E^2 \sin^4\left(\frac{\theta_l}{2}\right)} \quad (\text{I.7})$$

where  $\alpha_{\text{em}} = \frac{e^2}{4\pi} \approx \frac{1}{137}$  is the electromagnetic fine structure constant. It has to be noted that at fixed beam energy, the system is described by only one kinematic variable, either  $Q^2$  or  $\theta_l$ . If we now consider the spins of the probe and the target and include relativistic effects, we can derive the Mott cross section as follows:

$$\left(\frac{d\sigma}{d\Omega}\right)_{\text{Mott}} = \frac{\alpha_{\text{em}}^2}{4E^2 \sin^4\left(\frac{\theta_l}{2}\right)} \frac{E'}{E} \left[ \cos^2 \frac{\theta_l}{2} + \frac{Q^2}{2M_p^2} \sin^2 \frac{\theta_l}{2} \right] \quad (\text{I.8})$$

The Mott formula only applies for point-like particles, or in other words for low energetic processes (defined by  $Q^2 \ll M_p^2$ ). In this case the distance scanned by the photon probe is bigger than the size of the proton, and therefore considers the latter as point-like. This comes from the Fourier conjugated nature of position and momentum; a higher momentum for the photon will be able to probe smaller distances.

Therefore, one can scan smaller distances and probe the inner structure of the target, by increasing the virtuality of the photon  $Q^2$ . This is experimentally achieved by increasing the lepton beam energy. In this case, we have to consider the target as an extended object. This differentiation is displayed by the blob in the diagram **Fig. (I.4)**.

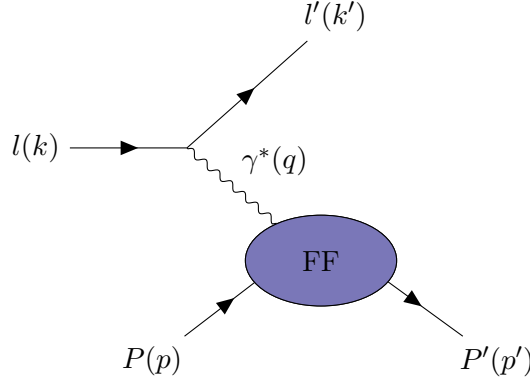


**Figure I.4:** Diagram of elastic scattering with a single photon exchange

Two Form Factors (FFs) are actually necessary and were introduced by Rosenbluth in 1950 in order to generalise the point-like Mott cross section to the extended target case [20]. The elastic scattering cross section finally reads:

$$\frac{d\sigma}{d\Omega} = \frac{\alpha_{\text{em}}^2}{16E^2 \sin^4\left(\frac{\theta_l}{2}\right)} \frac{E'}{E} \left[ \frac{G_E^2(Q^2) + \tau G_M^2(Q^2)}{1 + \tau} \cos^2\left(\frac{\theta_l}{2}\right) + 2\tau G_M^2(Q^2) \sin^2\left(\frac{\theta_l}{2}\right) \right] \quad (\text{I.9})$$

with  $\tau = \frac{Q^2}{4M_p^2}$ .  $G_E$  and  $G_M$ , given in unit of  $e$  and  $\mu_N = e\hbar/2M_p$ , are the electric and magnetic Sachs Form Factors respectively. The values of the two Form Factors  $G_E$  and  $G_M$  can be disentangled by measuring the cross section at the same  $Q^2$  but different beam energies. This method is called the Rosenbluth separation. Another parametrisation of the form factors was originally obtained using the Dirac and Pauli Form Factors. Their relations to the previous ones are:

$$\begin{aligned} F_1(Q^2) &= \frac{G_E(Q^2) + \tau G_M(Q^2)}{1 + \tau} \\ F_2(Q^2) &= \frac{G_M(Q^2) - G_E(Q^2)}{1 + \tau} \end{aligned} \quad (\text{I.10})$$

In a non relativistic interpretation with the following assumptions, the proton does not recoil,  $M_p \rightarrow \infty$  and  $Q^2 \ll M_p^2$ , the two Form Factors  $G_E(Q^2)$ ,  $G_M(Q^2)$  can be interpreted as the Fourier transform of the nucleon charge and magnetic distributions respectively.

$$G_E(\vec{q}) = \int \rho_E(\vec{r}) e^{i\vec{q}\cdot\vec{r}} d^3\vec{r} = 1 - \frac{q^2}{6} \langle r^2 \rangle + \mathcal{O}(q^4) \quad (\text{I.11})$$

The same equation stands for the magnetisation density. For these reasons we define the charge and magnetic proton radii as:

$$\langle r_{E/M}^2 \rangle = -6 \left. \frac{dG_{E/M}(Q^2)}{dQ^2} \right|_{Q^2=0} \quad (\text{I.12})$$

As of today, different techniques exist for the evaluation of the proton charge radius. Until 2010, the value derived from elastic cross section experiments (and Form Factors measurements) was 0.879(8) fm [21], and an alternative approach studying the spectroscopy of the hydrogen atom was providing a compatible value [22] as shown in two first entries of [Table \(I.1\)](#).

Institute or Collaboration	Determination method	$\sqrt{\langle r_E^2 \rangle}$ [fm]	Ref.
MAMI	e-p scattering	0.879(8)	[21]
CODATA	H and D spectroscopy	0.8759(77)	[22]
Max Planck Institute	Muonic hydrogen spectroscopy	0.84184(67)	[23]
PRad	e-p scattering	0.831(7 <sub>stat</sub> 12 <sub>sys</sub> )	[24]

**Table I.1:** Comparison of proton charge radii from different techniques in 2010

However in 2010, the Max Planck Institute of Munich obtained a result from the measurement of the lamb shift of muonic hydrogen spectroscopy, which was 0.841 84(67) fm, almost 5 standard deviations away from the CODATA value [23]. At this time, the origin of this discrepancy was commonly referred as the "proton radius puzzle". After 2010, new measurements have been performed on electronic and muonic hydrogen spectroscopy, and they seem to confirm a small radius. In addition, recent results from the PRad experiment at JLab, using electron proton scattering, are close to the muonic hydrogen spectroscopy ones [24]. Many theoretical developments have been performed to extract the derivative of the Form Factor at  $Q^2 = 0$  in a domain where there is exactly no measurement. Some of them [25] combine dispersion analysis and chiral effective field theory to implement the dynamics governing the shape of the low- $Q^2$  Form Factors. Recently another procedure has been applied [26]. It is based on interpolation via continued fractions supplemented by statistical sampling. This avoids assumptions about the function form. All these new theoretical analyses seem to confirm a small radius. At present new experimental program has started at JLab called PRad-II, which aims at reducing the experimental uncertainties of PRad by a factor 2.5. In parallel of this, other electron-proton scattering experiments are under preparation at MAMI, as well as muon-proton scattering at MUSE (PSI) and AMBER (CERN). All these complementary measurements might help unravelling the proton radius puzzle in the near future.

### 3 Deep inelastic scattering and Parton Distribution Functions

In the late 1960's a 20 GeV experimental program started at the Stanford Linear Accelerator (SLAC). The Deep Inelastic Scattering (DIS) process focuses on electron-proton collisions with a high virtuality with respect to the proton mass  $Q^2 \gg M_p$ . In this case the proton is likely to break-up, so that the hadronic final state is represented by the label  $X$  in **Fig. (I.5)**.

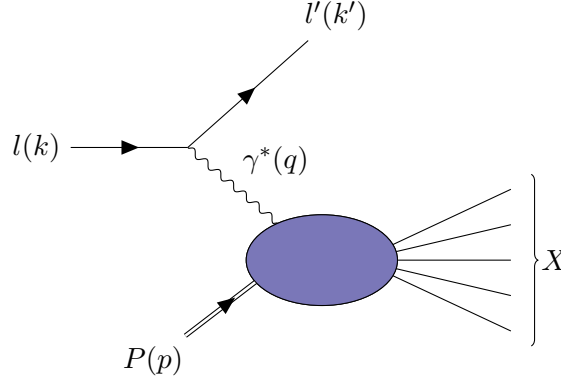


**Figure I.5:** Diagram of Deep Inelastic Scattering with a single photon exchange

In the DIS case, it is convenient to define additional variables

- $\nu = E - E'$  the energy difference between the incoming and outgoing lepton
- $y = \frac{q \cdot p}{k \cdot p}$  the lepton's energy loss. In the nucleon rest frame, we can rewrite  $y = \nu/E$
- $x_B = \frac{Q^2}{2p \cdot q}$  the Bjorken variable. In the nucleon rest frame we have  $x_B = \frac{Q^2}{2M_p \nu}$ .
- $W^2 = (p + q)^2 = M_p^2 + Q^2 \left( \frac{1}{x_B} - 1 \right)$  the invariant mass of the hadronic final state

The Bjorken variable  $x_B$  is a dimensionless scaling parameter of the DIS process, and represents the elasticity of the process ; for elastic collisions where the proton remains intact,  $x_B = 1$ . Thus, DIS processes are also characterized by  $W^2 \gg M_p^2$ . In this section we will consider a modern approach of DIS, laying on Quantum ElectroDynamics (QED) considerations. From **Fig. (I.5)** we introduce two bilinear forms ; one called leptonic tensor  $L_{\mu\nu}$  and a second one called hadronic tensor  $W^{\mu\nu}$ , both coupled to the exchanged virtual photon at the upper and lower vertices respectively. In lowest-order perturbation theory, the cross section then reads:

$$\frac{d\sigma}{d\Omega dE'} = \frac{\alpha_{em}^2}{Q^2} \frac{E'}{E} L_{\mu\nu} W^{\mu\nu} \quad (\text{I.13})$$

Both tensors are usually decomposed in their symmetric and anti-symmetric decomposition with the following convention

$$\begin{aligned} L_{\mu\nu} &= L_{\mu\nu}^{(S)} + iL_{\mu\nu}^{(A)} \\ W^{\mu\nu} &= W_{\mu\nu}^{(S)} + iW_{\mu\nu}^{(A)} \end{aligned} \quad (\text{I.14})$$

Introducing **Eq. (I.14)** in **Eq. (I.13)** the DIS cross section becomes

$$\frac{d\sigma}{d\Omega dE'} = \frac{\alpha_{em}^2}{Q^2} \frac{E'}{E} \left( L_{\mu\nu}^{(S)} W^{(S)\mu\nu} - L_{\mu\nu}^{(A)} W^{(A)\mu\nu} \right) \quad (\text{I.15})$$

The symmetric part of the hadronic tensor accounts for the unpolarised proton target case, and is parametrised by the two structure functions  $W_1$  and  $W_2$ . The unpolarised cross section is given by:

$$\frac{d\sigma}{d\Omega dE'} = \frac{\alpha_{\text{em}}^2}{4E^2 \sin^4\left(\frac{\theta_l}{2}\right)} \left[ W_2(x_B, Q^2) \cos^2\left(\frac{\theta_l}{2}\right) + 2W_1(x_B, Q^2) \sin^2\left(\frac{\theta_l}{2}\right) \right] \quad (\text{I.16})$$

At fixed beam energy, and contrary to the elastic case, DIS is described by two free variables, usually  $(x_B, Q^2)$ . The elastic cross section written in **Eq. (I.9)** can be recovered from the inelastic case by setting  $x_B = 1$  and integrating over  $E'$ . Introducing the Dirac distribution  $\delta$  we can therefore write:

$$\begin{aligned} W_1(x_B, Q^2) &= \frac{G_M^2(Q^2)}{2M_p} \delta(x_B - 1) \\ W_2(x_B, Q^2) &= \frac{2M_p}{Q^2} \frac{G_E^2(Q^2) + \tau G_M^2(Q^2)}{1 + \tau} \delta(x_B - 1) \end{aligned} \quad (\text{I.17})$$

These considerations can be developed in the context of the Parton model, considering the hadrons as a composed system. This idea was first raised by Gell-Mann and Zweig [27, 28], who introduced the *Eightfold Way* in order to classify the existing zoology of hadrons under the symmetries of the  $SU(3)$  Lie group. In algebraic terms, this refers to the fact that the  $SU(3)$  Lie group has an associated Lie algebra (or tangent space at the origin) of dimension 8. The Parton model was introduced in 1969 by Richard Feynman [29], and considers the hadrons as composed of point-like constituents named partons.

This model was immediately applied to deep inelastic scattering by Bjorken [30]. At high enough energies, we can consider that the photon interacts directly with the constituents of the proton. For this specific element, the elastic scattering  $q\gamma^*$  features a partonic cross section which is inferred from **Eq. (I.13)**, but involving trivial structure functions  $W_1^q$  and  $W_2^q$ . These structure functions are the point-like particle counterpart of **Eq. (I.17)**, *i.e.*  $G_E = G_M = e_q$  the parton's charge:

$x_q$  is the fraction of the proton momentum  $P$  carried by one of these constituents, noted  $p_q = x_q P$

$m_q = x_q M_N$  is the mass of the considered parton

$x_B^q = \frac{Q^2}{2m_q\nu} = x_B/x_q$  the fractional Bjorken variable for the considered parton.

$$\begin{aligned} W_1^q &= \frac{e_q^2}{2m_q} \delta(x_B^q - 1) = \frac{e_q^2}{2M_p} \delta(x_B - x_q) \\ W_2^q &= \frac{2m_q}{Q^2} e_q^2 \delta(x_B^q - 1) = \frac{2M_p x_q^2}{Q^2} e_q^2 \delta(x_B - x_q) \end{aligned} \quad (\text{I.18})$$

The nucleon's structure functions  $W_1$  and  $W_2$  can be related to the previous ones by incoherently summing over all the partonic contributions within the proton. By noting  $q(x_q)$  the probability of striking a parton with a momentum fraction  $x_q$ , we can write:

$$\begin{aligned} W_1 &= \sum_q \int_0^1 dx_q W_1^q q(x_q) = \frac{1}{2M_p} \sum_q e_q^2 q(x_B) \\ W_2 &= \sum_q \int_0^1 dx_q W_2^q q(x_q) = \frac{2M_p x_B^2}{Q^2} \sum_q e_q^2 q(x_B) \end{aligned} \quad (\text{I.19})$$

We also define the DIS structure functions originally introduced by Bjorken:

$$\begin{aligned} F_1^{\text{DIS}} &= M_p W_1 = \frac{1}{2} \sum_q e_q^2 q(x_B) \\ F_2^{\text{DIS}} &= \frac{Q^2}{2M_p x_B} W_2 = x_B \sum_q e_q^2 q(x_B) \end{aligned} \quad (\text{I.20})$$

The Parton model was successfully validated by experiments [31, 32] in the '60s, where three results were retrieved.

1. The Bjorken scaling law, stating that in the Bjorken limit of high  $Q^2$  and fixed  $x_B$ , the two structure functions  $F_1^{\text{DIS}}$  and  $F_2^{\text{DIS}}$  do not depend on  $Q^2$ . This is a consequence of the point-like nature of partons.
2. The Callan-Gross relation **Eq. (I.21)** was also confirmed, which is a consequence of the spin 1/2 nature of the quarks.

$$2x_B F_1^{\text{DIS}}(x_B) = F_2^{\text{DIS}}(x_B) \quad (\text{I.21})$$

3. The DIS cross section has been factorised in 2 terms: one for the evaluation of the elementary interaction between the virtual photon probe  $\gamma^*$  and the struck parton (with  $x = x_B$ ) and one for the PDF describing the proton. Therefore, the Parton Model implies a factorisation between the hard scattering with partons (*i.e.* small distance) and the soft physics (*i.e.* large distance) containing the PDF  $q(x)$ .

However, it has to be noted that the parton model only corresponds to the leading order results in  $\alpha_S$  of perturbative QCD. Indeed the proton constituents are not only composed of quarks, but also gluons, which only contribute at Next Leading Order (NLO). In addition, **Fig. (I.6a)** shows the evolution of the structure function  $F_2^{\text{DIS}}$  at different  $x_B$  and  $Q^2$  values. The experimental results obtained in the '60s was restricted to a smaller phase space region where  $F_2$  displays a rather flat evolution in  $Q^2$ . Nowadays the larger kinematical coverage presented indicates a  $Q^2$  dependence. This behaviour is called scaling violation but does not indicate a substructure of the partons ; this phenomena is fully explained by QCD radiative corrections where the active quark can emit and absorb gluons as shown in **Fig. (I.7)**. This leads to a logarithmic  $Q^2$  dependence which is governed by the DGLAP<sup>1</sup> evolution equations.

It is also worth mentioning the polarised target case, encompassed within the antisymmetric part of the hadronic tensor in **Eq. (I.15)**. The resulting cross section is parametrised by two additional structure functions called  $g_1$  and  $g_2$ , and are usually estimated by the cross section difference for either longitudinally or transversely polarised target in order to vanish the symmetric tensorial contribution.

The Parton model introduces the notion of Parton Distribution Functions (PDFs), as the probability density  $q_f(x_B)$  to find a quark of flavour  $f$  with a momentum fraction  $x_B$ . Therefore the function  $x \mapsto xq_f(x)$  represents the momentum distribution of quarks within the proton. The same definition stands for anti-quarks defining the probability density  $\bar{q}_f(x_B)$ . The evolution of PDFs as function of  $x$  is shown in **Fig. (I.8)**.

Denoting  $e_f$  the electric charge fraction carried by the quark of flavour  $f$  we obtain

$$\begin{aligned} F_1^{\text{DIS}}(x_B) &= \frac{1}{2} \sum_f e_f^2 (q_f(x_B) + \bar{q}_f(x_B)) \\ F_2^{\text{DIS}}(x_B) &= x_B \sum_f e_f^2 (q_f(x_B) + \bar{q}_f(x_B)) \end{aligned} \quad (\text{I.22})$$

---

<sup>1</sup>Dokshitzer, Gribov, Lipatov, Altarelli and Parisi

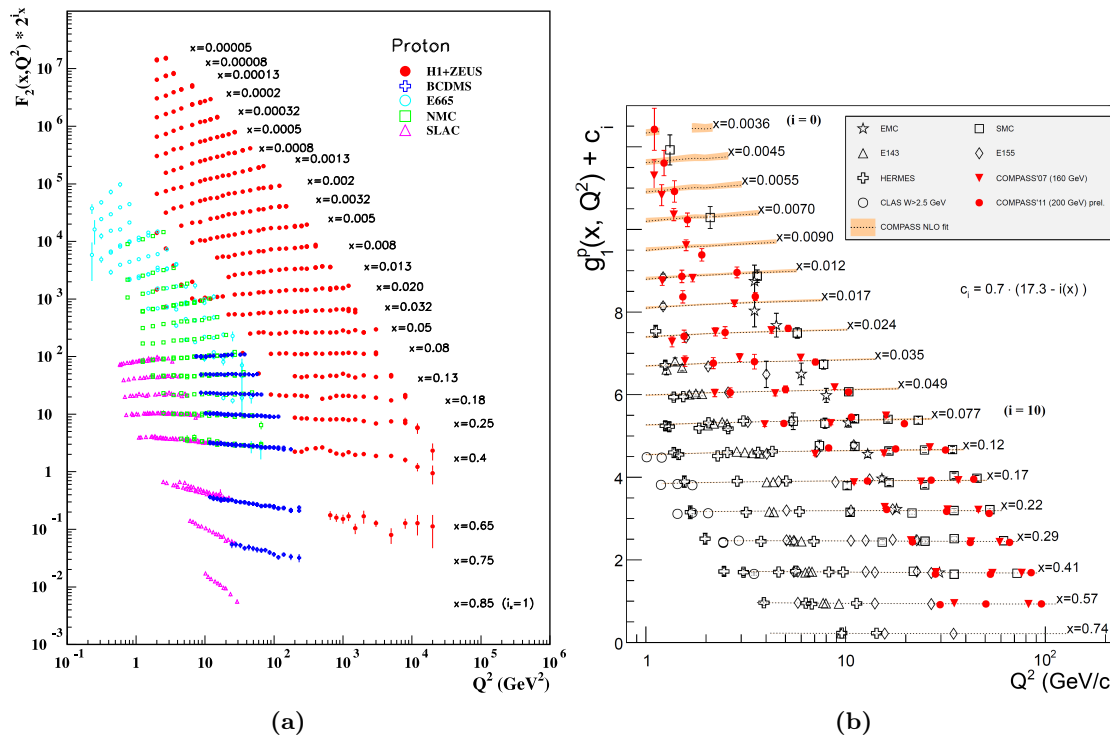


**Figure I.6:** (a) Evolution of  $F_2$  as a function of  $x_B$  and  $Q^2$ . (b) Evolution of  $g_1$  as a function of  $x_B$  and  $Q^2$ . Figures taken from [33].

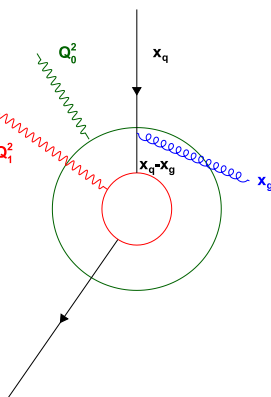


**Figure I.7:** Illustration of the interaction between a virtual photon and a parton. The green parts show the effect of a probe with a smaller virtuality than the red one. The distance scale probed is therefore smaller for the high virtual probe. The blue part illustrates the QCD radiative correction related to the scaling violation. So the virtual photon sees softer quarks.

We can also define polarised PDFs taking into account the quark and nucleon spins. The probability to find a quark of momentum fraction  $x_B$  and a parallel (resp. anti-parallel) helicity to the one of the nucleon is denoted  $q_f^{\rightarrow}(x_B)$ , resp.  $q_f^{\leftarrow}(x_B)$ . This system of variables is usually rewritten by their difference and sum, retrieving in the latter the unpolarised case.

$$\begin{aligned} \Delta q_f(x_B) &= q_f^{\rightarrow}(x_B) - q_f^{\leftarrow}(x_B) \\ q_f(x_B) &= q_f^{\rightarrow}(x_B) + q_f^{\leftarrow}(x_B) \end{aligned} \quad (\text{I.23})$$

With these notations, the structure function  $g_1$  reads

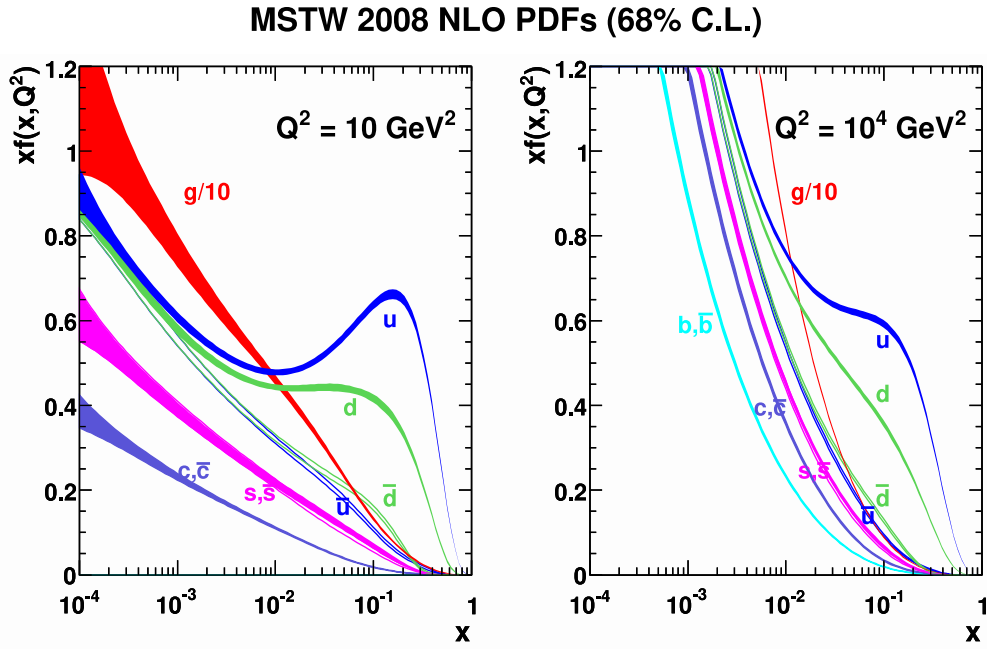


**Figure I.8:** Evolution of PDFs as function of  $x$  for two different  $Q^2$  values. The curves are determined by a fit over a large range of data. Figure taken from [33].

$$g_1(x_B) = \frac{1}{2} \sum_f e_f^2 (\Delta q_f(x_B) + \Delta \bar{q}_f(x_B)) \quad (\text{I.24})$$

The structure function  $g_2$  has no such interpretation within the parton model, and is expected to vanish in some approximations. Its contribution can still be measured in transversely polarised target experiments.

## 4 Generalised Partons Distributions

The concept and formalism of GPDs have been introduced by Dieter Müller [12], Xiangdong Ji [13, 14] and Anatoly Radyushkin [15, 16] at the end of the 90's. As developed in [Section I.1](#), GPDs are three dimensional projections of the Wigner distributions. Particularly, they give access to longitudinal momentum and transverse position distributions of the interacting parton. They also include the 1-dimension projections probed by Elastic Scattering with Form Factors and by Deep Inelastic Scattering with Partons Distribution Functions. This comprehensive three dimensional picture is governed by the GPDs' dependence on three kinematic variables :

- $x = \frac{k^+}{P^+}$  average longitudinal momentum fraction of the active parton  
with  $P = 1/2(p + p')$
- $\xi = \frac{-\Delta^+}{2P^+} = x_B \frac{1 + \frac{\Delta^2}{2Q^2}}{2 - x_B + x_B \frac{\Delta^2}{Q^2}} \approx \frac{x_B}{2 - x_B}$  longitudinal momentum transfer to the parton
- $t = (p - p')^2 = \Delta^2$  squared momentum transfer to the proton  $\Delta = p' - p$

A dependence on the photon virtuality  $Q^2$  is still present and is described by the QCD evolution equations (DGLAP). GPDs can be experimentally accessed by exclusive processes

using the concept of QCD factorisation, and the properties and interpretations of GPDs will be presented in the next sections.

#### 4.1 QCD factorisation and twist

The phenomenology of GPDs infers from QCD factorisation. For illustrative purposes, we will consider the diagram of a specific process involving GPDs called Deeply Virtual Compton Scattering (DVCS) **Fig. (I.9a)**. As shown in the plot, the process can be separated between a hard part consisting in the interaction of a lepton with a point-like constituent of the proton (a small distance phenomena), and the soft physics or large distance phenomena involving the structure functions of the proton such as FFs, PDFs or in this case GPDs. A fundamental corollary of factorisation is the universality of these structure functions. Therefore they can be scanned in different experimental channels like DVCS, TCS (Time-like Compton Scattering), HEMP (Hard Exclusive Meson Production), or Double DVCS.

In the case of DVCS, factorisation was formally brought up by Operator Product Expansion (OPE). Using this tool, the DVCS amplitude can be expanded in a Laurent series of local operators. This expansion introduces the notion of twist, defined as the dimension of these operators minus their spin (their spin being the dimension of their representation in the Lorentz group). The dominant terms of this series are carried by the lowest twist operators (the lowest twist being 2), and in addition the coefficients in front of these local operators can be perturbatively developed in series of  $\alpha_S$ . In conclusion, the DVCS amplitude can be written as a development in twist and in  $\alpha_S$ , and the diagram presented in **Fig. (I.9a)** shows the leading order and leading twist term.

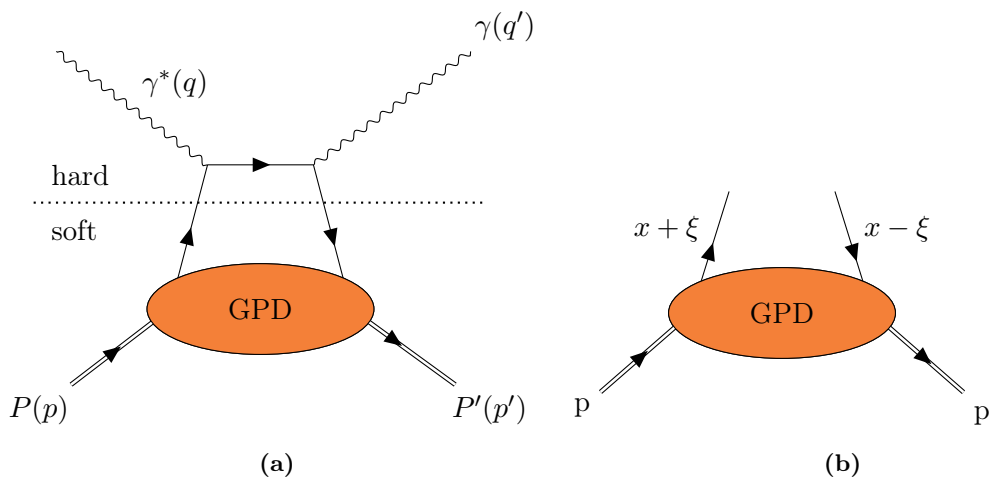


**Figure I.9:** (a): Handbag diagram representing the leading order and leading twist term for DVCS.

(b): GPD diagram and momentum fractions of an active quark.

The experimental study of GPDs is reviewed through the DVCS process in **Section I.5**, and the next section will present some of their properties.

#### 4.2 Support and partonic interpretations

GPDs are associated to the diagram shown in **Fig. (I.9b)**, where an active parton of longitudinal momentum fraction  $x + \xi$  is selected within the proton. The latter interacts before re-integrating the proton with a different longitudinal momentum fraction  $x - \xi$  at a different transverse position. The parton can be either a quark of flavour  $f$  or a gluon,

and defines thus two kinds of GPDs  $F^f$  and  $F^g$  (for lighter notations the superscripts will be dropped except if needed).

The variables  $x$  and  $\xi$  evolve both in the interval  $[-1, 1]$ . By comparing them, the partonic process can be interpreted differently:

- For  $-1 \leq x \leq -\xi \leq 0$ , both momentum fraction  $\xi - x$  and  $-x - \xi$  are negative. In this case the GPDs describe the emission and reabsorption of an antiquark. This domain is referred as the DGLAP region
- For the case  $x \in [-\xi, \xi]$ , one of the momentum fraction is negative, the other one positive. This corresponds to the emission of a pair  $q\bar{q}$  (meson-like). This is the ERBL<sup>2</sup> region, where the GPDs evolve under the so-called evolution equations.
- The region  $0 \leq \xi \leq x \leq 1$  is again the DGLAP region and correspond to a quark emission of momentum  $x + \xi$  and its reabsorbtion with a momentum  $x - \xi$ .

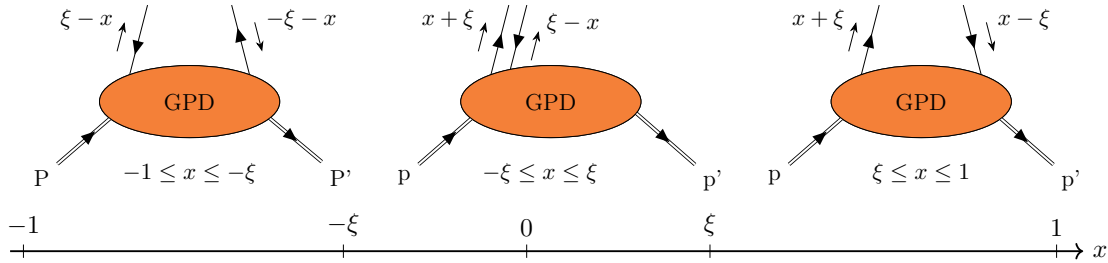


**Figure I.10:** Interpretation of GPDs based on different parts of its support. Adapted from [1].

For each kind of parton (quark or gluon) the different helicity configurations involved lead to eight GPDs, each one accounting for different helicity states of the parton and proton before and after reaction. The GPDs labeled  $H, E, \tilde{H}, \tilde{E}$  conserve the parton helicity as shown in **Fig. (I.11)** and are therefore called chiral-even GPDs, while the ones labeled  $H_T, E_T, \tilde{H}_T, \tilde{E}_T$  do not and are qualified as chiral-odd (or transversity GPDs). The latter GPDs are suppressed by factors of  $1/Q^2$ . The DVCS does not allow parton helicity flip, so we will be focused in this thesis on the chiral-even GPDs and their properties. On the other hand, exclusive meson production allows parton helicity flip, and are also sensitive to chiral-odd GPDs.

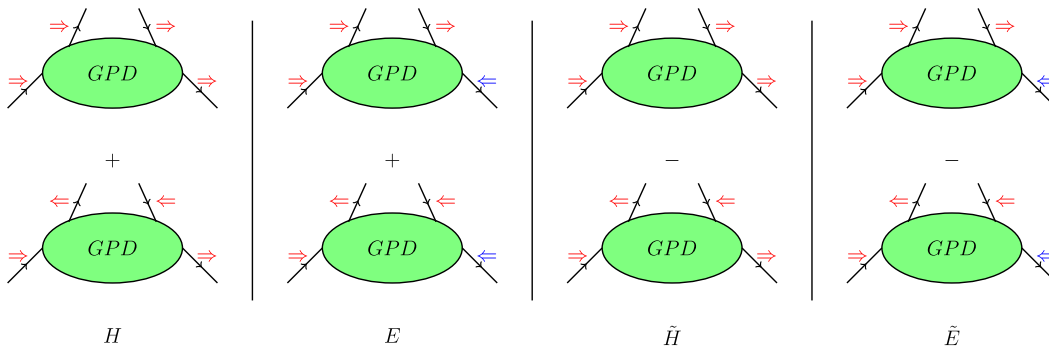


**Figure I.11:** Definition of the chiral-even GPDs from the different configuration of parton and nucleon helicities.

<sup>2</sup>Efremov, Radyushkin, Brodsky, Lepage

### 4.3 Properties and impact parameter

#### Boundary conditions

As displayed in **Fig. (I.2b)**, GPDs encompass the one dimensional projections probed in ES and DIS. Their relation to the elastic Form Factors is shown by the following sum rules:

$$\begin{aligned}
& \forall \xi \in [-1, 1] \\
& \sum_f e_f \int_{-1}^1 dx H^f(x, \xi, t) = F_1(t) \quad \text{the Dirac Form Factor} \\
& \sum_f e_f \int_{-1}^1 dx E^f(x, \xi, t) = F_2(t) \quad \text{the Pauli Form Factor} \\
& \sum_f e_f \int_{-1}^1 dx \tilde{H}^f(x, \xi, t) = G_A(t) \quad \text{the axial Form Factor} \\
& \sum_f e_f \int_{-1}^1 dx \tilde{E}^f(x, \xi, t) = G_P(t) \quad \text{the pseudo-scalar Form Factor}
\end{aligned} \tag{I.25}$$

The axial and pseudo-scalar Form Factors are defined in the Elastic Scattering process where one replaces the virtual photon mediator by a charged or a neutral weak boson respectively. One should note that the integration over  $x$  naturally removes the dependence on the skewness variable  $\xi$  [34], as it removes all references to the longitudinal direction. As stated in **Section I.1**, GPDs' interpretation only holds at vanishing skewness  $\xi = 0$ . Under this condition, a relation to one dimensional PDFs probed in DIS can be retrieved in the so-called forward limit, where  $t \rightarrow 0$ . These relations stand for each quark flavour  $f$ :

$$\begin{aligned}
H^f(x, 0, 0) &= q_f(x) & \tilde{H}^f(x, 0, 0) &= \Delta q_f(x) & \text{for } x > 0 \\
H^f(x, 0, 0) &= \bar{q}_f(-x) & \tilde{H}^f(x, 0, 0) &= \Delta \bar{q}_f(-x) & \text{for } x < 0
\end{aligned} \tag{I.26}$$

Similar relations exist for gluons GPDs. Defining  $g(x)$  and  $\Delta g(x)$  the spin independant and spin dependant gluon densities, we have:

$$H^g(x, 0, 0) = xg(x) \quad \tilde{H}^g(x, 0, 0) = x\Delta g(x) \quad \text{for } x > 0 \tag{I.27}$$

Corresponding relations stand for  $x < 0$  using the symmetry relations for gluon GPDs. However there are no such relations for the GPDs  $E$  and  $\tilde{E}$  [1, p. 15]. They have no counterparts in DIS as they allow for nucleon spin flip (**Fig. (I.11)**).

#### Transverse extension of partons

GPDs encompass the correlations between the longitudinal momentum and the transverse position of the active parton. Especially at  $\xi = 0$ , the incoming and outgoing partons have the same longitudinal momentum  $x$ ; therefore the momentum transfer  $t$  becomes a fully transverse quantity  $t = \Delta_\perp^2$ . Moreover the Fourier conjugate of the transverse momentum difference  $\Delta_\perp$  is the average transverse position  $b_\perp$  as introduced in **Section I.1**. The transverse position is also called impact parameter, and we can derive an impact parameter dependent PDF from the GPD  $H^f$  by its Fourier transform over  $\Delta_\perp$ :

$$q_f(x, b_\perp) = \frac{1}{(2\pi)^2} \int d^2 \Delta_\perp e^{-ib_\perp \cdot \Delta_\perp} H^f(x, \xi = 0, t = -\Delta_\perp^2) \tag{I.28}$$

The resulting distribution is interpreted as the probability to find a parton of flavour  $f$  with a longitudinal momentum  $xP^+$  at the distance  $b_\perp$  from the hadron's transverse centre of momentum [35, 36, 37]. Following this for a certain value of  $x$ , we can compute the dispersion of  $q_f(x, b_\perp)$  through its normalised second moment:

$$\langle b_\perp^2 \rangle_x^f = \frac{\int d^2 b_\perp b_\perp^2 q_f(x, b_\perp)}{\int d^2 b_\perp q_f(x, b_\perp)} = 4 \frac{\partial}{\partial t} \log H^f(x, \xi = 0, t) \Big|_{t=0} \quad (\text{I.29})$$

In addition if we assume the usual ansatz  $H^f \propto e^{B(x)t}$ , one can study the  $t$ -slope of  $\log H^f$  to extract the average transverse extension of partons of flavour  $f$ , which is the subject of this thesis:

$$\langle b_\perp^2 \rangle_x = 4B(x) \quad (\text{I.30})$$

We can also integrate over  $x$  and average over the different quark flavours  $f$  to compute the transverse extension of partons. On the right-hand side we also retrieve the Dirac Form Factor  $F_1$  in place of the GPD  $H^f$  from **Eq. (I.25)**<sup>3</sup>:

$$\langle b_\perp^2 \rangle = \sum_f e_f \frac{\int dx \int d^2 b_\perp b_\perp^2 q_f(x, b_\perp)}{\int dx \int d^2 b_\perp q_f(x, b_\perp)} = 4 \frac{\partial}{\partial t} \log F_1(t) \Big|_{t=0} \quad (\text{I.31})$$

### Symmetries

- *The GPDs are real-valued functions and even in  $\xi$ .*

Denoting  $\mathcal{F} \in \{H, E, \tilde{H}, \tilde{E}\}$  a generic GPD, we have

$$(\mathcal{F}(x, \xi, t))^* = \mathcal{F}(x, -\xi, t) = \mathcal{F}(x, \xi, t) \quad (\text{I.32})$$

with the operator  $.^*$  denoting the complex conjugation.

- *The gluons GPDs have parity relations in  $x$*

Gluons being their own antiparticles, the following relations stand

$$\begin{aligned} H^g(-x, \xi, t) &= H^g(x, \xi, t) & \tilde{H}^g(-x, \xi, t) &= -\tilde{H}^g(x, \xi, t) \\ E^g(-x, \xi, t) &= E^g(x, \xi, t) & \tilde{E}^g(-x, \xi, t) &= -\tilde{E}^g(x, \xi, t) \end{aligned} \quad (\text{I.33})$$

### Mellin moments and polynomiality

The GPDs first moments are related to the physical distributions of form factors **Eq. (I.25)**. We can consider higher order moments of GPDs in  $x$ , called the Mellin moments. The following polynomiality property ensues from Lorentz invariance arguments, and asserts that the  $n^{\text{th}}$  moment of a GPD is a finite polynomial even in  $\xi$ :

$$\int_{-1}^1 dx x^n H^f(x, \xi, t) = \begin{cases} a_0^{(n)}(t) + a_2^{(n)}(t)\xi^2 + \dots + a_n^{(n)}(t)\xi^n & \text{for } n \text{ even} \\ a_0^{(n)}(t) + a_2^{(n)}(t)\xi^2 + \dots + a_{n-1}^{(n)}(t)\xi^{n-1} + d_{n+1}^q(t)\xi^{n+1} & \text{for } n \text{ odd} \end{cases}$$

and

$$\int_{-1}^1 dx x^n E^f(x, \xi, t) = \begin{cases} b_0^{(n)}(t) + b_2^{(n)}(t)\xi^2 + \dots + b_n^{(n)}(t)\xi^n & \text{for } n \text{ even} \\ b_0^{(n)}(t) + b_2^{(n)}(t)\xi^2 + \dots + b_{n-1}^{(n)}(t)\xi^{n-1} - d_{n+1}^q(t)\xi^{n+1} & \text{for } n \text{ odd} \end{cases} \quad (\text{I.34})$$

<sup>3</sup>This relation is similar to **Eq. (I.12)** but here we consider the distribution of partons in a transverse plane (with a factor 4) and not in a volume (with a factor 6)!

The even property over  $\xi$  comes from [Eq. \(I.32\)](#). It can be noted that the last coefficient labeled  $d$  is common, as it accounts for the so-called the D-term that will be defined later. The same equalities hold for the  $n^{\text{th}}$ -moments of the GPDs  $\tilde{H}^q$  and  $\tilde{E}^q$ , beside the fact that there is no associated D-term, so that the polynomial order is  $n$  if  $n$  is even, and  $n - 1$  if  $n$  is odd. The gluons GPDs obey the same polynomiality properties. Note this time that the parity relations over  $x$  [Eq. \(I.33\)](#) provide vanishing  $n^{\text{th}}$ -moments when  $n$  is odd.

$$\int_{-1}^1 dx x^n H^g(x, \xi, t) = \begin{cases} c_0^{(n)}(t) + c_2^{(n)}(t)\xi^2 + \dots + c_n^{(n)}(t)\xi^n + d_{n+2}^g(t)\xi^{n+2} & \text{for } n \text{ even} \\ 0 & \text{for } n \text{ odd} \end{cases}$$

and

$$\int_{-1}^1 dx x^n E^g(x, \xi, t) = \begin{cases} e_0^{(n)}(t) + e_2^{(n)}(t)\xi^2 + \dots + e_n^{(n)}(t)\xi^n - d_{n+2}^g(t)\xi^{n+2} & \text{for } n \text{ even} \\ 0 & \text{for } n \text{ odd} \end{cases} \quad (\text{I.35})$$

The gluon GPDs  $\tilde{H}^g$  and  $\tilde{E}^g$  have the same form but the moments are this time vanishing for even  $n$ . Again no D-term is present for  $\tilde{H}^g$  and  $\tilde{E}^g$ .

As mentioned earlier, one can note that the highest order term of odd moments of the GPDs  $H^q$  and  $E^q$  is the same but with opposite sign ; the same behaviour holds for gluon GPDs. This series of terms ( $d_n(t)$ ) defines the so-called  $D$ -term through its moments:

$$\int_{-1}^1 d\alpha \alpha^n D(\alpha, t) = d_n(t) \quad (\text{I.36})$$

By construction the  $D$ -term is an odd function of  $\alpha$ . It also encompasses valuable information on the internal forces and the pressure distribution within the proton via the model independent formula [\[38\]](#):

$$d_1(t) \propto \int d^3r p(r) \frac{j_0(r\sqrt{-t})}{t} \quad (\text{I.37})$$

where  $j_0$  is the first Bessel function. The D-term can also be related to Compton Form Factors through dispersion relations (see [Section I.5.1](#)).

#### 4.4 Double distributions and D-term

The polynomiality property allows to restrict the functional form of the GPD models. An elegant way to naturally fulfill polynomiality is to define GPDs through the double distribution ansatz, also written DDs [\[39\]](#). The latter has been proven to be strictly *equivalent* to the polynomiality property, which makes the double distribution approach fundamental to define GPDs. In this section, the variable  $t$  will be set to a fixed value, since only  $(x, \xi)$  are concerned by polynomiality.

As a starting point, we can note that the equations [Eq. \(I.34\)](#) are a characterisation of the Radon transform. This mathematical tool is thoroughly used in medical imaging, providing 2-dimensional reconstruction of a function (or an image) based on all its integral over straight lines passing through its support. From the Radon inversion theorem one can derive the existence (and uniqueness) of a function  $DD$  such that for a generic GPD labeled  $F$ :

$$F(x, \xi) = \int d\alpha d\beta \delta(x - \beta - \xi\alpha) DD(\alpha, \beta) \quad (\text{I.38})$$

Double distributions were introduced independently by Müller et al. [12] and by Radyushkin [15, 16] under the denomination of "spectral functions". However it should be emphasised that this first double distribution approach led to vanishing highest order terms  $d_{n+1}^f$  and  $d_{n+1}^g$ . This incompleteness was pointed out and solved by Polyakov and Weiss [40], who introduced an additional double distribution function to the formalism to account for these highest order terms, and therefore the D-term.

## 5 Accessing GPDs through DVCS experiments

The Deeply Virtual Compton Scattering (DVCS) consists in scattering a lepton off a proton through a virtual photon interaction, which only produces a single real photon. The final state contains the scattered lepton, a recoil of the proton, and a real photon. The process has the following topology:

$$l + P \rightarrow l' + P' + \gamma \quad \text{or} \quad \gamma^* p \rightarrow \gamma p$$

The associated kinematic definitions are displayed in **Fig. (I.12a)**, and the 3-vector components are indicated either by boldface letters or vectors. It shall be noted that the effects of the weak interaction are neglected in the following, since the center of mass energy that can be reached at COMPASS with a muon beam of 160 GeV ( $\sqrt{s} \approx 17.3$  GeV) is not sufficient to produce a  $Z^0$  boson.

The DVCS process is an exclusive reaction which keeps the proton intact. In order to get the clearest possible experimental signature at 160 GeV, it is of importance to detect all the final state particles, including the recoiled proton<sup>4</sup>. In addition to the DIS kinematic variables ( $Q^2, x_B$ ), we define the following parameters

- $t = (p - p')^2 = \Delta^2$  the squared momentum transfer to the proton
- $\phi_{\gamma^*\gamma}$  the angle between the leptonic plane and the hadronic plane of the process as defined in **Eq. (I.39)** from [42] and illustrated in **Fig. (I.12b)**:

$$\phi_{\gamma^*\gamma} = \frac{(\mathbf{q} \times \mathbf{k}) \cdot \mathbf{q}'}{|\mathbf{q} \times \mathbf{k}| \cdot |\mathbf{q}'|} \arccos \frac{(\mathbf{q} \times \mathbf{k}) \cdot (\mathbf{q} \times \mathbf{q}')}{|\mathbf{q} \times \mathbf{k}| \cdot |\mathbf{q} \times \mathbf{q}'|} \quad (\text{I.39})$$

The quantity  $\phi_S$  in **Fig. (I.12b)** is defined as the angle between the lepton scattering plane and  $\vec{S}_\perp$  the transverse component of the target polarisation with respect to the virtual photon direction  $\vec{q}$ . It is worth mentioning that these definitions are consistent with the Trento conventions [44], which differ from the ones used in [45]. As the latter will be used in a next section we remind that:  $\phi_{\gamma^*\gamma} = \pi - \phi_{[45]}$  and  $\phi_{\gamma^*\gamma} - \phi_S = \pi + \varphi_{[45]}$ . Before developing the experimental aspects of the DVCS process, an overview of the link with GPDs is covered in the next section.

### 5.1 Compton Form Factors

The DVCS amplitude at leading order and leading twist obtained from the handbag diagram **Fig. (I.13a)** is parametrised by the GPDs. Due to the loop over the  $x$  variable, the amplitude calculation leads to singular integral operators named Compton Form Factor, one for each GPD, written with calligraphic letters as follow:

<sup>4</sup>If we do not detect the proton, the resolution on the missing mass is dominated by the resolution of the leptons energies. Using a muon beam of 160 GeV, a typical muon energy resolution of 0.5% cannot provide a resolution good enough to select a recoiling proton (see [41] and **Fig. (V.6)**). Moreover, this allows to perform a kinematic fit.

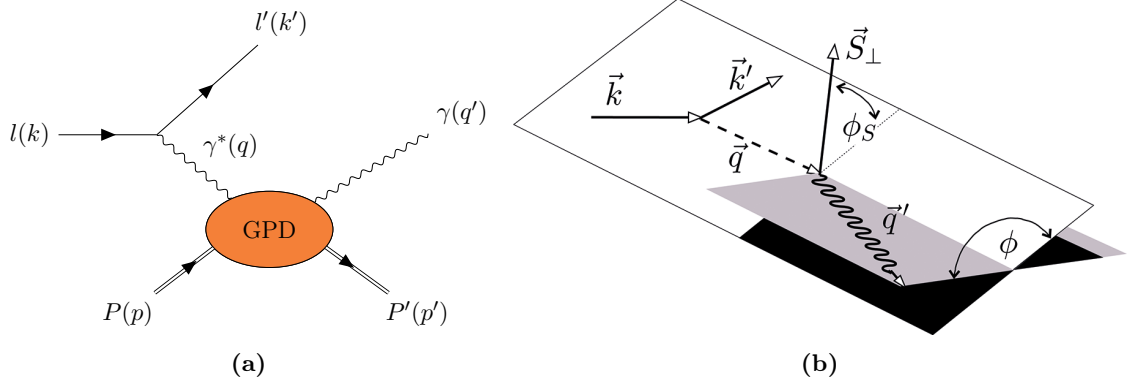


**Figure I.12:** (a) DVCS diagram and kinematic assignments. (b) Definition of  $\phi_{\gamma^*\gamma} = \phi$  in the plot. Taken from [43]

$$\mathcal{H}(\xi, t) = \sum_f e_f^2 \int_{-1}^1 dx C_\epsilon^-(x, \xi) H^f(x, \xi, t) \quad (\text{I.40})$$

The singular convolution kernel is the quark propagator defined by taking into account the crossed diagrams. This object can be calculated perturbatively and reads at leading order:

$$C_\epsilon^\pm(x, \xi) = \frac{1}{\xi - x - i\epsilon} \pm \frac{1}{\xi + x - i\epsilon} + \mathcal{O}(\alpha_S) \quad (\text{I.41})$$

Thanks to the Sokhotski-Plemelj theorem, one can simplify the evaluation of such singular convolutions with the GPDs. The full theorem should be applied on analytic functions, but GPDs do not have a priori such property. Hopefully the real-line version of the theorem only requires continuity on the real line of integration, which allows to write:

$$\lim_{\epsilon \rightarrow 0^+} \int_{-1}^1 dx \frac{H^f(x, \xi, t)}{\xi \pm x - i\epsilon} = \mathcal{P} \int_{-1}^1 dx \frac{H^f(x, \xi, t)}{\xi \pm x} + i\pi H^f(x = \mp \xi, \xi, t) \quad (\text{I.42})$$

where  $\mathcal{P}$  denotes the Cauchy principal value. This relation decomposes the Compton Form Factor  $\mathcal{H}$  in its real and imaginary parts. Finally the integration over  $x$  can be converted from  $[-1, 1]$  to  $[0, 1]$ . Thus one has:

$$\begin{aligned} \text{Re } \mathcal{H}(\xi, t) &\stackrel{\text{LO}}{=} \sum_f e_f^2 \mathcal{P} \int_0^1 dx C^-(x, \xi) [H(x, \xi, t) - H(-x, \xi, t)] \\ \text{Im } \mathcal{H}(\xi, t) &\stackrel{\text{LO}}{=} \sum_f e_f^2 \pi [H^f(\xi, \xi, t) - H^f(-\xi, \xi, t)] \\ \text{Re } \tilde{\mathcal{H}}(\xi, t) &\stackrel{\text{LO}}{=} \sum_f e_f^2 \mathcal{P} \int_0^1 dx C^+(x, \xi) [\tilde{H}(x, \xi, t) + \tilde{H}(-x, \xi, t)] \\ \text{Im } \tilde{\mathcal{H}}(\xi, t) &\stackrel{\text{LO}}{=} \sum_f e_f^2 \pi [\tilde{H}^f(\xi, \xi, t) + \tilde{H}^f(-\xi, \xi, t)] \end{aligned} \quad (\text{I.43})$$

with

$$C^\pm(x, \xi) = \frac{1}{\xi - x} \pm \frac{1}{\xi + x} \quad (\text{I.44})$$

The same equations stand for the GPDs  $E$  and  $\tilde{E}$ . In addition, dispersion relations connect the real and imaginary parts of the Compton Form Factors:

$$\text{Re } \mathcal{H}(\xi, t) = \frac{1}{\pi} \mathcal{P} \int_0^1 dx \left( \frac{1}{\xi - x} - \frac{1}{\xi + x} \right) \text{Im } \mathcal{H}(\xi, t) + \Delta(t) \quad (\text{I.45})$$

The residual term  $\Delta(t)$  is closely related to the D-term of the GPDs introduced in [Section I.4.3](#).

As of today, the relation between GPDs and Compton Form Factors remains a highly studied field of GPD phenomenology, trying to solve the so-called deconvolution problem to recover GPDs from CFFs. As the inverse problem of the drum mentioned in the beginning, it has been shown in the case of DVCS that unravelling GPDs through the CFFs does not possess a unique solution [\[46\]](#). However the universality of the GPDs makes them also accessible in other production channels such as Deeply Virtual Meson Production (HEMP), involving mesons as exclusive particles in the place of the real photon. Though these processes are more complicated and involve mesons distribution amplitudes in addition to GPDs, a multi-channel study of GPDs could help solving the deconvolution problem. This thesis is dedicated to the determination of CFF related quantities through the DVCS cross section measurement. The next section will cover the relation between the experimental measurements and CFFs.

## 5.2 Interferences and cross section

The DVCS channel is not the only process with the topology  $l + P \rightarrow l' + P' + \gamma$ . The Bethe-Heitler process shares the same signature, where the real photon is emitted by one of the lepton as displayed in the diagrams [Fig. \(I.13b\)](#). DVCS and Bethe-Heitler reactions are thus labeled as exclusive single photo-production.

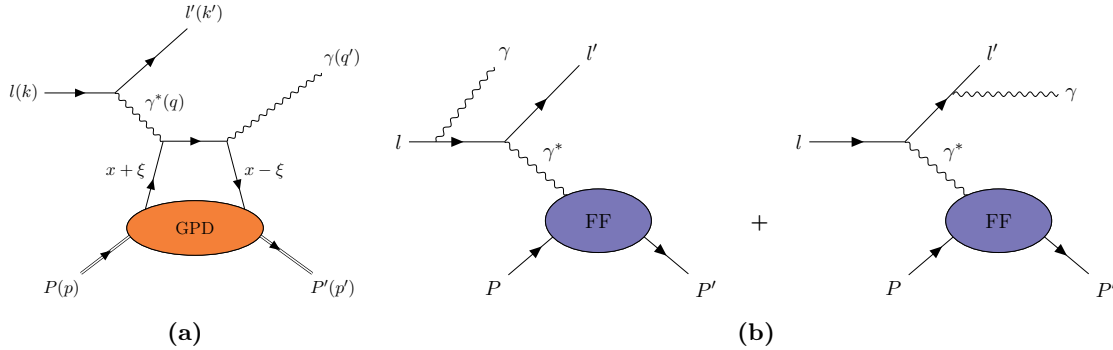


**Figure I.13:** (a) Handbag diagram of the DVCS process at leading order and leading twist. (b) Bethe-Heitler process diagrams; the real photon is emitted by the incoming or outgoing lepton.

Since the DVCS and Bethe-Heitler initial and final states are indistinguishable, both processes interfere and the differential cross section measured experimentally consists in the coherent sum of the amplitudes of both reactions:

$$\frac{d\sigma}{d\Omega} \propto |\mathcal{T}_{\text{DVCS}}|^2 + |\mathcal{T}_{\text{BH}}|^2 + \mathcal{I} \quad (\text{I.46})$$

$$\begin{aligned} \text{where } \mathcal{I} &= \mathcal{T}_{\text{DVCS}}^* \mathcal{T}_{\text{BH}} + \mathcal{T}_{\text{DVCS}} \mathcal{T}_{\text{BH}}^* \\ &= 2 \text{Re} (\mathcal{T}_{\text{DVCS}}^* \mathcal{T}_{\text{BH}}) \end{aligned}$$

Each term of this cross section can be decomposed along the different combinations of beam charge and polarisation, and target polarisation. An experimental overview of DVCS

observables can be found in [43], and is summarised here. For simplicity, the notation convention  $(\sigma_{XY})_{(X,Y) \in \{U,L,T\}^2}$  is used, where  $X$  and  $Y$  stand for the polarisation configuration of beam and target respectively while the set  $\{U, L, T\}$  stands for unpolarised, longitudinally polarised and transversely polarised cases. We also define  $d\Omega = dQ^2 dx_B dt d\phi d\phi_S$ , and the notation reduction  $d\sigma \equiv \frac{d\sigma}{d\Omega}$  is used. The full exclusive single photo-production cross section reads

$$\begin{aligned}
 d\sigma \propto & \quad d\sigma_{UU}^{\text{BH}} + e_l d\sigma_{UU}^{\mathcal{I}} + d\sigma_{UU}^{\text{DVCS}} \\
 & + e_l P_l d\sigma_{LU}^{\mathcal{I}} + P_l d\sigma_{LU}^{\text{DVCS}} \\
 & + e_l S_L d\sigma_{UL}^{\mathcal{I}} + S_L d\sigma_{UL}^{\text{DVCS}} \\
 & + e_l S_{\perp} d\sigma_{UT}^{\mathcal{I}} + S_{\perp} d\sigma_{UT}^{\text{DVCS}} \\
 + & P_l S_L d\sigma_{LL}^{\text{BH}} + e_l P_l S_L d\sigma_{LL}^{\mathcal{I}} + P_l S_L d\sigma_{LL}^{\text{DVCS}} \\
 + & P_l S_{\perp} d\sigma_{LT}^{\text{BH}} + e_l P_l S_{\perp} d\sigma_{LT}^{\mathcal{I}} + P_l S_{\perp} d\sigma_{LT}^{\text{DVCS}}
 \end{aligned} \tag{I.47}$$

where  $P_l$  and  $e_l$  are the lepton polarisation and charge in units of the elementary charge  $e$ ,  $S$  the target polarisation, and  $S_L$  and  $S_{\perp}$  the longitudinal and transverse target polarisation respectively.

Therefore, by experimentally changing the charge or the polarisation of the lepton beam, and using an unpolarised or a polarised target (longitudinally or transversely), one can reach different terms of the cross section. The COMPASS experiment described in this thesis uses a liquid hydrogen target without polarisation ( $S_L = S_{\perp} = 0$ ), and allows two types of muon beams: positively charged and negatively polarised, or negatively charged and positively polarised. The differential cross section of the exclusive single photo-production is in this case [47]:

$$d\sigma = d\sigma_{UU}^{\text{BH}} + (d\sigma_{UU}^{\text{DVCS}} + P_{\mu} d\sigma_{LU}^{\text{DVCS}}) + e_{\mu} (d\sigma_{UU}^{\mathcal{I}} + P_{\mu} d\sigma_{LU}^{\mathcal{I}}) \tag{I.48}$$

The COMPASS experiment can disentangle the different remaining terms using the beam charge and spin sum or difference of the DVCS cross section. Both cases will be depicted in the following section.

### 5.3 Beam charge and helicity measurements at COMPASS

#### Cross section sum

The COMPASS experiment makes use of either a negative muon beam positively polarised, or a positive muon beam negatively polarised. The two configurations of beams will be labeled  $\vec{\rightarrow}$  and  $\overleftarrow{\mp}$  respectively. Using **Eq. (I.48)**, the sum of the cross section for  $\mu^{\overleftarrow{\mp}}$  and  $\mu^{\vec{\rightarrow}}$  beams for an unpolarised target reads [47]:

$$\mathcal{S}_{CS,U} = d\sigma^{\overleftarrow{\mp}} + d\sigma^{\vec{\rightarrow}} = 2 (d\sigma_{UU}^{\text{BH}} + d\sigma_{UU}^{\text{DVCS}} - |P_{\mu}| d\sigma_{LU}^{\mathcal{I}}) \tag{I.49}$$

The subscript  $CS$  indicates that both the lepton charge and spin are reversed simultaneously. The different terms have been developed in terms of Fourier series of  $\phi_{\gamma^* \gamma}$ <sup>5</sup> up to twist-3 by Belitsky, Müller and Kirchner in [45]. This choice of development allows for a clear separation of the twist-2 and twist-3 sectors, and the corresponding diagrams involved are shown in **Fig. (I.14)**. The Fourier decomposition of the terms reads **Eq. (I.50)** and

<sup>5</sup>The article [45] provides a different definition of the azimuthal angle:  $\phi_{[45]} = \pi - \phi_{\gamma^* \gamma}$ , with  $\phi_{\gamma^* \gamma} = \phi_{\text{Trento}}$  [44]. The resulting changes of sign are taken into account in the formulae exposed here.

the correspondence to the different diagrams is displayed in **Table (I.2)**

$$\begin{aligned}
d\sigma_{UU}^{\text{BH}} &= \frac{e^6}{x_B^2 y^2 (1 + \epsilon^2)^2 t \mathcal{P}_1(\phi_{\gamma^* \gamma}) \mathcal{P}_2(\phi_{\gamma^* \gamma})} (c_0^{\text{BH}} - c_1^{\text{BH}} \cos \phi_{\gamma^* \gamma} + c_2^{\text{BH}} \cos 2\phi_{\gamma^* \gamma}) \\
d\sigma_{UU}^{\text{DVCS}} &= \frac{e^6}{y^2 Q^2} (c_0^{\text{DVCS}} - c_1^{\text{DVCS}} \cos \phi_{\gamma^* \gamma} + c_2^{\text{DVCS}} \cos 2\phi_{\gamma^* \gamma}) \\
d\sigma_{LU}^{\mathcal{I}} &= \frac{e^6}{x_B y^3 t \mathcal{P}_1(\phi_{\gamma^* \gamma}) \mathcal{P}_2(\phi_{\gamma^* \gamma})} (-s_1^{\mathcal{I}} \sin \phi_{\gamma^* \gamma} + s_2^{\mathcal{I}} \sin 2\phi_{\gamma^* \gamma})
\end{aligned} \tag{I.50}$$

with the kinematic term  $\epsilon^2$  given by

$$\epsilon^2 = 4x_B^2 \frac{M_p^2}{Q^2}$$

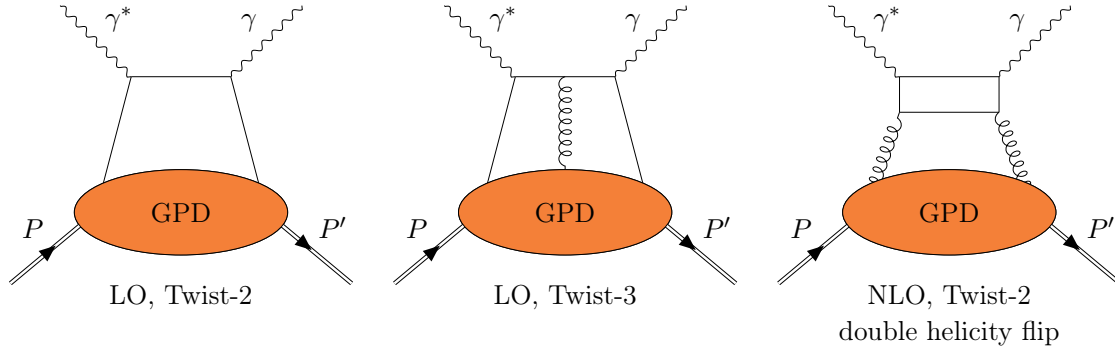


**Figure I.14:** DVCS amplitude terms at different order and twist.

Operation	LO, Twist-2	LO, Twist-3	NLO, Twist-2 double helicity flip
$\mathcal{S}_{CS,U} = d\sigma^{\leftarrow} + d\sigma^{\rightarrow}$	$c_0^{\text{DVCS}}, s_1^{\mathcal{I}}$	$c_1^{\text{DVCS}}, s_2^{\mathcal{I}}$	$c_2^{\text{DVCS}}$
$\mathcal{D}_{CS,U} = d\sigma^{\leftarrow} - d\sigma^{\rightarrow}$	$c_0^{\mathcal{I}}, c_1^{\mathcal{I}}$	$s_1^{\text{DVCS}}, c_2^{\mathcal{I}}$	$c_3^{\mathcal{I}}$

**Table I.2:** Correspondence between the Fourier coefficients and the different DVCS diagrams up to twist 3 and NLO.

All terms containing the superscript BH are coming from the Bethe-Heitler process and are analytically calculable in QED since the only inputs needed are Form Factors. Therefore after subtracting the Bethe-Heitler contribution, a Fourier analysis of the cross section sum is in principle able to separate all the remaining harmonics without mixed coefficients. The leading terms are  $c_0^{\text{DVCS}}$  and  $s_1^{\mathcal{I}}$  and can be extracted in the COMPASS kinematics. The latter is related to the interference terms, and involves thus both Form Factors from the Bethe-Heitler amplitude, and Compton Form Factors from the DVCS one. Their relation reads:

$$s_1^{\mathcal{I}} \propto \text{Im} \left( F_1 \mathcal{H} + \frac{x_B}{2 - x_B} (F_1 + F_2) \tilde{\mathcal{H}} - \frac{\Delta^2}{4M_p^2} F_2 \mathcal{E} \right) \tag{I.51}$$

The kinematic factors  $x_B$  and  $|t|$  being small, and using a proton target ( $F_1 > F_2$ ):

$$s_1^{\mathcal{I}} \propto \text{Im} (F_1 \mathcal{H}) \tag{I.52}$$

Thus the term  $s_1^{\mathcal{I}}$  is mostly sensitive to  $\text{Im } \mathcal{H}$  which give insight on the GPD  $H$  through **Eq. (I.43)**. Note that for the neutron case,  $F_1$  is rather small compared to  $F_2$ , so that  $s_1^{\mathcal{I}}$  is also sensitive to  $\text{Im}(F_2 \mathcal{E})$ .

The second term  $c_0^{\text{DVCS}}$  involves only the DVCS amplitude, and reads explicitly in terms of CFFs [45]:

$$c_0^{\text{DVCS}} = 2(2 - y + y^2) \frac{1}{(2 - x_B)^2} \left[ 4(1 - x_B) \left( \mathcal{H}\mathcal{H}^* + \tilde{\mathcal{H}}\tilde{\mathcal{H}}^* \right) - x_B^2 \frac{\Delta^2}{4M_p^2} \tilde{\mathcal{E}}\tilde{\mathcal{E}}^* \right. \\ \left. - x_B^2 \left( \mathcal{H}\mathcal{E}^* + \mathcal{E}\mathcal{H}^* + \tilde{\mathcal{H}}\tilde{\mathcal{E}}^* + \tilde{\mathcal{E}}\tilde{\mathcal{H}}^* \right) - \left( x_B^2 + (2 - x_B)^2 \frac{\Delta^2}{4M_p^2} \right) \mathcal{E}\mathcal{E}^* \right] \quad (\text{I.53})$$

By removing kinematically suppressed terms in the COMPASS domain, one gets:

$$c_0^{\text{DVCS}} \propto 4 \left( \mathcal{H}\mathcal{H}^* + \tilde{\mathcal{H}}\tilde{\mathcal{H}}^* \right) - \frac{\Delta^2}{M_p^2} \mathcal{E}\mathcal{E}^* \quad (\text{I.54})$$

Using two models KM15 and GK [48, 49, 50, 51, 52], one mainly gets sensitivity to the square of the imaginary part of the CFF  $\mathcal{H}^6$ :

$$c_0^{\text{DVCS}} \propto (\text{Im } \mathcal{H})^2 \quad (\text{I.55})$$

The experimental determination of  $c_0^{\text{DVCS}}$  and its kinematic dependence over  $t$  will be studied in this thesis.

### Cross section difference

$$\mathcal{D}_{CS,U} = d\sigma^{\leftarrow} - d\sigma^{\rightarrow} = 2 \left( -|P_\mu| d\sigma_{LU}^{\text{DVCS}} + |e_\mu| d\sigma_{LU}^{\mathcal{I}} \right) \quad (\text{I.56})$$

Applying the same philosophy, the different terms are developed in Fourier series of  $\phi_{\gamma^*\gamma}$  up to twist-3.

$$d\sigma_{LU}^{\text{DVCS}} = \frac{e^6}{y^2 Q^2} \left( s_1^{\text{DVCS}} \sin \phi_{\gamma^*\gamma} \right) \\ d\sigma_{LU}^{\mathcal{I}} = \frac{e^6}{x_B y^3 t \mathcal{P}_1(\phi_{\gamma^*\gamma}) \mathcal{P}_2(\phi_{\gamma^*\gamma})} \left( c_0^{\mathcal{I}} - c_1^{\mathcal{I}} \cos \phi_{\gamma^*\gamma} + c_2^{\mathcal{I}} \cos 2\phi_{\gamma^*\gamma} - c_3^{\mathcal{I}} \cos 3\phi_{\gamma^*\gamma} \right) \quad (\text{I.57})$$

The leading terms in this expansion are  $c_0^{\mathcal{I}}$ ,  $c_1^{\mathcal{I}}$ . Using the same simplifications as for the cross section sum, we can trim the relations in [45] between the coefficients and the CFFs. In the COMPASS kinematics at small  $x_B$  and small  $\Delta$ , we are mostly sensitive to the real part of the CFF  $\mathcal{H}$ :

$$c_0^{\mathcal{I}}, c_1^{\mathcal{I}} \propto \text{Re}(F_1 \mathcal{H}) \quad (\text{I.58})$$

Accessing both the imaginary part and the real part of the CFF  $\mathcal{H}$  is of interest for reaching the D-term through the dispersion relation **Eq. (I.45)**. However, this is challenging, and requires at least very precise measurements of the cross section for both muon beam charges.

## 5.4 Overview on other experiments

The GPD physics has been addressed in several experimental programs around the world. **Fig. (I.15)** illustrates the different contributions in terms of kinematical domain and available data on the DVCS channel. A review of these results and their experimental configuration is given in [43], and summarised in this part.

<sup>6</sup>The contribution from the real part of  $\mathcal{H}$  and the other CFFs amounts to 3% in the case of GK and to 6% for KM15.

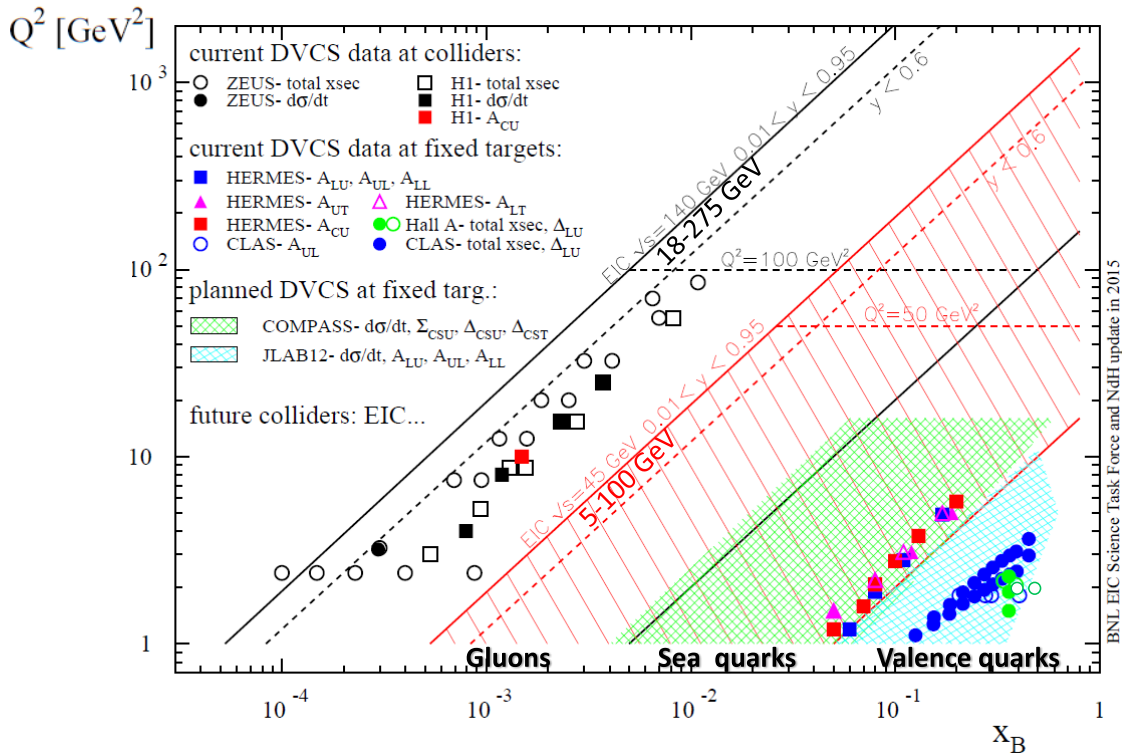


**Figure I.15:** Kinematical coverage of the worldwide DVCS experiments available and foreseen. The points are measurements at HERA from H1, ZEUS and HERMES, and JLab 6 GeV. The green and blue domains are presently investigated by COMPASS and JLab respectively. The future EIC domain is also indicated in red.

### HERMES, CLAS and Hall A in the valence quark region

As of today, the HERMES<sup>7</sup> experiment [53, 54, 55] has provided a rather complete set of inputs to the GPD program. It consisted in a fixed gaseous target experiment, making use of a 27 GeV electron or positron beam accelerated in the HERA<sup>8</sup> facility at the DESY laboratory in Hamburg. The data taking was between 1995 and 2007, and HERMES participated to the very first observation of DVCS in 2001. The data were recorded with the HERMES spectrometer. The exclusive events were selected using the missing mass technique without detecting the recoil proton, and the contamination by the  $\Delta^+$  resonance was estimated to be 17% and has been cross-checked using an additional recoil detector during the 2 last years of data taking. HERMES was a pioneer experiment and has provided an almost complete set of asymmetries using different beam charges and polarisations. These asymmetries were measured in the kinematic region of  $Q^2$  from 1 to 6 GeV<sup>2</sup> and  $x_B$  from 0.04 to 0.2 corresponding to the valence quark region, providing a convenient way to unfold the different CFFs contributions.

In addition to these measurements DVCS-dedicated experiments started also at the Jefferson Laboratory in Virginia, United States just after the first observation of DVCS signal in 2001 with CLAS. The facility provided a 6 GeV polarised electron beam through the CEBAF<sup>9</sup> accelerator, to be used in different fixed target experimental halls. The Hall A makes use of a high resolution spectrometer and electromagnetic calorimeters in conjunction of high luminosity. They measure the polarised and unpolarised cross section

<sup>7</sup>HERA MEasurement of Spin

<sup>8</sup>Hadron-Electron Ring Accelerator

<sup>9</sup>Continuous Electron Beam Accelerator Facility

and performed a  $Q^2$  scaling test to confirm the validity of QCD factorisation [56, 57]. They tried also to separate all the DVCS and interference terms using different beam energies [58]. These measurements were done around  $x_B = 0.36$  and for  $Q^2$  until 2.1 GeV<sup>2</sup>. The CLAS<sup>10</sup> experiment is installed in Hall B, making use of a high acceptance spectrometer compared to Hall A, albeit with a reduced luminosity. This experiment can reach a larger  $x_B$  domain as shown in **Fig. (I.15)**. A wide set of data and results were provided including beam spin, target spin and double spin asymmetries [59, 60, 61], and more recently unpolarised and beam helicity dependent cross-sections [62].

The combined results from HERMES, CLAS and Hall A were used to extract simultaneously all 8 Compton Form Factors [63, 64] (separating their real and imaginary parts, and all 8 variables considered as free parameters). The hypothesis of Leading Order and Leading Twist were assumed here. **Fig. (I.16)** displays the evolution of the dominant contribution  $\text{Im } \mathcal{H}$  as function of  $t$ , in different  $(\xi, Q^2)$  regions. A fit is further performed using a Regge behaviour ansatz to account for the  $t$ -dependence.

$$\text{Im } \mathcal{H}(\xi, t) \propto e^{B(\xi)t} \quad (\text{I.59})$$

The result of the fit is displayed in **Fig. (I.17)**. Since the variable  $t$  is the momentum transfer, the Fourier conjugated quantity  $B(\xi)$  is interpreted as an average position (see **Section I.4.3**). Nevertheless in order to provide such probabilistic interpretations, it is crucial to have a pure transverse momentum transfer to the nucleon, also written  $\Delta_\perp$ ; this means that interpretations only hold at vanishing longitudinal momentum transfer  $\xi = 0$ . Thus an extrapolation procedure has to be performed to retrieve the values of  $\text{Im } \mathcal{H}$  at vanishing  $\xi$ . Moreover the latter has to be connected to the valence GPD

$$H_-^f(x, \xi, t) = H^f(x, \xi, t) + H^f(-x, \xi, t) \quad (\text{I.60})$$

at  $\xi = 0$ , whose exponential  $t$ -slope called  $B_0$  is related to the average transverse position of the valence quarks  $b_\perp$ . This conversion from  $B(\xi)$  to  $b_\perp$  displayed in **Fig. (I.17)** is detailed in [63, 64]. It makes use of a single correction factor  $k$  to relate both quantities as follow:

$$\langle b_\perp^2 \rangle(x) = 4B_0(x) \approx k 4B(\xi) \quad (\text{I.61})$$

### H1 and ZEUS in the gluon region

The HERA facility was also the place for collider experiments between the 27 GeV electron/positron beam and a 920 GeV proton beam. The high center of mass energy achieved allows the H1 [65, 66] and ZEUS [67] experiments to measure pure DVCS cross sections along with its  $t$ -dependency, and beam charge asymmetries. The kinematics of these experiments probe the gluon and sea quark region, in a very low  $x_B$  domain between  $10^{-4}$  or  $10^{-2}$  and a wide virtuality range  $Q^2$  from 3.2 to 25 GeV<sup>2</sup>. These data have demonstrated the importance of considering gluon GPDs at such low  $x_B$ . As in the case of the valence quarks, the  $t$ -dependence of the measured cross section shows a decreasing exponential shape in agreement with a Regge behaviour:

$$\frac{d\sigma}{dt} \propto e^{B(W)t} \quad (\text{I.62})$$

as displayed in **Fig. (I.18)**. Moreover, the kinematic dependency of  $B$  is studied, and the parameter was found to be independent on  $W$ , with a weak evolution in  $Q^2$ .

<sup>10</sup>CEBAF Large Acceptance Spectrometer

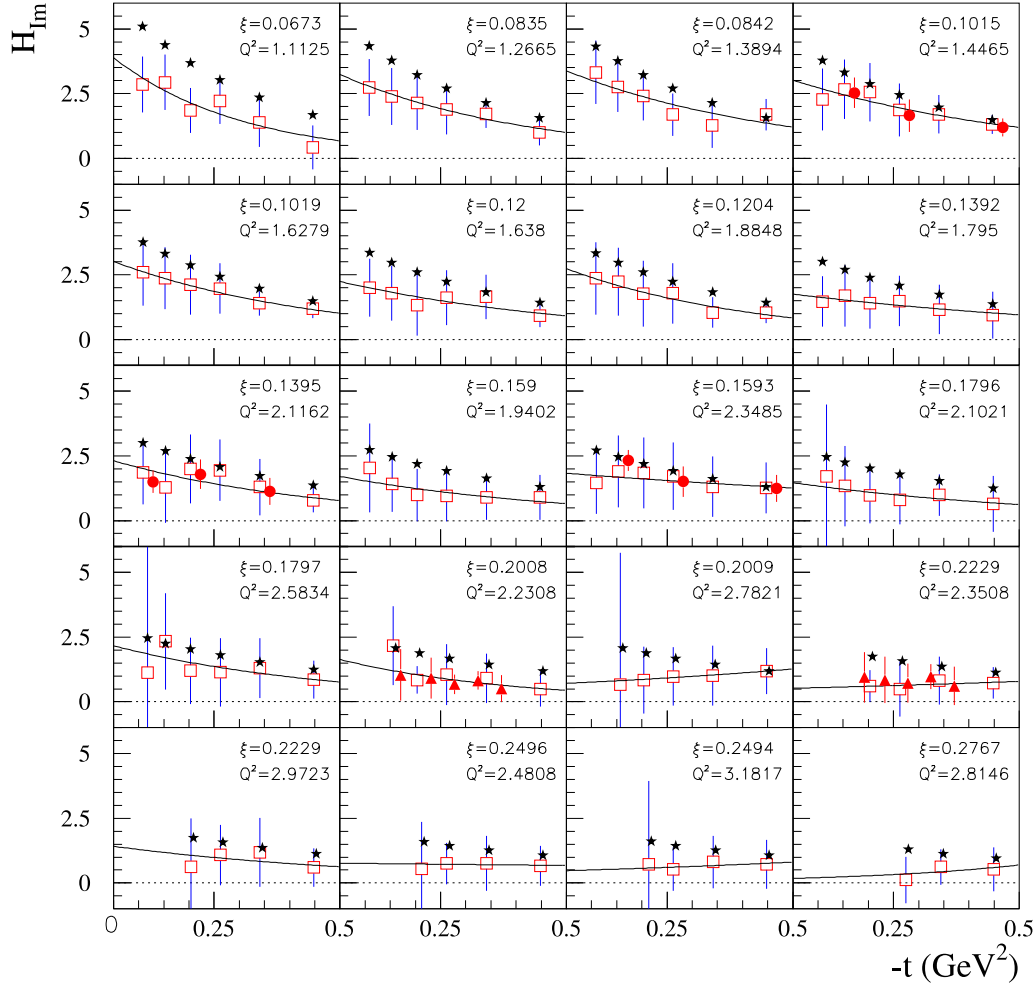


**Figure I.16:** Imaginary part of the CFF  $H$ , resulting from the fit of the eight CFFs at leading order and leading twist. Note that the fit was performed only for a few  $\xi$ . The red squares are unpolarised and polarised cross section inputs from CLAS ; the red triangles show the same results for Hall A ; The red dots displays the CLAS result for unpolarised and polarised beam asymmetries on a longitudinally polarised target. The blue stars indicate the theoretical values of the VGG model. Figure taken from [63].

### COMPASS in the sea quark region

The COMPASS experiment bridges the two previously investigated  $x_B$  domains from 0.01 to 0.1. The very high muon beam energy allows to measure the pure DVCS cross section using different beam charge and spin configurations on an unpolarised target. A feasibility study was performed during the 2012 pilot run from which the measurement of the DVCS cross section led to the estimation of the dominant contribution  $c_0^{\text{DVCS}}$ . The study of its  $t$ -dependence led to a  $B$  parameter estimation at  $x_B = 0.056$  and  $Q^2 = 1.8 \text{ GeV}^2$  [42].

Moreover due to the COMPASS kinematics at small  $x_B$  and small  $t$ ,  $c_0^{\text{DVCS}}$  is related to the square of imaginary part of the CFF  $\mathcal{H}$  ( $x = \xi$ ). Therefore, we can interpret this  $t$ -dependence in terms of transverse extension of partons. Though such interpretation only holds at vanishing skewness  $\xi$ , the COMPASS kinematics limited to small  $x_B$  allows us to write

$$x = \xi \approx x_B/2, \quad (\text{I.63})$$

and to consider  $\xi$  close enough to 0, so that:

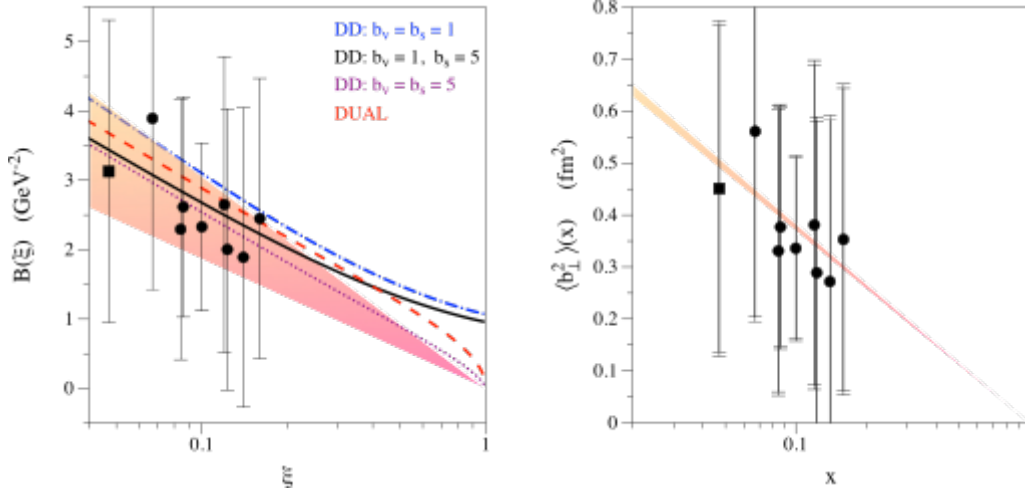


**Figure I.17:** Left: Evaluation of the B parameter of  $\text{Im}\mathcal{H}$  as function of  $\xi$ . Right: transverse extension of partons  $\langle b_{\perp} \rangle$  as function of  $x$ .

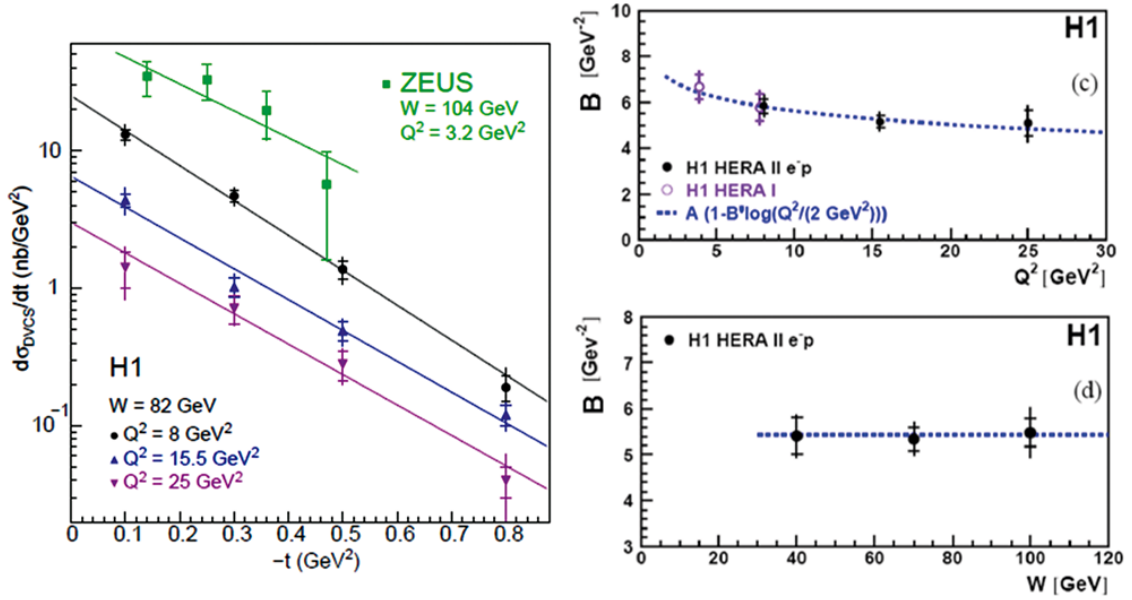


**Figure I.18:** Left:  $t$ -dependence of the DVCS cross section for different virtualities  $Q^2$  as measured at H1 and ZEUS. Right: Evaluation of the B parameter extracted from the left curves by an exponential fit ansatz. The values show the  $Q^2$  and  $W$  dependence on the top and bottom right plots respectively. Figure taken from [43].

$$\langle b_{\perp}^2(x) \rangle \approx 2B(\xi) \quad (\text{I.64})$$

Note that this equation is the same as **Eq. (I.61)** when we consider the cross section and not the amplitude. A comparison with the data from H1 and ZEUS, restricted to small  $Q^2$ , is displayed in **Fig. (I.19)**, and more points will come from the COMPASS 2016-2017 dedicated run. The quantity  $\langle r_{\perp}^2(x) \rangle$  or  $\langle b_{\perp}^2(x) \rangle$  in **Fig. (I.19)** is the average squared transverse extension of partons in the proton as probed by DVCS at the proton longitudinal momentum fraction  $x_B/2$ . The two theoretical curves from Kumerički-Müller (KM) and Goloskokov-Kroll (GK) show the  $x_B$  and  $Q^2$  dependence.

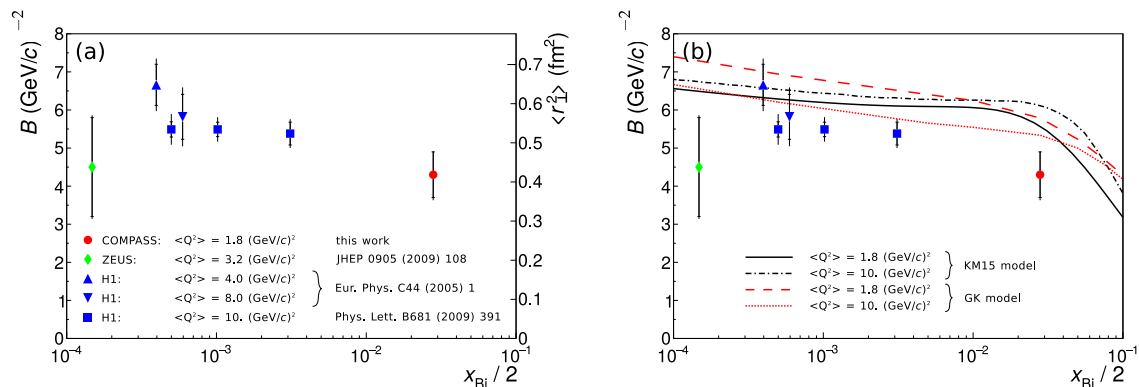


**Figure I.19:** Left: Results from COMPASS, H1 and ZEUS on the B parameter at different  $Q^2$  values. The red point shows the result from the COMPASS 2012 pilot run. Right: comparison of these results with the predictions of the GK and KM15 models. Figure taken from [42].

## Perspectives

The hadronic physics community has started the Electron-Ion Collider (EIC) project at Brookhaven National Laboratory. One goal is to use intense and polarised beams of electrons and ions in order to study the gluon GPDs.

Nonetheless, a possible lead to unravel the deconvolution problem of CFFs, is to use the universality property of GPDs, and perform measurements on other sensitive channels such as Deeply Virtual Meson Production ( $\pi^0$ ,  $J/\Psi$ , etc.) (see the review [68]). Finally, the overall data can be consistently used within global analysis frameworks, including global fitting techniques. Namely PARTONS answers to these needs [69], by its flexibility and modular design. Many models or parametrisations as those provided by Kumerički and Müller (KM), Goloskokov and Kroll (GK) and Liuti [70] are also essential in the phenomenology of GPDs.

# CHAPTER II

---

## THE COMPASS EXPERIMENT

---

### Contents

---

<b>1</b>	<b>The polarised muon beam</b> . . . . .	<b>32</b>
1.1	Spill structure and intensity . . . . .	32
1.2	Beam momentum reconstruction . . . . .	33
<b>2</b>	<b>The target</b> . . . . .	<b>34</b>
<b>3</b>	<b>The spectrometer and trackers</b> . . . . .	<b>35</b>
<b>4</b>	<b>Particle identification</b> . . . . .	<b>37</b>
4.1	Muon filters . . . . .	37
4.2	RICH detector . . . . .	37
4.3	Electromagnetic and hadronic calorimeters . . . . .	38
<b>5</b>	<b>The CAMERA detector</b> . . . . .	<b>40</b>
5.1	Proton identification in CAMERA . . . . .	42
5.2	CAMERA characterisation and improvements . . . . .	43
5.3	Readout electronics and data acquisition framework . . . . .	44
5.4	Reconstruction principle . . . . .	44
<b>6</b>	<b>The trigger system</b> . . . . .	<b>45</b>
6.1	The muon trigger . . . . .	45
6.2	The random trigger . . . . .	46
<b>7</b>	<b>Data acquisition</b> . . . . .	<b>46</b>
<b>8</b>	<b>Event reconstruction</b> . . . . .	<b>48</b>

---

COMPASS is a fixed-target experiment located at the CERN Preveessin North-Area at the end of the M2-beamline of the Super Proton Synchrotron (SPS). COMPASS stands for COmmon Muon Proton Apparatus for Structure and Spectroscopy, and aims at studying the structure and spectrum of hadrons. It consists in a versatile setup making use of high rate and high energy beams up to 200 GeV made of muons or hadrons ( $\pi$ ,  $K$ ,  $p$ ). Proposed in the first time in 1996, a second experimental program has been approved in 2010 [47] called COMPASS-II, allowing two different physics programs and setups. The first one, with the muon beam and an unpolarised liquid hydrogen target ( $\text{LH}_2$ ) proposes to investigate GPDs and hadron tomography by considering exclusive reactions (like DVCS, HEMP). It also allows to study TMDs and Fragmentation Functions in SIDIS. The second program with a hadron beam and a polarised target is a test of the universality of TMDs in polarised  $\pi - p$  Drell-Yan experiment.

This chapter will present the main devices, and notably the new ones involved in the GPD experimental program. A complete description of the COMPASS spectrometer can be found in [71, 72].

## 1 The polarised muon beam

The polarised muon beam is generated by collision of the 450 GeV protons extracted from the SPS on a beryllium target (T6). The adjustable length of the T6 target allows for different intensities of the secondary beam. This secondary beam consists in mainly pions with an admixture of 3.6% of kaons. It is transported along a 600 m long decay tunnel. A pion momentum selection is performed within ( $\pm 10\%$ ) through bending magnets inside the decay tunnel [71, 73]. The remaining not decayed hadrons are filtered by hadrons absorbers. The weak decay of pions and kaons lead to a tertiary muon beam, with branching ratios of 0.999877 and 0.6355 respectively. Moreover the parity violation and helicity conservation of the weak decay ( $\pi^- \rightarrow \mu^- + \bar{\nu}$  and  $\pi^+ \rightarrow \mu^+ + \nu$ ) allows for a naturally polarised muon beam, positively polarised for  $\mu^-$  and negatively polarised for  $\mu^+$ . In the following the polarization sign will be indicated by the arrow superscript  $\mu^{\rightarrow}$  and  $\mu^{\leftarrow}$ . The polarization in the laboratory frame of the tertiary muon beam depends on the meson and muon momenta as:

$$P_{\mu^\mp} = \pm \frac{M_{\pi,K}^2 + \left(1 - 2 \frac{E_{\pi,K}}{E_\mu}\right) M_\mu^2}{M_{\pi,K}^2 - M_\mu^2}$$

A factor of merit has been optimised for a polarisation of  $P_{\mu^\mp} = (80 \pm 5)\%$ . Higher polarisation values could be reached, but at the expense of less intense muon fluxes, as it is displayed in **Fig. (II.1)**. The muon beam momentum has been selected at 160 GeV in order to reach a comfortable polarisation of 80%, a good muon flux, and to allow high  $Q^2$  values. Finally, the tertiary muon beam is injected into a 800 m tunnel, where it is shaped and focused before arriving in the target area of the COMPASS experiment. A large halo of muons is surrounding the muon beam.

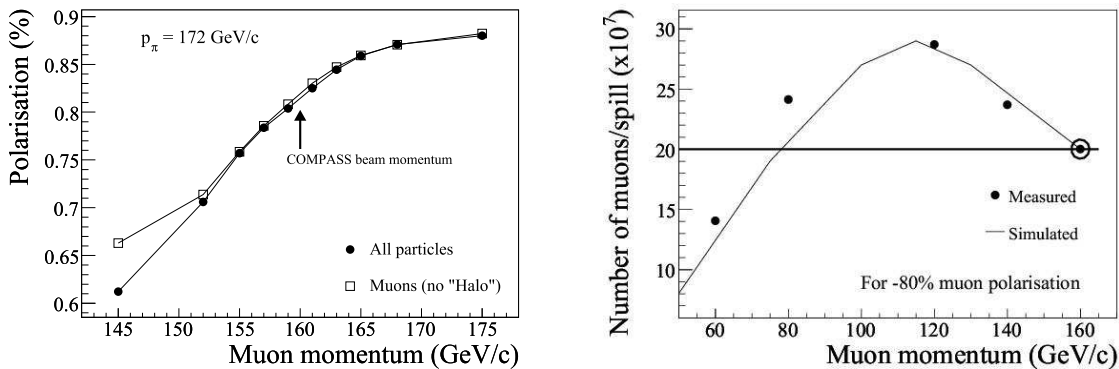


**Figure II.1:** **Left:** Absolute value of the muon beam polarisation as function of its momentum assuming a hadron momentum of 172 GeV. **Right:** Maximal beam intensity as function of the muon beam momentum, assuming a polarisation ratio of 80%. Figure taken from [71].

### 1.1 Spill structure and intensity

The beam is delivered by the SPS in bunches called spills over a duration 4.8 s. **Fig. (II.2)** displays two spills delivered in a total cycle of 36 s. It has to be noted that for the same T6 target the  $\mu^+$  beam intensity is 2.7 larger than the  $\mu^-$  one. In order to get the best experimental conditions to study the DVCS cross section for both  $\mu^+$  and  $\mu^-$  beams, it has been decided to work with the same beam fluxes. To do this, the T6 target length has been adjusted for the different muon charges. A 100 mm length is used for the  $\mu^+$  beam, allowing a flux of about  $7.6 \cdot 10^7$  muons per spill, while a 500 mm length is used for  $\mu^-$ ,

reaching about  $6.3 \cdot 10^7$  muons per spill. This correspond to approximately  $1.4 \cdot 10^7$  muons per second.

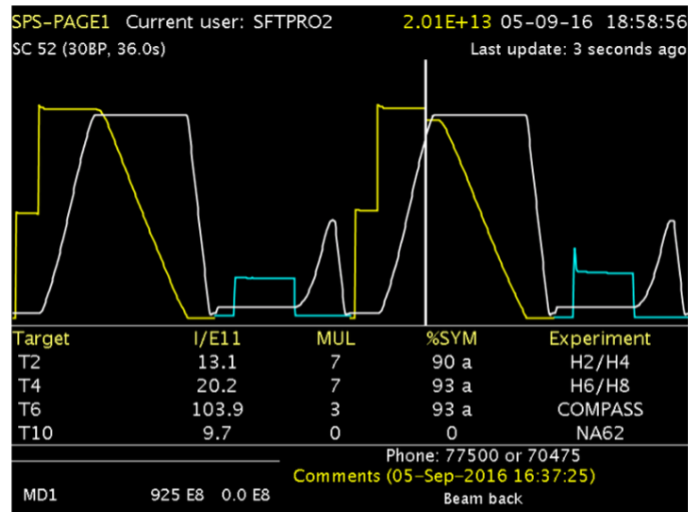


**Figure II.2:** Spill time structure with two proton spills (white curves) delivered in a supercycle of 36 s by the SPS.

## 1.2 Beam momentum reconstruction

The nominal energy of the muon beam is 160 GeV and the beam optics allows a momentum spread of 5%. In order to retrieve the kinematics of the virtual photon in DIS processes, a precise momentum measurement of each individual muon is performed 100 m upstream of the target by the so-called Beam Momentum Station (BMS).

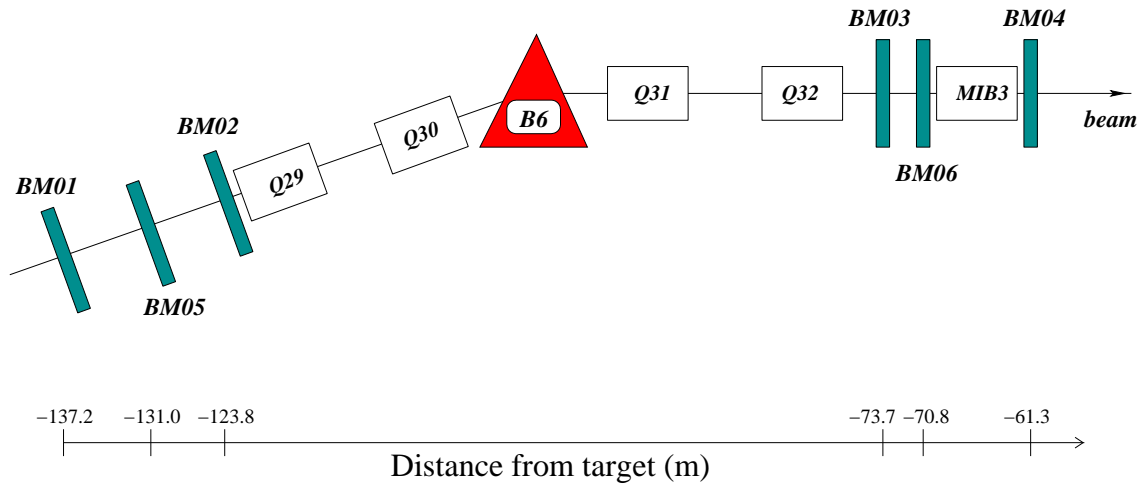


**Figure II.3:** The Beam Momentum Station. Taken from [71]

As depicted in **Fig. (II.3)**, the BMS is composed by three consecutive dipole magnets (noted together B6), surrounded by six beam detectors. Four of them (BM01-BM04) are hodoscope planes measuring the momenta of particles through the bending of their trajectory, and two scintillating fibre hodoscopes (BM05-BM06) are placed one in between each hodoscope pairs in order to provide additional redundancy. The BMS provides a reconstruction of momenta within an uncertainty of 1%, with a track reconstruction efficiency of  $\approx 93\%$ . The detection efficiency is further improved by using the tracking detectors

located in front of the target ; the tracks are extrapolated to the BMS region and spatially correlated with the BMS hits to select within ambiguous beam candidates.

## 2 The target

For the DVCS physics program, the COMPASS setup features an unpolarized liquid hydrogen target [74] schemed in **Fig. (II.4)**. In order to reach a luminosity of about  $2 \times 10^{32} \text{ cm}^{-2} \text{ s}^{-1}$ , the target length was chosen to be 2.5 m, while its diameter is 40 mm to match the transverse beam size. The target cell is located in a cryostat made of carbon fiber, and the operative temperature of the liquid hydrogen is 18 K at a pressure of 1020 mbar.

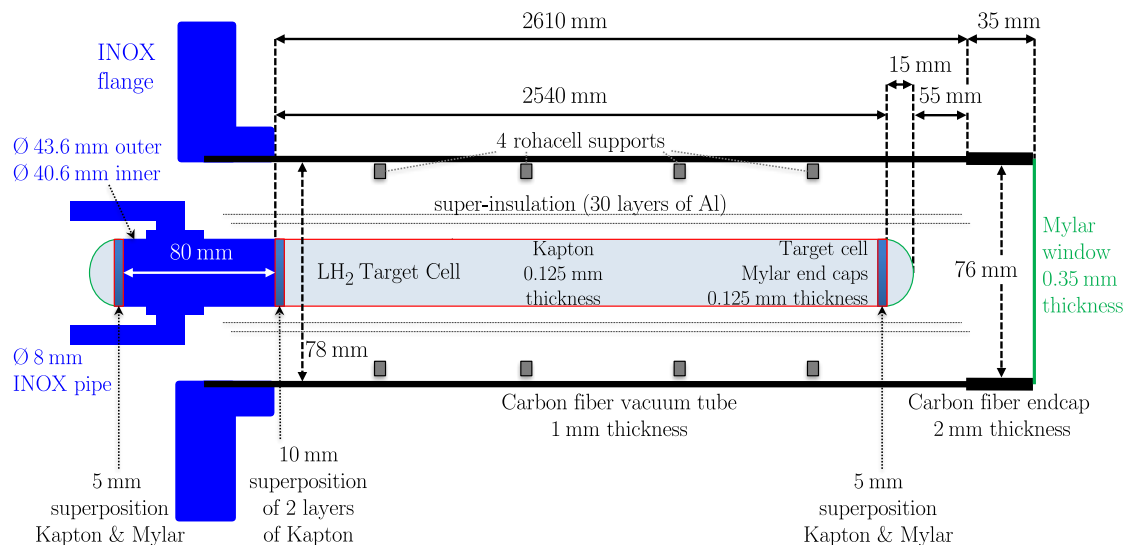


**Figure II.4:** Schematic view of the  $\text{LH}_2$  target taken from [74]. The beam direction goes from the left side of the plot to the right.

A first attempt of measuring recoiled target protons issued from a  $\text{LH}_2$  target was successfully achieved during the 2012 pilot run using the CAMERA detector surrounding the target region. The same setup was pursued during the 2016-2017 run. Two key points have to be emphasised:

- For the physics described in **Chapter (I)**, it is necessary to study exclusive reactions at low momentum transfer. Thus, the cryostat material budget has been lightened in order to reach a minimum momentum transfer  $|t| = 0.07 \text{ GeV}^2$ , corresponding to a recoiled proton momentum down to  $270 \text{ MeV}/c$ .
- Moreover the physics program goal consists mainly in measuring exclusive cross sections, so that a particular attention must be paid on a precise luminosity determination. In that sense, the target density has to be homogeneous along its 2.5 m length, and a careful estimation of the fiducial target volume has to be done [75]. This will allow for a luminosity determination up to an uncertainty of a few percent.

### 3 The spectrometer and trackers

In order to cover a large  $Q^2$  and  $x_B$  domain, the COMPASS experiment uses a two-stage spectrometer[71, 72] of approximately 60 m, composed of tracker planes and particle identification detectors as schemed in **Section II.3**. Each stage is built around one of the two spectrometer dipole magnets (SM1 and SM2 shown in red). The first stage is the Large Angle Spectrometer (LAS) designed for large scattering angles up to 180 mrad, while the Small Angle Spectrometer (SAS) focuses on scattering angle acceptance down to 30 mrad.

The full parametrization of charged tracks passing through the tracker detectors is given by their bent trajectories affected by the magnetic field. Charged tracks are detected all along the spectrometer using different types of tracker technologies depending on their radial distance to the beam axis. The trackers are thus decomposed in three sections: in the Very Small Area Tracker (VSAT) close to the beam axis, a very high rate stability time and space resolutions are necessary, while these requirements can be relaxed at larger distance to the beam, namely in the Small Area Tracker (SAT) and Large Area Tracker (LAT), focusing more on area coverage. One can also note the high number of tracking detector planes, allowing a high redundancy on the measurement and thus an improved reconstruction efficiency. The different types of detectors used are displayed in **Table (II.1)** and more details can be found in [71].

Stage	Type	$A$ [cm <sup>2</sup> ]	$\delta_x$ [μm]	$\delta_t$ [ns]
VSAT	SCIFI <sup>a</sup>	$3.9^2 - 12.3^2$	130 – 210	0.4
	SILICON	$5 \times 7$	8 – 11	2.5
	Pixel-GEM <sup>b</sup>	$10 \times 10$	95	9.9
VSAT SAT	Pixel-MicroMegas <sup>c</sup>	pixels on $5 \times 5$ area on $40 \times 40$	90	9
SAT	GEM <sup>b</sup>	$31 \times 31$	70	12
LAT	MWPC <sup>d</sup>	$178 \times 90 - 120$	1600	N/A
	DC <sup>e</sup>	$180 \times 127$	190 – 500	N/A
	Straw	$280 \times 323$	190	N/A

**Table II.1:** Overview of the different tracker technologies used in the COMPASS spectrometer.  $A$  denotes the active area of the detector while  $\delta_x$  and  $\delta_t$  denote its space and time resolutions respectively.

<sup>a</sup> **SCI**ntillating **FI**bers

<sup>b</sup> **G**as **E**lectron **M**ultiplier

<sup>c</sup> **P**ixel **M**icro-**M**esh **G**aseous **S**tructure

<sup>d</sup> **M**ulti**W**ire **P**roportional **C**hambers

<sup>e</sup> **D**rift **C**hambers

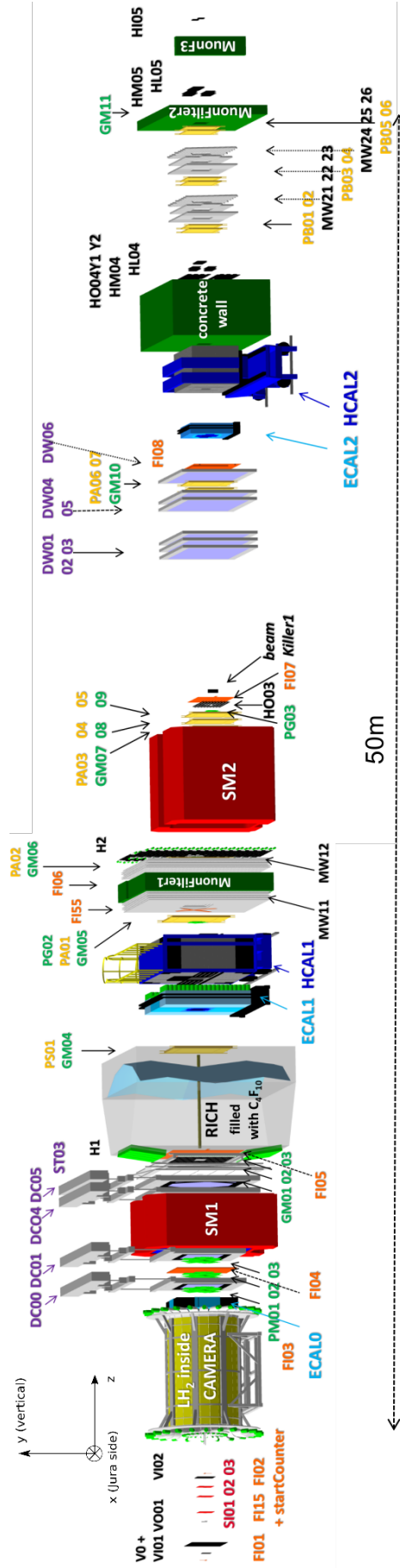


Figure II.5: Schematic view of the 2016-2017 setup [76]

## 4 Particle identification

The particle identification is realised by different techniques. As displayed in [Section II.3](#), the muons are selected using muon filters (in green). A RICH detector (in grey) is used in order to separate contributions coming from pions, kaons, and protons. Moreover, three electromagnetic calorimeters (ECAL0, ECAL1, ECAL2 in light blue) are used to detect photons, while two hadron calorimeters (HCAL1, HCAL2 in dark blue) can detect hadrons. These detectors are briefly described in the following.

### 4.1 Muon filters

The detection of muons relies on their large life-time and their small interaction with matter through electromagnetic processes. The identification is done by heavy absorbers that only the muons can pass. They are surrounded by tracking detectors so that a muon is selected by coincident hits before and after the muon filters. The detection is performed by two detector systems, one in the LAS and one in the SAS. The former consists in two tracking stations called muon walls (MW1) placed around a 60 cm thick iron absorber (Muon Filter 1) as displayed in [Section II.3](#). In the SAS, the tracking behind SM2 is used in combination with a 2.4 m thick concrete absorber (Muon Filter 2), followed by two tracking stations (MW2). The MW1,2 systems are made of gaseous wire detectors in drift tubes.

### 4.2 RICH detector

The LAS stage comprises a Ring Imaging Cerenkov detector. It is filled with  $C_4F_{10}$  so that passing particles emit Cerenkov radiation under a characteristic light cone angle. The measurement of this angle is obtained from the radii of the Cerenkov rings detected, and provides the particle velocity. Combined with a momentum measurement from preceding trackers the particle's mass is deduced. The RICH detector is used to discriminate the different hadrons passing through, as displayed in [Fig. \(II.6\)](#). Note that the RICH is not used in the DVCS analysis.

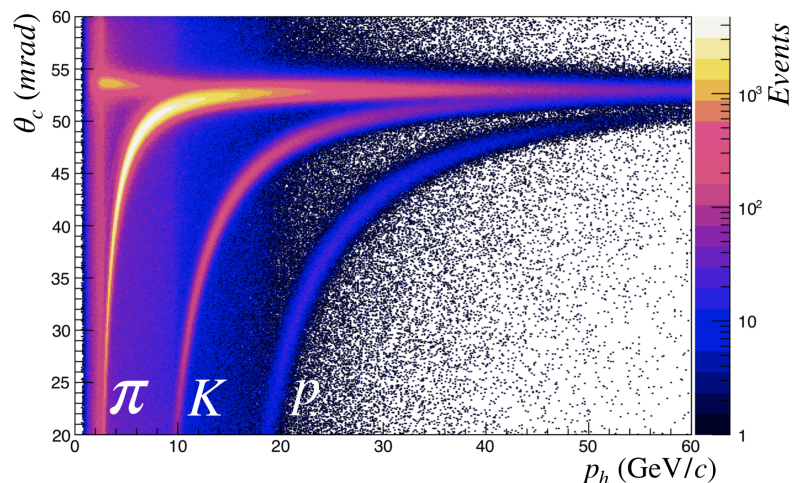


**Figure II.6:** Reconstructed Cerenkov angles as function of the measured momentum of tracks in the spectrometer. One can easily distinguish the different hadron contributions, though the PID is performed with a more technical likelihood method described in [\[77\]](#). Taken from [\[77\]](#).

### 4.3 Electromagnetic and hadronic calorimeters

Three electromagnetic calorimeters (ECAL0, ECAL1, ECAL2) are placed along the different spectrometer stages to intercept at best all the emitted photons. ECAL0 has been newly installed in 2012 for the DVCS-dedicated program. It is situated at about 3 m from the target center and before the RICH detector and allows the detection of large angle photons (see Fig. (II.7)). For the 2016-2017 run, the size of the detector has been increased in order to get an enlarged acceptance coverage in the high  $x_B$  region. Intermediate photon angles are detected in the LAS stage in ECAL1, placed at 13 m from the target center, while ECAL2 is placed after SM2 in the SAS stage, at 35 m detecting low photon angles. These calorimeters are built from either lead glass or shashlik modules of different sizes as schemed in Fig. (II.8). In the case of lead glass, the absorbing and detecting material is the same: the incoming photon radiates  $e^+e^-$  pairs within the material. The resulting Cerenkov light is then detected by photomultiplier tubes. Shashlik modules are alternating layers of lead and scintillating material. The incoming photon produces  $e^+e^-$  pairs, radiating visible light in the scintillating layer. The light is then collected by 16 wavelength shifting light fibers and guided into photomultipliers or micro-pixel avalanche photodiodes (MAPD). With both lead glass and Shashlik modules, the energy deposit collected in all neighbouring cells is proportional to the total energy of the initial photon, and a careful calibration has to be done as depicted in Section II.6.

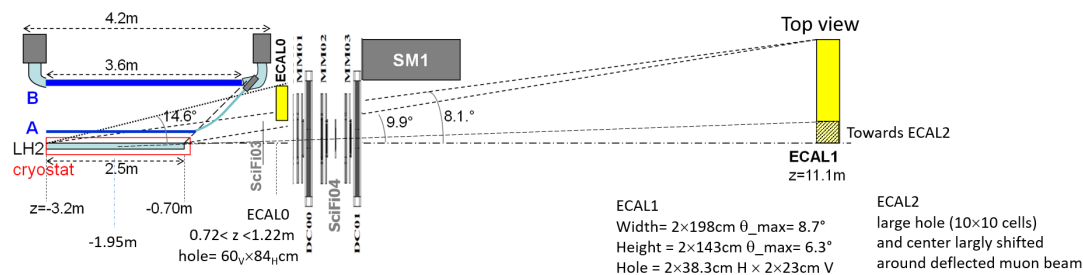


**Figure II.7:** Schematic view of acceptances for the ECALS considering the long target.

Hadronic calorimeters HCAL1 and HCAL2 are placed in each one of the spectrometer stages (LAS and SAS respectively). The detection principle is very similar to the shashlik modules as they are also sampling calorimeters, made of iron as absorbing material.

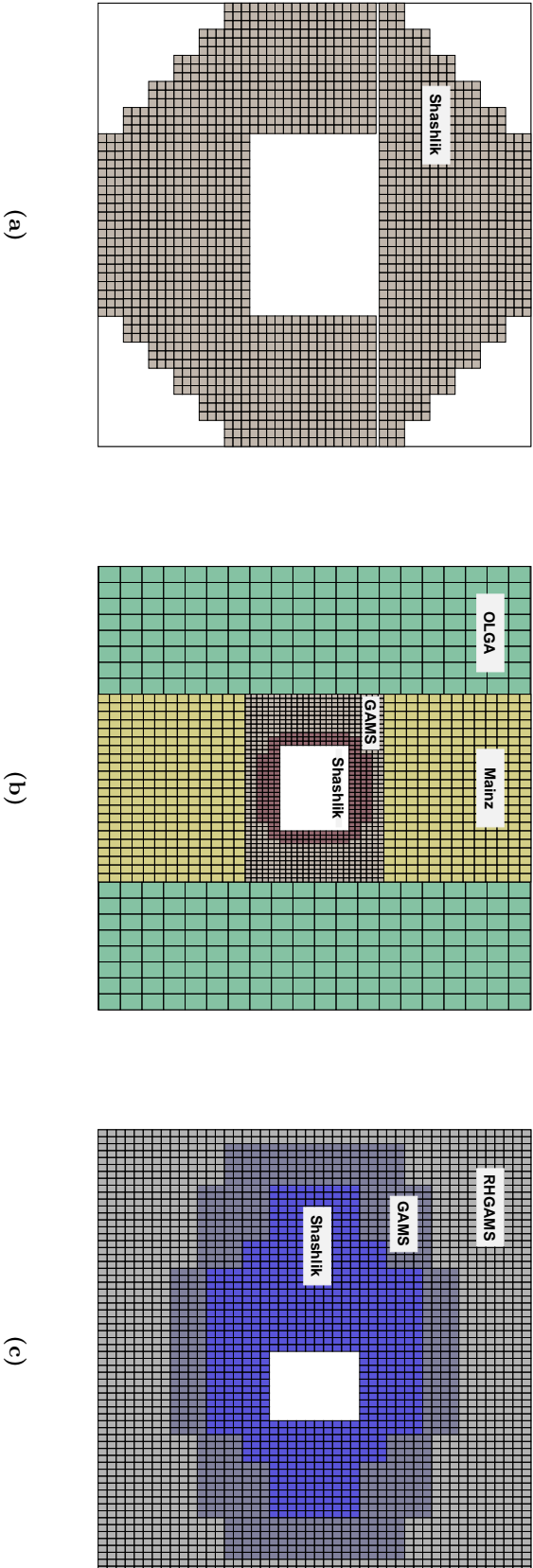


**Figure II.8:** (a) ECAL0 is exclusively made out of shashlik modules with a transverse size of  $3.83 \times 3.83 \text{ cm}^2$ . Its overall size is  $102 \times 102 \text{ cm}^2$ . (b) ECAL1 is composed in its central region of shashlik modules and lead glass cells (named "GAMS") of the same size  $3.83 \times 3.83 \text{ cm}^2$ . The outer parts consist in so-called "Mainz" cells (resp. "Olga" cells) with a size of nearly 4 times (resp. 16 times) a GAMS cell. Its overall size is  $397 \times 286 \text{ cm}^2$ . (c) ECAL2 is made of the same cell sizes  $3.83 \times 3.83 \text{ cm}^2$ , but with different radiation hardness, decreasing from the center to the outer cells. Its overall size is  $244 \times 183 \text{ cm}^2$ . Figures generated by the PHAST software [78].

## 5 The CAMERA detector

The CAMERA detector, namely Apparatus for Measurement of Exclusive ReActions, is a time of flight device placed around the target, aiming at detecting recoiled protons from exclusive reactions shown in **Figs. (II.9) to (II.11)**. It consists in two concentric rings of different radii, each one measuring the energy deposit of passing particles. The coincident hit positions and time are then reconstructed, from which a distance of flight and a time of flight are derived, and thus the velocity of the particle.

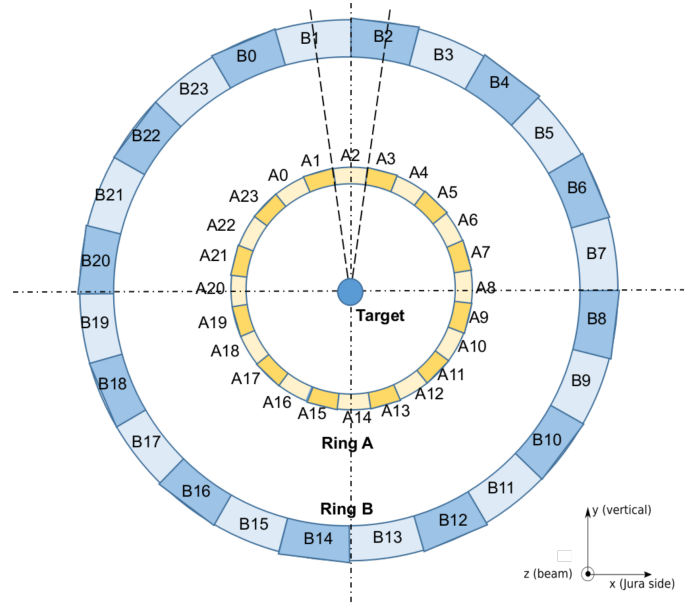


**Figure II.9:** Transverse sketch of CAMERA displaying the upper part of both rings. The scintillators of the ring B are rotated by  $7.5^\circ$  with respect to the ones of ring A. The corresponding radii and widths are denoted by  $r_A$ ,  $r_B$  and  $w_A$ ,  $w_B$  respectively and the nominal values are recorded in **Table (II.2)**

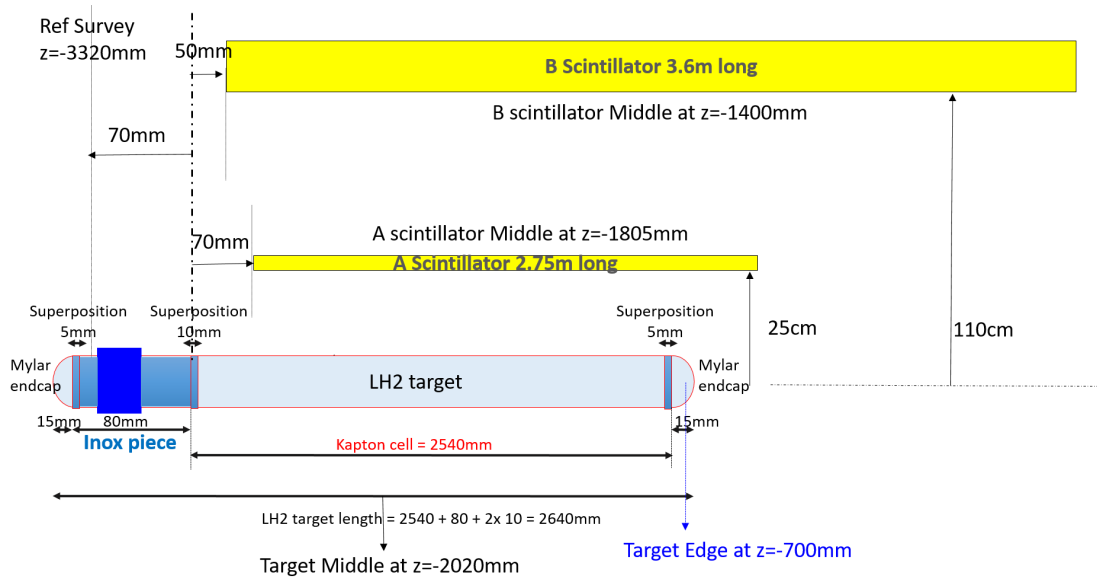


**Figure II.10:** Exact positions of the target and the recoil detector CAMERA.

Each ring is built with 24 scintillators placed around the target to cover the full azimuthal range, and to detect protons generated at any longitudinal position in the 2.5 m target length. The azimuthal coverage of each ring element is thus  $15^\circ$ ; as shown in **Fig. (II.9)**, this resolution is improved by rotating one ring with respect to the other by half this number, so that the final azimuthal resolution reached by CAMERA is  $7.5^\circ/\sqrt{12}$ . The characteristics of each ring are displayed in **Table (II.2)** [79].

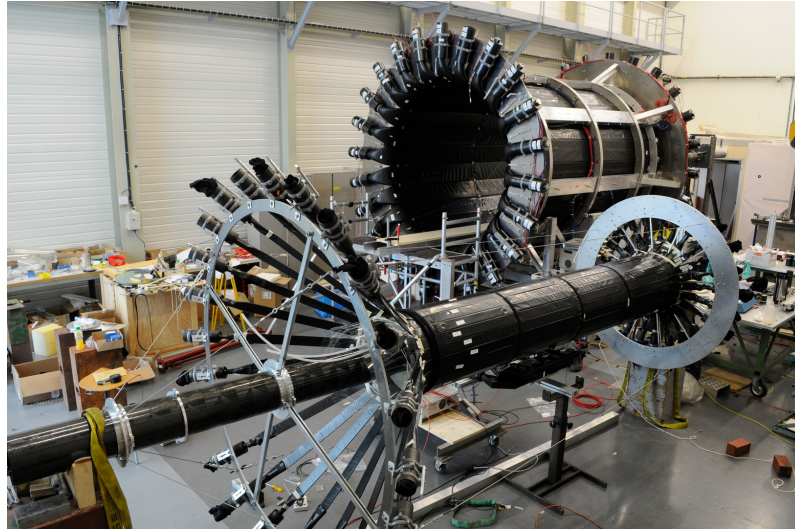


**Figure II.11:** Photograph of the CAMERA detector during its assembly. The inner ring A is shown in the foreground on its support structure. The latter is removed after insertion in the outer ring B shown in the background, so that the  $\text{LH}_2$  target can be inserted. The long lightguides for the inner ring allow to place the photomultipliers outside of the spectrometer forward acceptance. The outer ring photomultipliers are turned at  $90^\circ$  to minimise the space requirement, especially due to ECAL0 positioning right after the target.

Specification	Inner ring A	Outer ring B
radius [cm]	25	110
length [cm]	275	360
thickness [cm]	0.4	5
width [cm]	6.55	29.65
material	BC408	
attenuation length [cm]	170	300
refraction index	1.58	
PMT	HR10533	ET9823B
photo-cathode diameter [mm]	51	130
light guide length [cm]	upstream 54	59
	downstream 107	

**Table II.2:** Nominal characteristics of the inner ring A and outer ring B.

### 5.1 Proton identification in CAMERA

In order to detect the energy deposit of a charged particle within a scintillator, lightguides and photomultipliers are placed at both end of each of the 48 scintillators to detect the upstream and downstream propagation of light. It should be emphasised that thanks to the lightguides, the photomultipliers are placed outside of the spectrometer acceptance to minimise the material budget around the target and the possible absorption of photons (see Fig. (II.10)). The outer barrel is made of 3.6 m long scintillators with a thickness of 5 cm, placed at a nominal distance of 110 cm from the target axis. The PMTs are coupled to the scintillators through lightguides that turn the light direction by  $90^\circ$  Fig. (II.12a). Protons emitted from the target are detected in the outer barrel starting from  $\beta \approx 0.2$  (corresponding to a proton momentum of 270 MeV/c). Fig. (II.12b) shows the characteristic signal of the proton's energy loss detected in the outer ring as function of its velocity. The outer ring completely stops the protons up to  $\beta \approx 0.4$ , while the proton escapes the outer barrel for  $\beta > 0.4$  (corresponding to a proton momentum larger than 460 MeV/c).

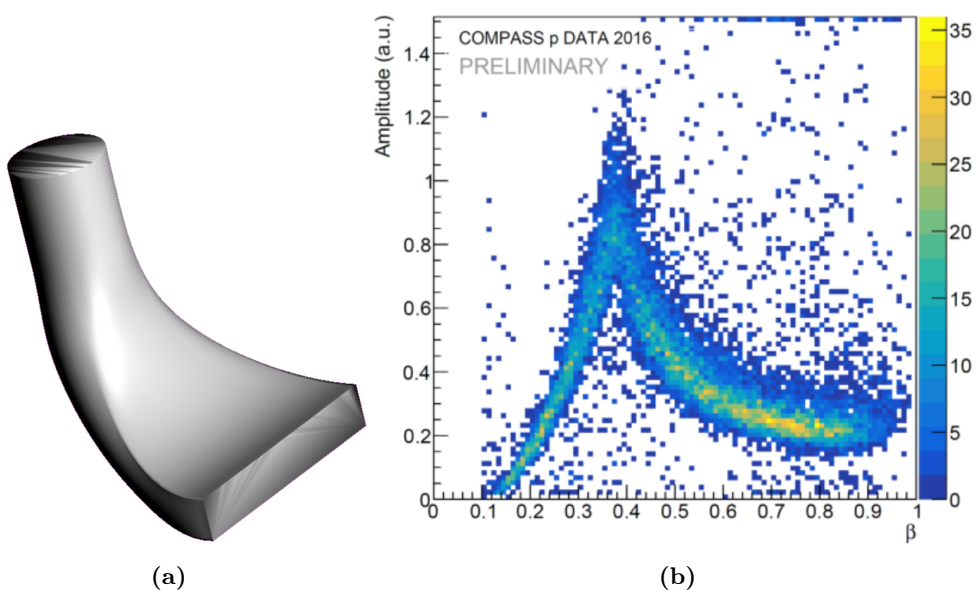


**Figure II.12:** (a): CAD model of the plexiglass lightguide used for the outer scintillators. Taken from [79]. (b): Measured energy deposit in the outer scintillators as a function of the proton velocity.

The inner scintillators are 4 mm thick and 2.75 m long, placed at a nominal distance of 25 cm from the target axis. Their thickness has been optimised to reduce the amount of material crossed by the recoiling particles, while keeping the light yield in the scintillators high enough to have a good quality of the time measurements. On the downstream side, the PMTs are coupled to the scintillators with 1 m long light guides in order to bring them outside of the spectrometer acceptance. On the upstream side the light guides are twisted by  $90^\circ$  to cope with space budget limitations.

## 5.2 CAMERA characterisation and improvements

The scintillators of each ring are made of BC408, emitting light at 430 nm. They are connected through different lengths of lightguides to photomultipliers, whose maximum efficiency lies in between 350 nm and 450 nm. The scintillators of the outer barrel are characterised by a mean attenuation length of  $\lambda = 280$  cm, and a time resolution of 160 ps (see Fig. (II.13)).

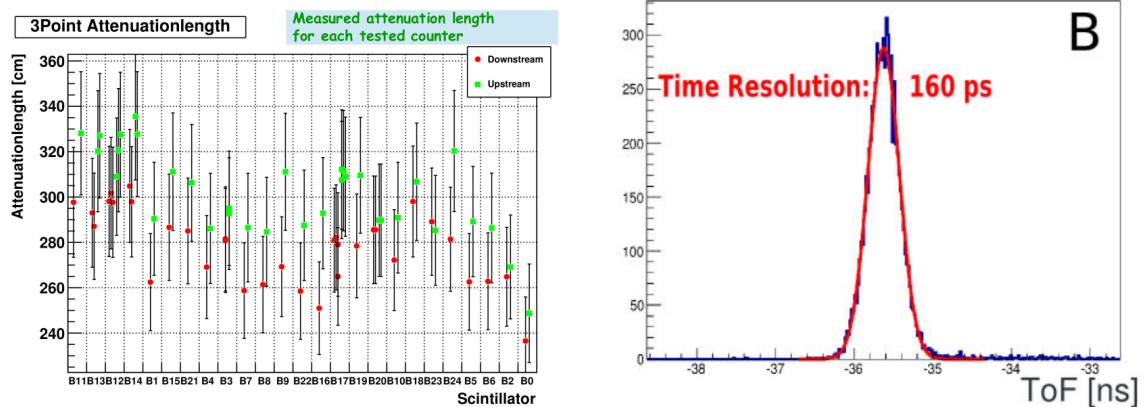


**Figure II.13:** Left: measured attenuation length for each outer barrel scintillator. Right: time resolution for one scintillator. Figures taken from [79]

Due to their small thickness and limited light yield, the inner scintillators feature a generally worse performance. A careful measurement and selection of the scintillators allowed an average attenuation length of 150 cm (see Fig. (II.14a)) with a time resolution of approximately 350 ps. During the 2012 pilot run, a drop of efficiency was observed in the ring A scintillators. Since the attenuation length of the scintillators were too small, a high value of the high voltage had to be set to the photomultipliers in order to detect the small propagated signal. However a too high voltage value made the closest signals too large, exceeding the dynamic range of the readout electronics. The too low attenuation lengths were a consequence of defaults in the manufacturing process. In the 2016 setup, the ring A scintillators have been refurbished, and a careful selection of the scintillators allowed to obtain an average attenuation length above 150 cm. The comparison between the 2012 and the 2016-2017 scintillators' attenuation lengths is illustrated in Fig. (II.14b).

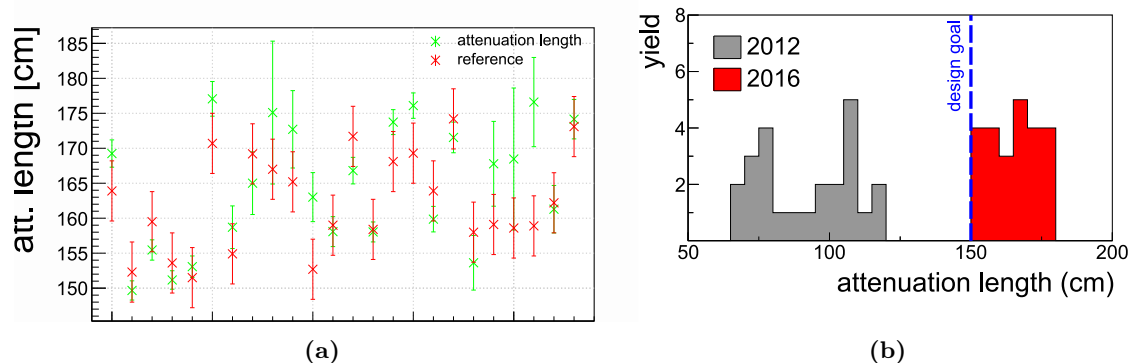


**Figure II.14:** (a): Measurement of the attenuation length of the inner barrel scintillator for the 2016 run. The measurement was performed with cosmic rays before and after assembly. Taken from [79]. (b): Distribution of the attenuation lengths for the 24 scintillators of the ring A built in 2012 and refurbished in 2016. Taken from [80].

### 5.3 Readout electronics and data acquisition framework

A summary is given in the following based on the references [81, 79]. The signals from the 96 PMTs are read-out via a dedicated front-end electronics. The GANDALF<sup>1</sup> framework has been developed by the Freiburg University for the 2012 pilot run [81], and allows for an advanced on-board signal processing and data compression. In practice, the signals are digitized by Sampling Analog-to-Digital Converters (SADC) at a frequency of 1 GHz with a resolution of 12 bits. The digitised signals are then read by an on-board Field Programmable Gate Array (FPGA) processor on which a pulse-feature extraction is performed based on a digital constant fraction discrimination method (dCFD). After the signal processing, each pulse is represented by a time stamp, an amplitude and an integral, which are sent to the DAQ.

The 2012 pilot run has shown some instabilities in the recorded time stamps between the inner and outer scintillators. A bias was observed in the time of flight between the two rings which had to be calibrated on a run by run basis. This is due to the fact that the inner and outer PMT signals are read-out by different GANDALF modules, which therefore have to be synchronised. Biterrors in the sampling process appeared within the data transfer from SADC to FPGA, and lead to an exclusion of approximately 10% of the data from the analysis. The two issues are closely connected and solve by a new time synchronisation method applied for the 2016-2017 run, which has shown stable and reliable results [80, p. 170].

### 5.4 Reconstruction principle

The detection of a particle inside CAMERA consists in four measured time stamps. Let's consider a charged particle that deposits its energy in the scintillator couple  $A_i, B_j$ ,  $(i, j) \in [[0, 23]]^2$ . Let  $t_{A_i}^{\text{up}}, t_{A_i}^{\text{down}}, t_{B_j}^{\text{up}}, t_{B_j}^{\text{down}}$  be the four corresponding time stamps in the upstream and downstream PMTs for each ring.

From these measurements, a time of flight and a distance of flight have to be estimated. Beforehand, the  $z$ -position of the original hit can be reconstructed using the effective speed of light inside the scintillators  $v_{A_i}, v_{B_j}$  and calibration constants  $C_{A_i}, C_{B_j}$ , with **Eq. (II.1)**:

$$\begin{aligned} z_{A_i} &= \frac{1}{2}v_{A_i}(t_{A_i}^{\text{up}} - t_{A_i}^{\text{down}}) + C_{A_i} \\ z_{B_j} &= \frac{1}{2}v_{B_j}(t_{B_j}^{\text{up}} - t_{B_j}^{\text{down}}) + C_{B_j} \end{aligned} \quad (\text{II.1})$$

Let  $R_{A_i}$  and  $R_{B_j}$  be the radii of the inner and outer scintillators respectively. From this, one can derive the distance of flight  $D$  as in **Eq. (II.2)**

$$D = \sqrt{(R_{B_j} - R_{A_i})^2 + (z_{B_j} - z_{A_i})^2} \quad (\text{II.2})$$

The time of flight  $T$  of the particle between the two rings is derived as the difference of the mean times measured in the upstream and downstream photomultipliers, plus an additional calibration constant  $C_{A_i B_j}$ .

$$T = \frac{(t_{B_j}^{\text{up}} + t_{B_j}^{\text{down}})}{2} - \frac{(t_{A_i}^{\text{up}} + t_{A_i}^{\text{down}})}{2} + C_{A_i B_j} \quad (\text{II.3})$$

From these equations, the reconstruction of the velocity and momentum of the charged particle denoted as  $\beta$  and  $p$  follows in **Eq. (II.4)**, where the mass of the proton  $M_p$  is assumed for the measured particle.

---

<sup>1</sup>Generic Advanced Numerical Device for Analog and logic Functions

$$\beta = D/T \quad (\text{II.4})$$

$$p = M_p \beta \gamma = M_p \frac{\beta}{\sqrt{1-\beta^2}}$$

Moreover, it has to be emphasised that the momentum measured in the CAMERA detector by Eq. (II.4) does take not into account the energy losses within the target and other materials traversed by the proton during its propagation. One has to correct for such effect to reconstruct the momentum of the particle at the vertex of interaction using the Bethe-Bloch formula. The details of such correction procedure and the material budget can be found in [82, p. 81–85]. Finally, the calibration procedure of the CAMERA detector will be covered in Section II.2.

## 6 The trigger system

The trigger system [83] aims at selecting physics events within a high rate environment. In order to do so, the trigger system relies on the detection of the scattered muon, in addition to veto systems to remove halo muon events.

### 6.1 The muon trigger

The main trigger used for the selection of deep inelastic events allows for a wide range in  $Q^2$  and  $x_{Bj}$ , and consists in the detection of a scattered muon [83, 73, 77]. The detection principle relies on the space-time coincidence of the measurements in fast hodoscope planes placed before and after the muon filters (see Fig. (II.15)). Each hodoscope element is read out by two photomultipliers at the ends, whose signals are combined by mean timers to obtain the signals that are fed into coincidence matrices producing the trigger signal. If two hodoscope hits arrive within a certain time gate for a matrix pixel consistent with a scattering occurring in the target, the trigger is fired. In addition, the coincidence matrix between the slabs of the coupled hodoscope comprises inactive areas in order to remove halo muons as shown in Fig. (II.16). On top of this a complete veto system is added before the target.

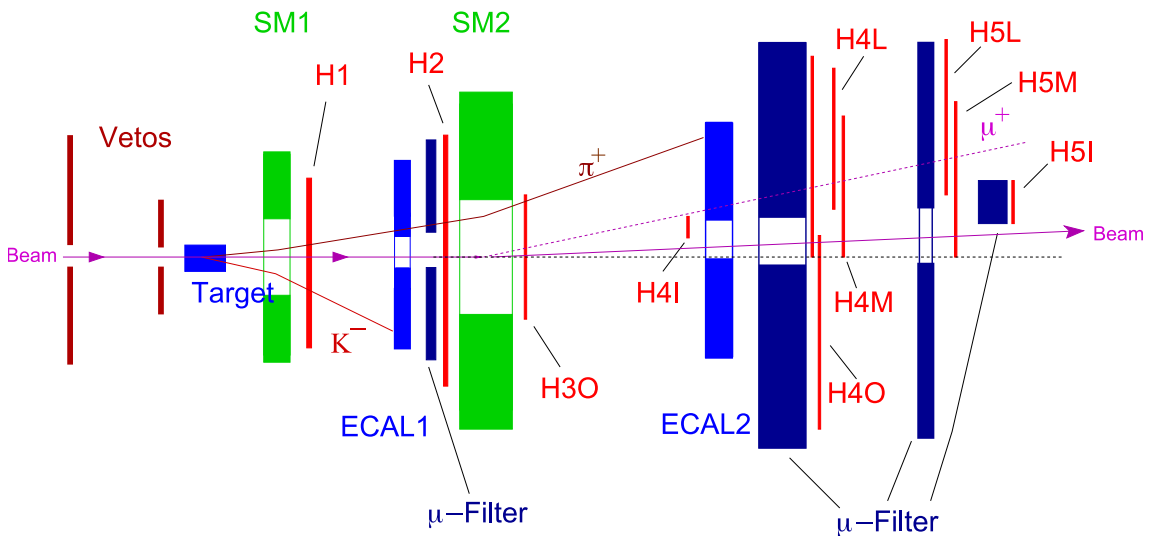
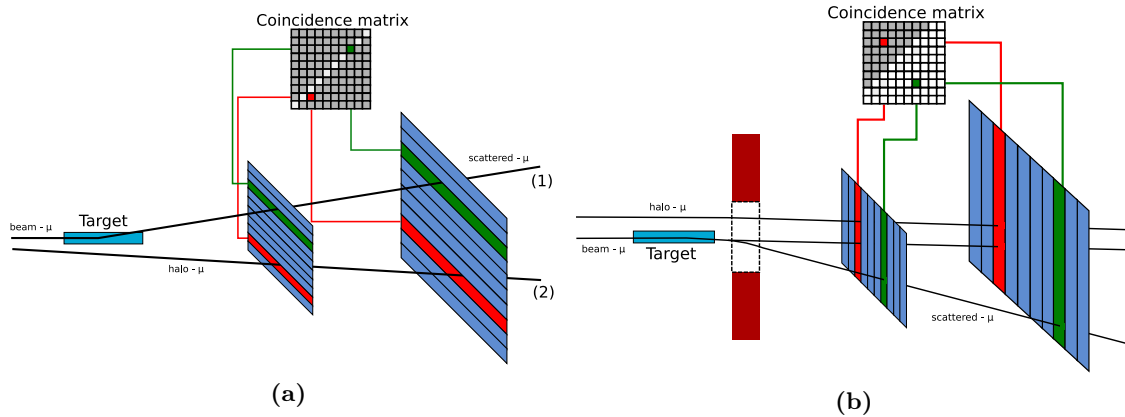


Figure II.15: Main components of the trigger system in the 2016-2017 setup.



**Figure II.16:** (a): Sketch of the target pointing principle with horizontal hodoscope slabs. (b): Sketch of the energy loss principle with vertical hodoscope slabs. Figure taken from [84].

Depending on the value of  $Q^2$ , a wide geometrical position range is probed by different hodoscopes pairs, as displayed in Fig. (II.17). In consequence, different methods have to be used to estimate the scattered muon kinematics.

- For muons with  $Q^2 > 0.5$  ( $\text{GeV}/c^2$ ), a vertical target pointing method is used. In the plane  $Z - Y$ , particles are not bent by the magnetic field, thus two hodoscope planes with horizontal strips measures the scattered angle of the muon. If this angle is compatible with a vertex inside the target, the event is validated by the trigger system. This method is used for the Middle Trigger (MT, hodoscopes H4M and H5M), the Outer Trigger (OT, hodoscopes H3O and H4O) and the LAS Trigger (LAST, hodoscopes H1 and H2).
- In case the scattered vertical angle is too low, or similarly if  $Q^2 < 0.5$  ( $\text{GeV}/c^2$ ), the previous method does not work anymore. In that case the scattered muon sustains a large energy loss in the target and has a large magnetic deflection. The muon momentum is then measured by its bending trajectory under the magnetic field using hodoscopes with vertical strips. This is the method used for the Ladder Trigger (LT, hodoscopes H4L, H5L).

## 6.2 The random trigger

The random trigger consists in a radioactive  $^{22}_{11}\text{Na}$  source, whose decay signature defines a random trigger signal sent to the experimental hall. The  $\beta^+$  decay of the source provides a positron which annihilates with an electron. This creates two back-to-back photons of 511 keV, detected in coincidence by two scintillators placed around the source.

The random trigger is a totally decoupled trigger from the experiment. In order to get rid of correlations with the muon beam, it is placed far from the experimental hall. Moreover, it is the key ingredient for the measurement of the beam flux, as depicted in Section II.3.

## 7 Data acquisition

The data acquisition framework (DAQ) manages information coming from 1400 detectors, featuring a total of 250000 electronic channels. The acquisition flow is displayed in Fig. (II.18). The first stage comprises the so-called front-end electronics. It has the task

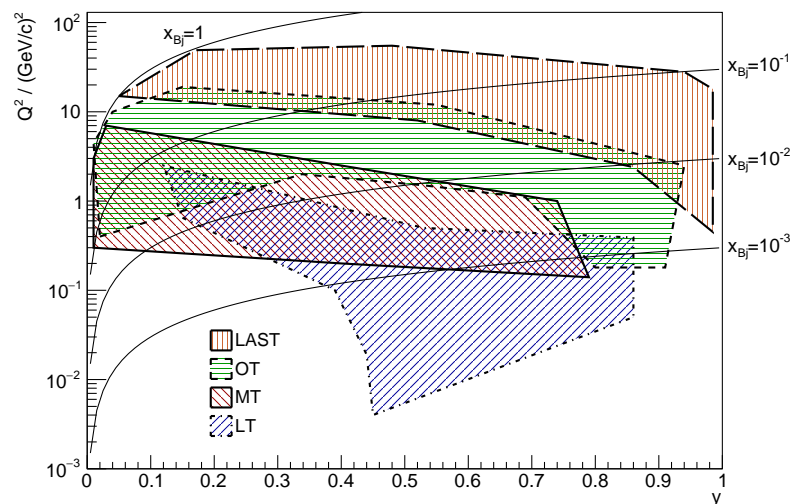


**Figure II.17:** Acceptance of the different parts of the trigger system as function of  $y$  and  $Q^2$ . Taken from [77].

to preamplify the signals if necessary, and convert the raw analog detector signals into digitized information. Depending on the detector purpose, the front-end can be of three different types

- a combination of discriminator and time-to-digital converters (TDCs) for recording time stamps
- analog-to-digital converters (ADCs) to sample and digitize raw analog pulses
- combination of discriminator and scaler to record hit rates

The digital data is then transmitted to different readout boards: CATCH (COMPASS Accumulate, Transfer and Control Hardware) or GeSICA (GEM and Silicon Control and Acquisition), which are all connected to the COMPASS TCS (Trigger Control System). Whenever a trigger signal is sent by the TCS, the readout boards collect data in addition to the TCS metadata (spill and event number), at a global frequency of 10 kHz. These serialised data packages encompass data from one event, coming from different readout boards, and are then transmitted to readout buffers via optical S-Link. Their goal is to store these data in 512 MB spill buffer, containing all recorded information during a spill. In order to release the required bandwidth, the event building task is performed during the on and off-spill time. This is done through eventbuilders and the final data files contain all the detectors information. The typical size of an event is 45 kB. Finally, these raw data are then transferred to the CERN Advanced STORage manager (CASTOR) for long-time storage.

In the particular case of CAMERA, the readout electronics was reviewed for the 2012 pilot run and developed by the university of Freiburg. The front-end electronic comprises the above-mentioned GANDALF ADCs modules ([Section II.5.3](#)). These boards are general-purposes and can be combined with up to two mezzanine boards such as the GIMLI cards, to allow for clocking and clock distribution. A complete description is available in [85, 81]. The acquired data is then transmitted to TIGER<sup>2</sup> modules used here as multiplexers. Generally they allow to combine data up to 18 GANDALF modules, but for

<sup>2</sup>Trigger Implementation for GANDALF Electronic Readout [86]

the CAMERA detector only 12 GANDALF modules were necessary. The TIGER module allows to gather data coming from 96 channels, which is then transmitted to the spill buffer through a single S-Link fibre. In comparison, the classical SMUX module is capable to gather data up to 4 modules.

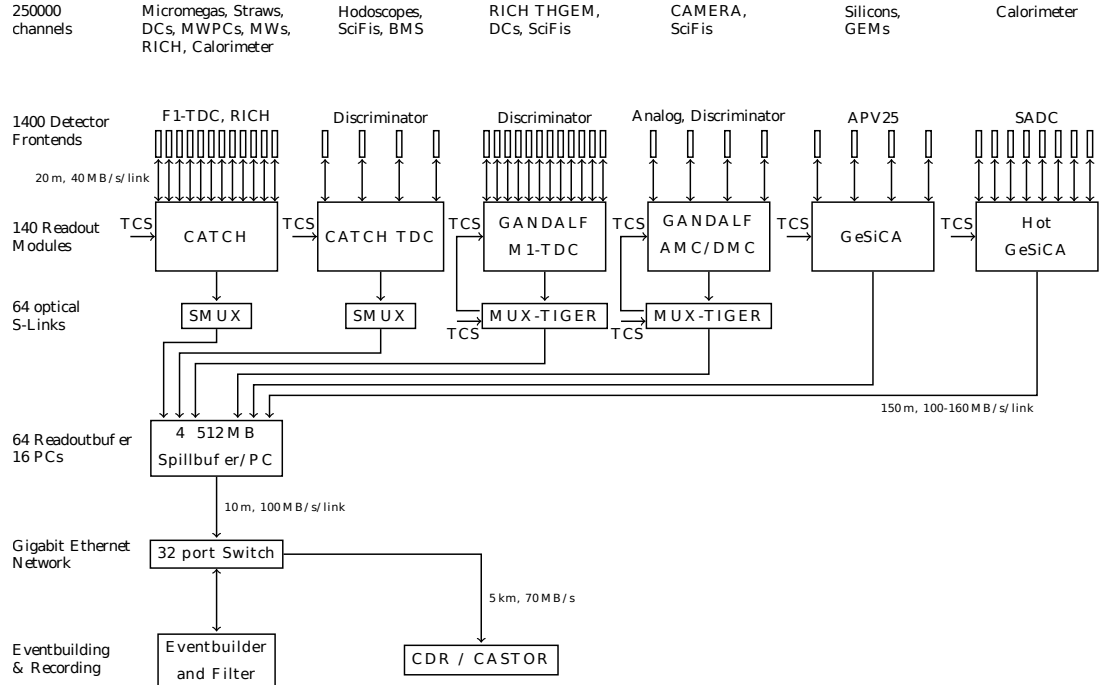


**Figure II.18:** Description of the COMPASS data acquisition system (DAQ). Taken from [85].

## 8 Event reconstruction

The event reconstruction of the latter stored data in CASTOR is called data production and is performed offline by the COMPASS Reconstruction AnaLysis software (CORAL). It is written in C++ in a modular way so that it can handle both real data and Monte Carlo simulations, and makes use of a certain number of configuration files such as detectors alignments, calibration files, detector efficiencies in case of simulations, etc. The principle is depicted in **Fig. (II.19)**. The first stage comprises a decoding of the real data collected using the DAQ Data Decoding (DDD) library while the Monte Carlo simulations goes through a digitization of the Monte Carlo hits to mimic ADC/TDC responses. In general, a particle fires more than one detector channel so that a clusterisation procedure of the hits is necessary, and merges neighbouring hits or detector channels together. The resulting cluster properties (such as its position and time) are then derived in the laboratory frame. From this step, the Monte Carlo simulations and real data are handled by the same parts of code, comprising the tracking part, RICH and calorimeter reconstruction. The charged tracks are determined by a Kalman filter algorithm [87], which are then combined into a vertex fit. More particularly, the Kalman filter allows to decide whether some hits belong to the same track, and inversely whether some tracks belong to a same vertex. The final step is to produce an output file containing all the reconstructed information, within the mDST format<sup>3</sup>. The physics information is then extracted using the software package PHAST<sup>4</sup>, which provides a versatile functional architecture with tool-kits to account for

<sup>3</sup>mini Data Summary Table

<sup>4</sup>Physics Analysis Software Tools

the variety of users applications. This framework is based on the ROOT software provided by CERN [88].

It shall be emphasised that the reconstruction procedure of the CAMERA detector's information is not performed within the CORAL framework. Specific codes have been developed to treat the raw data transmitted by CORAL in a PHAST-integrated library, usually mentioned as "CAMERA code". Two versions have been established for the 2012 pilot run for cross-check purposes, one developed by the Freiburg University (Matthias Gorzellik, Philipp K. Jörg, et al.) and the other one by the Saclay group (Andrea Ferrero). The Saclay code has been maintained by A. Vidon, and further refurbished and improved by myself, and is as of today the official version used in exclusive reactions studies in COMPASS. The code aims at applying the different calibrations and integrates corrections for the energy losses in the target. Specific Monte Carlo information are also treated such as PMTs efficiencies and a digitisation procedure.

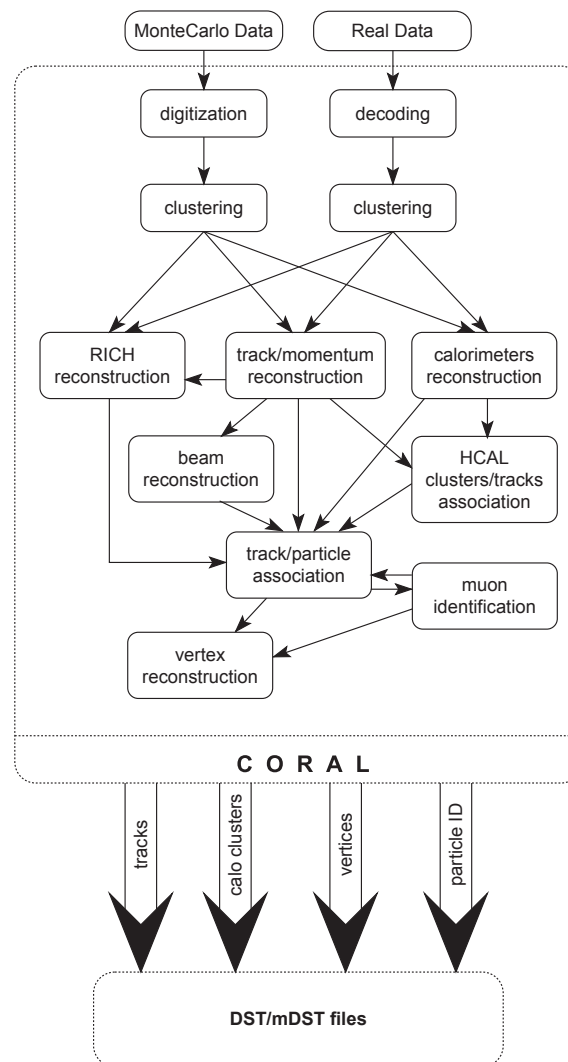


**Figure II.19:** Description of the COMPASS reconstruction software. Taken from [71].



# CHAPTER III

---

## PREPARATORY WORK ON THE 2016-2017 DATA

---

### Contents

---

<b>1</b>	<b>Target position evaluation and vertex selection</b> . . . . .	<b>52</b>
<b>2</b>	<b>Muon beam and spill selection</b> . . . . .	<b>54</b>
2.1	The muon beam quality . . . . .	54
2.2	Time in spill and bad spills determination . . . . .	54
<b>3</b>	<b>Luminosity determination</b> . . . . .	<b>55</b>
<b>4</b>	<b>Scattered muon selection and trigger efficiencies</b> . . . . .	<b>57</b>
4.1	Scattered muon selection . . . . .	57
4.2	Trigger efficiencies . . . . .	57
<b>5</b>	<b>Monte Carlo simulation and validation using the structure function <math>F_2</math></b> <b>59</b>	
5.1	The physics generators . . . . .	59
5.2	Particle propagation and reconstruction . . . . .	59
5.3	Comparison and extraction of the structure function $F_2$ . . . . .	60
<b>6</b>	<b>ECALs calibrations and quality</b> . . . . .	<b>62</b>
6.1	Time calibration and bad cells determination . . . . .	62
6.2	Energy calibration . . . . .	66
6.3	Monte Carlo simulation . . . . .	76

---

This chapter will go through the different tools and preparatory work in order to determine the DVCS cross section. The configuration of the incident muon impinging the liquid hydrogen target has to be precisely determined to evaluate the luminosity. In addition the determination of the efficiencies of the hodoscopes and of the muon trigger electronics used in the scattered muon detection are essential to provide inputs to the Monte Carlo simulation. Finally, the quality of the Monte Carlo can be validated from an analysis extracting the structure function  $F_2$  in DIS. The different analysis steps concerning the incident muon and the scattered muon are described in this chapter, which ends with the calibration of the electromagnetic calorimeters for the detection of the outgoing photon. The next chapter will be devoted to the calibration of the recoil-proton detector.

## 1 Target position evaluation and vertex selection

The estimation of the target position is an essential work in order to calculate the fiducial volume in which stands the interaction vertex between an incoming muon and an outgoing muon. It is also essential in order to estimate the luminosity of the experiment. For the 2016-2017 run, the work has been done by Antoine Vidon which details can be found in [75] for the real-data case, while the description in the Monte Carlo simulation has been performed by Nicolas Pierre in [77]. A summary is presented in the following for the 2016 data case.

First of all, the 2.5-meter long  $\text{LH}_2$  target is cut in 27 transverse slices whose center is estimated by the presence of vertices. The event selection is optimised to improve the vertex resolution, by considering only vertices featuring at least 3 charged tracks (the incoming muon and at least two outgoing tracks). In addition, the statistical robustness is also ensured by the huge statistics of events considered at  $Q^2 > 0.1 \text{ GeV}^2$ , from which a tomography procedure is applied. The method is similar to a Hough Circle Transform (HCT<sup>1</sup>) which detects the circle parameters  $(x, y, R)$  from the gradient of the vertex distribution within the target.

The density of vertices is maximum along the beam trajectories in the central part of the target, and also in the kapton cell where the beam halo interacts. The target cell made of kapton is a cylinder of radius 2 cm which can be easily observed in the vertex reconstruction. The position of the cell is exactly determined at 27 positions along the  $z$ -axis. In fine, the target tomography shows a "banana shape" with an average tilt along  $z$  [75]. Two-dimensional projections of the vertices distribution within the target are shown in **Figs. (III.1)** and **(III.2)**. Note that these plots are only for illustration purposes and were not the ones used in the tomography procedure. The fiducial volume estimation consists first in a  $z$ -dependent radial cut (shown in red) on the real data target of 1.9 cm around the estimated target center, to get rid of the surrounding mylar sheath. Also due the aforementioned tilt, a gaseous part in the upstream region of the target is highlighted by a vertex density depletion. Thus an additional filter along  $y$  ( $y < 1.2 \text{ cm}$ ) (shown in green) is applied to remove it.

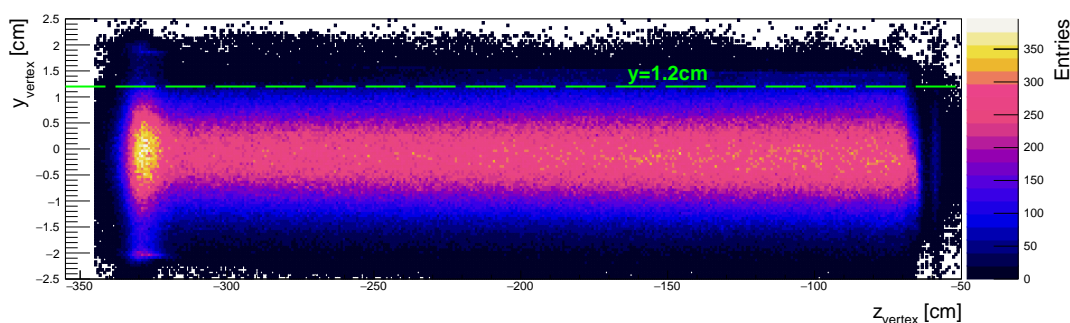


**Figure III.1:** Vertex distribution in the target in the Y-Z plane. The upstream part of the target shows a vertex depletion which is filtered by the  $y$ -cut at 1.2 cm.

Moreover, due to its complicated "banana shape", the real-data target description in the Monte Carlo simulation software is not absolutely accurate. Different solutions have been analysed to overcome this and details can be found in [77]. The selected solution consists

<sup>1</sup>The Hough Transform is able to detect straight lines, circles or ellipses based on a polar transform of the points' coordinates. It is thoroughly used in numerical imaging, for tomography or shape recognition purposes.

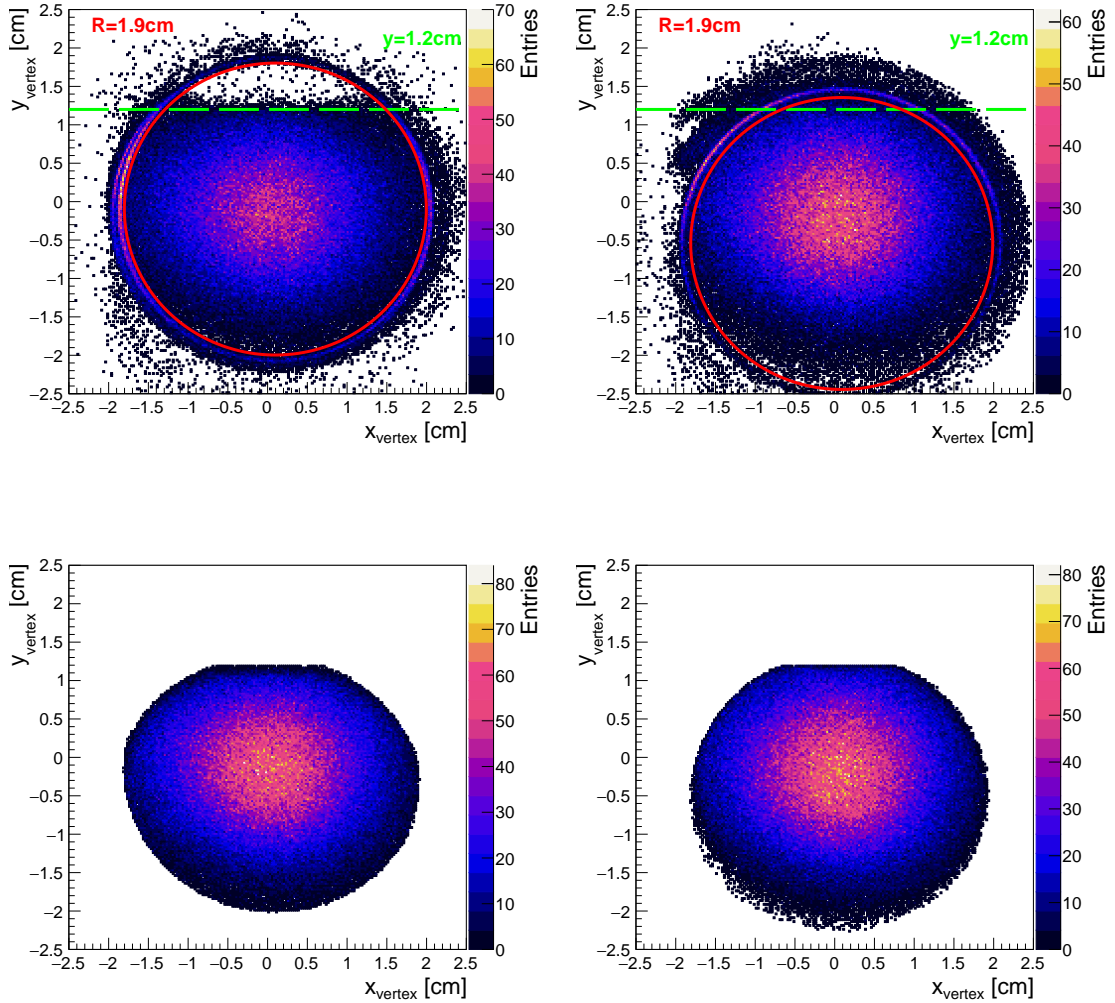


**Figure III.2:** Vertex distribution in the  $X - Y$  planes at different  $z$  position. **Left:** upstream part of the target between  $-323.79 \text{ cm} < z < -303.79 \text{ cm}$ . The top plot shows the distribution of all vertices fitted by at least 3 charged tracks. The bottom plot displays the vertex distribution at the same  $z$ -position after all the DIS event selection. **Right:** Same distributions for the downstream part of the target  $-123.79 \text{ cm} < z < -103.79 \text{ cm}$ .

in simulating the target as a tilted cylinder, which volume matches 99.5% of the real-data target one. The resulting 0.5% difference is covered by a simultaneous cut on real-data and Monte Carlo volumes to only keep the overlap between the two. Due to the following requirements on the muon beam to cross the full target length (see [Section III.2.1](#)), and the edge-effect nature of this discrepancy, the effect of this cut was found to be negligible, but nevertheless applied. The summary of the target cuts which are applied in the following are:

- $-318.5 \text{ cm} < z_{\text{vertex}} < -78.5 \text{ cm}$
- $r_{\text{vertex}}(\text{vertex}, \text{TargetCenter}(z_{\text{vertex}})) < 1.9 \text{ cm}$
- $y_{\text{vertex}} < 1.2 \text{ cm}$

## 2 Muon beam and spill selection

### 2.1 The muon beam quality

In the COMPASS experiment, the cross section estimations are done with the prior of having a proper muon beam. Thus as a starting point, quality filters have to be applied to get this proper muon beam and the corresponding muon flux. The incoming muon track is asked to create at least a certain amount of hits in the BMS detector placed before the target:

- 2 hits in the scintillating fibers (Sci Fi)
- 3 hits in the silicon detector (SI)
- 3 hits in the beam momentum station (BMS)

The two first conditions ensure a proper estimation of the muon beam track, while the last one is necessary for the momentum measurement. In addition, the measured momentum has to be close to the nominal beam energy of 160 GeV within a 2.5% resolution:

$$\begin{aligned} 140 [\text{GeV}/c] < |p_\mu| < 180 [\text{GeV}/c] \\ |\sigma(p_\mu)/p_\mu| < 0.025 \end{aligned} \quad (\text{III.1})$$

Moreover, the muon beam track is asked to pass across the full target length in order to precisely evaluate the data luminosity. This condition is sketched by the green track in **Fig. (III.3)**. The red track examples do not fully cross the yellow target volume to be considered, and are rejected.

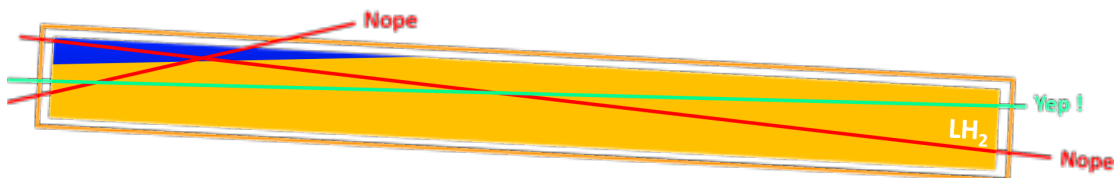


**Figure III.3:** Examples of muon beam tracks (red and green) passing the target volume in yellow. The blue area indicates the gaseous region excluded by the  $y < 1.2$  cm cut. Figure taken from [75].

### 2.2 Time in spill and bad spills determination

The last requirement on the muon beam is the stability of the intensity. A complete study of the spill profile for the 2016 year can be found in [89], and the basic principle is summarised here.

The data taking is divided in 10 periods of runs cumulated over a total of 6 months. Each period is divided in subperiods of about 5 days, alternating the muon beam charge. As said in **Section III.1**, the  $\mu^+$  beam setup uses a 100 mm T6 target, which has a slightly larger intensity than the  $\mu^-$  beam, which makes use of a 500 mm T6 target. The beam intensity profile is reconstructed for each spill based on the output of a scaler connected to the scintillating fiber tracking plane FI02. A typical beam intensity profile is displayed in **Fig. (III.4)** with respect to the time in the spill.

A global intensity range window is first defined based on the mean intensity per subperiod of data taking. This intensity window provides a threshold for the stability study of the beam profile performed per spill as shown in **Fig. (III.4)**. The time in spill is optimised for each spill in order to use all data with a rather constant and high intensity

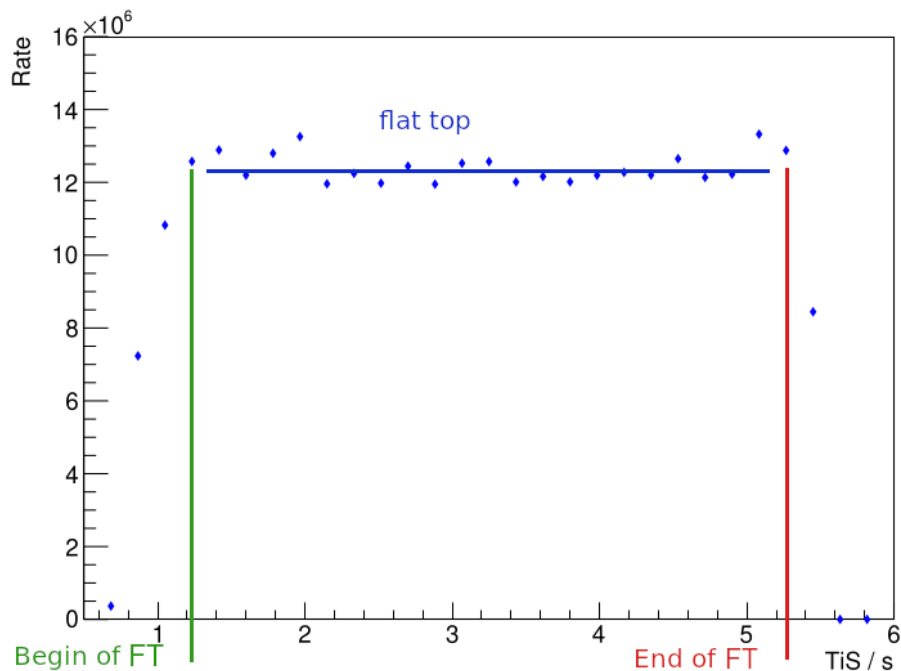


**Figure III.4:** Example of a spill profile. The stable flat top region is indicated by the blue line. The green and red lines show the lower and upper limit of the flat top region (FT), defining the time in spill cuts. Taken from [89].

above the threshold. In the following we will note  $\Delta t_{\text{spill}}$  the time of the spill as defined above. It has to be noted that the beam conditions and profile can vary a lot between spills. Therefore the procedure handles these fluctuations and also creates a bad spill list to record the low-intensity or non-flat spill profiles. The bad spill list also accounts for additional issues detected during the data taking, such as unstable rates detected in the ECALs, in the RICH detector or in the four different triggers. Therefore, different bad spills can be applied based on the nature of the analysis and detectors used. In total, the amount of bad spills for one period of data taking fluctuates between 6% and 12%, among which the strongest contribution is made of empty spills (they represent around 50% of the bad spills).

### 3 Luminosity determination

After the target fiducial volume definition, the qualification of the muon beam and the spill profile, one can evaluate the luminosity of the data taking. The integrated luminosity  $\mathcal{L}^{\pm}$  for the  $\mu^{\pm}$  beams is calculated according to **Eq. (III.2)**:

$$\mathcal{L}^{\pm} = \frac{\rho_{LH_2} l \mathcal{N}_A}{M_p} \Phi_{eff}^{\pm} \quad (\text{III.2})$$

where  $\rho_{LH_2} = 0.070146 \text{ g cm}^{-3}$  is the target density,  $l = 240 \text{ cm}$  the target length,  $\mathcal{N}_A = 6.022 \times 10^{23} \text{ mol}^{-1}$  the Avogadro constant, and  $M_p = 1.0078 \text{ g mol}^{-1}$ . The flux  $\Phi_{eff}^{\pm}$  denotes the effective number of muons traversing the target during the data taking, and is the subject of the following paragraph.

### The random trigger method

The flux determination relies on the analysis of the random trigger events (see [Section III.6.2](#)) on a spill-by-spill basis as done in [90, 89]. For one spill, let  $N_{\text{RT}}^{\text{tracks}}$  be the number of good muon beam tracks selected as in [Sections III.2.1](#) and [III.2.2](#) for events in which the random trigger has been fired. These tracks are selected during a time window  $\Delta T_{\text{window}}$  around the random trigger time (as shown in [Fig. \(III.5\)](#)). Due to the nature of the random trigger, a flat distribution of events is expected around the random trigger time, limited by the time gate of the event reconstruction in the CORAL software. The value of  $\Delta T_{\text{window}}$  is chosen to be 4 ns (indicated by the red lines in [Fig. \(III.5\)](#)) where both a flat plateau and a good amount of statistics are ensured.

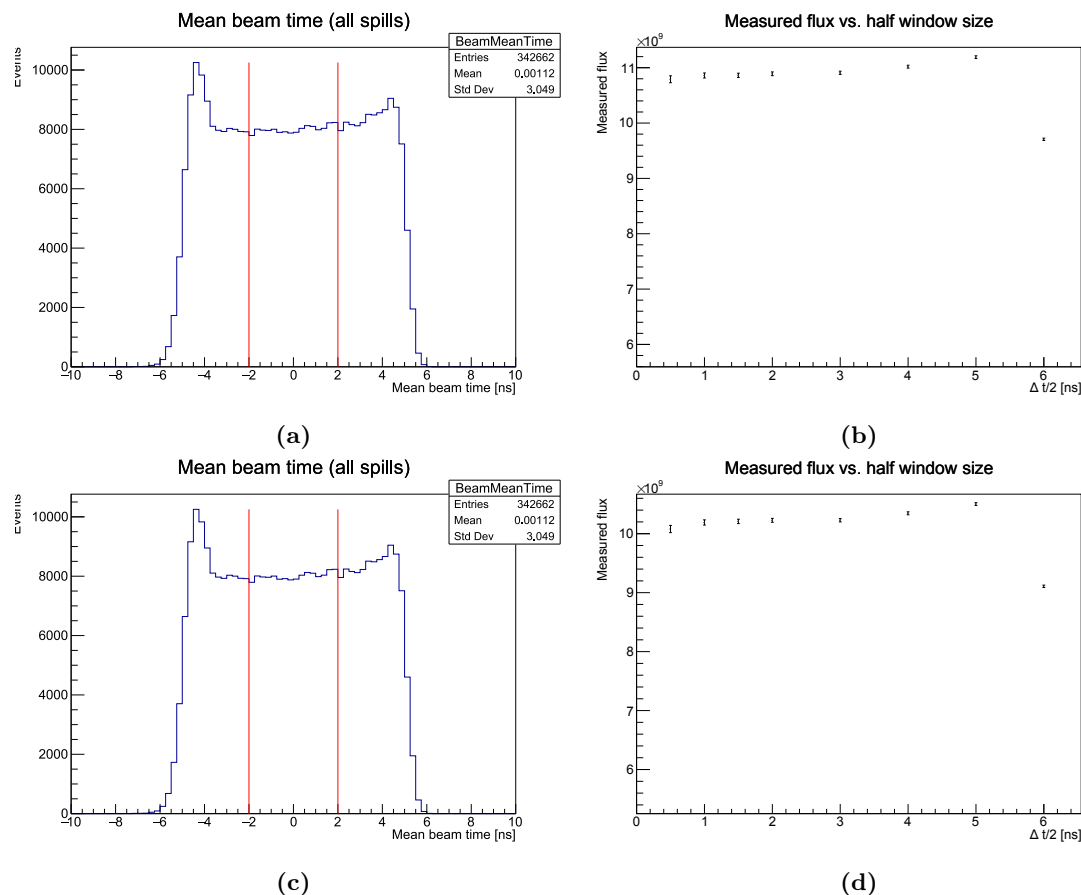


**Figure III.5:** (a) and (c): Mean time distributions of beam tracks for two runs of P09 (275478  $\mu^+$  above and 275536  $\mu^-$  below). The interval  $\Delta T_{\text{window}}/2 = 2$  ns chosen for the analysis is indicated by the red lines.

(b) and (d): Flux value as function of the time window  $\Delta T_{\text{window}}/2$ . The value  $\Delta T_{\text{window}}/2 = 2$  ns is chosen for the flux calculation.

Let  $RT_{\text{accepted}}$  be the number of reconstructed random triggers recorded during the time of the spill  $\Delta t_{\text{spill}}$  (defined in [Section III.2.2](#)). Then one can compute the corresponding flux:

$$\Phi_{\text{no DAQ corr}}^{\pm} = \frac{N_{\text{RT}}^{\text{tracks}} / \Delta T_{\text{window}}}{RT_{\text{accepted}} / \Delta t_{\text{spill}}} \quad (\text{III.3})$$

The data acquisition system also features a dead time which has to be taken into account. To do so, one has to consider the total number of *attempted* random trigger events,

independently of the data acquisition of events. We will label this quantity  $RT_{\text{attempted}}$ , which is accessible from the DAQScaler database and has to be integrated over the time  $\Delta t_{\text{spill}}$ <sup>2</sup> and introduced in [Eq. \(III.3\)](#):

$$\Phi_{\text{DAQ corr}}^{\pm} = \frac{N_{\text{RT}}^{\text{tracks}} / \Delta T_{\text{window}}}{RT_{\text{attempted}} / \Delta t_{\text{spill}}} \quad (\text{III.4})$$

The random trigger is completely decorrelated from the muon beam, which is a key point for the muon flux estimation. However one caveat of this method is that in contrary of the physics triggers, the random trigger is not connected to the beam veto system which avoids the registration of events coming from a halo muon. During this dead-time, good tracks are still counted in the flux, but not in the data selection where physics triggers are used. Thus, one has to take into account this veto dead time through a so-called veto dead-time factor  $c_{\text{vdt}}$  in order to get the effective flux value as in [Eq. \(III.5\)](#).

$$\Phi_{\text{eff}}^{\pm} = \Phi_{\text{no DAQ corr}}^{\pm} (1 - c_{\text{vdt}}) \quad (\text{III.5})$$

Note that the selection of events is also affected by the DAQ dead time, and as the cross section is the ratio of events to flux, the effective flux is not corrected by the DAQ dead time.

## 4 Scattered muon selection and trigger efficiencies

### 4.1 Scattered muon selection

The scattered muon is detected in the spectrometer and its measured track has to fulfill certain requirements. An outgoing track has to pass 15 radiation lengths in the detector's material to be considered as a muon. It is also asked to have the same charge as the incoming muon. Additionally in order to have a precise measurement on its momentum, the corresponding track has to be detected before and after the first spectrometer dipole SM1. Finally, the track can be extrapolated at the longitudinal position of the hodoscope planes, where it should be contained within the active areas of the hodoscopes. In summary, the requirements on the scattered muon track are:

- same charge as beam muon
- traversed radiation length  $X/X_0 > 15$
- $z$ -position of the first and last measured point:

$$z_{\text{first}} < 350 \text{ cm} \quad \text{and} \quad z_{\text{last}} > 350 \text{ cm}$$

- extrapolations within the active areas of the hodoscopes (new PointHodoscope function)

### 4.2 Trigger efficiencies

After the Drell-Yan run in 2014-2015, several improvements have been made for the preparation of the DVCS 2016-2017 run regarding the trigger setup. Especially, a few hodoscope planes have been replaced and 6 inner slabs of HO04 and HO03 were exchanged from the Drell-Yan setup. Also a Monte Carlo simulation was done to optimise the Outer Trigger

---

<sup>2</sup>The scaler rate is very constant over the time so that one can use any time window  $\Delta t$  for integrating the scaler, as the ratio  $RT_{\text{attempted}}(\Delta t) / \Delta t$  is constant.

(OT) setup based on the specific 2016  $z$ -position of the  $\text{LH}_2$  target. The target center is indeed shifted at  $z = -198.5$  cm instead of a nominal value around  $z = 0$  for the other experiments, due to the footprint of the CAMERA detector around the target. All the details can be found in [91].

In order to describe the data, the Monte Carlo simulation needs the inputs on the efficiencies of the trigger hodoscopes and of the trigger electronics made of trigger matrices. A special trigger called the calorimeter trigger is used to determine unbiased trigger efficiencies for scattering events. The calorimeter trigger relies on the detection of a shower in one or the two hadron calorimeters, and the reconstructed muon tracks stemming from the target material are selected for the efficiency analysis. The latter is splitted in two parts:

- the 2D hodoscope efficiencies
- the trigger logic efficiencies

These studies have been done by Johannes Giarra for each subperiods of the two years of data taking [84]. The 2D hodoscope efficiencies are extracted as the inverse ratio of the number of muons tracks passing through the fiducial area of a specific hodoscope (disabled for the reconstruction procedure) with the number of muons which have also an associated hit in this hodoscope. In this way the efficiency along each hodoscope element is obtained as in Fig. (III.6).

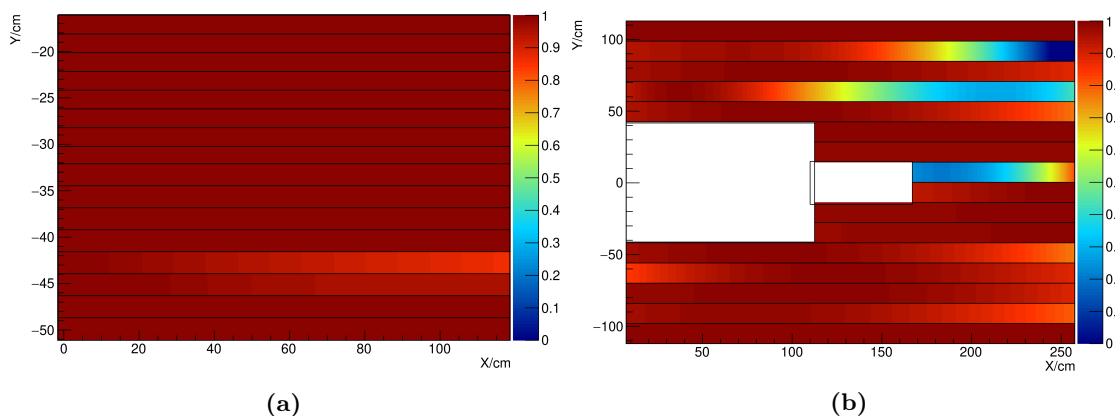


**Figure III.6:** (a): 2D efficiencies for one hodoscope plane of the lower Middle trigger system. (b): 2D efficiencies for one half hodoscope plane of the Outer trigger system.

The middle trigger consists in small hodoscopes in the high rate region to cope with the small scattering muon angles. They are made of new scintillating material and very uniform efficiencies close to 100% are observed. The large angle area hodoscopes of the Outer trigger are made from material already used 40 years ago, and can present some drops of efficiencies for few elements at one or both ends ; the signal quality in the far photomultiplier is not good enough to obtain a good mean time of the signal.

In a similar way, the efficiency of the trigger logic was determined for each used pixel of the coincidence matrices. Tracks with hits on both hodoscopes of a trigger subsystem that belongs to one matrix pixel are selected and it is checked that an online trigger exists for this event. The obtained matrix efficiencies are high (above 98%) as it can be seen in Fig. (III.7), except for a timing issue in the slat 15 of HL05X1.

Moreover the hodoscope efficiency study has raised possibilities of optimisations on the positioning of the hodoscope elements. Therefore, a detailed investigation of the position of all 226 individual scintillator elements has been conducted, yielding improved input for the

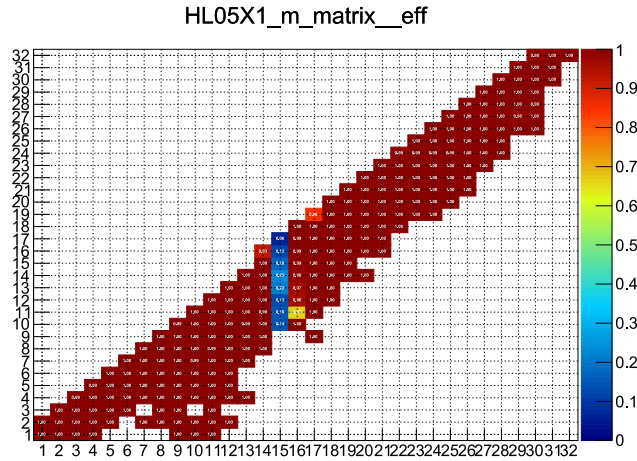


**Figure III.7:** Trigger matrix for the Ladder Trigger. The slabs of HL05X1 are displayed on the horizontal axis, and the HL04X1 ones on the vertical axis.

data and Monte Carlo reconstruction. This analysis also included a detailed comparison with the Monte Carlo simulation, providing common spatial masks for both data and Monte Carlo samples to account for inactive regions or areas where no reliable efficiencies could be computed.

## 5 Monte Carlo simulation and validation using the structure function $F_2$

The Monte Carlo simulations of the experiment can be split in three parts : the physics generation, the propagation of the particles through the detectors' geometry and the reconstruction of the events.

### 5.1 The physics generators

The generator LEPTO 6.1 consists in the generation of various particles produced in deep inelastic scattering processes and their pending kinematic properties. It accounts for semi-inclusive production mechanisms (SIDIS). Another generator developed in COMPASS is DJANGO<sup>3</sup> which generates DIS and SIDIS events in the 1-photon exchange approximation including radiative corrections.

### 5.2 Particle propagation and reconstruction

The Monte Carlo setup needs various kind of input to properly simulate the data. In the very first step, the simulation needs a real data beam-file in order to reproduce the muon beam phase space distribution. In addition, pile-up tracks and halo contribution around the beam are also extracted from real data to be plugged in the Monte Carlo simulation. The simulation environment also needs to propagate the particles through the different materials. This is handled by the GEANT4<sup>4</sup> toolkit, which has been integrated in the Monte Carlo framework of the COMPASS collaboration. This framework is called

<sup>3</sup>The DJANGO generator has been integrated in the COMPASS Monte Carlo framework TGEANT by Nicolas Pierre, and details can be found in [77]

<sup>4</sup>GEometry ANd Tracking

TGEANT<sup>5</sup> and features all the detectors geometries as well as a user interface to feed it with different physics generators and diverse options. A very complete description can be found in [92].

After the propagation of the particles in the setup, the reconstruction part takes place. The energy deposits in each detector are first digitised in so-called Monte Carlo hits and diverse information are plugged in to reproduce the real-data behaviour. In particular the efficiencies of all the detectors are applied as well as smearing effects. All these steps are performed separately from the generation level in order to gain flexibility on the update of these inputs, and avoid the time consuming generation and propagation part. Although these are specific to the Monte Carlo treatment, the very same reconstruction procedure is applied on both real and Monte Carlo data.

As mentioned in [Section III.2.6](#), a specific treatment has to be applied to the CAMERA detector. Since the latter is not taken into account in the COMPASS reconstruction software, specific codes have been developed in the purpose of reconstructing the CAMERA information into proton track candidates. As the geometry of the detector was refined by the tomography of CAMERA detailed in [Section III.2.3](#), the results have also been propagated to the Monte Carlo software at the generation level. Moreover the CAMERA reconstruction code also encompasses inputs on the photomultiplier's efficiencies as well as a raw digitisation procedure, in order to have a more complete and accurate simulation with respect to the real data.

### 5.3 Comparison and extraction of the structure function $F_2$

With the aforementioned improvements on the hodoscopes and trigger description, a detailed investigation on the quality of the Monte Carlo simulation is performed by measuring the well-known  $F_2^p$  structure function, done by Marlene Gerstner [93]. The physics generation is taken in charge by the DJANGO generator.

A first step is the comparison of various distribution for inclusive deep inelastic scattering events from data and Monte Carlo. [Fig. \(III.8\)](#) shows an example for the muon scattering angle distribution for the Outer trigger, where the Monte Carlo reproduces the data quite well.

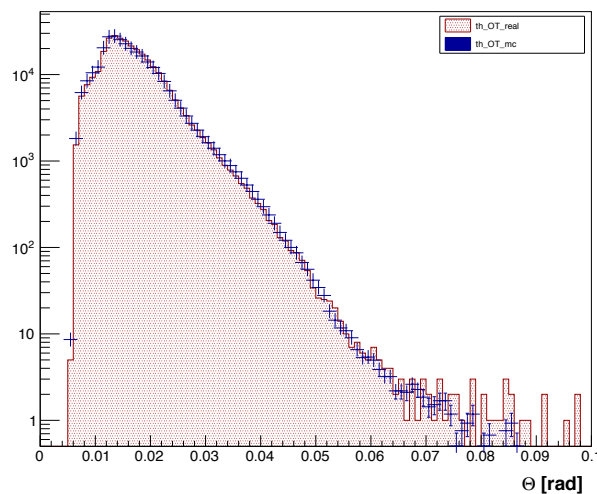


**Figure III.8:** Muon scattering angle for the Outer trigger system. The red line indicates the real data while the blue points display the Monte Carlo events.

<sup>5</sup>Total GEometry ANd Tracking

A second step of the Monte Carlo quality investigation is given by an analysis extracting the structure function  $F_2$ . The Monte Carlo simulation is used to calculate the acceptances for each trigger system in a fine binning in  $(x_B, Q^2)$ . The luminosity is measured from the random trigger method and the DIS cross section and the structure function  $F_2$  can be extracted from the data for the different triggers. The DIS cross section reads:

$$\frac{d\sigma}{dx_B dQ^2} = \frac{4\pi\alpha_{\text{em}}^2}{Q^4 x_B} F_2^p(x_B, Q^2) \left[ 1 - y - \frac{Q^2}{4E_\mu^2} + \left( 1 - \frac{2M_\mu^2}{Q^2} \right) \frac{y^2 + Q^2/E_\mu^2}{2(1 + R(x_B, Q^2))} \right]$$

with  $R(x_B, Q^2) \equiv \frac{\sigma_L}{\sigma_T} = F_2^p(x_B, Q^2) \frac{1 + 4M_p^2 x_B^2 / Q^2}{2x_B F_1^p(x_B, Q^2)} - 1$

(III.6)

The method to extract  $F_2$  relies on the one developed by the SMC collaboration from which a precise parametrisation was obtained [94]. An example is given in **Fig. (III.9)** for the data period P09 in 2016, for the Outer trigger in the domain of  $0.04 < x_B < 0.06$  and  $Q^2 > 1\text{GeV}^2$ , and for  $\mu^+$  and  $\mu^-$  beams separately. The open points show the acceptance ; as expected, the  $\mu^+$  and  $\mu^-$  acceptances are rather similar since the beam line magnets and the polarity of the two spectrometer magnets (SM1 and SM2) were reversed when changing the charge of the beam. The  $F_2$  values for  $\mu^+$  and  $\mu^-$  beams are in good agreement between each other and also with the precise parametrisation obtained by the NMC collaboration.

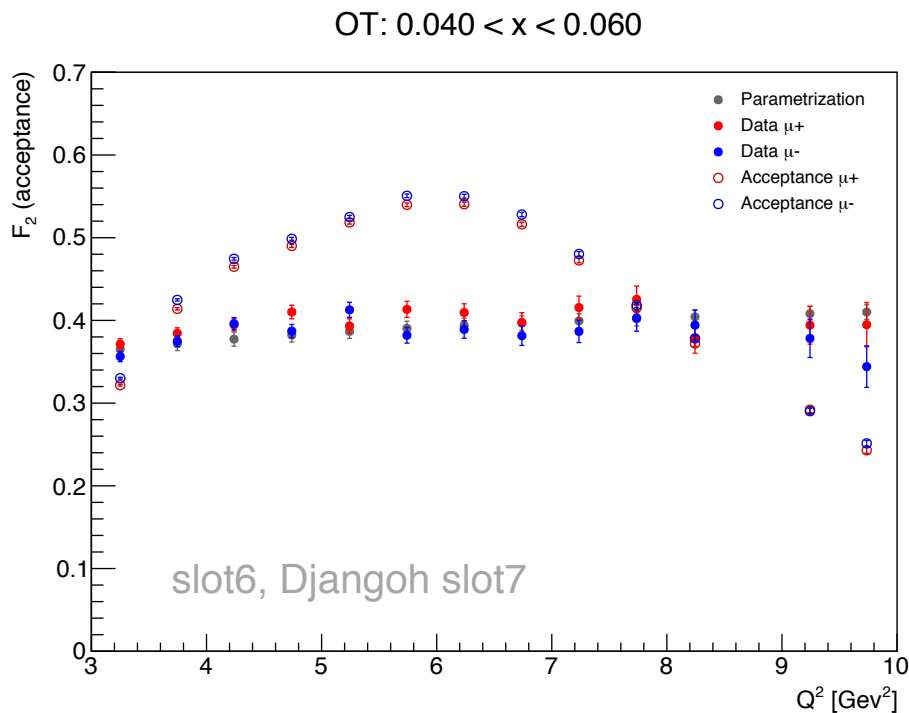


**Figure III.9:**  $Q^2$  dependence of  $F_2$  (full points) and acceptance (open points) for the Outer trigger system in comparison to the NMC parametrisation.

## 6 ECALs calibrations and quality

The purpose of the electromagnetic calorimeters (ECALs) is to detect the outgoing photon from the exclusive single photon topology. Three calorimeters are composed of different types of cells (introduced in [Section III.4.3](#) and are covering different angular regions, from the high angle region with ECAL0 to the lowest one with ECAL2. ECAL2 is important for the detection of the outgoing photon from the Bethe-Heitler process, which therefore serves as the reference region to quantify the quality of the agreement between the Monte Carlo simulation to the data. On the other hand, ECAL0 and ECAL1 aims at detecting the photons coming from DVCS events. In conclusion, all three calorimeters need to be calibrated in energy and time and qualified in order to obtain the most accurate measurement of the outgoing photon.

### 6.1 Time calibration and bad cells determination

The analog signal coming from the PMTs of each ECAL cell passes through a shaper module to enlarge the signal and match with a Sampling Analog-to-Digital Converter (SADC). The 32 samples obtained from the signal waveform are recorded and used to extract the amplitude and the time of a signal relative to the trigger time.

A study of the time response of each of the 6424 cell of the three calorimeters has been performed. This study allows to first calibrate the cells in time with respect to the trigger time<sup>6</sup>, and possibly detect pathologic cells. In particular, this analysis is asked to detect either dead or noisy cells. In these cases, the cell is muted at the reconstruction step in order not to pollute the signals of the other cells with noise, and to improve the clusterisation procedure. The high number of cells (6424) features many types of background shapes, where a single peak has to be found. A typical clean cell response is shown in [Fig. \(III.10\)](#), where the fitting algorithm is applied.

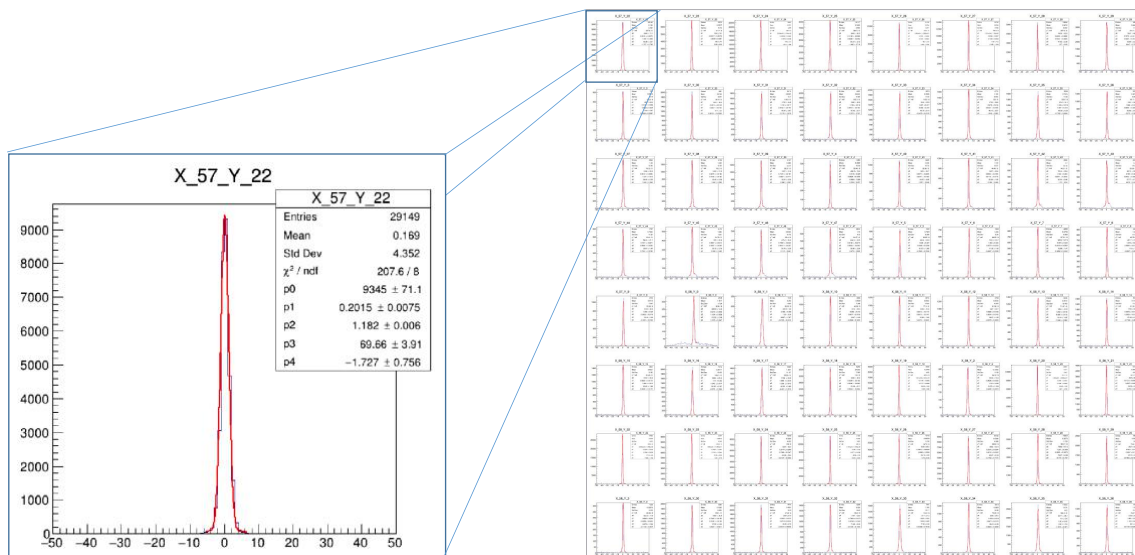


**Figure III.10:** Example of clean cell responses in blue. The red line indicates the fit result with a model function of gaussian plus a 1-order polynomial.

<sup>6</sup>The calibration is performed so that the time difference between the cluster time and the mean time of the beam track is 0 ns

### The selection and calibration procedure

In order to clean the cell response, and simplify the peak detection algorithm, the calibration procedure is applied after selecting events where the virtual photon features  $Q^2 > 0.8 (\text{GeV}/c)^2$ . An additional requirement on the clusters energy  $E_\gamma > 1 \text{ GeV}$  is asked, leading to a better signal quality to identify a peak defining the time calibration.

Nevertheless, the analysis has shown different kind of cell response. **Fig. (III.11a)** shows an example of a good cell behaviour, whereas **Fig. (III.11b)** display a noisy cell without visible signal (despite the 1 GeV threshold), which is therefore excluded from the reconstruction procedure. Other pathologic cases have been exhibited such as double peak responses (shown in **Fig. (III.11c)**) and have been further investigated.

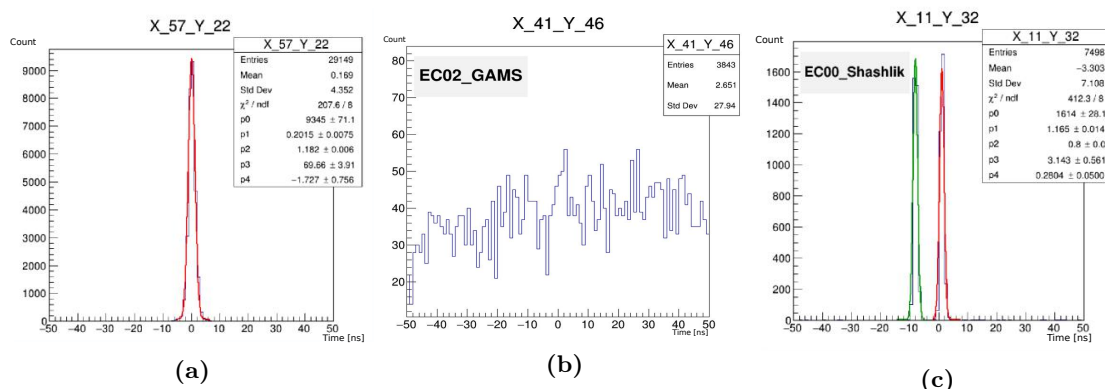


**Figure III.11:** (a): Time distribution for an ECAL2 cell, showing a signal. The fit is indicated by the red line whose the mean value indicates the calibration to be applied. (b): Example of time distribution for a noisy cell. (c): Time distribution showing two peaks for an ECAL0 cell. The two fits are indicated by the red and green curves.

In the above-mentioned cases of double peaks, a correlation has been established with the run number during the periods of data taking, and shows time jumps in the response for some blocks of cells. Therefore, a more granular analysis in time has been suggested and performed. For illustration purposes, **Fig. (III.12)** displays the timing calibration to be applied in the case of ECAL0 cells, with one example of dead cell and an example of time jump within the period. As the run-wise statistics precludes any calibration or analysis, the cell signals have been integrated in blocks of runs (also called sub-periods) from the data-taking, usually separated by a beam charge modification. Nonetheless, some cells have shown unstable behaviours within subperiods. **Fig. (III.13)** shows such examples for two cells of ECAL1 GAMS. As the two peaks are close to each other, the algorithm has not distinguished the two regimes. Those cells still show a clear signal, and they are not considered as bad in the analysis. In order to accept such responses, the cluster timing cut in the following paragraphs shall not be chosen too tight<sup>7</sup>.

### Bad cells detection

In addition to the dead cells, the algorithm should also be able to detect bad cells behaviours such as the one in **Fig. (III.11b)** and not be too sensitive on the background: indeed the statistics available per sub-period is pretty limited and the algorithm might find artificial peaks within the background statistical fluctuations. To account for this, a quality criteria on the fit result is applied based on a minimum signal-over-background ratio. In cases

<sup>7</sup>The cut on the cluster timing is set at  $3\sigma$  in this analysis. The effect of such a cut can be investigated in the future (for instance at  $6\sigma$ ).

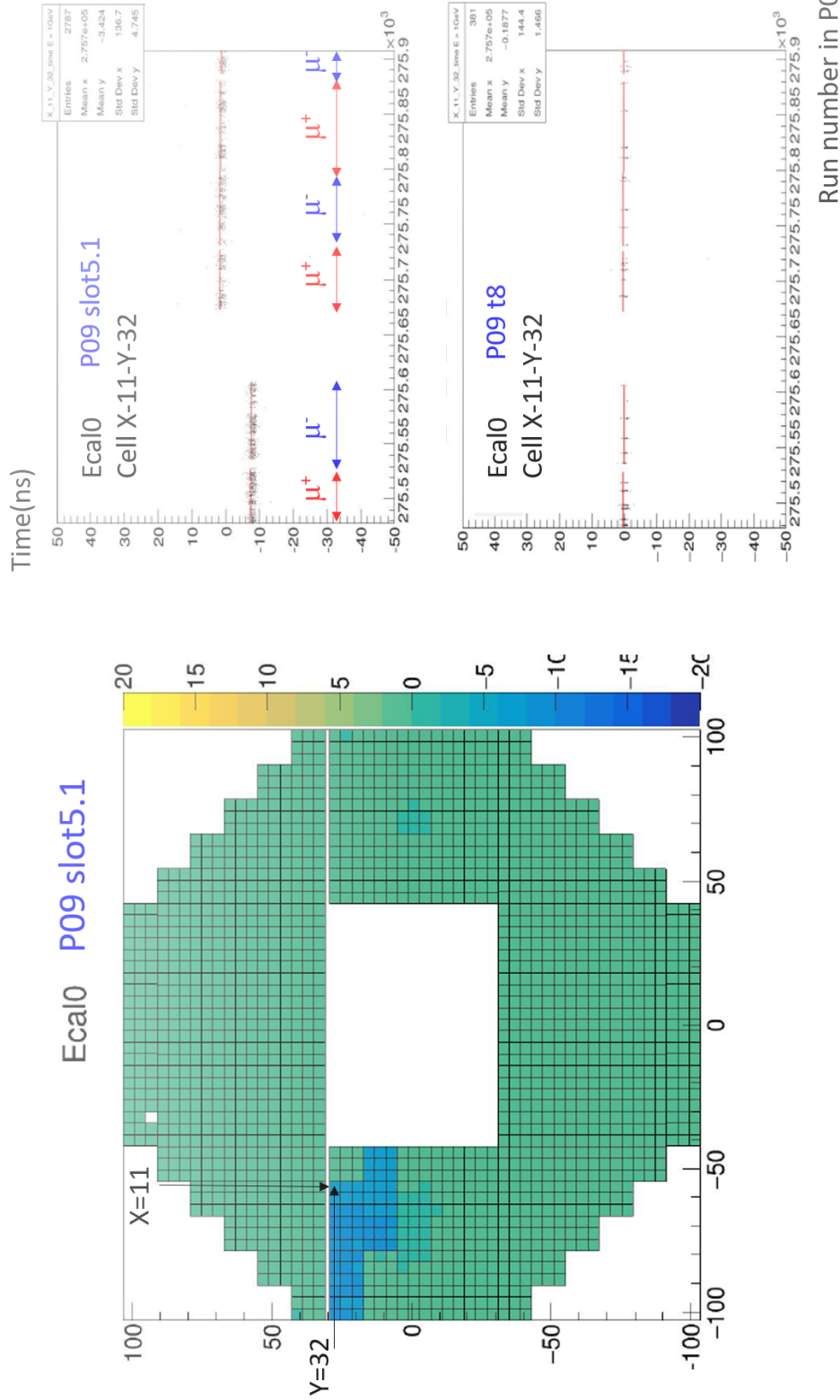


**Figure III.12: Left:** Timing calibration displayed for each cell of ECAL0. The value is indicated by the  $z$ -axis. A dead cell X\_17\_Y\_48 on the top left corner is observed, and a block of cells on the left reveals a miscalibration. Obtained from the first sub-period of the un-calibrated period P09slot5.1. **Right:** Evolution of the peak position as function of the run number for the period P09 and the cell X\_11\_Y\_21 (ECAL0 Shashlik). The top plot shows the evolution before the calibration, and the bottom plot after the calibration.

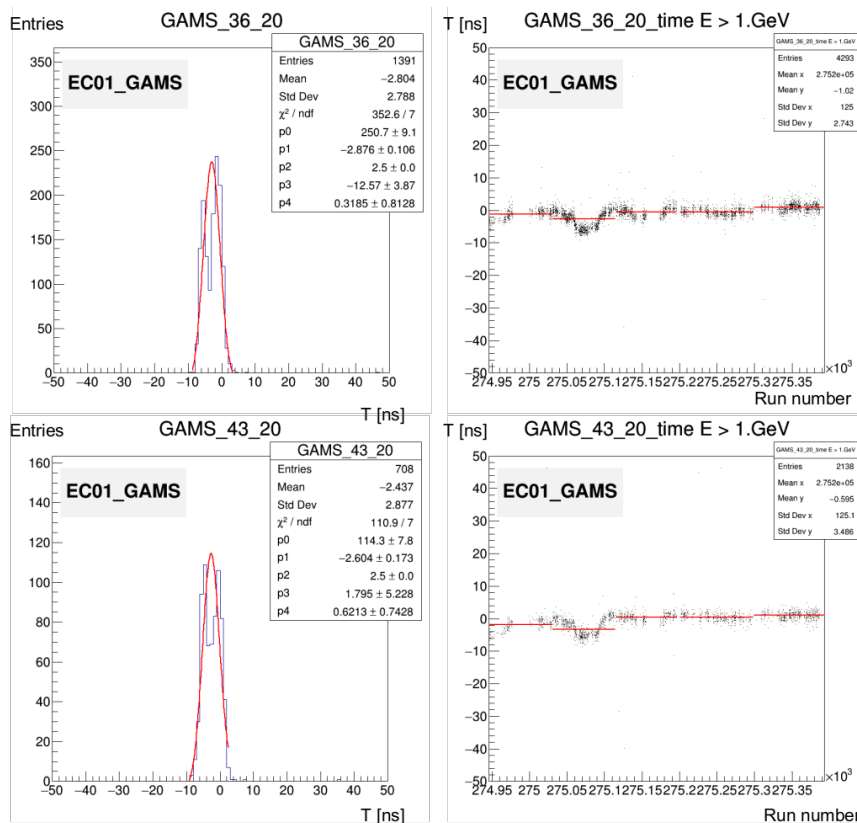


**Figure III.13: Left column:** Time response of two GAMS cells in ECAL1 for the second subperiod of P09. A double peak is observed. **Right column:** Time response as function of the run number. The two regimes are visible within the second subperiod.

multiple peaks candidates are found, the one with the best signal over ratio is selected. For certain cells, the statistics accumulated over a sub-period might not be enough to detect a real peak signal and perform a reliable calibration. In these cases a recovery procedure is ignited in which the behaviour of the cell is studied with an energy threshold lowered at 300 MeV from which the calibration is extracted. In other cases, some cells feature sub-periods noisier than others, where no signal can be seen due to too much background. For this, a stability criteria is asked for each cell along the full period. The number of good spills from each sub-period is recorded for each successfully fitted sub-period. Each cell featuring less than 70% successfully fitted spills out of the total number of spills of the period is marked as a bad cell. Two examples are shown in Fig. (III.14) where one sees a clear signal for the beginning of the period and a noisy behaviour or no signal after. These unstable behaviours tag the cell as bad. <sup>8</sup>

### Ecals timing cut

Finally these time calibrations serve as basis for a quality cut on the cluster's timing. For this the cluster time<sup>9</sup> is displayed against its energy for the different types of cells as in Fig. (III.15). We can observe a maximum density for a timing peak around event if a few other peaks still persist. The origin of the secondary peak at 12.5 ns for all cell types is still

<sup>8</sup>At the reconstruction level the bad cell list is defined for the full period and not run-wise. This is why a stability criteria is asked along the full period.

<sup>9</sup>As for the calibrations, the  $y$ -axis displays here the time difference between the cluster time and the mean time of the beam track.

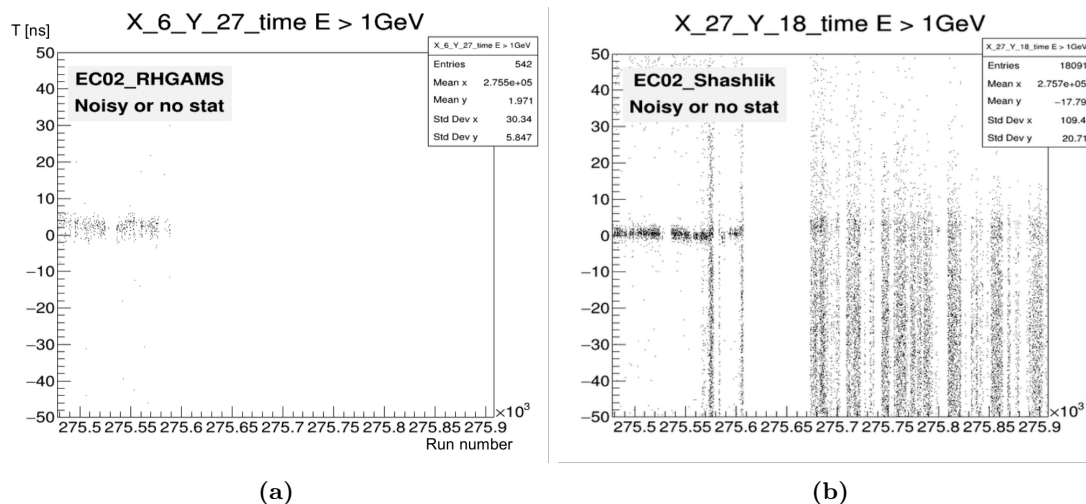


**Figure III.14:** Time response for two cells with respect to the mean beam track time, as function of the run number for the period P09. **(a):** Example of a bad cell with no signal after the second subperiod. **(b):** Example of a bad cell with a too noisy signal after the second subperiod.

unknown and does not seem to be related to miscalibrations. Nonetheless, these clusters are of very low statistics compared to the main peak, especially after applying the DVCS energies thresholds (indicated by the orange lines on the plots). An energy-dependent timing cut is applied, indicated by the purple dashed lines. Due to the various shapes of the different type of cells, a polynomial parametrisation has been chosen [95, 96] adjusted at a distance of  $3\sigma$  to the mean of the signal.

## 6.2 Energy calibration

The energy reconstruction procedure from the electromagnetic calorimeters is performed in different steps.

### First step

The ECAL1 and ECAL2 are calibrated by exposing all their cells to a 40 GeV electron beam. An automatised calibration procedure changes the position of the calorimeter between two consecutive spills. The total cluster charge deposited, *i.e.* the sum of the charges of the module being calibrated and the neighbouring ones, is compared to the electron beam energy. Several iterations are necessary to determine the HV<sup>10</sup> settings for all modules. The calibration coefficients, which relate the charge measured by each SADC to the energy deposited in the corresponding module, take into consideration the photon energy range for each module. For the exclusive single photon production, the energy ranges are indicated in **Fig. (III.16)**.

On the other hand, the ECAL0 calorimeter can not move with respect to the beam axis. A first calibration is therefore done with the muon beam, taking advantage of the muon halo crossing each cell of ECAL0. The energy deposit in the 25 cm-long shashlik modules gives then a first reference to tune the HV setting. The domain of energy for exclusive single photon production is below 40 GeV for these large photon angles.

<sup>10</sup>High Voltage

### Second step

In addition to the first calibration step using the 40 GeV electron beam (or the halo muon beam) which is done *once per year* of data taking, the stability of the PMTs gains of all the 6426 cells is monitored during the data taking using a Light-Emitting-Diode (LED) monitoring system<sup>11</sup>. The recorded LED monitoring amplitudes are used to correct the response of all ECALs cells on a run-by-run basis. At this step of the calibration, the energy conversion follows the relation **Eq. (III.7)**. Considering a cell  $i$  and a run  $j$ , with  $j_0$  the electron-beam run used for calibration, we can write:

$$A_{[\text{GeV}]}^{i,j} = A_{[\text{ADC}]}^{i,j} \times C^{i,j_0} \times \frac{L^{i,j_0}}{L^{i,j}} \quad (\text{III.7})$$

where:

- $A_{[\text{GeV}]}^{i,j}$  is the energy deposited in a cell  $i$  for the run  $j$
- $A_{[\text{ADC}]}^{i,j}$  is the ADC amplitude in a cell  $i$  for the run  $j$
- $C^{i,j_0}$  is the conversion coefficient from ADC to GeV for a cell  $i$  given by the electron beam calibration during the run  $j_0$
- $L^{i,j}$  is the ADC amplitude of the monitoring amplitude of the cell  $i$  for the run  $j$
- $L^{i,j_0}$  is the ADC amplitude of the monitoring amplitude of the cell  $i$  taken during the electron beam calibration run  $j_0$

---

<sup>11</sup>ECAL0 and ECAL2 are monitored by a LED system, while ECAL1 is monitored by a laser/LED system

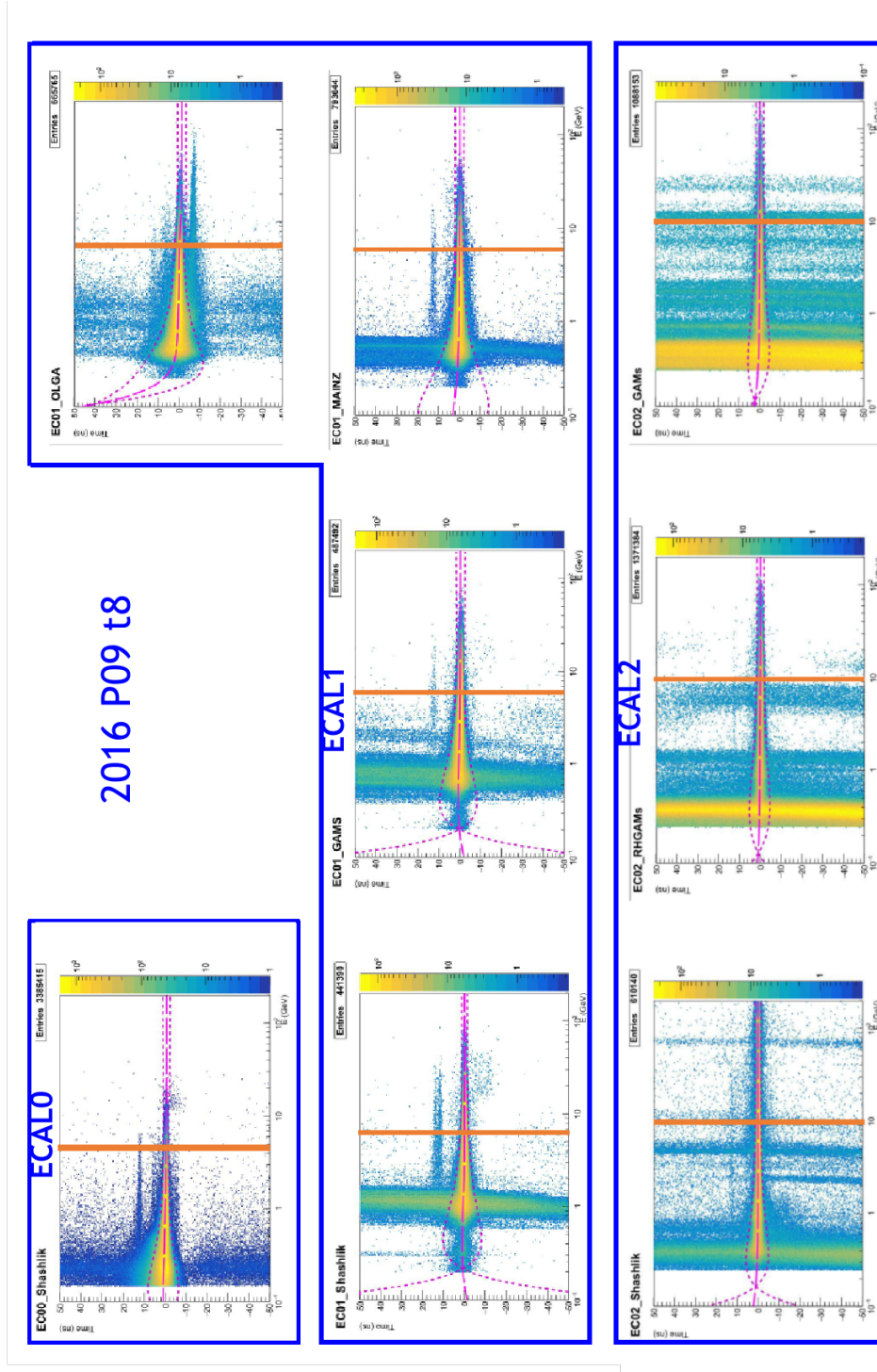
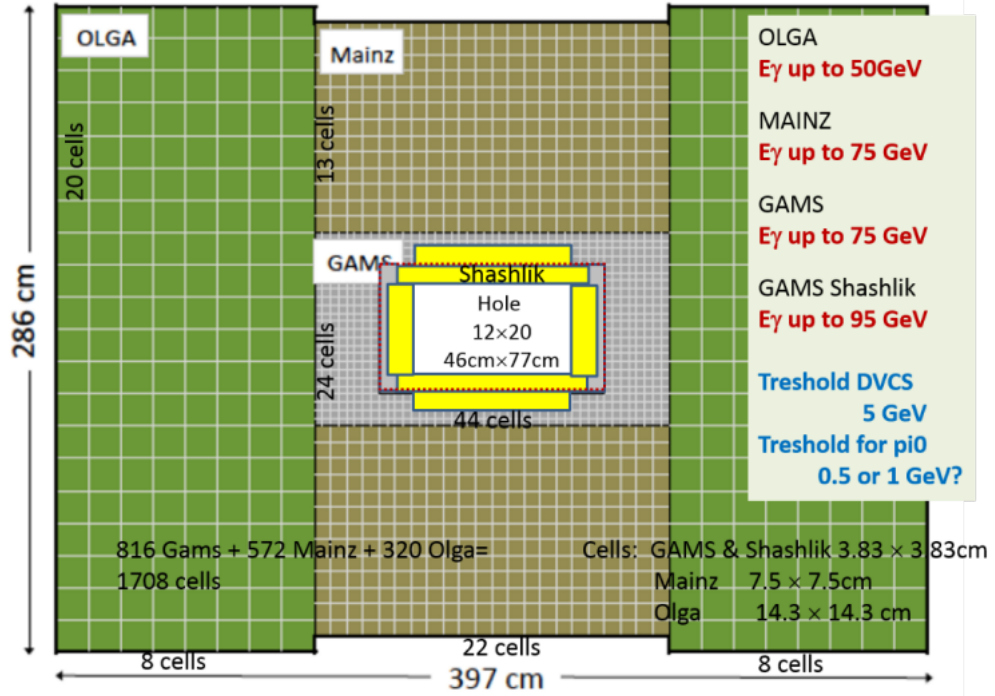
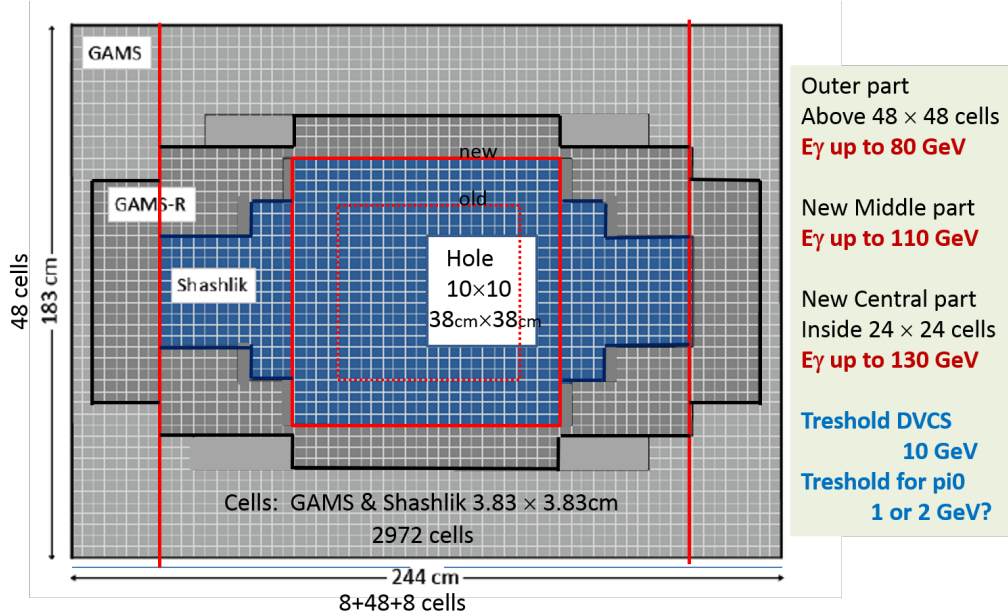


**Figure III.15:** Difference between the time of the cluster and the mean time of the beam track as function of the cluster's energy, for each type of calorimeter cells: ECAL0 made of shashlik modules, ECAL1 made of Shashlik, GAMS, MAINZ and OLGA, and ECAL2 made of Shashliks, GAMS and RadHardGAMs. The vertical orange line indicates the DVCS energy thresholds for the different calorimeters (4,5,10 GeV for ECAL0,1,2 respectively). The purple dashed line indicates the timing cut to be applied at a distance of  $3\sigma$  from the main signal.



(a)



(b)

**Figure III.16:** (a): ECAL1 sketch indicating the size and number of cells. The energy range of the different cell types are indicated in red. (b): Same for ECAL2.

The LED system should be a priori very stable, but an instability of the power supply for ECAL2 was identified, causing jumps in the LED signal output as seen in **Fig. (III.17)**. This issue has been corrected by applying an additional renormalisation factor which was evaluated based on the comparison of the global behaviour of all the LEDs between runs.

$$N_j = \frac{\sum_{i=1}^N \frac{L^{i,j}}{L^{i,j_0}}}{N}, \quad N \text{ being the number of cells in ECAL2} \quad (\text{III.8})$$

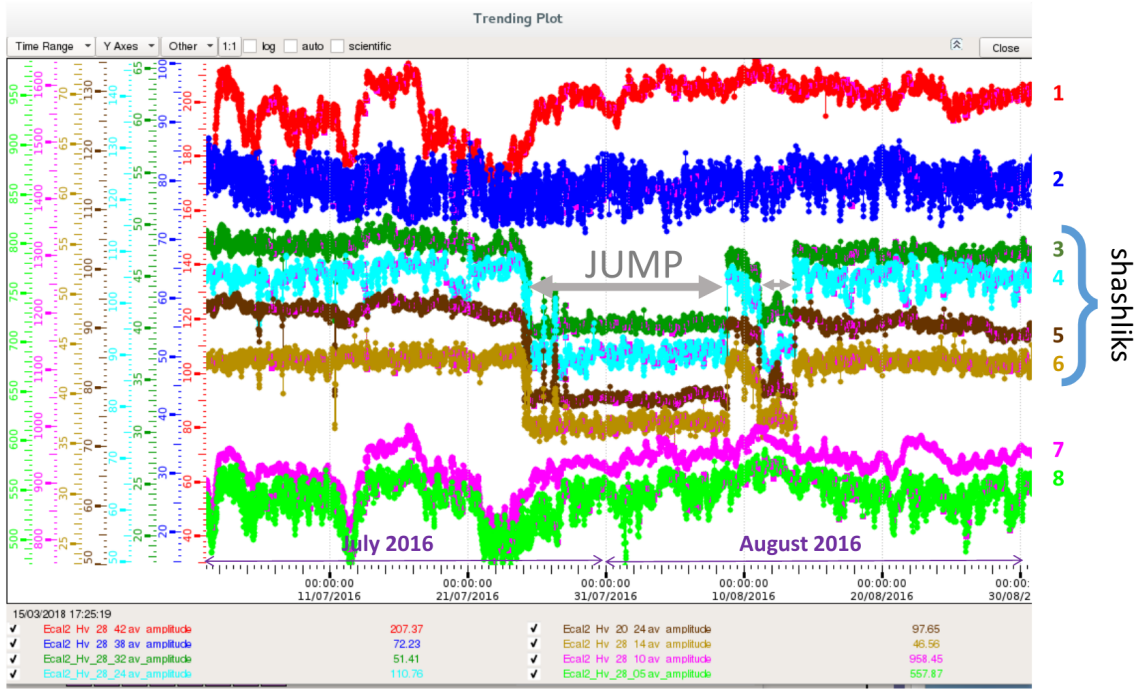


**Figure III.17:** ECAL2 LED response as function of time for 8 blocks of cells recorded during the 2016 data taking.

This LED correction assumes that the LED response ratio  $\frac{L^{i,j}}{L^{i,j_0}}$  is statistically centered around 1 so that it smoothes the LED responses and corrects efficiently the cells with large LED jumps without affecting significantly the other cells. The effect of applying this additional correction factor is illustrated in **Fig. (III.18)**.

### Third step:

The calibration procedure is further fine-tuned using the reconstructed mass of the  $\pi^0$  (as  $\pi^0 \rightarrow \gamma\gamma$ ). A complex iterative procedure [97] is performed where the photon signal of each cell is associated with all the photon signals of the other cells to reconstruct the best peak at the  $\pi^0$  mass. In a first approach, the data used to perform such calibration were taken during a reasonably short time, using the interaction of a pion beam with the hydrogen target. However it has been shown that the obtained calibrations do not preserve a good stability along the complete 2016 campaign, and that the cells on the edges of the calorimeters do not collect a statistics of data large enough to perform the calibration. The alternative solution which has been selected is to perform the same calibration procedure using the data collected with the muon beam integrated over a complete period of data taking for  $Q^2 > 0.5 \text{ GeV}$ . This method allows a period-wise calibration in addition to a broader illumination region of the calorimeters as seen in **Figs. (III.19) to (III.21)**. This procedure is performed in usually a dozen of iterations and provides a cell-by-cell correction

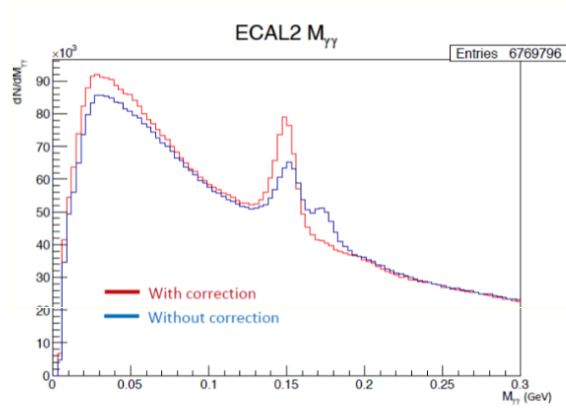


**Figure III.18:** Invariant mass of two-photon clusters registered in ECAL2 during the 2016 P09 period (test production t2). The two peak structures around the  $\pi^0$  mass disappear after applying the correction factor in [Eq. \(III.8\)](#).

factor for each period. In addition, a final additional correction has been established on a run-by-run scale, but for each calorimeter (instead of a cell-wise correction), which evolution is shown in [Fig. \(III.22\)](#). Note that although this last factor is rather stable for ECAL0, it is still needed for ECAL1 and ECAL2<sup>12</sup>.

### Summary

In fine, the calibration formula is depicted in [Eq. \(III.9\)](#), using the same notations as [Eq. \(III.7\)](#), for a cell  $i$ , and a run  $j$  belonging to the period  $p$ :

$$A_{[\text{GeV}]}^{i,j} = A_{[\text{ADC}]}^{i,j} \times C^{i,j_0} \times \frac{L^{i,j_0}}{L^{i,j}} \times \left( \frac{\sum_{i=1}^N \frac{L^{i,j}}{L^{i,j_0}}}{N} \right) \times S^{i,p} \times S^j \quad (\text{III.9})$$

where:

$S^{i,p}$  is the final tuning energy calibration using the  $\pi^0$  mean reconstruction

$S^j$  is the run by run dependant additional correction

<sup>12</sup>These corrections can be applied in the PHAST software by using the UserEvent 15

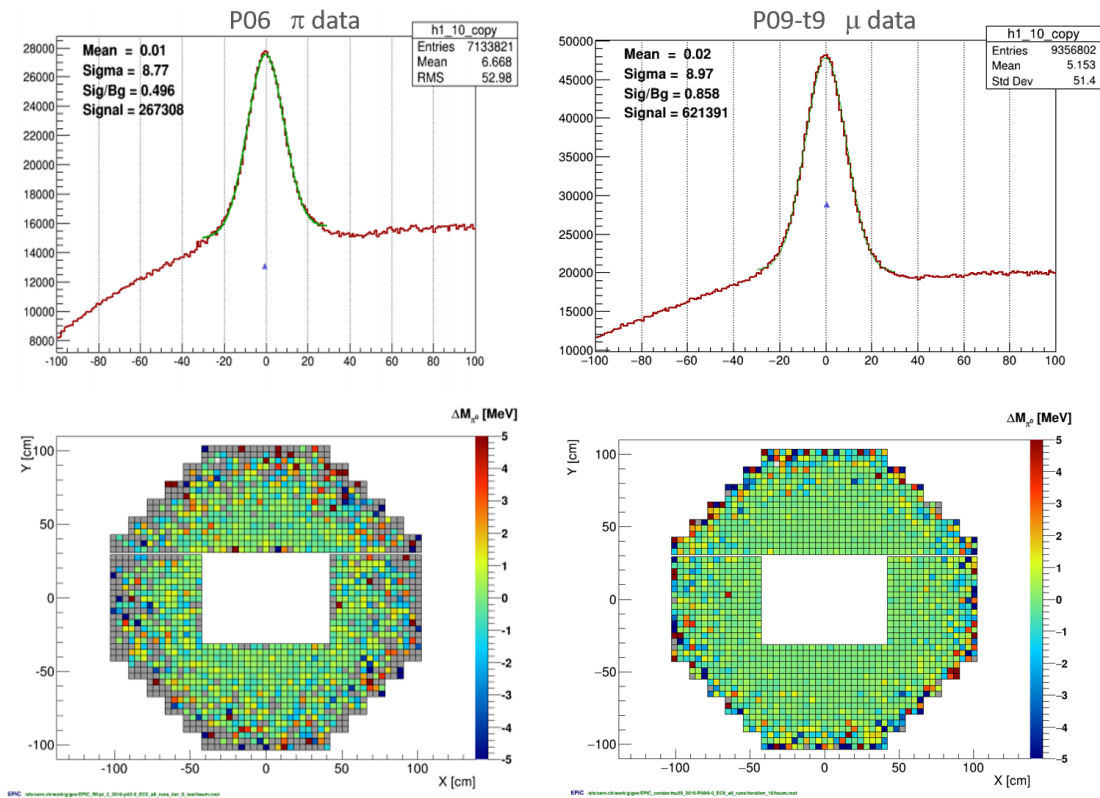


**Figure III.19: Left:** Calibration of ECAL0 using the pion beam during the period P06. The distribution of the difference between the two-photons invariant mass and the nominal  $\pi^0$  mass is shown on the top plot. The extracted value of the peak position for each cell is displayed on the  $z$ -axis of the bottom plot. In this case, nine iterations of the algorithm were needed.

**Right:** Calibration of ECAL0 using the muon beam data. The same distributions are shown as in left. Figures from [97]

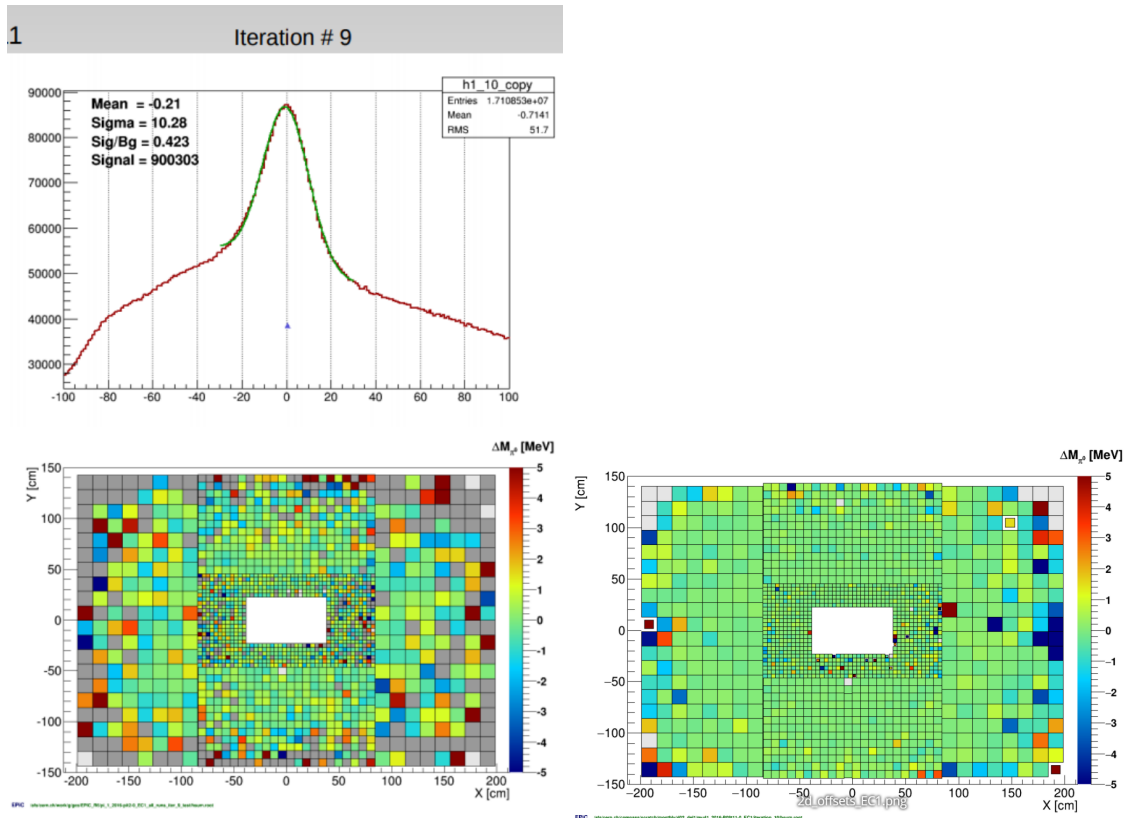


**Figure III.20: Left:** Calibration of ECAL1 using the pion beam during the period P06. The distribution of the difference between the two-photons invariant mass and the nominal  $\pi^0$  mass is shown on the top plot. The extracted value of the peak position for each cell is displayed on the  $z$ -axis of the bottom plot.  
**Right:** Calibration of ECAL1 using the muon beam data for the period P09. The result for each cell is shown as in left. Figures from [97]

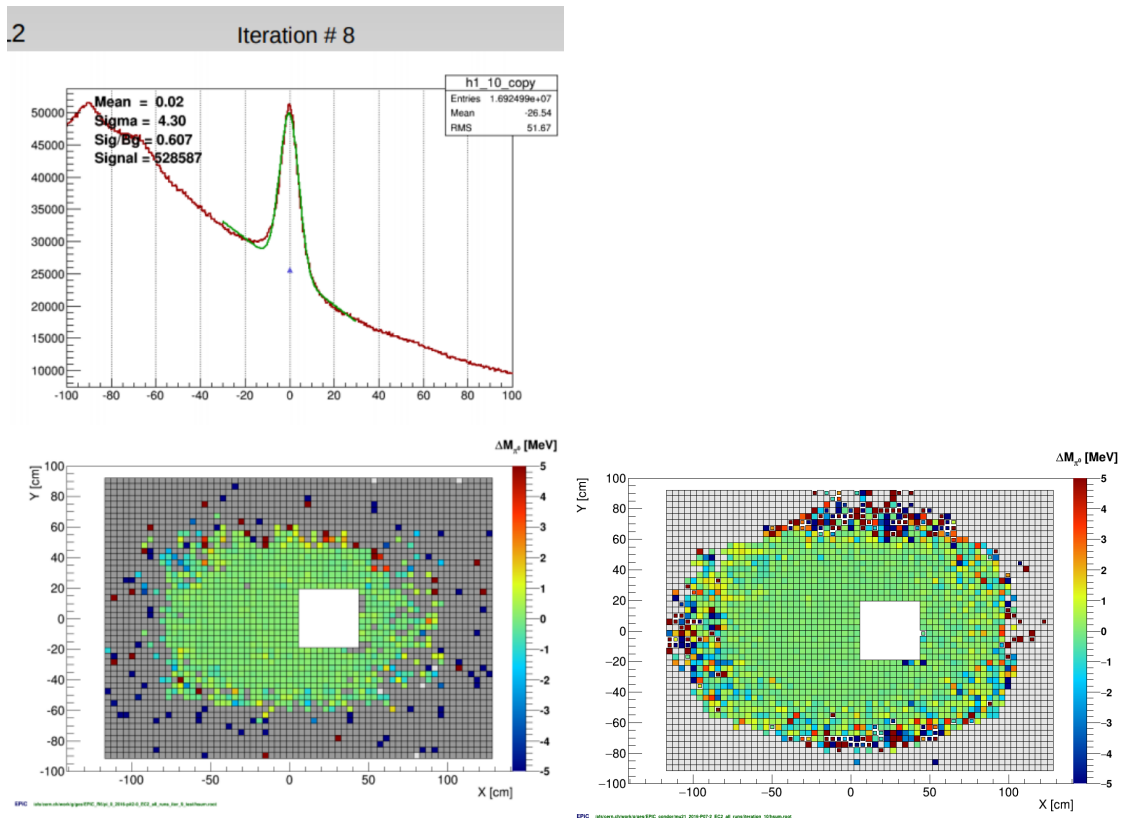


**Figure III.21: Left:** Calibration of ECAL2 using the pion beam during the period P06. The distribution of the difference between the two-photon invariant mass and the nominal  $\pi^0$  mass is shown on the top plot. The extracted value of the peak position for each cell is displayed on the  $z$ -axis of the bottom plot.

**Right:** Calibration of ECAL2 using the muon beam data for the period P09. The result for each cell is shown as in left. Figures from [97]

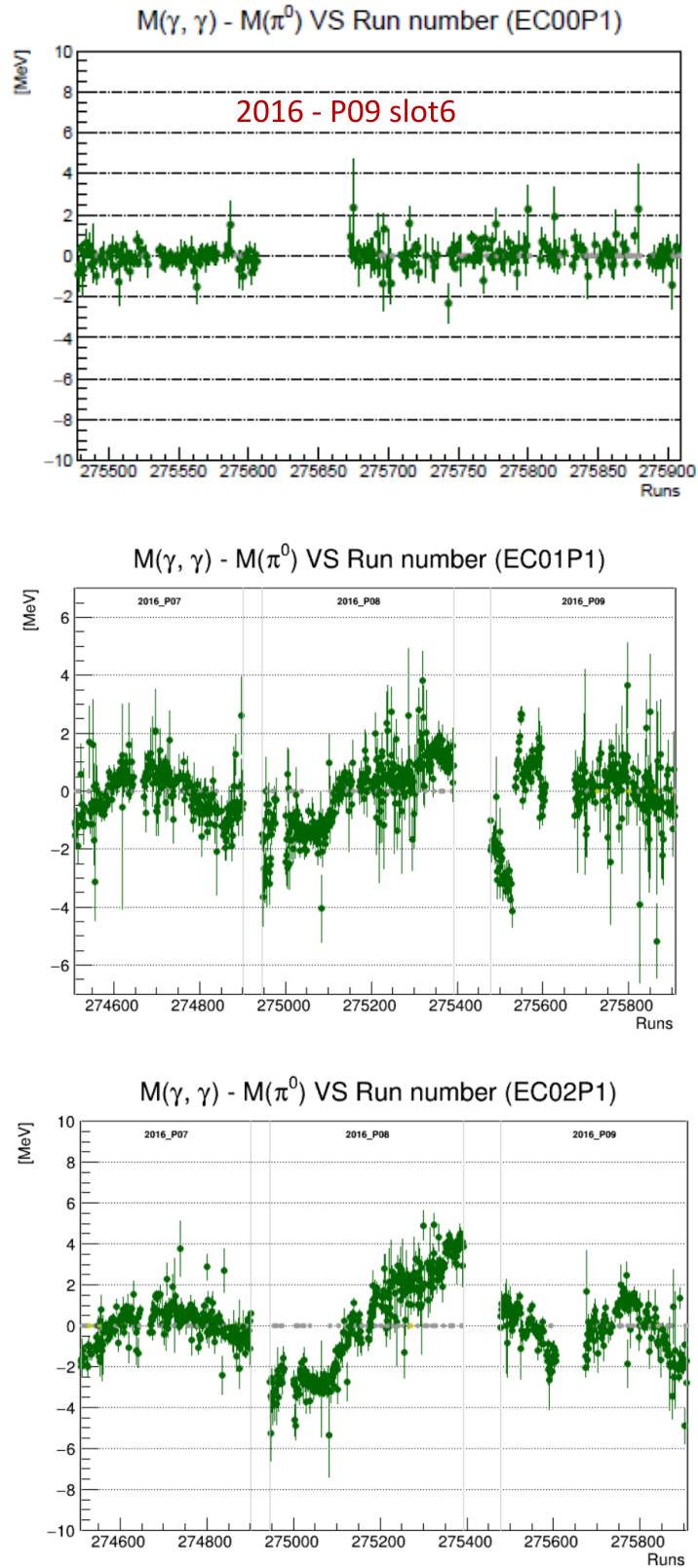


**Figure III.22:** Distribution of the  $\pi^0$  mass deviation on a run-by-run basis for the different calorimeters and different periods. This final correction provides the term  $S^j$  in **Eq. (III.9)**. Figures from [97]

### 6.3 Monte Carlo simulation

#### Modelisation and shower profile parametrisation

The Monte Carlo simulations are based on the GEANT4 software to orchestrate the particle propagation and interactions within the sensitive volumes of the detectors. However high energetic interactions within the electromagnetic calorimeters create complex and extended showers made of secondary particles, each one being tracked and propagated by GEANT4. Therefore the simulation of electromagnetic showers is often the most time consuming part of a simulation. Although the GEANT4 software includes a parameter called *production cut* which tunes the precision of the simulation, this parameter is not sufficient to provide both a precise simulation and a decent processing time of the electromagnetic shower. In the case of the COMPASS setup, the processing time skyrockets by a factor  $10^2 - 10^3$ s between a not-enough precise simulation and a reasonable one [92].

To compensate such increase, an adaptative tool called GFlash [98] has been developed by a team from the Max-Planck-Institut of Munich and integrated by the GEANT4 community in order to provide a general fast simulation technique to be shared between different communities. The principle consists in replacing the detailed simulation of the incoming particle with directly energy depositions representing the energy deposit of all particles from the shower development. The strength of this software is its adaptability on any kind of detectors and experiments which makes it less costly to integrate. A tweaking procedure is still needed, based on certain parametrisation ansatz and an evolutionary (or genetic) algorithm for finding the best parameters set. The details on the selection, recombination and mutation of the algorithm can be found in [92], where the tweaking procedure is applied in the case of the 3 electromagnetic calorimeters of the COMPASS experiment. Since GFlash only applies in homogeneous volumes, the shower propagation near interfaces between different cell types or holes is covered by the GEANT4 tracking. The validation of the GFlash ansatz and parameter set has been performed by toy Monte Carlo comparing the results from GFlash and GEANT4 [92].

#### Energy calibration

The simulated energy deposit is not explicitly tuned by the algorithm and has to be calibrated so that it matches the energy of the incident particle after the cluster reconstruction. These calibrations have been performed for the 2012 setup but since then, several updates have been made notably on the description of ECAL1 and ECAL2 Shashlik modules to correctly describe the materials within.

A re-calibration was necessary and performed by Po-Ju Lin on a cell-type basis with a reasonable linear parametrisation ansatz using a coefficient  $b$ . The Monte Carlo residual energy is displayed in **Fig. (III.23)** from which the  $b$  values are extracted per cell type in **Table (III.1)**. The values of  $b$  are slightly above 1 as the consequence of the energy-dependent leakage at the interface between the calorimeter cells.

After the integration of the  $b$  correction factor, a last correction is performed on the relative residual distribution as function of the reconstructed cluster's energy. A parametrisation of the form  $\frac{\Delta E}{E} = a + b/E + c/E^2$  is fitted as shown in **Fig. (III.24)**<sup>13</sup>.

<sup>13</sup>These corrections can be applied in the PHAST software by using the UserEvent 16

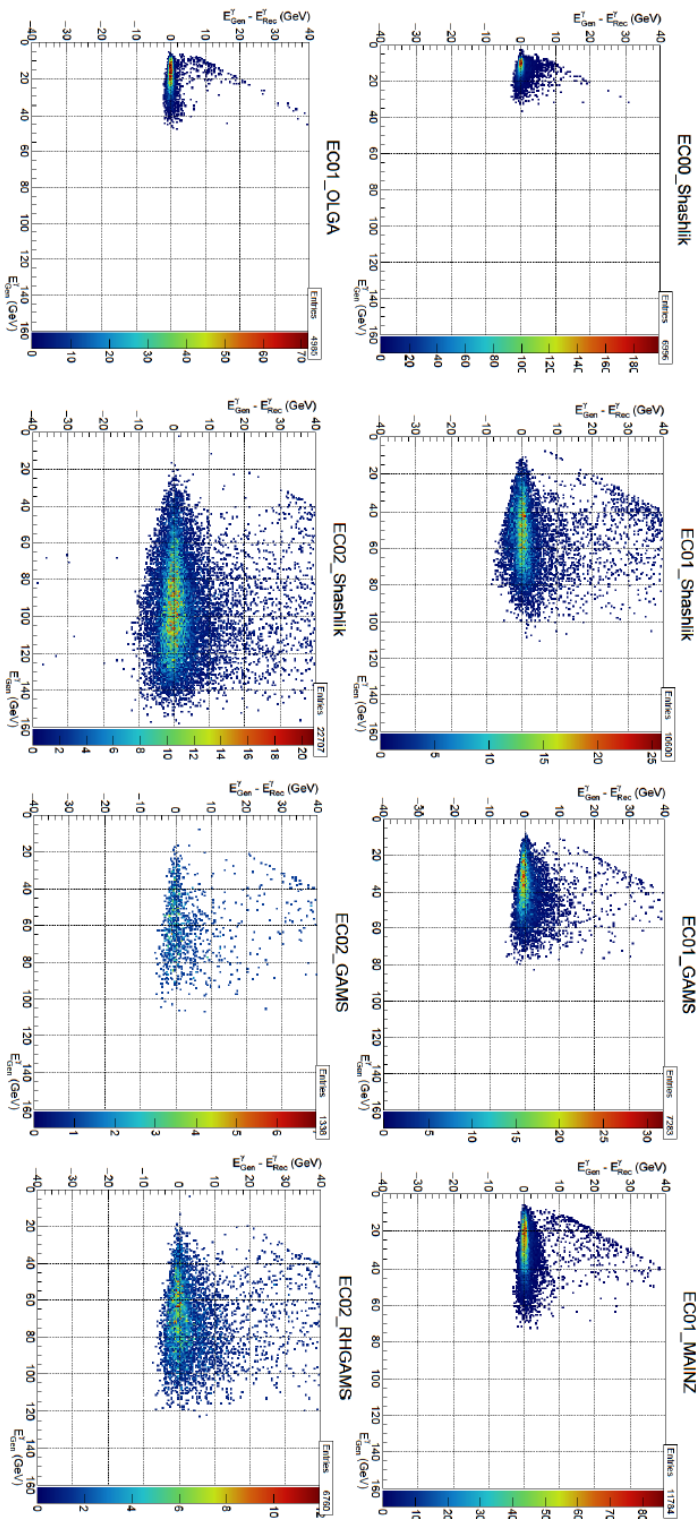
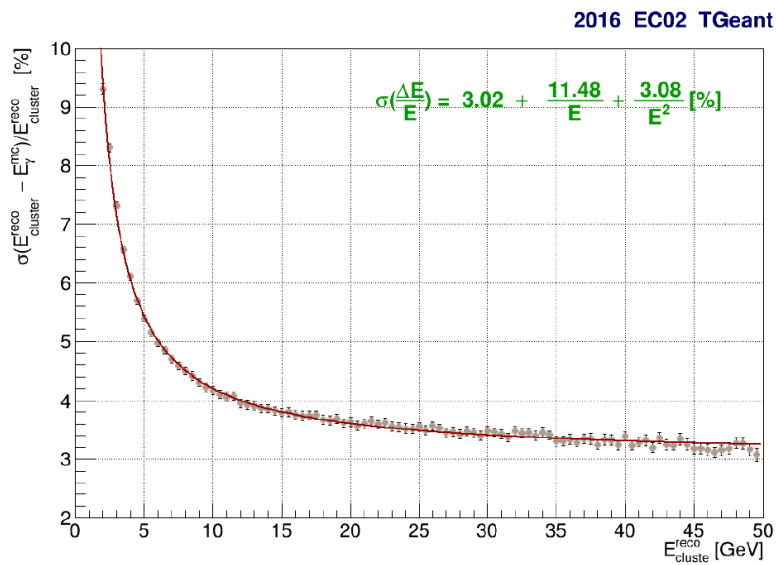
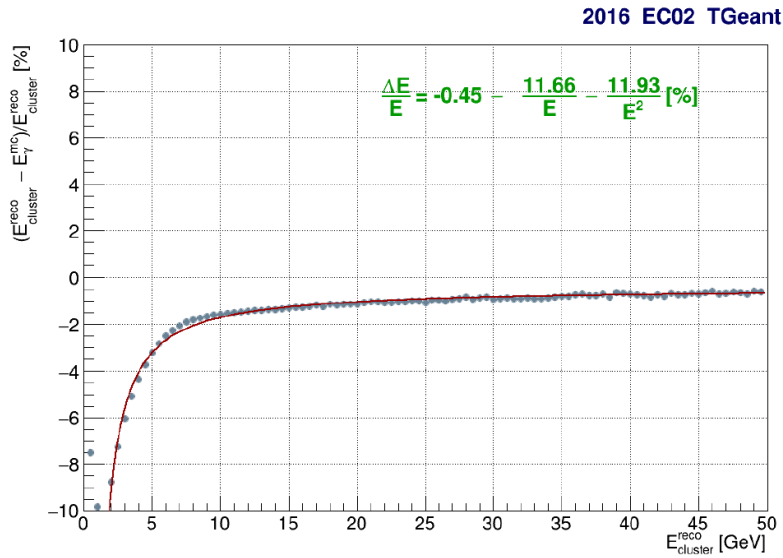


Figure III.23: Residual energy ( $E_{\text{Generated}}^{\gamma} - E_{\text{Reconstructed}}^{\gamma}$ ) as function of  $E_{\text{Generated}}^{\gamma}$  for the different cell types

Cell type	$b-1$
ECAL0 Shashlik	0.8409
ECAL1 Shashlik	0.8440
ECAL1 GAMS	0.8980
ECAL0 MAINZ	0.9762
ECAL0 OLGA	0.9598
ECAL2 Shashlik	0.8304
ECAL2 RHGAMS	0.8735
ECAL2 GAMS	0.8706

Table III.1: Energy calibration factors  $b$  extracted for the different cell types.



**Figure III.24:** (a): Mean values of the relative residual of the reconstructed cluster's energy with respect to the reconstructed cluster's energy in ECAL2. The parametrisation function is written in green and is shown by the red curve. (b): Standard deviation values of the relative residual of the reconstructed cluster's energy with respect to the reconstructed cluster's energy in ECAL2. Figures from [97]

# CHAPTER IV

---

## EXCLUSIVE REACTIONS AND CAMERA CALIBRATIONS

---

### Contents

---

<b>1</b>	<b>Exclusive processes and multivariate analysis</b>	<b>80</b>
1.1	The mathematical framework	80
1.2	Application to the exclusive $\rho^0$ events	87
<b>2</b>	<b>CAMERA calibrations</b>	<b>90</b>
2.1	Exclusive $\rho^0$ event selection	90
2.2	Azimuthal calibration	90
2.3	Radial tomography	92
2.4	Longitudinal calibration	95
2.5	Time of flight calibration and momentum adjustment	96
2.6	Monte Carlo simulation	97

---

This chapter will present an essential tool to analyse the exclusive processes. For an identified process, the full kinematics can be reconstructed by only a few observables. A kinematic fit, *i.e.* a multivariate analysis, provides the best set of values for all the observables of the process. In addition, the procedure gives a score of closeness to the assumed topology in terms of a  $\chi^2$  value. A detailed presentation of the mathematical framework will be done in this chapter. The application of this tool will improve the kinematic variables of the DVCS process (*cf.* [Chapters \(V\)](#) and [\(VI\)](#)). Another application is used for the calibration of the recoil proton detector CAMERA that I performed, using the prediction of the recoil proton momentum and angles using only the measurement of the muons and the  $\rho^0$  which decays in  $\pi^+\pi^-$  in the forward COMPASS spectrometer for the exclusive  $\rho^0$  production. My contribution has been to provide a rigorous and convenient software interface for the kinematic fitting procedure of DVCS/HEMP processes. In addition I improved the reconstruction code for the CAMERA detector and its Monte Carlo simulation.

## 1 Exclusive processes and multivariate analysis

One remarkable property of the COMPASS experiment is the redundancy of the measurement. One can especially take advantage of this in exclusive reactions. If the topology of the event is known and if we measure all the particles involved in the process, the kinematics is over-determined. It is therefore possible to correct the values of the measurements within their covariances, in order to make them fit better certain physics constraints such as the topology of the exclusive process, or geometrical constraints like a common vertex for the interaction. This method is called a kinematic fit, and allows us to make use of the different measurements for the same observables in order to reduce the associated error.

In this part, the mathematical framework and objects involved will be first defined, in order to understand the following description of the algorithm. Then two study cases will be thoroughly described as application examples in the COMPASS experiment. The first application will be on the exclusive  $\rho^0$  sample and using only information coming from the spectrometer. This sample will be used for the calibration of the CAMERA detector described in [Section IV.2](#). Then, the second application will focus on the exclusive  $\gamma$  events, where the information of CAMERA will be added to the kinematic fit. The latter will show the full potential of this multivariate approach, with the extension to any exclusive meson measurement.

### 1.1 The mathematical framework

The idea of the kinematic fit is to associate to each event a real number describing how close it is to the exclusive event topology sought. In addition the optimisation procedure provides a modification of the measurements within covariances in order to better fit the underlying constraints of the topology. It is not necessary to measure all the parameters involved to have an overconstraint problem, so that we have to distinguish what is measured in the experiment and what is unmeasured. An example is on the measurements related to the photon ; from electromagnetic calorimeters, one can measure its energy, however its azimuthal and polar angle remain unmeasured.

Let  $M, U$  be the number of measured (resp. unmeasured) parameters in the analysis, and  $\vec{k} \in \mathbb{R}^M, \vec{h} \in \mathbb{R}^U$  be the vector of measured (resp. unmeasured) parameters. Then we can define an optimisation function as:

$$\chi^2(\vec{k}) = \Delta \vec{k}^T C^{-1} \Delta \vec{k} \quad (\text{IV.1})$$

with  $\Delta \vec{k} = \vec{k} - \vec{k}_{\text{init}}$

where  $\vec{k}_{\text{init}}$  is the vector of initial measurements and  $C$  its associated covariance matrix<sup>1</sup>. This function has to be minimised with respect to the constraints defined by the set of equations  $\vec{g}(\vec{k}, \vec{h}) = \vec{0}_I, I$  being the number of constraints

The minimisation procedure is based on the Lagrange multiplier method, defining the Lagrangian

$$\mathcal{L} = \chi^2(\vec{k}) + 2 \sum_{i=1}^I \lambda_i g_i(\vec{k}, \vec{h}) \quad (\text{IV.2})$$

---

<sup>1</sup>The operation consisting in dividing by the covariance matrix serves the purpose of obtaining a sum of normal distributions (by definition of a  $\chi^2$  function). This is sometimes referred as "feature renormalisation" in machine learning techniques.

$(\lambda_i)_{i \in \llbracket 0, I \rrbracket}$  being the Lagrange multipliers. The Lagrange multiplier method provides an analytic solution for this system. In the case of linear constraints, the problem can be transcribed in terms of matrices as done in [99, 80], where an explicit solution is provided. However due to the physics origin of these constraints, the set of equations to be solved is non-linear which precludes any general treatment.

$$\forall (i, j, l) \in \llbracket 1, I \rrbracket \times \llbracket 1, M \rrbracket \times \llbracket 1, U \rrbracket \begin{cases} \frac{\partial \mathcal{L}}{\partial \lambda_i} = 0 \\ \frac{\partial \mathcal{L}}{\partial k_j} = 0 \\ \frac{\partial \mathcal{L}}{\partial h_l} = 0 \end{cases} \quad (\text{IV.3})$$

The various kind of sets of non-linear constraints affects the generality of the form of the solution. In order to make use of the explicit solution in the linear case, [99] proposes an iterative algorithm based on a linearisation of the constraints using their first order Taylor expansion.

$$\begin{aligned} g_i \left( \vec{k}^{(n)}, \vec{h}^{(n)} \right) &\approx g_i \left( \vec{k}^{(n-1)}, \vec{h}^{(n-1)} \right) \\ &+ \sum_{j=1}^M \frac{\partial g_i}{\partial k_j} \Big|_{(\vec{k}^{(n-1)}, \vec{h}^{(n-1)})} \left( \vec{k}_j^{(n)} - \vec{k}_j^{(n-1)} \right) \\ &+ \sum_{l=1}^U \frac{\partial g_i}{\partial h_l} \Big|_{(\vec{k}^{(n-1)}, \vec{h}^{(n-1)})} \left( \vec{h}_l^{(n)} - \vec{h}_l^{(n-1)} \right) \end{aligned} \quad (\text{IV.4})$$

where  $n$  is the iteration step number.

By doing so, the algorithm finds the best solution for a certain iteration at the first order, reevaluates the input parameters, and reprocesses another iteration. The initial parameters of the algorithm are the initially measured parameters  $\vec{k}^0 = \vec{k}_{\text{init}}$  and estimates of the unmeasured parameters  $\vec{h}^0 = \vec{h}_{\approx}$ . The convergence of the procedure is achieved if and only if the three following conditions are fulfilled

$$\begin{aligned} &n < 100 \\ &\left| \frac{\chi^2 \left( \vec{k}^{(n)} \right) - \chi^2 \left( \vec{k}^{(n-1)} \right)}{ndf} \right| < \epsilon_\chi \\ &\sum_{i=1}^I \left| g_i \left( \vec{k}^{(n)}, \vec{h}^{(n)} \right) \right| < \epsilon_g \end{aligned} \quad (\text{IV.5})$$

where  $ndf$  denotes the number of degrees of freedom of the problem, defined as it will be addressed in **Sections IV.1.2** and **IV.3.6**.  $\epsilon_\chi$  and  $\epsilon_g$  are arbitrarily small numbers<sup>2</sup> indicating respectively the convergence of the  $\chi^2$  and the satisfaction level of the constraints.

### Definition of the covariance matrix

The reconstruction software of COMPASS provides tracks information with covariance matrices in a certain frame. In order to make them compatible with the other measurements to apply constraints, jacobian transformations have to be performed first. It has been chosen to use the cartesian representation for the kinematic fit and the application of

---

<sup>2</sup> $\epsilon_\chi = 0.00005$  and  $\epsilon_g = 0.0001$ .

constraints; the resulting jacobians are detailed in [80] for the different types of measurements. One can assume that the measurements between two particles in the spectrometer are uncorrelated, so considering  $N$  particles, one can assume the following matrix block form for the input correlation matrix

$$\tilde{C} = \begin{pmatrix} \tilde{C}_1 & 0 & \dots & 0 \\ 0 & \tilde{C}_2 & \dots & 0 \\ \vdots & \vdots & \ddots & \vdots \\ 0 & 0 & \dots & \tilde{C}_N \end{pmatrix} \quad (\text{IV.6})$$

The submatrices  $\tilde{C}_i$  will be described in the following for different types of particles and will be labeled  $\tilde{C}$  for simplicity. Of course one has only measurements and correlation matrices related to measured parameters. As explained just before, the unmeasured parameters have to be estimated a priori. Therefore their covariance matrices are set to be diagonal with an arbitrarily high variance in order to let them vary freely during the procedure, as they will be further adjusted automatically by the fit based on the constraints of the problem. For this reason, in the following parts the covariance matrix will be only displayed for measured parameters, and labeled as  $\tilde{C}_{|\text{meas}}$  as submatrix of  $\tilde{C}$ . Similarly, the observables associated to the previous covariance matrices will be labeled  $\vec{S}$  and  $\vec{S}_{|\text{meas}}$ .

### Treatment of charged tracks

The charged track parameters consist in five measurements as described by  $\vec{S}$ , correlated through the matrix  $\tilde{C}$

$$\vec{S} = \begin{pmatrix} x \\ y \\ X \\ Y \\ |\vec{p}|^{-1} \end{pmatrix} = \vec{S}_{|\text{meas}}$$

$X, Y$  are short-hands for  $\frac{dx}{dz}$  and  $\frac{dy}{dz}$ . This initial vector  $\vec{S}_{|\text{meas}}$  is given by an extrapolation of the track parameters at the  $z$ -position of the interaction vertex, which is given by the vertex fit done in the reconstruction software CORAL. The extrapolation through the magnetic field is performed by the software analysis PHAST, and takes into account energy loss effects and multiple scattering uncertainties inside the covariance matrix  $\tilde{C}$ . One advantage of this procedure is to be able to write the vertex constraints analytically in the magnetic field free region (considering straight line propagations), and to have a good estimates of the energy losses and multiple scattering from the  $z$ -position of the vertex obtained in CORAL<sup>3</sup>.

In order to homogenise the representations from different particles and apply the constraints, the measured parameters are translated into the cartesian frame through the

---

<sup>3</sup>Note that the track parameters extrapolation is not performed at each iteration, but only once using the initial  $z$ -position of the vertex given by CORAL. The re-vertexing done by the fit is not subject to iterative extrapolations

jacobian  $J$ . The details of the transformation can be found in [80, p. 53–57]. The input of the kinematic fit is then of the form

$$\vec{S}_{\text{input}} = \begin{pmatrix} x \\ y \\ p_x \\ p_y \\ p_z \end{pmatrix} = \vec{S}J \quad \text{and} \quad \tilde{C}_{\text{input}} = J\tilde{C}J^T$$

One can note in this case that all the parameters of a charged track are measured.

### Treatment of photons

The measurement of a photon cluster is performed in one of the electromagnetic calorimeters, from which one can extract its  $x$ - $y$  position at the  $z$ -position of the respective calorimeter, and its energy.

$$\vec{S}_{|\text{meas}} = \begin{pmatrix} x \\ y \\ |\vec{p}| \end{pmatrix} \quad \tilde{C}_{|\text{meas}} = \begin{pmatrix} \tilde{C}_{x,y} & 0 \\ 0 & \sigma_{|\vec{p}|}^2 \end{pmatrix}$$

In order to get the full parametrisation of the photon, the two additional unmeasured parameters  $(\theta_\gamma, \phi_\gamma)$  are added.

$$\vec{S} = \begin{pmatrix} x \\ y \\ |\vec{p}| \\ \theta_\gamma \\ \phi_\gamma \end{pmatrix}$$

These two additional parameters  $(\theta_\gamma, \phi_\gamma)$  have to be determined by the fit. Their initial values are estimated using the initial vertex position, and their variances are by definition set to arbitrarily high numbers since there exist no measurements of these parameters, in order to let them evolve freely during the procedure. As before, a jacobian transformation is applied to retrieve these matrices in the cartesian frame.

### Treatment of CAMERA hits

The measurements within CAMERA consist in the hits position detected in the two rings, in addition to the proton momentum so that they can be summarised in

$$\vec{S}_{\text{meas}} = \begin{pmatrix} r_A \\ \phi_A \\ z_A \\ r_B \\ \phi_B \\ z_B \\ |\vec{p}| \end{pmatrix} \quad \vec{S} = \begin{pmatrix} r_A \\ \phi_A \\ z_A \\ r_B \\ \phi_B \\ z_B \\ |\vec{p}| \\ \theta_p \\ \phi_p \end{pmatrix}$$

As for the photon, the quantities  $(\theta_p, \phi_p)$  are considered unmeasured, and the associated covariance matrix to the measured parameter is of the following form

$$\tilde{C}_{\text{meas}} = \begin{pmatrix} \tilde{C}_A & 0 & 0 \\ 0 & \tilde{C}_B & 0 \\ 0 & 0 & \sigma_{|\vec{p}|}^2 \end{pmatrix}$$

Since the reconstruction software CORAL does not take care of the CAMERA detector, one has to create the covariance matrix manually. For the hits covariance matrices  $\tilde{C}_{[A,B]}$ , one writes

$$\tilde{C}_{[A,B]} = \begin{pmatrix} \sigma_{R_{[A,B]}}^2 & 0 & 0 \\ 0 & \sigma_{\phi_{[A,B]}}^2 & 0 \\ 0 & 0 & \sigma_{z_{[A,B]}}^2 \end{pmatrix}$$

The radial uncertainty has been chosen to be at the order of the width of the different types of counters

$$\sigma_{R_A} = 0.4 \text{ cm} \quad \sigma_{R_B} = 5 \text{ cm}$$

The azimuthal uncertainty comes from the discrete number of counters per ring ; assuming a rectangular distribution of the hits for each counter, we obtain

$$\sigma_{\phi_{[A,B]}} = \frac{2\pi}{24\sqrt{12}}$$

where  $\frac{1}{\sqrt{12}}$  stands for the variance of the unitary rectangular distribution. The longitudinal uncertainties are estimated through Monte Carlo method based on a comparison of the

width of the longitudinal distributions with respect to data. These are the same as stated in Eq. (IV.26)

$$\sigma_{z_A} = 3.54 \text{ cm} \quad \sigma_{z_B} = 2.47 \text{ cm}$$

Finally the value of  $\sigma_{|\vec{p}|}$  is again estimated through Monte Carlo simulation as shown in Fig. (IV.1). The relative resolution  $\sigma_{|\vec{p}|}/|\vec{p}|$  is parametrised as function of  $|\vec{p}|$  and used as input for the measured covariance matrix.

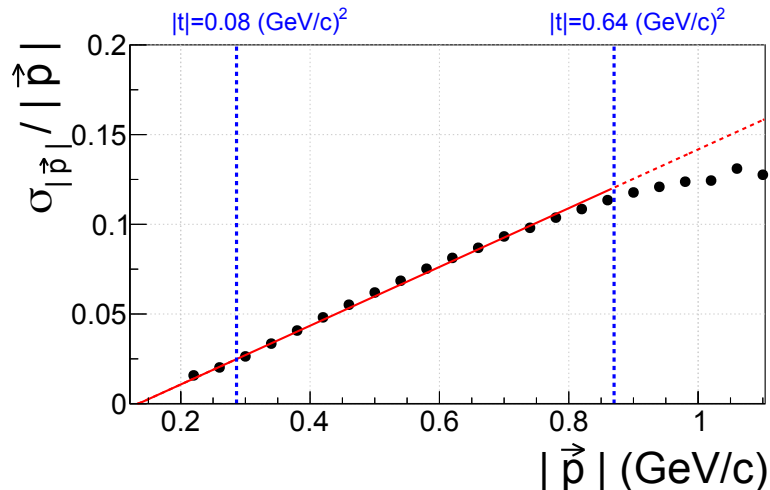


**Figure IV.1:** Momentum resolution of the protons calculated by Monte Carlo simulation for single photon events. Taken from [80].

### Constraints

The constraints on an exclusive process can be separated in two contributions, either coming from physics or geometry. The physics constraints consist in the energy-momentum conservation of the process, with a total of four equations. Naming  $(\vec{p}^{[i]}, E^{[i]})_{i \in [1, I]}$  the four-vector components of the ingoing particles and  $(\vec{p}^{[j]}, E^{[j]})_{j \in [1, O]}$  the ones of the outgoing particles, one obtains then:

$$\begin{aligned} \sum_{i=1}^I \vec{p}^{[i]} - \sum_{j=1}^O \vec{p}^{[j]} &= \vec{0}_3 \\ \sum_{i=1}^I E^{[i]} - \sum_{j=1}^O E^{[j]} &= 0 \end{aligned} \tag{IV.7}$$

On top of these, an additional constraint can be added in the case of meson production, where the invariant mass of the decaying particles system is constrained to the meson mass. This is considered for exclusive production of mesons such as  $\pi^0 \rightarrow \gamma\gamma$ ,  $\rho^0 \rightarrow \pi^+\pi^-$  and  $J/\Psi \rightarrow \mu^+\mu^-$ .

The geometric constraints ensure the convergence of all particle tracks to come from one unique vertex of interaction. In absence of magnetic field, these tracks can be parametrised as straight lines. This can be further assumed since all the tracks parameters considered are extrapolated to the vertex  $z$ -position.

Let  $\vec{v} = (v_x, v_y, v_z)$  be the components of the vertex of interaction,  $\vec{p} = (p_x, p_y, p_z)$  the direction of the track and  $\vec{a} = (a_x, a_y, a_z)$  a known point of the measured track.

The track direction is parametrised in three dimensions by the intersection of two planes. The normal vector  $\vec{n}$  of each plane defines their cartesian equation which has to fulfill

$$\vec{p} \cdot \vec{n} = 0 \iff p_x n_x + p_y n_y + p_z n_z = 0$$

where  $\vec{p} = (p_x, p_y, p_z)^T$ . In order to explicit those two planes, the trivial solutions  $n_{\perp x} = (0, p_z, -p_y)$  and  $n_{\perp y} = (p_z, -p_x, 0)$  are chosen, defining the planes  $\mathcal{P}_x$  and  $\mathcal{P}_y$  respectively. Using the affine equation of a plane passing by the point  $A$ , one obtains the two vertex constraints

$$\vec{v} \in \mathcal{P}_x \cap \mathcal{P}_y \iff \begin{cases} p_z (v_x - a_x) - p_x (v_z - a_z) = 0 \\ p_z (v_y - a_y) - p_y (v_z - a_z) = 0 \end{cases} \quad (\text{IV.8})$$

These two vertex constraints are applied for each measured track. Of course the vertex parameters are set to be unmeasured, so that these will be optimised by the kinematic fit.

In addition to these equations, the two hits coming from CAMERA have to constrain also the optimisation procedure. Conceptually, the idea is exactly the same as the vertex handling ; this is done by turning the vertex constraints into extrapolation constraints for the hits measured in the ring  $[A, B]$ , applying simply the following substitutions

$$\begin{aligned} \vec{v} &\rightarrow \vec{r}_{[A,B]} \\ \vec{a} &\rightarrow \vec{v} \end{aligned}$$

One obtains then

$$\vec{v} \in \mathcal{P}_x \cap \mathcal{P}_y \iff \begin{cases} p_z (r_{x[A,B]} - v_x) - p_x (r_{z[A,B]} - v_z) = 0 \\ p_z (r_{y[A,B]} - v_y) - p_y (r_{z[A,B]} - v_z) = 0 \end{cases} \quad (\text{IV.9})$$

where this time  $\vec{p}$  is the measured momentum of the outgoing proton.

To summarize, the kinematic fit needs jacobian adjustments from the output of the reconstruction software CORAL. Moreover, it also needs to be setup accordingly to the exclusive process seeked, with the respective measured, unmeasured parameters, and constraints, as it will be shown in [Sections IV.1.2](#) and [IV.3.6](#). To simplify consequently this setup, a kinematic fit interface has been developped and proposed to the collaboration in order to ease the setup and not to forget any parameter. This interface is adapted to DVCS and HEMP processes where the common particles are treated in the same way, namely the incoming muon, proton, and the outgoing muon and proton. Moreover the interface allows the user to consider any kind of additional particles, such as neutral ones (one or two photons, in the case of DVCS or exclusive  $\pi^0$  production respectively), or even consider more charged particles. The latter can be used to consider HEMP processes such as exclusive  $\rho^0 \rightarrow \pi^+ \pi^-$  or  $J/\Psi \rightarrow \mu^+ \mu^-$  production. An additional invariant mass constraint on part of all of the outgoing particles can also be added. Finally, all the respective constraints are automatically setup and applied by the interface, and the user can have access transparently to all the outputs from the kinematic fit.

The particular case of the recoil proton detector calibration will be reviewed in the next section. The goal is to adjust the proton observables given by CAMERA only to the proton observables estimated by the kinematic fit using only the forward COMPASS spectrometer information. To this end, one needs to consider the recoil proton as unmeasured in the procedure, so that the kinematic fit setup has also to be adjusted for this. An option is added to the previous interface, in order to switch between one setup using only the spectrometer, and the full one including the CAMERA detector information in the final analysis.

## 1.2 Application to the exclusive $\rho^0$ events

The exclusive  $\rho^0$  event topology is as follows:  $\mu p \rightarrow \mu' p' \rho^0 \rightarrow \mu' p' \pi^+ \pi^-$ . This section is focused on the kinematic fit application for the purpose of calibrating the CAMERA detector. Thus, there can be no information coming from the hits in the A or B ring and the outgoing proton  $p'$  must be considered as unmeasured. The latter will be estimated by the kinematic fit. Using [Section IV.1.1](#), one can retrieve the number of measured parameters by the spectrometer to be 23 as follows:

$$\vec{k} = \begin{pmatrix} k_1 \\ \vdots \\ k_{23} \end{pmatrix} := \begin{pmatrix} \vec{a}_\mu \\ \vec{p}_\mu \\ \vec{0}_{18} \end{pmatrix} + \begin{pmatrix} \vec{0}_5 \\ \vec{a}_{\mu'} \\ \vec{p}_{\mu'} \\ \vec{0}_{13} \end{pmatrix} + \begin{pmatrix} \vec{0}_{10} \\ \vec{a}_{\pi^+} \\ \vec{p}_{\pi^+} \\ \vec{0}_8 \end{pmatrix} + \begin{pmatrix} \vec{0}_{15} \\ \vec{a}_{\pi^-} \\ \vec{p}_{\pi^-} \\ \vec{0}_3 \end{pmatrix} + \begin{pmatrix} \vec{0}_{20} \\ \vec{p}_p \end{pmatrix}$$

The quantities labeled as  $\vec{a}_X$ ,  $\vec{p}_X$  denotes the position  $(x, y)$  and momentum  $(p_x, p_y, p_z)$  of a charged track as described in [Section IV.1.1](#). The target proton is considered at rest and given by  $\vec{p}_p$ . The number of unmeasured parameters is 6 given by the outgoing proton momentum and the vertex position

$$\vec{h} = \begin{pmatrix} h_1 \\ \vdots \\ h_6 \end{pmatrix} := \begin{pmatrix} \vec{p}_{p'} \\ \vec{0}_3 \end{pmatrix} + \begin{pmatrix} \vec{0}_3 \\ \vec{v} \end{pmatrix}$$

### Constraints and degrees of freedom

The energy-momentum conservation of the exclusive process leads to four constraints. In addition, all the particles should come from a common vertex, so that two constraints are added for each of the four measured charged tracks  $\mu, \mu', \pi^+, \pi^-$ . One has to note that the ingoing proton is considered at rest. Though its transverse coordinates at a given longitudinal position are unmeasured, they would be trivially fixed by the two corresponding vertex constraints. This zero-sum game is thus not considered in the procedure. For the outgoing proton, the very same procedure is applied, so that both the ingoing and outgoing proton transverse positions variables are not considered, and thus do not add any constraints to the problem.

In total  $4 + 2 \times 4 = 12$  constraints are applied while 6 free parameters have to be estimated by the fitting procedure. For an overconstrained problem the number of degrees of freedom is given by the difference between the number of constraints and the free parameters as described in the literature [[99](#), page I30]. Thus the number of degree of freedom is  $ndf = 12 - 6 = 6$ .

### Impact on $\theta_{p'}$

As explained in [Section IV.2.4](#), a longitudinal estimation of the recoiled proton observables is necessary for the calibration of the CAMERA detector. In particular, one needs to calibrate the longitudinal position of the proton in the CAMERA scintillators based on the vertex position and the angle  $\theta_{p'}$ . The naive approach is to reconstruct the outgoing

proton from exclusive  $\rho^0$  events, detecting all the outgoing particles in the spectrometer apart from the proton. One can then define

$$\tan \theta_{p'} = \frac{(\vec{p}_{p'})_T}{(\vec{p}_{p'})_L} = \frac{(\vec{p}_{\mu'} + \vec{p}_{\rho^0} - \vec{p}_{\mu})_T}{(\vec{p}_{\mu'} + \vec{p}_{\rho^0} - \vec{p}_{\mu})_L} \quad (\text{IV.10})$$

where  $\vec{v}_T$  and  $\vec{v}_L$  are defined as the transverse and longitudinal components of the vector  $\vec{v}$ .

However, in the COMPASS kinematics using a 160 GeV muon beam<sup>4</sup> and due to the study of exclusive reaction at small transfer  $|t|$ , the longitudinal quantity of the denominator is smaller than 1 GeV, but with an error larger than 1 GeV. So the denominator is not determined and  $\theta_p$  can take all possible values between 0 and  $\pi$ .

In order to illustrate this fact, a toy Monte Carlo is tested in two cases: one simulation considering perfect detectors (see **Fig. (IV.2a)**), and one with only longitudinal resolutions of 0.5% applied on the muons measurements (see **Fig. (IV.2b)**). These resolutions for the incoming and outgoing muons are extracted according to the FWHM presented in **Figs. (IV.2d)** and **(IV.2e)** respectively.

It is shown in **Fig. (IV.2a)** that the reconstructed angle of the proton as described in **Eq. (IV.10)** in the case of perfect detectors is around 1.3 rad, while the smeared simulation proposes angles around zero or in the unphysical backward region (see **Fig. (IV.2b)**). Moreover **Fig. (IV.2c)** shows clearly that there is no correlation between the reconstructed and generated proton angle. This means that due to the high energy of the experiment at 160 GeV and in the domain of small  $|t| < 1 \text{ GeV}^2$ , the longitudinal information given by the forward spectrometer for the outgoing proton has no meaning.

However one can use the over-constraint kinematics of the exclusive  $\rho^0$  events measurements, through a kinematic fit procedure as described in **Section IV.1.2**. The result is shown in **Fig. (IV.3b)** where one retrieves the expected angle of the recoiled proton. Moreover the similarity between **Fig. (IV.3a)** and **Fig. (IV.2a)** reinforces the fact that the individual measurements from the spectrometer do not hold the longitudinal information on the outgoing proton anymore. Nonetheless, correlations can be exhibited and used through both topological and geometrical constraints, by the means of a kinematic fit procedure.

<sup>4</sup>Typical example for DVCS (or exclusive  $\rho$ ) kinematics :

$E_{\mu} = 160 \text{ GeV}$ ,  $Q^2 = 1.8 \text{ (GeV}/c)^2$ ,  $x_B = 0.056$

$E_{\mu'} = 142.9 \text{ GeV}$ ,  $\theta_{\mu'} = 0.5 \text{ deg.}$ ,  $E_{\gamma^*} = 17.1 \text{ GeV}$ ,  $\theta_{\gamma^*} = 4.2 \text{ deg.}$ ,

$|t| < 0.7 \text{ (GeV}/c)^2$ ,  $16.7 < E_{\gamma \text{ or } \rho} < 17.1 \text{ GeV}$ ,  $\theta_{\gamma \text{ or } \rho} < 2.7 \text{ deg.}$  around the virtual photon direction  $\mu, \mu', \gamma$  or  $\rho$  momentum vectors of are all in very forward directions,  $|(\vec{p}_{\mu'} + \vec{p}_{\rho^0} - \vec{p}_{\mu})_L| < 1 \text{ GeV}/c$  and with  $\mu$  and  $\mu'$  energy resolution of 0.5% we have  $\Delta|\vec{p}_{\mu}| = 0.8 \text{ GeV}/c$  and  $\Delta|\vec{p}_{\mu'}| = 0.7 \text{ GeV}/c$ .

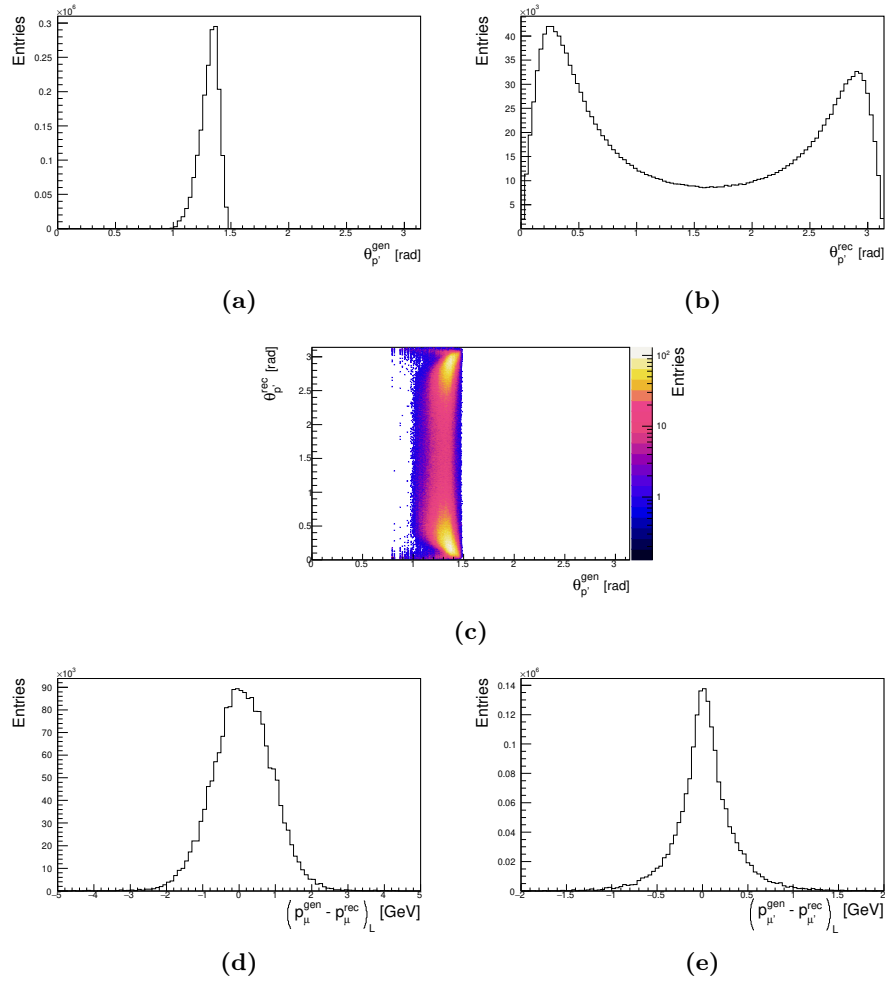


**Figure IV.2:** This figure displays the toy Monte Carlo results.

(a):  $\theta_{p'}^{\text{gen}}$  distribution as calculated in Eq. (IV.10) in the case of perfect detectors.

(b): Same as (a) applying a smearing on the longitudinal momenta of the muons. The variable is labeled  $\theta_{p'}^{\text{rec}}$ .

(c): Correlation between  $\theta_{p'}^{\text{gen}}$  and  $\theta_{p'}^{\text{rec}}$ .

(d) and (e): Residual of the longitudinal momenta of the incoming and outgoing muon. The FWHM shows the experimental resolution achieved by the spectrometer, of around 1 GeV and 0.2 GeV respectively.

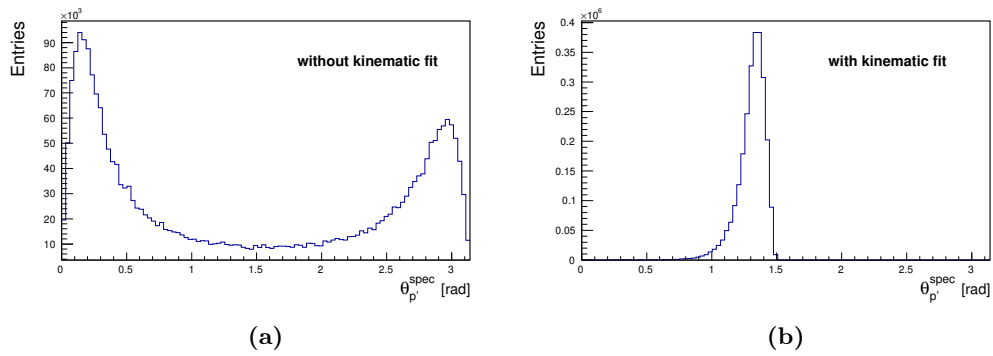


**Figure IV.3:** (a):  $\theta_{p'}$  distribution as calculated in Eq. (IV.10). (b):  $\theta_{p'}$  distribution as calculated in Eq. (IV.10), applying first a kinematic fit.

## 2 CAMERA calibrations

### 2.1 Exclusive $\rho^0$ event selection

The exclusive  $\rho^0$  process  $\mu p \rightarrow \mu' p' \rho^0$  has a kinematics close to the DVCS process, with a relatively higher cross section. Therefore this process provides a large sample of data for a robust calibration of the CAMERA detector. The  $\rho^0$  decays in ( $\rho^0 \rightarrow \pi^+ \pi^-$ ) and the invariant mass of the two opposite charged hadrons is reconstructed to select only a mass  $0.5 \text{ GeV}/c^2 < M_{h^+ h^-} < 1.1 \text{ GeV}/c^2$ . Since the recoil proton is not detected, the exclusive  $\rho^0$  events are selected by a cut on the missing mass (or missing energy). The full event selection is indicated in **Table (IV.1)**.

However, as explained in **Section IV.1.2**, the independent measurements of the particles in the spectrometer cannot produce a decent reconstruction of longitudinal observables such as  $\theta_p^{\text{spec}}$ , so that the kinematic fit has to be applied as described in **Section IV.1.2**. This also improves the physics observables used in these calibrations. Thus we can adjust the proton observables given by CAMERA to the proton observables labeled "spec", given by the kinematic fit.

In order to get rid of the background present in these distributions, a soft *vertex-pointing cut* is applied between the hit position and the outgoing proton four vector obtained from the spectrometer, as written in **Eq. (IV.11)**. These constraints are a direct application of **Eq. (IV.8)**, and are only displayed here in the case of ring B.

$$\begin{aligned} C_{XZ} &= p_z^{\text{spec}} (r_B \cos \varphi_{B_j} - v_x) - p_x^{\text{spec}} (z_{B_j} - v_z) \\ C_{YZ} &= p_z^{\text{spec}} (r_B \sin \varphi_{B_j} - v_y) - p_y^{\text{spec}} (z_{B_j} - v_z) \\ \chi_{\text{vertex}}^2 &= C_{XZ}^2 + C_{YZ}^2 < 10 \end{aligned} \quad (\text{IV.11})$$

However, this technique requires to have an estimation a priori of  $\varphi_{[A,B]_i}$  and  $z_{[A,B]_i}$  of the hit, so the calibration procedure has to be done in several steps.

### 2.2 Azimuthal calibration

The two cylindrical rings A and B are divided in 24 sectors each. The nominal central azimuthal position of each sector should be:

$$\forall i \in \llbracket 0, 23 \rrbracket \begin{cases} \varphi_{A_i}^{\text{nom}} = 120 - \frac{360}{24}i \\ \varphi_{B_i}^{\text{nom}} = 120 - \frac{360}{24}i + 7.5 \end{cases} \quad (\text{IV.12})$$

The exact azimuthal positions are obtained from the correlation of the signal received in each sector and the expected azimuthal distribution of the proton obtained from the spectrometer prediction  $\varphi_{[A,B]_i}^{\text{spec}}$ . The resulting histograms **Fig. (IV.4)** show the difference between this quantity and the nominal value  $\varphi_{[A,B]_i}^{\text{nom}}$ . Due to the fact that the spectrometer provides measurements at the interaction vertex, one has to correct this deviation and provide azimuthal angles relatively to the axis  $X = Y = 0$  in the laboratory frame as corrected in **Appendix (2)**.

The parameters  $\varphi_{A_i}^{\text{calib}}$ ,  $\varphi_{B_i}^{\text{calib}}$  are extracted for each sector, leading to the definition of the azimuthal calibration of the 48 sectors (the exact calibration values and figures for all sectors are given in **Figs. (A.1)** and **(A.2)**):

$$\forall i \in \llbracket 0, 23 \rrbracket \begin{cases} \varphi_{A_i} = \varphi_{A_i}^{\text{calib}} + \varphi_{A_i}^{\text{nom}} \\ \varphi_{B_i} = \varphi_{B_i}^{\text{calib}} + \varphi_{B_i}^{\text{nom}} \end{cases} \quad (\text{IV.13})$$

DIS	Vertex	Vertex contained in the fiducial volume of the target: <ul style="list-style-type: none"> <li>• <math>-318.5 \text{ cm} &lt; z_{\text{vertex}} &lt; -78.5 \text{ cm}</math></li> <li>• <math>r_{\text{vertex}}(\text{vertex}, \text{TargetCenter}(z_{\text{vertex}})) &lt; 1.9 \text{ cm}</math></li> <li>• <math>y_{\text{vertex}} &lt; 1.2 \text{ cm}</math></li> </ul> Best primary vertex from CORAL <sup>a</sup>
	Beam muon	<ul style="list-style-type: none"> <li>• One incoming charged track with:               <ul style="list-style-type: none"> <li><math>\geq 2</math> hits in SciFi</li> <li><math>\geq 3</math> hits in SI</li> <li><math>\geq 3</math> hits in the beam momentum station (BMS)</li> </ul> </li> <li>• A momentum measurement such that:               <math display="block">140 \text{ [GeV/c]} &lt;  p_{\mu}  &lt; 180 \text{ [GeV/c]}</math> <math display="block"> \sigma(p_{\mu})/p_{\mu}  &lt; 0.025</math> </li> <li>• The beam track traverses the full target length and is contained within the fiducial volume of the target</li> </ul>
	Scattered muon	One unique outgoing charged track with: <ul style="list-style-type: none"> <li>• same charge as beam muon</li> <li>• traversed radiation length <math>X/X_0 &gt; 15</math></li> <li>• <math>z</math>-position of the first and last measured point:               <math display="block">z_{\text{first}} &lt; 350 \text{ cm} \quad \text{and} \quad z_{\text{last}} &gt; 350 \text{ cm}</math> </li> <li>• extrapolations within the active areas of the hodoscopes (new PointHodoscope function)</li> </ul> Inclusive scattering variables (wide): <ul style="list-style-type: none"> <li>• <math>0.7 \text{ GeV}^2 &lt; Q^2</math></li> <li>• <math>0.05 &lt; y &lt; 0.95</math></li> </ul>
$\rho^0$	Topology	Two outgoing charged tracks ( $h^+$ , $h^-$ ) with opposite charges and with traversed radiation length of $X/X_0 < 10$ .
	Exclusivity selection	Mass selection assuming $(h^+, h^-) = (\pi^+, \pi^-)$ $0.5 \text{ GeV}/c^2 < M_{h^+h^-} < 1.1 \text{ GeV}/c^2$ Missing energy cut <sup>b</sup> $-4 \text{ GeV} < E_{\text{miss}} < 4 \text{ GeV}$ Convergence of the kinematic fit with a score $\chi_{\text{red}}^2 < 10$

**Table IV.1:** Exclusive  $\rho^0$  event selection for the CAMERA calibration.

<sup>a</sup> A primary vertex is a vertex featuring the beam particle. In case there is more than one primary vertex in an event, the reconstruction software CORAL tags the best primary vertex among them, which is the best fitted one. In principle it corresponds to the one having the largest number of outgoing tracks.

<sup>b</sup>  $E_{\text{miss}} = \frac{(p+q-\kappa)^2 - M_p^2}{2M_p}$ , where  $p, q, \kappa$  are respectively the four-vectors of the target proton, the virtual photon and the  $\rho^0$  candidate.

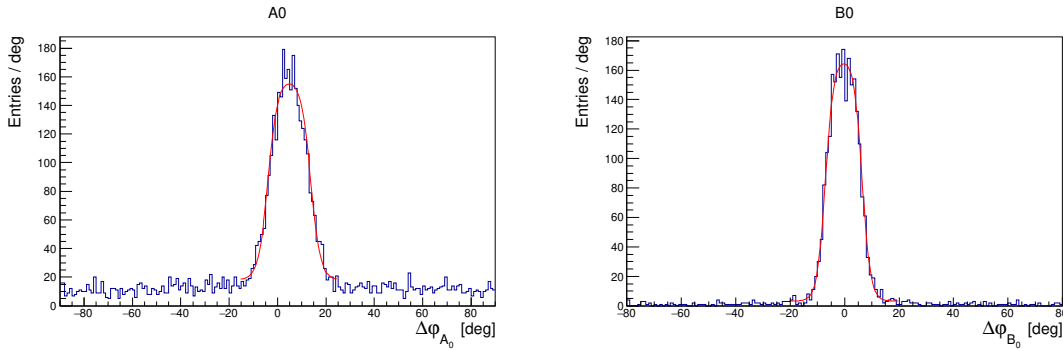


**Figure IV.4:** Distribution of the azimuthal angle of the proton pulled at its nominal value:

$$\Delta\varphi_{[A,B]_i} = \varphi_{[A,B]_i}^{\text{spec}} - \varphi_{[A,B]_i}^{\text{nom}}$$

A fit is applied using a symmetric sigmoid function from which the translation parameters  $\varphi_{[A,B]_i}^{\text{calib}}$  is extracted.

### 2.3 Radial tomography

The 24 scintillating slats of each ring have been assembled one by one to form the A and B barrels, with nominal radii of 25 cm and 110 cm respectively. The B slats are 5 cm thick, 29 cm large and 360 cm long; the A slats are 4 mm thick, 6.6 cm large and 275 cm long. At both ends of each 48 slats there are lightguides and a PMT fixed on a solid flange. In the case of the ring B slats, massive lightguides are used, while in the case of the A slats, rather long and flexible ones are used. Based on geometrical surveys, some reasonable assumptions can be made:

- the A and B rings are of cylindrical shape with a horizontal revolution axis.
- the A and B transverse sections are circles but their radii are found to be slightly higher:

$$\begin{aligned} r_A^{\text{nom}} &= 25.7 \text{ cm} \\ r_B^{\text{nom}} &= 111.6 \text{ cm} \end{aligned} \tag{IV.14}$$

- The A and B ring axes are not exactly on the axis  $X = Y = 0$ , and not around the same axis. They are slightly out-of-focus.

On top of these remarks, there is a possibility of having a twist of the A scintillators along the  $z$ -axis. This effect was slightly observed in the 2012 pilot run. However the ring A has been completely refurbished: the scintillating material and the lightguides are new, and the assembling has been done with more care, and as a consequence no twist has been considered for the analysis.

From the azimuthal calibration of CAMERA, one can estimate the alignment of the rings based on the deviation to the nominal azimuthal position of each scintillator. This deviation is displayed in **Fig. (IV.5a)** for each scintillator of ring A. A clear oscillation is observed, which confirms that the 24 scintillators are not concentrically placed around the  $z$ -axis, but slightly out-of-focus.

By fitting these distributions with the function  $F(\varphi)$  defined in **Eq. (IV.15)**, one can extract the effective center of the considered ring in polar coordinates  $\vec{C} = (r_C, \varphi_C)$  with respect to the origin (see **Appendix (2)**):

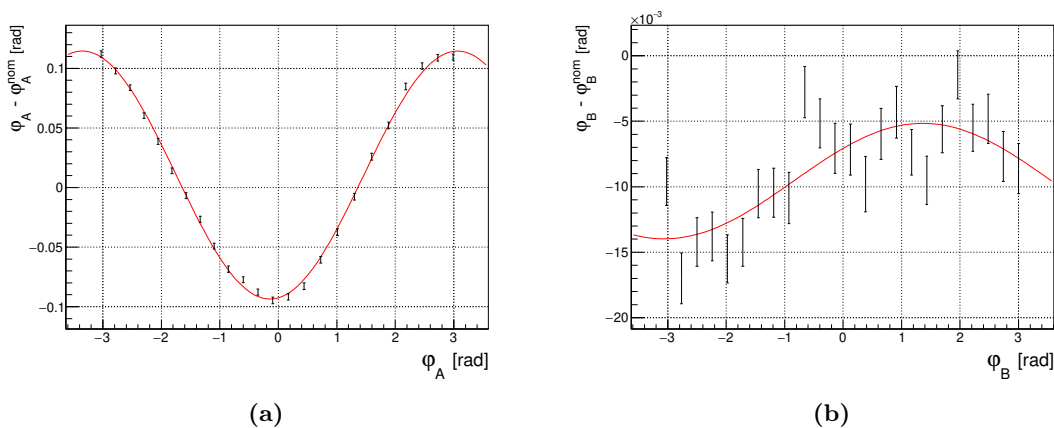


**Figure IV.5:** (a): Azimuthal deviation from the nominal position defined in Eq. (IV.12) as function of the azimuthal position for the 24 scintillators of the inner ring A. The fit  $F(\varphi)$  is shown in red. (b): Same for the outer ring B.

$$F(\varphi) := p_0 + p_1 \sin(p_2 \cdot \varphi + p_3) \quad (\text{IV.15a})$$

$$\begin{pmatrix} r_C \\ \varphi_C \end{pmatrix} = \begin{pmatrix} r^{nom} \cdot \tan |p_1| \\ -p_3 \end{pmatrix} \quad (\text{IV.15b})$$

Using the following definitions, one can compute the radius  $r$  as function of the azimuthal angle  $\varphi$  with respect to the axis  $X = Y = 0$  (see Appendix (2)):  $\forall \varphi \in \{\varphi_{A_i}, i \in \llbracket 0, 23 \rrbracket\}$

$$\vec{v} := \begin{pmatrix} 1 \\ \varphi \end{pmatrix} \quad (\text{IV.16a})$$

$$p := -2\vec{v} \cdot \vec{C} \quad (\text{IV.16b})$$

$$q := |\vec{C}|^2 - r_{nom}^2 \quad (\text{IV.16c})$$

$$r(\varphi) = -p/2 + \sqrt{p^2/4 - q} \quad (\text{IV.16d})$$

An alternative approach proposed in [85] consists in using the information of the width of the  $\Delta\varphi_{[A,B]_i}$  distributions (Eq. (IV.13)). Since the size of a scintillator is known, it is theoretically possible to retrieve the radial distance from this method. However as shown in the 2012 data, the blurred edges of the azimuthal distributions do not provide a sufficient quality for extraction, though it can be used to ensure the perfect circle assumption.

The resulting tomography is shown in Fig. (IV.6), where one can observe an out-focus of the inner ring A of  $(x = -0.373 \text{ cm}, y = -2.66 \text{ cm})$ . The deviation for the outer ring B is rather small as shown in Fig. (IV.5b) and the resulting center is  $(x = -0.405 \text{ cm}, y = 0.279 \text{ cm})$ . As compared to the nominal radius of the B ring  $r_{nom}^B = 111.6 \text{ cm}$  and the poor quality of the fit obtained in Fig. (IV.5b), this out-focus is neglected in the further analysis and the B ring scintillators are considered as concentric around the origin.

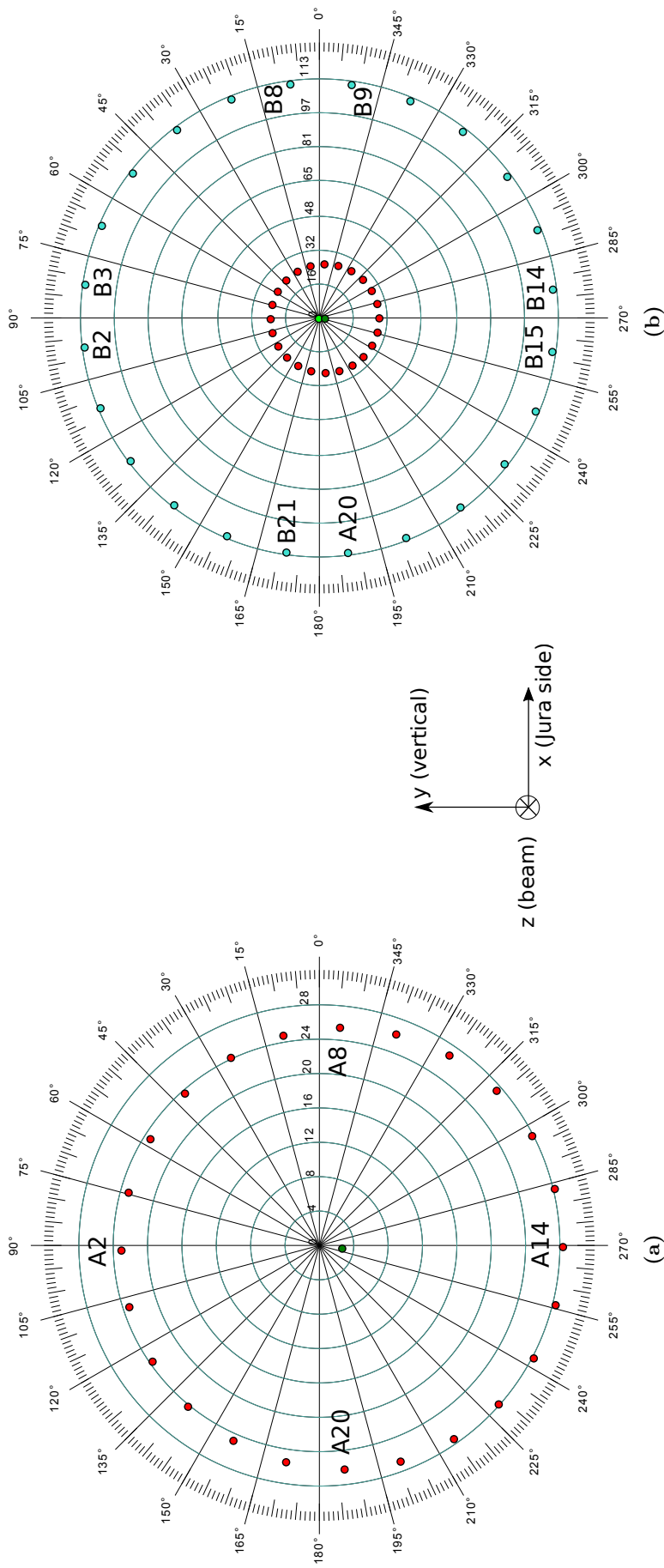


**Figure IV.6:** (a): Tomography of the inner ring A ; the azimuthal positions of the 24 scintillator centers are shown in red, the effective center of the A ring in green and the nominal azimuthal position center of each scintillator slab center are shown by the radial lines in black every 15°. (b): Same as (a) with the ring B scintillators added in turquoise and its effective center in light green. The radial lines in black show the nominal positions of the A scintillator centers.

## 2.4 Longitudinal calibration

For each of the 48 scintillators of CAMERA, the longitudinal position of a hit is reconstructed from the difference of the two time stamps recorded in the upstream and downstream photomultipliers, as shown in Eq. (IV.17).

$$\begin{aligned} z_{B_i} &= \frac{(t^{\text{up}B_i} - t^{\text{down}B_i})}{2} \cdot v_{B_i} + C_{B_i} \\ z_{A_i} &= \frac{(t^{\text{up}A_i} - t^{\text{down}A_i})}{2} \cdot v_{A_i} + C_{A_i} \end{aligned} \quad (\text{IV.17})$$

In order to extract the calibration parameters  $v_{B_i}$  and  $C_i$ , one needs to have an estimation of  $z_{B_i}$ . This is achieved from the spectrometer measurements combined with a kinematic fit to have a proper longitudinal estimation of the observables, such as  $\theta_{p'}^{\text{spec}}$ . This resulting estimation is labeled as  $z_{B_i}^{\text{spec}}$ , defined using Fig. (IV.7) and Eq. (IV.18).

$$z_{B_i}^{\text{spec}} = \frac{R_{B_i} - d_v}{\tan(\theta_{p'}^{\text{spec}})} + v_z \quad (\text{IV.18})$$

where  $v = (v_x, v_y, v_z)$ ,  $v_\varphi = \arctan(v_y/v_x)$ , and

$$d_v = \sqrt{v_x^2 + v_y^2} \cdot \cos(\varphi^{\text{spec}} - v_\varphi)$$

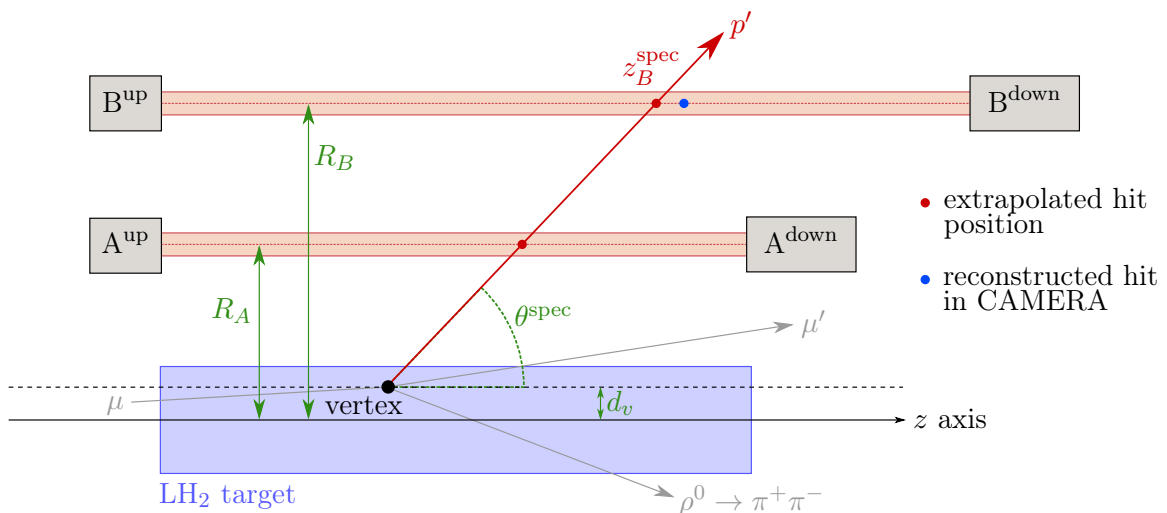
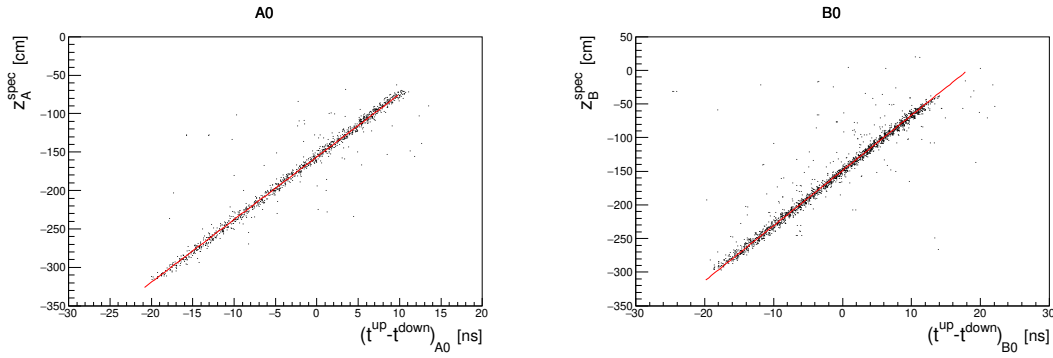


Figure IV.7: Longitudinal view of CAMERA detection principle

Fig. (IV.8) shows the correlation between  $z_{B_i}^{\text{spec}}$  and  $(t^{\text{up}B_i} - t^{\text{down}B_i})$ . Combining Eqs. (IV.17) and (IV.18) one can extract the calibration parameters  $v_{B_i}$  and  $C_{B_i}$  from a straight line fit. For estimating the longitudinal position  $z_A^{\text{interp.}}$  of the ring A, an interpolation between the vertex position and the already calibrated hit position in the ring B is chosen as illustrated in Fig. (IV.7) using

$$z_{A_i}^{\text{interp.}} = \frac{R_{B_i} - d_v}{R_{A_i} - d_v} \cdot (z_{B_i} - v_z) + v_z \quad (\text{IV.19})$$



**Figure IV.8:** Two dimensional distributions of the estimated longitudinal position from the spectrometer and kinematic fit  $z_{A,B}^{\text{spec}}$  with respect to the difference of the two time stamps in upstream and downstream photomultipliers, for the scintillators A0 (left) and B0 (right). The correlation is fitted as a straight line fit according to formula [Eq. \(IV.17\)](#). The figures and result for all the sectors are available in [Figs. \(A.5\)](#) and [\(A.6\)](#)

## 2.5 Time of flight calibration and momentum adjustment

As shown in [Fig. \(IV.6b\)](#), the azimuthal positions of the 24 scintillators of ring B are displaced by about  $7.5^\circ$  from the ones of ring A. This is to get a finer resolution of the azimuthal angle measured by CAMERA. Thus, a passing track within CAMERA is detected in correlated angular sectors between the inner ring A and the outer ring B, defined by  $(A_i, B_j)$ , with  $i \in \llbracket 0, 23 \rrbracket$ ,  $j \in \{i, (i+1) \bmod 24\}$ . For the rest of this section, let  $A_i$  and  $B_j$  be two correlated angular sectors of CAMERA.

After the longitudinal calibration of the 48 scintillators done in [Section IV.2.4](#), one can derive the distance of flight of a detected particle in  $(A_i, B_j)$  using [Eq. \(IV.20\)](#)

$$D_{i,j} = \sqrt{(R_{B_j} - R_{A_i})^2 + (z_{B_j} - z_{A_i})^2} \quad (\text{IV.20})$$

In order to extract the corresponding time of flight, the relative time response of the two rings has to be calibrated one to the other, through the calibration constant  $C_{i,j}$  as in [Eq. \(IV.21\)](#)

$$\begin{aligned} T_{i,j}^{\text{raw}} &= \frac{t_{B_j}^{\text{up}} + t_{B_j}^{\text{dn}}}{2} - \frac{t_{A_i}^{\text{up}} + t_{A_i}^{\text{dn}}}{2} \\ T_{i,j} &= T_{i,j}^{\text{raw}} + C_{i,j} \end{aligned} \quad (\text{IV.21})$$

Using [Eqs. \(II.4\)](#) and [\(IV.21\)](#) one can derive the calibration constant in [Eq. \(IV.22\)](#) as function of the velocity  $\beta$  of the detected particle.

$$C_{i,j} = \frac{D_{i,j}}{\beta c} - \frac{t_{B_j}^{\text{up}} + t_{B_j}^{\text{dn}}}{2} + \frac{t_{A_i}^{\text{up}} + t_{A_i}^{\text{dn}}}{2} = \frac{D_{i,j}}{\beta} - T_{i,j}^{\text{raw}} \quad (\text{IV.22})$$

In order to retrieve  $C_{i,j}$  one needs an estimation of  $\beta$  which is of course unknown and subject to energy loss corrections in the target for particles of low momentum such as the recoiling proton. In order to overcome these issues, two possible studies have been conducted, using particles featuring a velocity  $\beta$  close to 1 (speed of light). A first approach consist in using the cosmic muon signals as described in [\[75\]](#); this method has the advantage of being totally uncorrelated to any physics process. The second method chosen here is based on the strong correlation existing between the raw time of flight  $T_{i,j}^{\text{raw}}$  and the distance of flight  $D_{i,j}$  as presented in [Fig. \(IV.9a\)](#). One can assume that this correlation is due

to the  $\delta$ -rays traveling at the speed of light from the target to the inner and outer rings, and **Eq. (IV.22)** is applied replacing  $\beta$  with  $\beta_{\delta\text{-ray}}$ . The latter is of course close to 1 and is obtained from the slope of a straight line fit in **Fig. (IV.9a)**. The intercept of the fit is by definition  $-C_{i,j}$ , but to reduce the uncertainty, the 2 dimensional distribution is projected perpendicularly to the previous slope as shown in **Fig. (IV.9b)** from which the mean value is extracted. To improve the purity of the  $\delta$ -rays sample, the coplanarity conditions described in **Eq. (IV.11)** are reverted considering  $\chi^2 > 10$ , in order to remove the  $\rho^0$  events with which all the other calibrations are estimated.

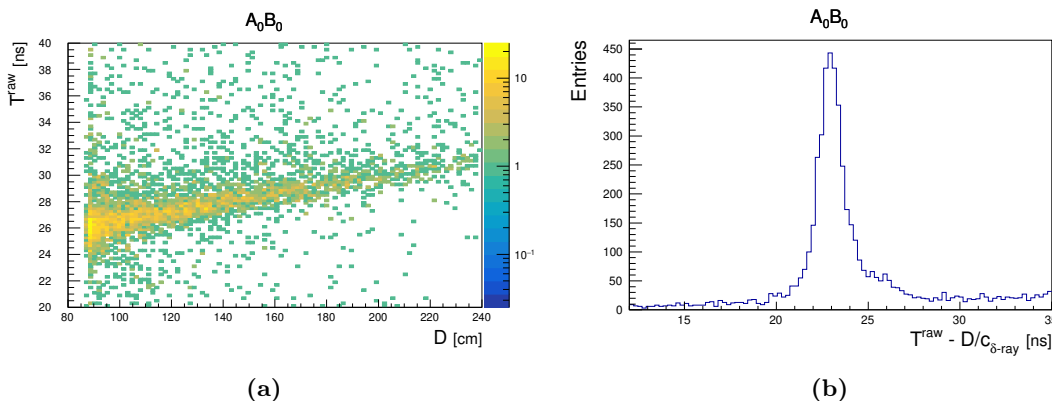


**Figure IV.9:** (a):  $T^{\text{raw}}$  as function of  $D$  for the pair  $(A_0, B_0)$ . A straight line fit is applied to extract the mean velocity of the selected particles ( $\beta' = 0.94$ ). (b): shows the projection of (a) perpendicularly to the measured slope. The central value leads to the calibration constant  $C_{i,j}$

The momentum of a track passing through the scintillators  $A_i, B_j$  can be reconstructed through **Eq. (IV.23)**

$$\beta = \frac{D_{i,j}}{T_{i,j}} ; \quad |\vec{p}| = \frac{M_p \beta}{\sqrt{1 - \beta^2}} ; \quad \theta = \arctan \frac{R_{B_j} - R_{A_i}}{z_{B_j} - z_{A_i}} ; \quad \varphi = \frac{\varphi_{B_j} + \varphi_{A_i}}{2} \quad (\text{IV.23})$$

In order to check the quality of the calibration procedure, the proton momentum from the exclusive  $\rho^0$  events measured by CAMERA is compared to the measurement expected from the spectrometer, as shown in **Fig. (IV.10)**. As for previous analyses [85, 75], this comparison suggests the presence of a bias either in estimating the radii or the time of flight calibration. To avoid changing the geometrical description of **Section IV.2.3**, it has been chosen to add a time of flight of 400 ps to be added to  $C_{i,j}$ . **Fig. (IV.9b)** shows a slight asymmetry and a slope in the background, which can be due to impurities in the  $\delta$ -ray data sample with particles travelling slower than  $c$ . This causes a slight bias in the time of flight calibration extraction from a fit. This trend is present in all sectors of CAMERA as visible in **Figs. (A.7)** and **(A.8)**. This consolidates the use of a same additional time of flight.

## 2.6 Monte Carlo simulation

This part will address the specific treatment that has to be done for the Monte Carlo simulations, and the handling of the Monte Carlo hits.

### Monte Carlo hits propagation and clustering

The basic information in a Monte Carlo simulation of CAMERA is composed of Monte Carlo hits, characterized by  $(X_{MC}, Y_{MC}, Z_{MC}, T_{MC}, dE_{MC})$  for each of the 48 scintillators

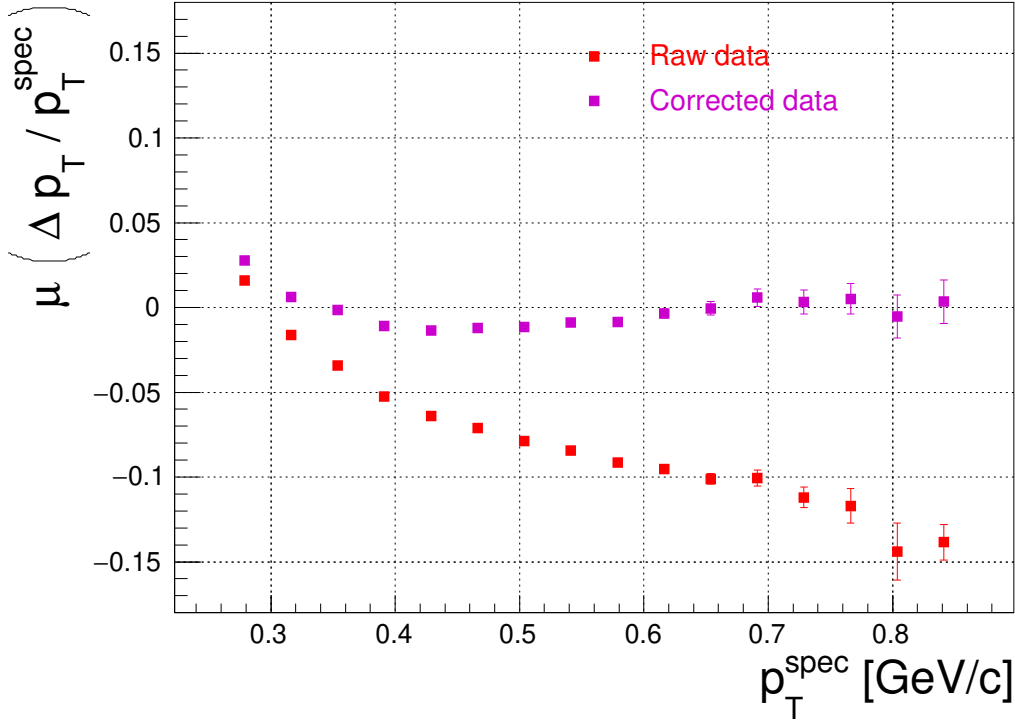


**Figure IV.10:** Mean value of the transverse momentum difference measured by CAMERA and the spectrometer, as function of the transverse momentum measured by the spectrometer. The Corrected data in purple shows the effect of the additional 400 ps on the time of flight fitted value.

of the rings A and B. These hits are then propagated to the photomultipliers' positions upstream and downstream. The formulae are obtained by reverting [Eq. \(IV.17\)](#) as follows:

$$\begin{aligned}
 t_{[A,B]_i}^{\text{up}} &= T_{[A,B]_i}^{\text{MC}} + \frac{Z_{\text{MC}} - C_{[A,B]_i}}{v_{[A,B]_i A,B}} \\
 t_{[A,B]_i}^{\text{down}} &= T_{[A,B]_i}^{\text{MC}} - \frac{Z_{\text{MC}} - C_{[A,B]_i}}{v_{[A,B]_i}}
 \end{aligned}
 \tag{IV.24}$$

where the constants  $C_{[A,B]_i}, v_{[A,B]_i}$  are extracted from the data in the previous calibrations steps. From these time stamps, each Monte Carlo hit and thus the corresponding track can be reconstructed, using the very same procedure as followed by the data. The only exception is that the time of flight calibration constants for the Monte Carlo are set to 0.

One has to note that there is no digitization procedure available for the Monte Carlo hits within CAMERA. This means that in a Monte Carlo simulation, the time difference between two consecutive hits in CAMERA can be smaller than the minimal separation time between two recorded signals which can be reached by the hardware. Therefore the Monte Carlo simulations records more Monte Carlo hits and more combinatorial background is created than what is present in the real data. Two hits in an upstream scintillator in time coincidence with one hit in the downstream scintillator will provide two proton candidates. And more hits will provide more combinatorial possibilities.

The digitization procedure is of importance for removing part of the combinatorial noise which does not exist in the real data case due to the integration of signals performed by the electronics. [Fig. \(IV.11\)](#) shows the time difference between two consecutive hits in a data sample for the upstream photomultiplier of the scintillator A0. From this, it is

chosen to integrate all the Monte Carlo hits arriving at the photomultiplier position within less than 10 ns into clusters. Due to the high amount of  $\delta$ -rays in the ring A, the Monte Carlo simulation records a greater amount of "fake" proton candidates. This has an impact in the exclusive single photon event selection when requiring a unique proton candidate among other cuts, which is now handled by this CAMERA clusterisation procedure.

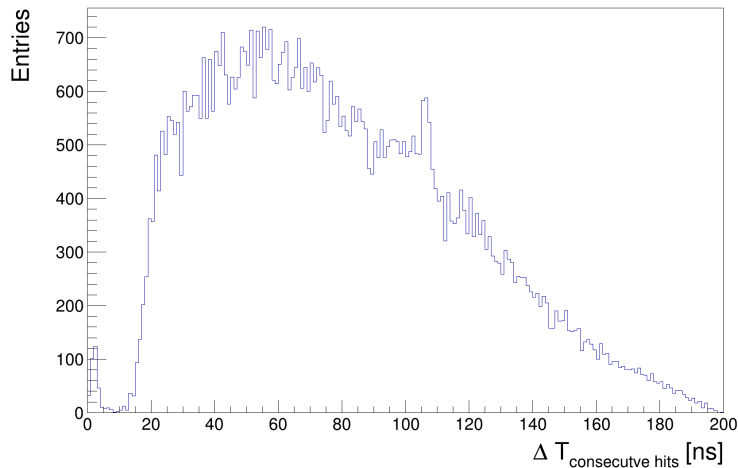


**Figure IV.11:** Time difference between two consecutive hits recorded by CAMERA in the real data, for the upstream photomultiplier of the scintillator A0.

### Momentum reconstruction

The momentum reconstruction in Monte Carlo simulations follows the very same scheme as presented for the data. In this case, the time of flight calibrations are set to 0. Indeed **Eqs. (IV.21)** and **(IV.24)** lead to  $T^{\text{raw}} = T_{B_j}^{MC} - T_{A_i}^{MC}$ , which does not need further correction between the two rings. Still, a very slight shift is observed in the momentum residual  $p_T - p_T^{MC}$ . This could be due to the fact that the Monte Carlo interaction point in the ring B is not considered at the entrance of the ring but lies inside the 5 cm thick scintillator, depending on the momentum of the proton, and leading to a slight underestimation of the distance of flight with respect to the real time of flight. To address this and avoid modifying the ring's radius values, a similar correction can be considered for the Monte Carlo on the time of flight estimation of about 10 ps. Note that this correction is very slight compared to the one in the data, so that the effect is almost not visible. The final result and comparison to the data is shown in **Fig. (IV.12)**

### CAMERA resolutions

In order to address the experimental resolution on the time measurements, a smearing procedure has to be applied on the 4 time stamps  $t_{[A,B]_i}^{\text{up,down}}$ . Using:

$$z_{[A,B]} = \frac{(t_{[A,B]_i}^{\text{up}} - t_{[A,B]_i}^{\text{down}})}{2} \cdot v_{[A,B]_i} + C_{[A,B]} \quad (\text{IV.25})$$

one can derive the following relations:

$$\sigma(z_{[A,B]}) = \frac{\sqrt{\sigma^2(t_{[A,B]_i}^{\text{up}}) + \sigma^2(t_{[A,B]_i}^{\text{down}})}}{2} \cdot v_{[A,B]_i} \quad (\text{IV.26})$$

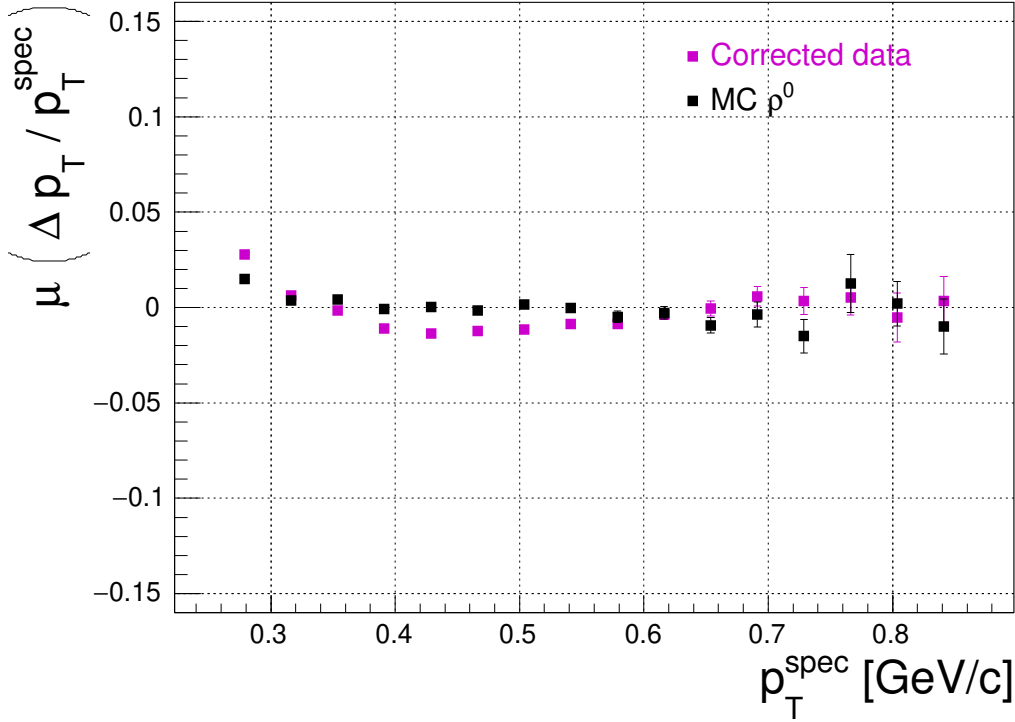


**Figure IV.12:** Mean value of the transverse momentum difference measured by CAMERA and the spectrometer, as function of the transverse momentum measured by the spectrometer. The data are drawn in purple and the Monte Carlo in black.

Assuming that the upstream and downstream photomultiplier have the same resolution, **Eq. (IV.26)** leads to

$$\sigma(t_{[A,B]_i}) = \frac{\sqrt{2}}{v_{[A,B]_i}} \cdot \sigma(z_{[A,B]}) \quad (\text{IV.27})$$

The longitudinal resolutions  $\sigma(z_{[A,B]})$  are extracted from the distributions of  $\Delta z_{[A,B]}^{\text{data}} = z_{[A,B]} - z_{[A,B]}^{\text{spec}}$ , the difference between the measurement in CAMERA and the one from the spectrometer and the kinematic fit as shown in **Fig. (IV.13)**.

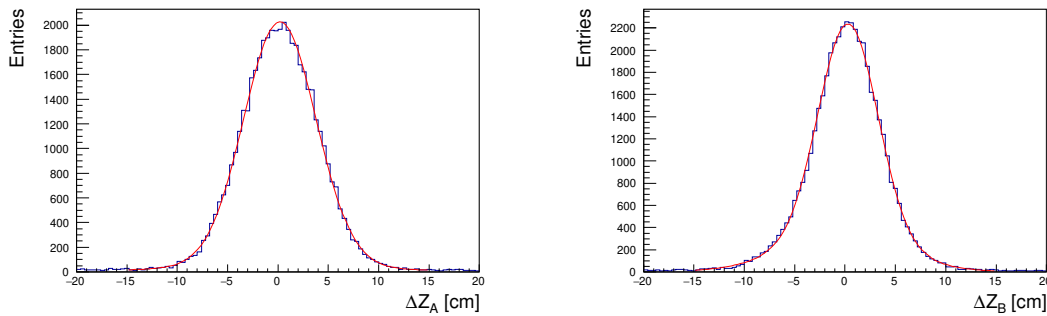


**Figure IV.13:** Distribution of  $\Delta z_{[A,B]} = z_{[A,B]} - z_{[A,B]}^{\text{spec}}$  for the inner ring A (left) and outer ring B (right). The red line shows a gaussian fit applied to the data distribution.

However one has to keep in mind that these distributions are convolution of the spec-

trometer resolution with the sought bare CAMERA resolution. In order to disentangle both contributions, a Monte Carlo simulation is performed *without* including any smearing of the CAMERA time stamps, which observables will use the superscript "MC". The standard deviation of the distribution  $\Delta z_{A,B}^{\text{MC}} = z_{[A,B]} - z_{[A,B]}^{\text{spec}}$  is labeled  $\sigma(z_B)^{\text{MC}}$ . Since CAMERA is decorrelated from the spectrometer measurements, the bare resolution of CAMERA can be extracted using the following relation:

$$\sigma^2(z_{[A,B]}) = \sigma^2(z_{[A,B]})^{\text{data}} - \sigma^2(z_{[A,B]})^{\text{MC}} \quad (\text{IV.28})$$

assuming that the resolution effect of both the spectrometer and CAMERA are simple convolution with a gaussian distribution. The extracted smearing values are the following

$$\begin{aligned} \sigma(z_A) &= 3.54 \text{ cm} \\ \sigma(z_B) &= 2.47 \text{ cm} \end{aligned} \quad (\text{IV.29})$$

One can also check the final agreement on the longitudinal distributions  $\Delta z_{A,B}$  in **Fig. (IV.14)**, and also on the momentum distribution  $\Delta p_T$  in **Fig. (IV.15)**. As shown in **Fig. (IV.1)**, the relative resolution  $\sigma(|\vec{p}|) / |\vec{p}|$  of CAMERA increases about linearly with  $|\vec{p}|$ . **Fig. (IV.15a)** shows that the resolution of the measurement is better for CAMERA than the spectrometer at low momentum value, so that the spectrometer resolution is dominant and the two curves are close to each other. In contrary at higher momentum value, the spectrometer measurement has a better resolution than CAMERA's, as shown by the black line for a pure spectrometer considerations. When including the smearing of the CAMERA measurements, one obtains **Fig. (IV.15b)**, where the higher momentum resolution of the data is retrieved, due to the dominance of CAMERA's resolutions.

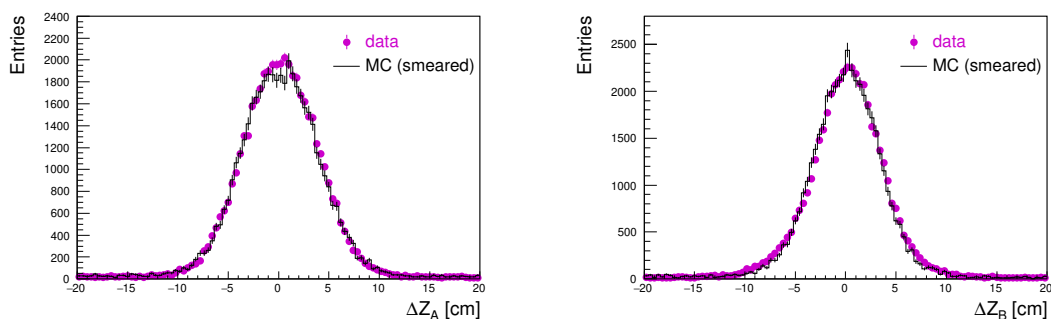


**Figure IV.14:** Distribution of  $\Delta z_{A,B} = z_{A,B} - z_{A,B}^{\text{spec}}$  for the inner ring A (left) and outer ring B (right). The Monte Carlo distribution in black has been smeared in order to fit the data points in purple using **Eq. (IV.29)**.

### CAMERA efficiencies

A proton track is detected in CAMERA if and only if CAMERA records four correlated time stamps in the upstream and downstream photomultipliers for the inner and outer rings. Thus, the efficiency of the CAMERA detector is decomposed for each of the four photomultiplier separately, as the ratio between the measured and expected protons yields passing through:

$$\epsilon = \frac{N^{\text{measured}}}{N^{\text{expected}}} \quad \sigma_\epsilon = \frac{1}{N^{\text{expected}}} \sqrt{1 - \frac{N^{\text{measured}}}{N^{\text{expected}}}} \quad (\text{IV.30})$$

For illustrating purposes in the following part, the efficiency is computed for the upstream photomultiplier of ring B, as shown in **Fig. (IV.16)**. The complete and detailed

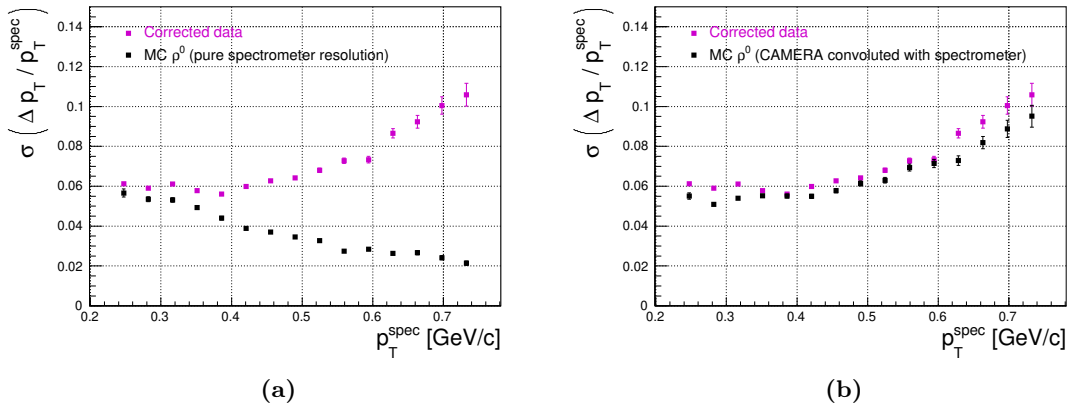


**Figure IV.15:** Standard deviation value of the transverse momentum difference measured by CAMERA with respect to the spectrometer expectation, as function of the spectrometer measurement.

analysis is performed by Sandro Scherrers for the 2016 run as described in [80, 100], from which the principle is reported here.

These efficiencies are computed using the same exclusive  $\rho^0$  events used in Section IV.2. Since we know the proton kinematics thanks to the spectrometer measurements and the kinematic fit, one can check whether the ring B upstream photomultiplier has recorded a correlated time stamp or not. To do this, one has to use Eq. (IV.17), which relies on the time measured in the ring B downstream photomultiplier.

For the ring A, the philosophy is the same as in the longitudinal calibrations ; in order to reduce the background, the interpolation between the measured position in the ring B and the vertex is used.

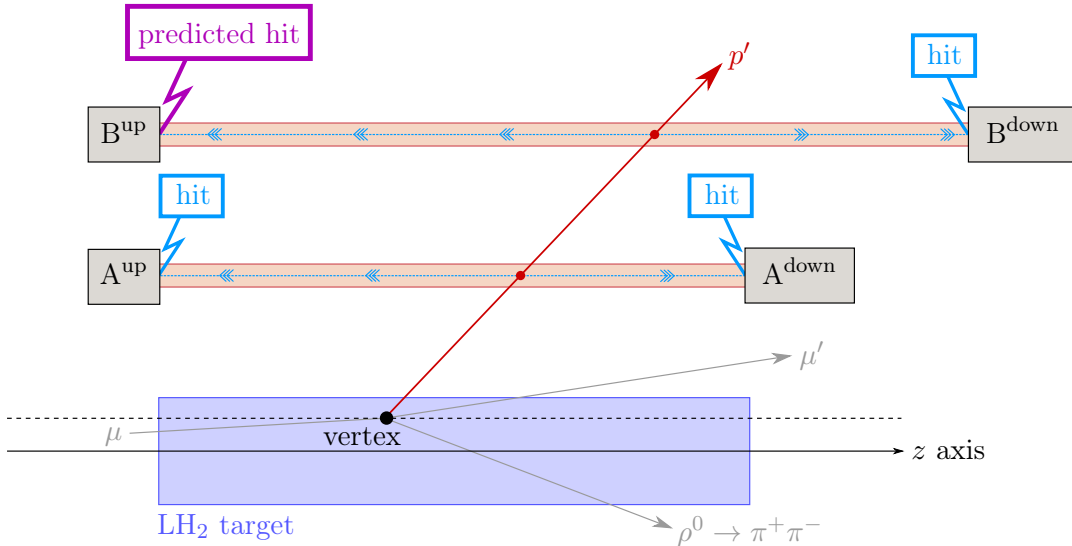


**Figure IV.16:** CAMERA efficiency calculation principle

These efficiencies are computed based on the knowledge that 3 other measurements have been recorded by the other photomultipliers. One can extract the efficiency of each of the 48 photomultipliers independently as shown in Fig. (IV.17). One can see that the efficiency decreases as function of the distance of the hit to the photomultiplier. Moreover,

due to the larger thickness of the ring B with respect to the ring A, the number of photon-electron is larger, the quality of the light propagation is better for the B ring, and in consequence the efficiency is higher.

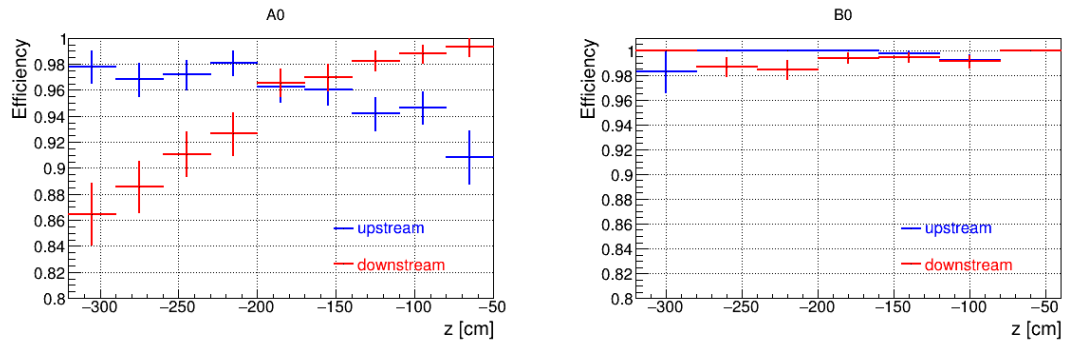


**Figure IV.17:** Efficiencies of the photomultipliers upstream and downstream for the scintillators A0 on the left and B0 on the right, as function of  $z$  for  $0.08 < |t| < 0.64$ .



---

THE EXCLUSIVE SINGLE PHOTO-PRODUCTION  
EVENT SELECTION

---

Contents

---

<b>1</b>	<b>The 2016 data and luminosity per period . . . . .</b>	<b>106</b>
<b>2</b>	<b>Monte Carlo simulations for Bethe-Heitler, DVCS and <math>\pi^0</math> . . . . .</b>	<b>107</b>
<b>3</b>	<b>The exclusive single photon event selection . . . . .</b>	<b>109</b>
3.1	Overview of the different cuts . . . . .	109
3.2	Vertex and muons selection . . . . .	109
3.3	Photon selection . . . . .	110
3.4	Proton selection . . . . .	112
3.5	Exclusivity cuts . . . . .	112
3.6	Kinematical fit . . . . .	116
<b>4</b>	<b>Strategy of the DVCS analysis with a 160 GeV muon beam . . . . .</b>	<b>124</b>
<b>5</b>	<b>Comparison of the data with the Bethe-Heitler prediction at large <math>\nu</math> . . . . .</b>	<b>124</b>
5.1	Quality of the Monte Carlo description . . . . .	124
5.2	Quality of the agreement between the data and the Monte Carlo Bethe-Heitler prediction . . . . .	129
<b>6</b>	<b>The <math>\pi^0</math> contamination at small <math>\nu</math> . . . . .</b>	<b>130</b>
6.1	The visible $\pi^0$ background . . . . .	130
6.2	The invisible $\pi^0$ contamination . . . . .	130
6.3	Evaluation of the sharing ratio between exclusive and semi- inclusive productions . . . . .	131
<b>7</b>	<b>The DVCS contribution at small <math>\nu</math> . . . . .</b>	<b>134</b>
<b>8</b>	<b>Summary and <math>\phi_{\gamma^*\gamma}</math> azimuthal distributions . . . . .</b>	<b>137</b>

---

A first part of this chapter will be dedicated to a summary of the data and Monte Carlo generators used in this analysis. It will be followed by the description of the exclusive single photon event selection, comparing the different beam charge yields. The kinematic fitting procedure is also applied in order to improve the observables. Its impact will be illustrated and quantified. A detailed comparison between the data and the Bethe-Heitler Monte-Carlo will be shown in the kinematic region where this contribution should be dominant at high  $\nu$  ( $80 < \nu < 144$  GeV) in order to be confident in the simulation and the evaluation of the Bethe-Heitler contribution. In the domain at small  $\nu$  ( $10 < \nu < 32$  GeV) the Bethe-Heitler contribution will be subtracted as well as the  $\pi^0$  contamination in order to highlight the DVCS and interference contribution which be further analysed in the last section.

## 1 The 2016 data and luminosity per period

The 2016 DVCS data are divided into periods of about 2 weeks each, with alternating  $\mu^+$  and  $\mu^-$  sub-periods. The periods and productions used in the present work are given in [Table \(V.1\)](#).

**Table V.1:** Real data (RD) production used in this work

periods	production	bad spill list	$N_{\mu^+}$ ( $10^{11}$ )	$N_{\mu^-}$ ( $10^{11}$ )
P04	slot7.1	from slot7.1	9.69	7.60
P05	slot7.1	from slot7.1	8.05	7.10
P06	slot7.1	from slot7.1	7.83	6.36
P07	slot7.1	from slot4	9.45	8.45
P08	slot7.1	from slot7.1	9.53	8.42
P09	slot7.1	from slot4	7.44	7.03
		TOTAL	51.99	44.96
		TOTAL		96.95

The integrated muon flux for 6 periods for  $\mu^+$  and  $\mu^-$  data is given in [Table 1](#) and presented in [Fig. \(V.1\)](#). The statistics presented here represents approximately 2.5 times the one taken during the 2012 pilot run.

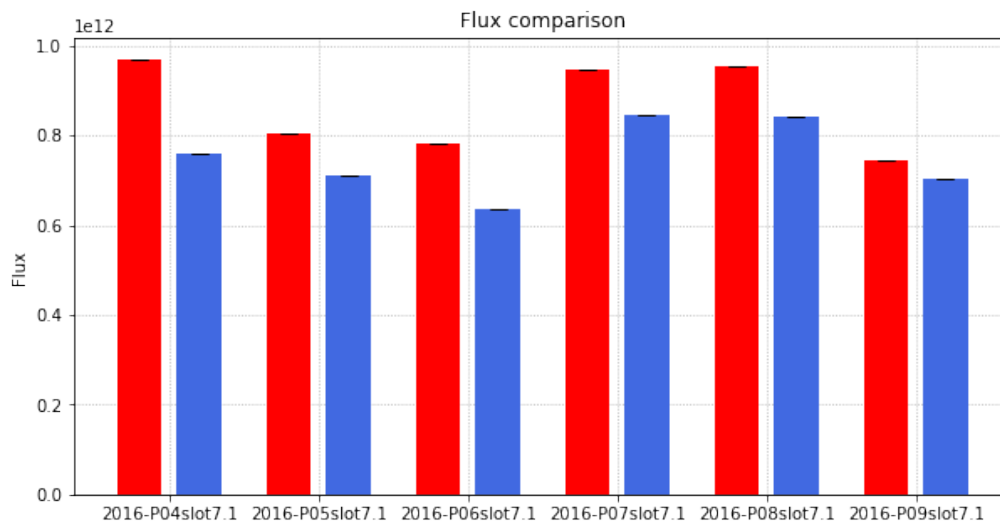


**Figure V.1:** Integrated muon flux per period for  $\mu^+$  in red and  $\mu^-$  in blue separately. The total integrated muon flux used in this analysis is  $9.7 \cdot 10^{12}$  muons.

## 2 Monte Carlo simulations for Bethe-Heitler, DVCS and $\pi^0$

An overview of the Monte Carlo simulation has already been described in [Section V.5](#) and we will present here the generators used in the following of this analysis:

- HEPGEN-BH to evaluate the BH contribution which is exactly computed using the muon mass
- HEPGEN-DVCS to evaluate the DVCS contribution using a model
- HEPGEN-DVCS+BH to evaluate the DVCS and BH contributions with their interferences using a model for DVCS and an approximation for BH with muon mass only included in the propagators
- HEPGEN-pi0 to evaluate the exclusive  $\pi^0$  production
- LEPTO to evaluate the semi-inclusive  $\pi^0$  production (the exclusive  $\pi^0$  generation have been removed using the JETSET information (see [\[85, p. 193\]](#))

HEPGEN<sup>1</sup> is a dedicated Monte Carlo generator of events [\[101, 102\]](#), which is used for studies of hard exclusive leptonproduction processes at the COMPASS experiment kinematic domain. The studied reactions comprise both single photon production via Deeply Virtual Compton Scattering (DVCS) and Bethe-Heitler (BH) process as well as hard exclusive production of various mesons (HEMP). HEPGEN++ is the corresponding software written in c++. The phase space of the event generation for HEPGEN++ is the following:

- $2 \text{ GeV} < \nu < 170 \text{ GeV}$
- $0.5 \text{ GeV}^2 < Q^2 < 80 \text{ GeV}^2$
- $0.001 \text{ GeV}^2 < |t - t_{min}| < 1.2 \text{ GeV}^2$

The 4-momentum transfer to the proton,  $t$ , is defined as:

$$t = -\frac{Q^2}{x_B} \times \frac{2M_p^2 x_B^2 / Q^2 + 1 - \sqrt{1 + 4M_p^2 x_B^2 / Q^2} \cos \theta_{\gamma^* \gamma}}{2M_p^2 x_B / Q^2 + 1 - \sqrt{1 + 4M_p^2 x_B^2 / Q^2} \cos \theta_{\gamma^* \gamma}} \quad (\text{V.1})$$

Each event is assigned a weight, which is proportional to the cross section corresponding to the values of kinematic variables for that event.

HEPGEN-BH uses the Bethe-Heitler cross section exactly evaluated by P.A.M. Guichon [\[103\]](#) using the muon mass. The code has been cross checked with an analytic and a numeric approach. The corresponding event weight is noted  $w_{\text{BH}}$ .

HEPGEN-DVCS uses the DVCS cross section based on the DVCS model of Frankfurt, Freund and Strikman [\[104, 105\]](#). The corresponding event weight is noted  $w_{\text{DVCS}}$ .

HEPGEN-DVCS+BH is adapted by A. Sandacz to evaluate the DVCS and BH contributions with their interferences using the previous model for DVCS and an approximation for BH with muon mass only included in the propagators. The corresponding event weight is noted  $w_{\text{DVCS}} + w_{\text{I}} + w_{\text{BH}}$ . This model provides an evaluation of the full exclusive single photon cross section, including the muon mass at least in an approximate way. A full comparison of this model with the COMPASS 2012 data is performed in [\[80\]](#).

HEPGEN- $\pi^0$  uses the exclusive  $\pi^0$  cross sections according to the GPD model of Goloskokov and Kroll. They are computed in tables. A detailed description of the model

---

<sup>1</sup>Hard Exclusive Physics GENerator

and the used GPD parameters are given in [106, 102]. The corresponding event weight is noted  $w_{\pi^0}$ .

It has been shown that the kinematic generation using HEPGEN is not really suited or efficient for the Bethe-Heitler process due to the very high variation of the cross section notably when the photon is emitted in a direction close to that of the incident or outgoing muon. In a particular region, few events generated could have a very high weight, whereas more events could be generated in another region, with a lower weight. This has an impact to the Monte Carlo statistical error propagation, and can lead to instabilities and non-uniformity of the statistical error bars. Studies have been performed in order to generate kinematic distributions using an analytical function, such as the Bethe-Heitler calculation from P.A.M. Guichon [103]. This technique makes use of the VEGAS algorithm developed by G. Peter Lepage [107, 108], and provides results displayed in [109] and in **Appendix (C)**. Nevertheless the integration into the HEPGEN++ software is still too preliminary and not yet included in the present thesis.

The HEPGEN MC luminosity has to be computed by the user. It is defined as:

$$\mathcal{L}_{\text{MC}} = \frac{N^{\text{gen}}}{\sigma} = \frac{\sum_{\Delta\Omega}^{\text{gen}} w_{\text{DVCS}}}{\int_{\Delta\Omega} \left( \frac{d\sigma_{\text{DVCS}}}{d\Omega} \right) d\Omega} \quad (\text{V.2})$$

The numerator accounts for the sum of weights for the generated events within the phase space  $\Delta\Omega$ , while the denominator reads the integrated cross section used in the generation process of HEPGEN++ over the very same phase space.

In addition, the determination of the luminosity of the COMPASS data and the selection of exclusive events are performed requiring a few conditions on the beam muon given in **Table (V.2)**. The same quality filters have to be applied on the Monte Carlo when computing the numerator of **Eq. (V.2)**.

In principle we can replace "DVCS" in **Eq. (V.2)** by "BH" or "BH", the outcome should be exactly the same. However the DVCS cross section is rather smooth comparatively to the Bethe-Heitler cross section, and so the numerical integrations are more stable.

At the end the HEPGEN MC luminosity has to be scaled to the data luminosity. For example we define:

$$c_{\text{BH}} = \frac{\mathcal{L}_{\text{data}}}{\mathcal{L}_{\text{MC}}} \quad (\text{V.3})$$

### 3 The exclusive single photon event selection

#### 3.1 Overview of the different cuts

DIS	General	<ul style="list-style-type: none"> <li>• Bad spills rejected<sup>a</sup></li> <li>• Event time within the time in spill limits<sup>a</sup></li> <li>• Trigger types considered: MT, OT, LT</li> </ul>
	Vertex (1)	One vertex contained in the fiducial volume of the target <sup>a</sup> : <ul style="list-style-type: none"> <li>• <math>-318.5 \text{ cm} &lt; z_{\text{vertex}} &lt; -78.5 \text{ cm}</math></li> <li>• <math>r_{\text{vertex}}(\text{vertex}, \text{TargetCenter}(z_{\text{vertex}})) &lt; 1.9 \text{ cm}</math></li> <li>• <math>y_{\text{vertex}} &lt; 1.2 \text{ cm}</math></li> </ul>
	Beam muon	<ul style="list-style-type: none"> <li>• One charged track with:<sup>a</sup> <ul style="list-style-type: none"> <li><math>\geq 2</math> hits in SciFi</li> <li><math>\geq 3</math> hits in SI</li> <li><math>\geq 3</math> hits in the beam momentum station (BMS)</li> </ul> </li> <li>• A momentum measurement such that:<sup>a</sup> <math display="block">140 [\text{GeV}/c] &lt;  p_{\mu}  &lt; 180 [\text{GeV}/c]</math> <math display="block"> \sigma(p_{\mu})/p_{\mu}  &lt; 0.025</math> </li> <li>• The beam track traverses the full target length and is contained within the fiducial volume of the target<sup>a</sup></li> </ul>
	Scattered muon	One unique outgoing charged track with: <ul style="list-style-type: none"> <li>• same charge as beam muon</li> <li>• traversed radiation length <math>X/X_0 &gt; 15</math></li> <li>• <math>z</math>-position of the first and last measured point:               <math display="block">z_{\text{first}} &lt; 350 \text{ cm} \quad \text{and} \quad z_{\text{last}} &gt; 350 \text{ cm}</math> </li> <li>• extrapolations within the active areas of the hodoscopes (new PointHodoscope function)</li> </ul> Inclusive scattering variables (wide): <ul style="list-style-type: none"> <li>• <math>0.8 \text{ GeV}^2 &lt; Q^2 &lt; 1000 \text{ GeV}^2</math></li> <li>• <math>0.01 &lt; y &lt; 0.99</math></li> </ul>

**Table V.2:** Overview of the selection of exclusive single photon events (part 1)

<sup>a</sup> these filters are applied also for the flux calculation

#### 3.2 Vertex and muons selection

The vertex is selected inside the fiducial volume of the target as done in [Section V.1](#), and the beam muon according the criteria mentioned in [Section V.2](#) for the muon flux determination. Unlike the DIS event selection, a loop on all the possible vertices featuring the previous requirements is performed, and the vertex is not necessarily the same as the *best primary* vertex tagged by the reconstruction software CORAL. From all these vertex candidates, the scattered muon is chosen as it must pass in the well-defined domains of the hodoscopes, and traverse more than 15 radiation lengths. The following wide inclusive scattering conditions are applied:

DVCS-BH	Photon (2)	One unique photon with: <ul style="list-style-type: none"> <li>• a time correlated with the event <math display="block"> t_{\text{cluster}} - t_{\text{beam}} - \mu_t  &lt; 3\sigma_t</math> </li> <li>• a cluster energy above 4,5 and 10 GeV in ECAL0,1,2 respectively</li> </ul>
	Recoiled proton (3)	One track detected in CAMERA with a velocity $0.1 < \beta < 0.95$
	Exclusivity conditions	All combinations of (1) (2) (3) which satisfy: <ul style="list-style-type: none"> <li>• <math> \Delta\varphi  &lt; 0.4</math> rad</li> <li>• <math> \Delta p_T  &lt; 0.3</math> GeV/c</li> <li>• <math> \Delta z_A  &lt; 16</math> cm</li> <li>• <math> M_{\text{undet}}^2  &lt; 0.3 (\text{GeV}/c^2)^2</math></li> </ul>
	Kinematic fit quality	The kinematic fitting procedure must have converged with a score: $\chi_{\text{red}}^2 < 10$ Kinematical cuts (after the fit): <ul style="list-style-type: none"> <li>• <math>1 \text{ GeV}^2 &lt; Q_{\text{kinfit}}^2 &lt; 10 \text{ GeV}^2</math></li> <li>• <math>0.05 &lt; y_{\text{kinfit}} &lt; 0.9</math></li> <li>• <math>0.08 [(\text{GeV}/c)^2] &lt;  t_{\text{kinfit}}  &lt; 0.64 [(\text{GeV}/c)^2]</math></li> </ul>
	Combinatorics	Exactly one topological combination must be left
	Visible $\pi^0$ removal	Remove visible $\pi^0$ events fulfilling the condition: $ M_{\gamma\gamma} - M_{\pi^0}^{\text{PDG}}  < 20 \text{ MeV}/c^2$

**Table V.3:** Overview of the selection of exclusive single photon events (part 2)

- $0.8 \text{ GeV}/c^2 < Q^2 < 1000 \text{ GeV}/c^2$
- $0.01 < y < 0.99$

These kinematic cuts are wide and will be further tighten from the values obtained by the kinematically constrained fit to accept the smearing effects on the edges.

### 3.3 Photon selection

The outgoing photon is selected in the three electromagnetic calorimeters excluding the bad cells. The underlying cluster selection is based on two criteria:

- a cluster in time with respect to the mean beam :  $|t_{\text{cluster}} - t_{\text{beam}} - \mu_t| < 3\sigma_t$ .  $\mu_t$  and  $\sigma_t$  are determined per period and for each type of ECAL cells in [Section V.6.1](#).
- a cluster energy  $E_\gamma$  above the energy threshold of 4, 5, 10 GeV in ECAL0,1,2 respectively.

The energy threshold values are evaluated by taking into account the final kinematic values of the analysis  $y > 0.05$  and  $|t| < 0.64 \text{ (GeV/c)}^2$  within their resolution and are illustrated in the simulation presented **Fig. (V.2)**. Note that all the charged clusters are ignored thanks to the charged track association performed in CORAL.

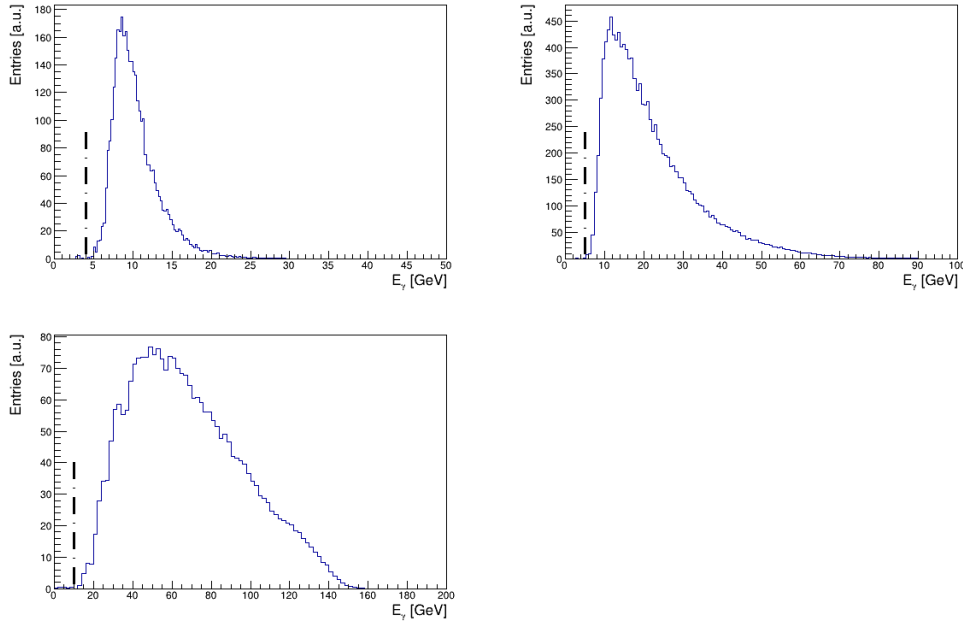


**Figure V.2:** Reconstructed photon energy in the different calorimeters (top left: ECAL0, top right: ECAL1, bottom left: ECAL2) after applying the DVCS event selection omitting the energy thresholds. The black dashed line shows the energy thresholds chosen in the final event selection. These distributions were obtained from a HEPGEN DVCS Monte Carlo for an exclusive single photon muoproduction corresponding to the DVCS process (the Bethe-Heitler process is not included), and for  $8 \text{ GeV} < \nu$ ,  $0.05 < y < 0.9$ ,  $0.08 \text{ (GeV/c)}^2 < |t| < 0.64 \text{ (GeV/c)}^2$ ,  $1 \text{ (GeV/c)}^2 < Q^2 < 20 \text{ (GeV/c)}^2$ .

For illustration, **Fig. (V.3)** shows the position distribution of clusters in the different ECALs after the full exclusive single photon event selection presented in **Table. (V.2)** and **(V.3)**. It will be shown that the DVCS events are mostly distributed in ECAL0,1, while ECAL2 features more Bethe-Heitler events.

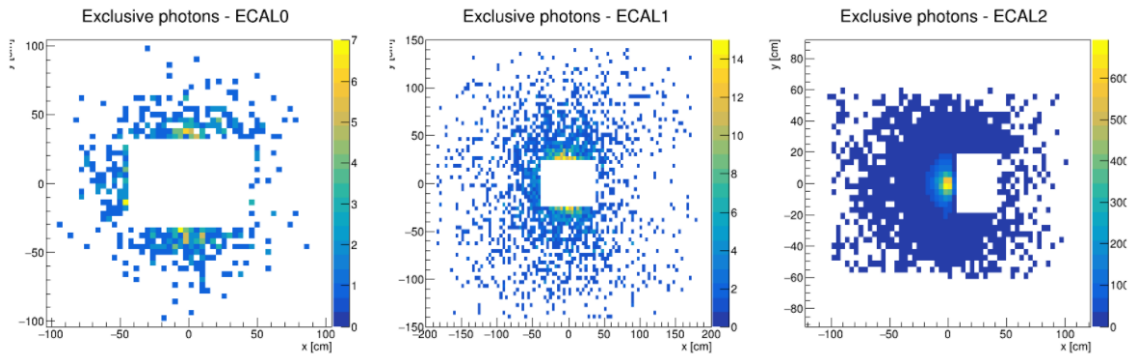


**Figure V.3:**  $X$  and  $Y$  positions of the clusters in ECAL0,1,2 from left to right, for both  $\mu^+$  and  $\mu^-$  samples. The plots are produced for  $1 < Q^2 < 10 \text{ (GeV/c)}^2$ ,  $0.05 < y < 0.9$  and  $0.08 < |t| < 0.64 \text{ (GeV/c)}^2$

### 3.4 Proton selection

A combination of hits in the inner and outer barrels of CAMERA is considered to be a good proton candidate if:

- the hits belong to azimuthal sectors that are geometrically correlated
- the reconstructed velocity  $\beta$  is such that:  $0.1 < \beta < 0.95$

**Fig. (V.4)** displays the proton track signal after the full exclusive single photon event selection **Table. (V.2)** and **(V.3)**. As the ring B is composed of 5 cm thick scintillators, the proton can be either totally absorbed in the B ring (for a proton momentum between  $260 \text{ MeV}/c < p_p < 460 \text{ MeV}/c$ ) or escape out of it. This is illustrated on the left picture where one sees an increase of the energy loss in the B ring as function of  $\beta$  up to  $\beta \approx 0.4$ , followed by a decreasing energy loss where the proton escapes the ring B. One has to note that the velocity  $\beta$  is corrected for the energy loss in the target, and corresponds to the velocity at the vertex.

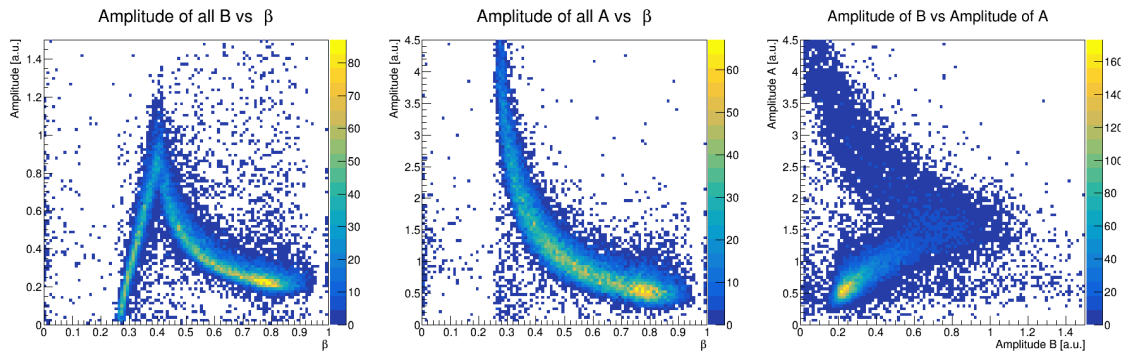


**Figure V.4:** Distribution of the energy losses in the outer (inner) ring B (A) as a function of the velocity of the selected protons in left (middle) plots, and energy loss in the inner ring A as a function of the outer ring B in the right plot, for both  $\mu^+$  and  $\mu^-$  samples. The plots are produced for  $1 < Q^2 < 10 \text{ (GeV}/c)^2$ ,  $0.05 < y < 0.9$ . Note that no  $|t|$  cut is applied

### 3.5 Exclusivity cuts

When a proton track candidate is selected, the kinematics is over-determined and we can compare the observables given either only by the spectrometer or only by CAMERA. All the good proton candidates are combined with all the vertices and ECAL clusters selected in the previous steps, and a list of possible exclusive event candidates is filled subsequently. At this stage, the list of candidates still contains a significant fraction of non-exclusive background events, which are removed by applying suitable exclusivity conditions.

Without the use of CAMERA information, the exclusive reaction  $\mu p \rightarrow \mu p \gamma$  can be selected with the detection of only the incident and outgoing muons and the photon, using a cut on the missing energy or on the missing mass of a particle that is assumed to be a proton:

$$E_{miss} = (M_{miss}^2 - M_p^2)/2M_p = \nu - E_\gamma + t/2M_p \quad (\text{V.4})$$

$$M_{miss}^2 = M_{X=p'}^2 = (k + p - k' - q')^2 = 2M_p(\nu - E_\gamma) + M_p^2 + t \quad (\text{V.5})$$

The detection of the proton in CAMERA allows to perform cuts on a zero missing mass to remove any background particle:

$$M_{undet}^2 = M_{X=0}^2 = (k + p - k' - q' - p')^2 \quad (\text{V.6})$$

We can also build the differences between azimuthal angles and transverse momenta of the proton (with respect to the direction of the incident muon) reconstructed by either the forward spectrometer or CAMERA:

$$\Delta\varphi = \varphi^{CAMERA} - \varphi^{miss} \quad (\text{V.7})$$

$$\Delta p_T = |p_T^{CAMERA}| - |p_T^{miss}| \quad (\text{V.8})$$

$\Delta p_T$  can be evaluated either on the virtual photon direction or on the laboratory  $z$ -axis. In fact the last one gives better width and is used in the plots presented in the following.

In addition, we can compare the  $z$ -position of the hits in the inner CAMERA ring given either by the scintillator or by the interpolation between the vertex and the outer ring position:

$$\Delta Z = z_{\text{ring A}} - z_{\text{interp}}. \quad (\text{V.9})$$

The cuts applied to the exclusivity variables are the following:

- $|\Delta\varphi| < 0.4$  rad
- $|\Delta p_T| < 0.3$  GeV/ $c$
- $|\Delta Z| < 16$  cm
- $|M_{undet}^2| < 0.3$  (GeV/ $c^2$ )<sup>2</sup>

The exclusivity variable distributions,  $\Delta\varphi$ ,  $\Delta p_T$ ,  $\Delta Z$  and  $M_{undet}^2$  for exclusive single photon production have been produced for each period. The comparison between the distributions of  $\mu^+$  (in red) and  $\mu^-$  (in blue) beams, normalised to the same muon flux is presented for the total statistics of all the periods in **Fig. (V.5)**. Note the good agreement between the distributions of opposite charge. This is an important achievement, which was not obtained in 2012 due to the use of very different intensities for the  $\mu^+$  and  $\mu^-$  beams.

The  $E_{miss}$  distribution is an excellent indicator of the quality of the energy measurement of the incident muon, outgoing muon and photons. We recall  $E_{miss} = (M_{miss}^2 - m_p^2)/2m_p = \nu - E_\gamma + t/2m_p$ . For exclusive single photon production,  $E_{miss}$  should be at the zero value within the resolutions. The resolution is mainly due to the resolution of the incoming and outgoing muons, on top of that the resolution of the photon energy enters in the game. This is why the resolution increases from ECAL0 (with low photon energy) to ECAL2 (with high photon energy) (see the 6 plots on bottom in Fig V.6. A shift of +0.4, -0.5, +1.1 GeV is also observed in ECAL0, ECAL1, ECAL2. The cause has different origins: the not perfect determination of the muon beam energy, of the scattered muon or of the ECAL energy calibration.

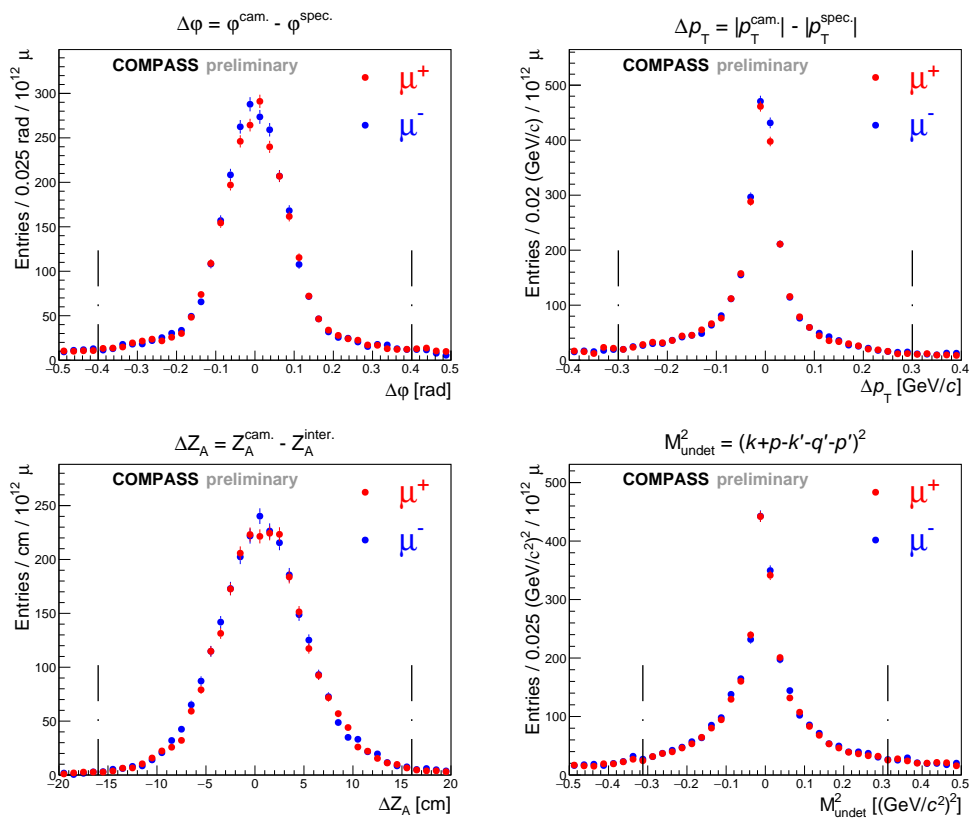


**Figure V.5:** Exclusivity variable distributions for exclusive single photon production for the sum of all the 6 periods.

All cuts are applied except those related to the presented variable.

Each sample for  $\mu^+$  (in red) or  $\mu^-$  (in blue) beams is normalized to a muon flux of  $10^{12}$  for comparison.

The plots are produced for  $1 < Q^2 < 10 \text{ (GeV}/c)^2$ ,  $0.05 < y < 0.9$  and  $0.08 < |t| < 0.64 \text{ (GeV}/c)^2$ . ( $Q^2, y, t$  given by the kinematic fit).

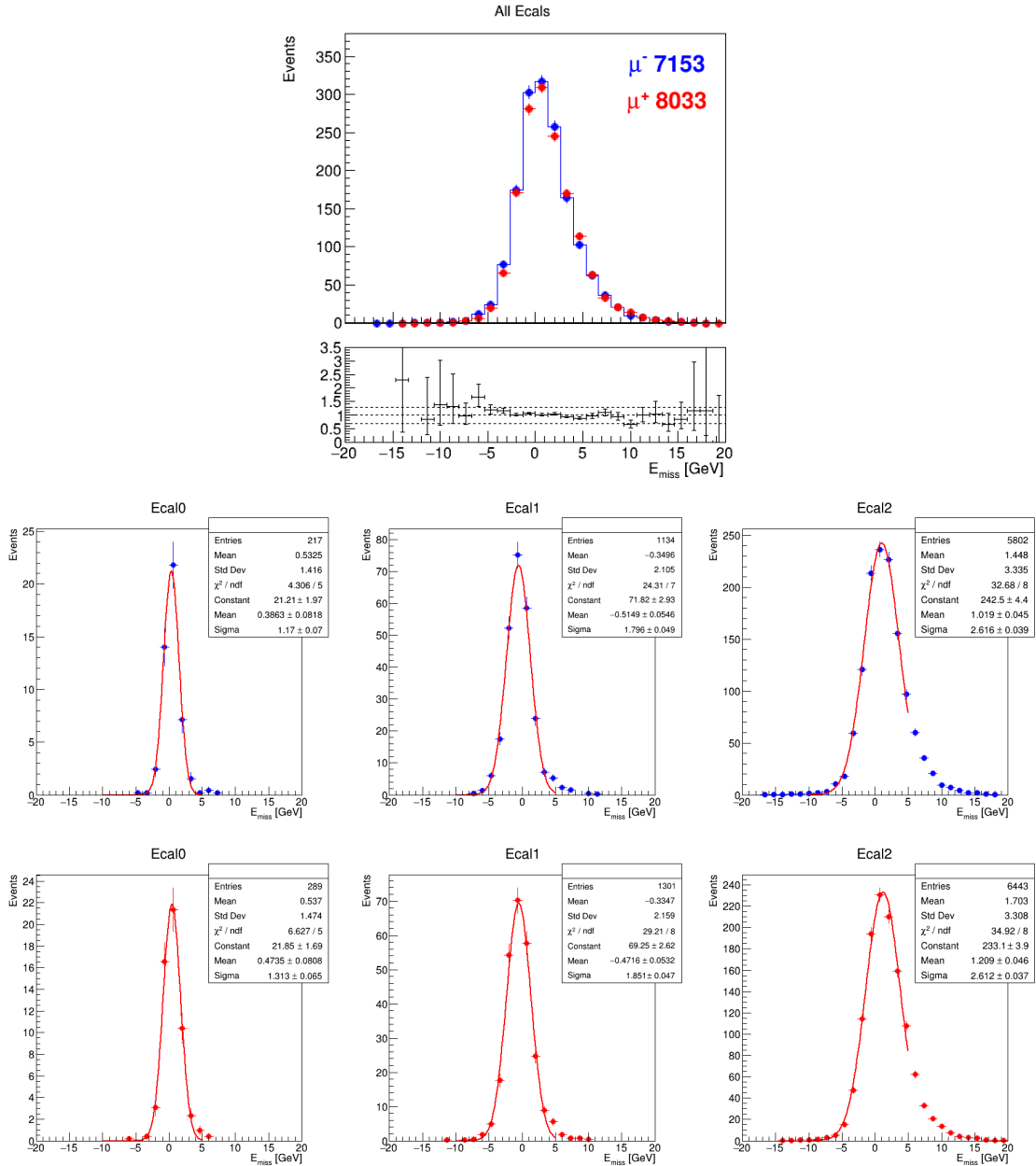


**Figure V.6:**  $E_{miss}$  distributions for exclusive single photon production for the sum of all the 6 periods. All exclusivity cuts are applied. Each sample for  $\mu^+$  (in red) or  $\mu^-$  (in blue) beams is normalized to a muon flux of  $10^{12}$  for comparison.

The 6 plots in bottom represent the distribution for each ECAL and each beam charge. A fit is applied to give resolution (Sigma) and shift (Mean) of  $E_{miss}$  for each ECAL.

The plot on top left represents the total contribution for the 3 ECALs. The plots are produced for  $1 < Q^2 < 10$  (GeV/c) $^2$ ,  $0.05 < y < 0.9$  and  $0.08 < |t| < 0.64$  (GeV/c) $^2$ , where  $Q^2, y, t$  are given by the kinematic fit.

### 3.6 Kinematical fit

#### Application to the exclusive photon events

The exclusive photon event topology is as follow:  $\mu p \rightarrow \mu' p' \gamma$ . In contrary to **Section V.1.2**, this kinematic fit setup assumes the measurement of the outgoing proton through the CAMERA detector, handled as shown in **Section V.1.1**. This setup makes use of all the available information measured, so that it features the best possible estimation of the process parameters and resolutions. The number of measured parameters of the problem from the spectrometer and CAMERA is 23 as follows:

$$\vec{k} = \begin{pmatrix} k_1 \\ \vdots \\ k_{23} \end{pmatrix} := \begin{pmatrix} \vec{a}_\mu \\ \vec{p}_\mu \\ \vec{0}_{18} \end{pmatrix} + \begin{pmatrix} \vec{0}_5 \\ \vec{a}_{\mu'} \\ \vec{p}_{\mu'} \\ \vec{0}_{13} \end{pmatrix} + \begin{pmatrix} \vec{0}_{10} \\ r_A \\ \phi_A \\ z_A \\ r_B \\ \phi_B \\ z_B \\ |\vec{p}| \\ \vec{0}_{20} \end{pmatrix} + \begin{pmatrix} \vec{0}_{20} \\ \vec{p}_p \end{pmatrix}$$

As previously the quantities labeled as  $\vec{a}_X$ ,  $\vec{p}_X$  denotes the position  $(x, y)$  and momentum  $(p_x, p_y, p_z)$  of a charged track as described in **Section V.1.1**. The target proton is again considered at rest and given by  $\vec{p}_p$ . The number of unmeasured parameters is 6 given by

$$\vec{h} = \begin{pmatrix} h_1 \\ \vdots \\ h_7 \end{pmatrix} := \begin{pmatrix} \vec{v} \\ \vec{0}_4 \end{pmatrix} + \begin{pmatrix} \vec{0}_3 \\ \theta_\gamma \\ \phi_\gamma \\ \vec{0}_2 \end{pmatrix} + \begin{pmatrix} \vec{0}_5 \\ \theta_{p'} \\ \phi_{p'} \end{pmatrix}$$

#### Constraints and degrees of freedom

The energy-momentum conservation of the exclusive process leads to four constraints. In addition, all the particles should come from a common vertex. For each track, two coplanarity conditions are used to constrain the vertex to be part of the track direction, so that two constraints are added for each charged track  $\mu, \mu'$  and two more for the outgoing photon  $\gamma$ . One also needs to constraint the CAMERA hits to be along the outgoing proton charged track, which adds two constraints for each of the measured hit in the A and B rings.

In total  $4 + 2 \times 3 + 2 \times 2 = 14$  constraints are applied while 7 free parameters have to be estimated by the fitting procedure. Thus the number of degree of freedom is  $ndf =$

$14 - 7 = 7$ . This number can also be retrieved in an alternative way by using the traditional physical phase-space basis. The exclusive single photon kinematics is parametrised by the variables  $Q^2$ ,  $x_B$ ,  $t$ ,  $\phi_{\gamma^*\gamma}$  for fixed incoming beam parameters. Therefore adding the 3 beam parameters  $\vec{p}_\mu$ , we reach the number of 7 degrees of freedom.

### Improvement of the observables

**Fig. (V.7)** and **Fig. (V.8)** show the pull distributions of all the input quantities with respect to the output quantities of the kinematic fitting procedure. The agreement between data and MC is quite satisfactory although there are visible deviations notably for the incoming muon energy and the reconstructed cluster energy in the calorimeters. The measured quantities are noted "meas" and the fitted ones "fit". The quantity  $\sigma$  in each distribution is given by the respective elements of the covariance matrix before and after the fit by  $\sigma = \sqrt{C_{i,i}^{\text{meas}} - C_{i,i}^{\text{fit}}}$ . As stated by the Gauss-Markov theorem, the best linear unbiased estimator (best in the sense of minimum variance) is given by the least squared method. Therefore the matrix  $C^{\text{meas}} - C^{\text{fit}}$  is positive definite. In addition by propagation of errors, the variance on the quantity  $\Delta y = y^{\text{meas}} - y^{\text{fit}}$  is exactly  $\sigma = \sqrt{C_{i,i}^{\text{meas}} - C_{i,i}^{\text{fit}}}$  [99]. Therefore in perfect conditions and in the case of gaussian-distributed observables, the pull distributions behave as normal distributions.

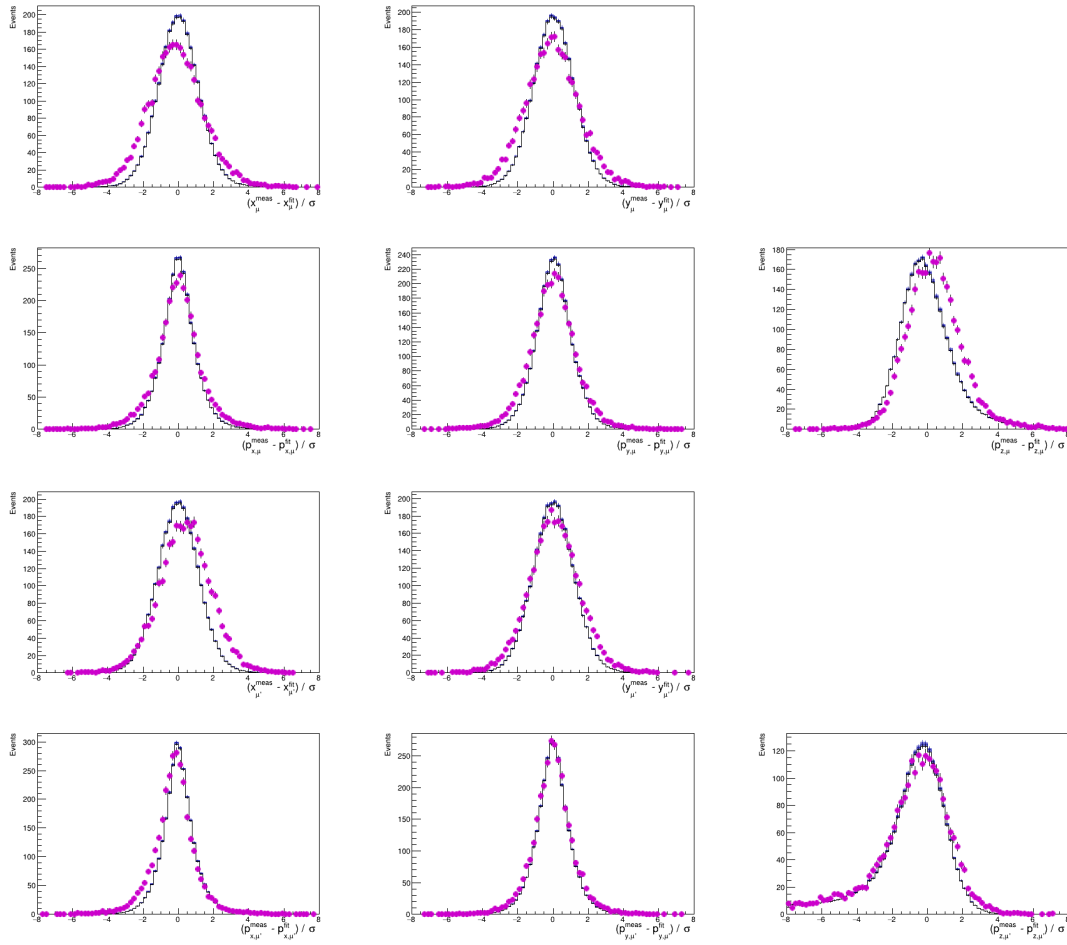


**Figure V.7:** Pull distributions using the real data (in purple) or the HEPGEN-BH MC events (in blacks) for

- 1st row: the track parameters of the incoming muon,
- 2nd row: the momentum of the incoming muon,
- 3rd row: the track parameters of the outgoing muon,
- 4th row: the momentum of the outgoing muon.

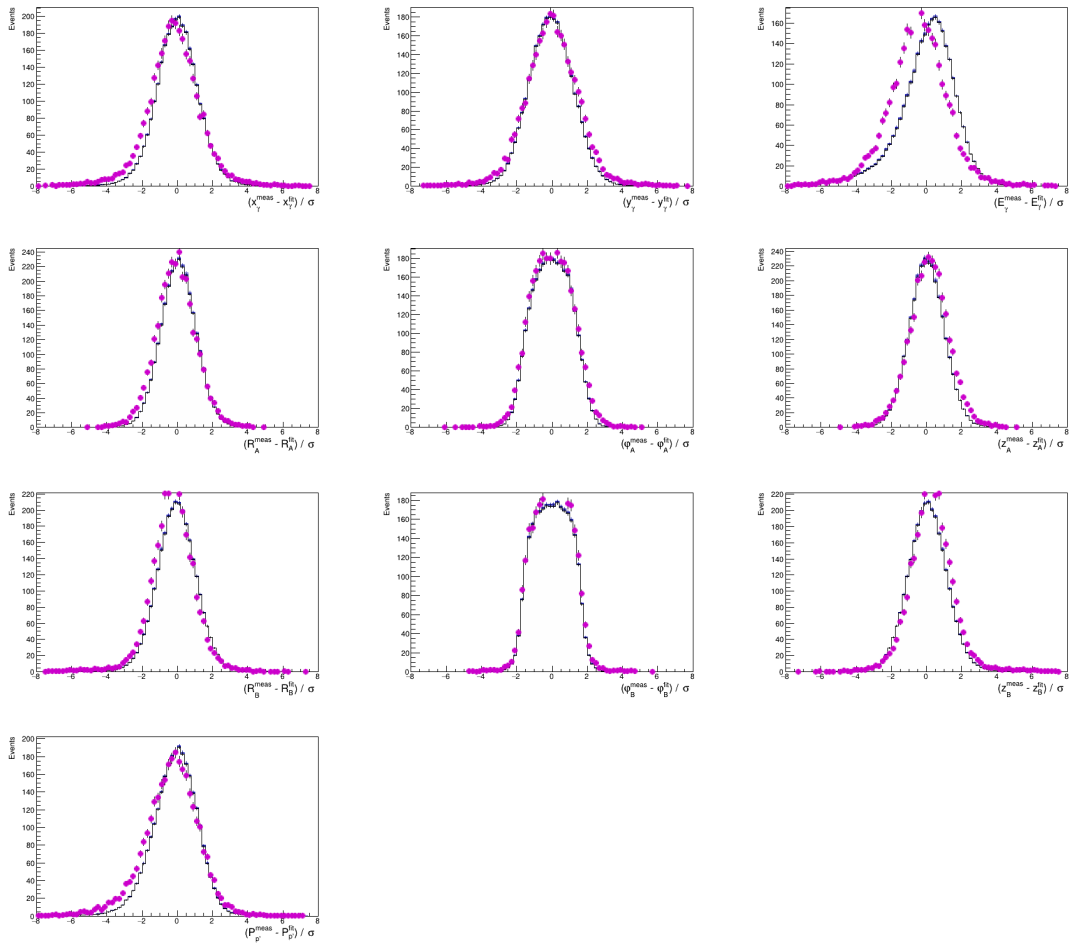


**Figure V.8:** Pull distributions using the real data (in purple) or the HEPGEN-BH MC events (in blacks) for  
 1st row: the positions of the reconstructed calorimeter cluster and the reconstructed cluster energy,  
 2nd row: the track parameters of the outgoing proton for the reconstructed hit positions in CAMERA Ring A,  
 3rd row: the track parameters of the outgoing proton for the reconstructed hit positions in CAMERA Ring B,  
 4th row: the reconstructed proton momentum.

### Impact on $|t|$

The main role of the kinematic fit is to improve the  $|t|$ -resolution, which is a key issue to study the  $|t|$ -dependence of the DVCS cross section.  $|t|$  can be evaluated using only CAMERA or only the forward COMPASS spectrometer:

$$t_{CAMERA} = (p - p')^2 = 2M_p(M_p - E_p) \quad (\text{V.10})$$

$$\begin{aligned} t_{spec} &= (q - q')^2 = -Q^2 - 2E_\gamma(\nu - \sqrt{\nu^2 + Q^2}\cos\theta_{\gamma^*\gamma}) \\ &= \frac{-Q^2 - 2\nu(\nu - \sqrt{\nu^2 + Q^2}\cos\theta_{\gamma^*\gamma})}{1 + \frac{1}{m_p}(\nu - \sqrt{\nu^2 + Q^2}\cos\theta_{\gamma^*\gamma})} \text{ without using } E_\gamma \end{aligned} \quad (\text{V.11})$$

The kinematic fit takes advantage of both the good  $t$ -resolution given by the ToF detector CAMERA at small  $|t|$  and by the COMPASS spectrometer at large  $|t|$  as illustrated in **Fig. (V.9)**. This improvement is due to the correlations on the different measurements introduced by the topological and geometrical constraints.

It has to be noted that the  $t$ -resolution given by the ToF detector CAMERA is about 2 times its proton momentum resolution which was shown in **Fig. (IV.1)**. This is due to the relation:

$$\frac{\Delta t}{t} = (1 + M_p/E_p) \frac{\Delta p}{p} \approx 2 \frac{\Delta p}{p} \text{ at small } t \quad (\text{V.12})$$

which is observed in the two figures.

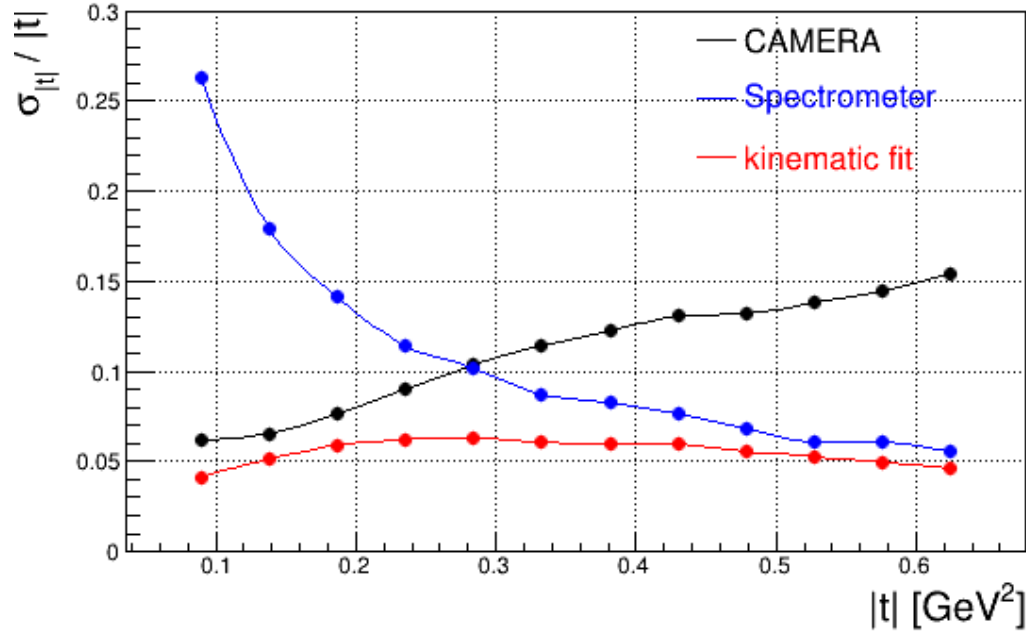


**Figure V.9:**  $|t|$ -resolution evaluated for an exclusive single photon Monte Carlo simulation using the information from either CAMERA **Eq. (V.10)** only, the spectrometer **Eq. (V.11)** only, or the resulting value of the kinematic fit as a function the generated  $|t|$ -value.

### Efficiency and purity of the kinematic fit

After the application of the above described exclusivity selection criteria, the kinematic fit minimisation procedure is performed. In addition of improving the measured kinematics of the event, the kinematic fitting procedure provides a score, or  $\chi^2$  as defined in [Eq. \(IV.1\)](#), illustrating how close the measurements are matching to an exclusive single photon topology. As the number of degree of freedom is 7, the reduced  $\chi^2$  is defined as  $\chi_{\text{red}}^2 = \chi^2/7$ . A cut on the reduced  $\chi^2$  is applied:  $\chi_{\text{red}}^2 < 10$ .

This cut consists in an elegant multidimensional way of selecting exclusive single photon events out of the data, by selecting them within a sphere in dimension 7. Instead of applying a raw cut, further studies can be made in order to associate to each event a probability of being an exclusive single photon event, by studying the shape of the  $\chi^2$  distribution in 7 dimensions, or in lower dimensions using dimensionality reduction tools such as non-linear PCA<sup>2</sup>, or even Manifold Learning. These studies have not been conducted in this thesis. In addition the kinematic fit is of course sensitive to the input parameters (measurements and resolutions), and the next paragraphs will show slight differences between the data and Monte Carlo behaviour under the fitting procedure, due to miscalibrations or underestimated resolutions. These discrepancies are also visible in the previous pull distributions, and are the main reason of having a wide reduced  $\chi^2$  cut of  $\chi_{\text{red}}^2 < 10$ , which is not mathematically based on the  $\chi^2$  tables with 7 degrees of freedom.

The quality of the fitting procedure considered here consists in two steps:

- the convergence of the fit has to be reached
- the final score has to fulfill  $\chi_{\text{red}}^2 < 10$

At the first step only less than 1% of events in the exclusive single photon sample are lost, both in data and in MC. The impact of the second step has to be evaluated. [Fig. \(V.10\)](#) shows that the Monte Carlo simulation does not behave exactly as the real data under the kinematic fitting procedure, which ends up with different  $\chi_{\text{red}}^2$  distribution. Therefore a tight cut on the  $\chi_{\text{red}}^2$  distribution will not affect Monte Carlo and data in the same way and may bias the acceptance calculation and cross-section extraction. This is why it has been chosen to perform a weak selection on the reduced  $\chi_{\text{red}}^2$  distribution in order to remove events too far from the exclusive single photon event topology without dramatically affecting the statistics. Note also that the effect of the cut  $\chi_{\text{red}}^2 < 10$  is part of the systematic studies. This selection is quantified in [Table \(V.4\)](#) for different kinematic regions for the data, the Bethe-Heitler Monte Carlo and the invisible  $\pi^0$  contamination evaluated by MCs as it will be explained in [Section V.6](#).

---

<sup>2</sup>Principal Component Analysis

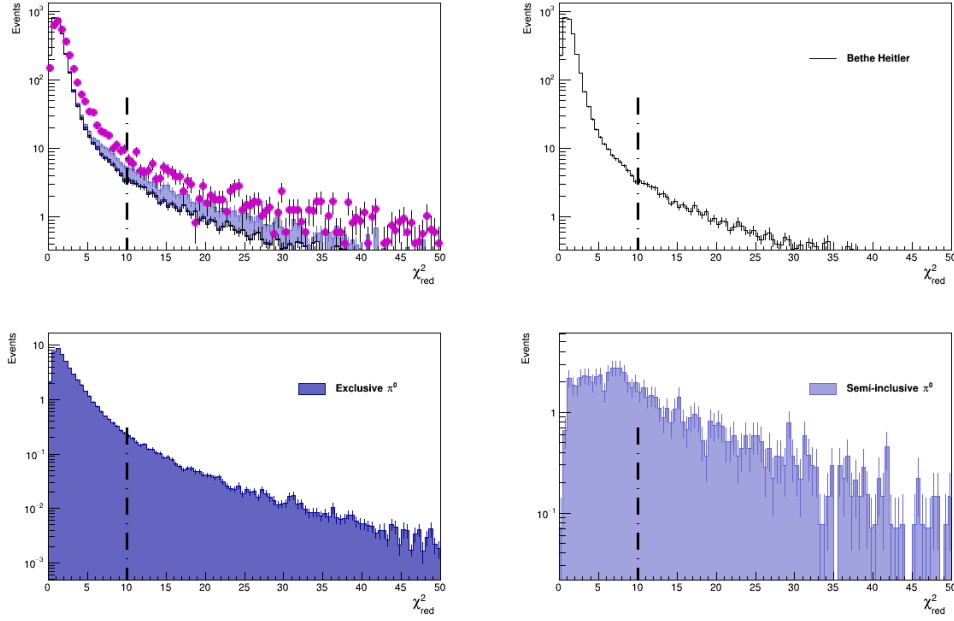


**Figure V.10:**  $\chi_{\text{red}}^2$  distributions for data (in purple) and samples generated by HEPGEN Bethe-Heitler (upper part) and by HEPGEN- $\pi^0$  (bottom left) and by LEPTO (bottom right).

phase space	type	no $\chi_{\text{red}}^2$ cut	$\chi_{\text{red}}^2 < 10$	removal ratio (%)
$80 < \nu < 144$	data	9874	9424	4.6
	BH	9722.3	9558	1.7
	$\pi^0$	1.9	1.5	21
$32 < \nu < 80$	data	3673	3414	7
	BH	3389.6	3315.7	2.2
	$\pi^0$	17.0	14.3	16
$10 < \nu < 32$	data	1841	1689	8.3
	BH	648.2	634.2	2.2
	$\pi^0$	207.1	170.6	17.6
	semi incl. $\pi^0$	89.1	77.1	13.5
	excl. $\pi^0$	118.1	93.5	21

**Table V.4:** Effect of a reduced  $\chi^2$  cut  $\chi_{\text{red}}^2 < 10$ . The cut also includes a convergence criteria for the kinematic fit which presents a loss of event of less than 1% for all samples (the minimisation procedure must have found an extrema satisfying the constraints under an arbitrary small value and less than 100 iterations).

We can see:

- The  $\chi_{\text{red}}^2$  cut affects the BH sample in the same way in the 3  $\nu$  domains. This is expected as the exclusive single photon event topology is generated for this Monte Carlo. The loss of events is about 2%.
- The invisible  $\pi^0$  contribution, present in the small  $\nu$  domain, is the most strongly suppressed. This means that the kinematic fitting procedure is almost able to separate the exclusive single photon event topology from the remaining  $\pi^0$  background, with a weak efficiency of approximately 20%. This effect is illustrated by the larger  $\chi_{\text{red}}^2$  distribution from the invisible  $\pi^0$  contribution shown in **Fig. (V.10)** with respect to the one from the Bethe-Heitler.
- The data sample is reduced from 5% in the high  $\nu$  domain to 8% in the low  $\nu$  domain. We can understand this increase as at small  $\nu$ , the data include also more  $\pi^0$  background. At high  $\nu$  the BH contribution reproduces well the data, however the  $\chi_{\text{red}}^2$  distributions are not the same. So this difference of 3% between the reduction of data and of the BH sample has to be considered in the systematic uncertainty.

After the kinematic fit, we require a kinematical cut on  $|t|$  to be:

$$0.08 < |t| < 0.64 (\text{GeV}/c)^2$$

The justification of this cut is twofold:

- $0.08 (\text{GeV}/c)^2 < |t|$  is comfortably above the natural cut for protons to reach the outer ring of CAMERA ( $|t| \approx 0.07 (\text{GeV}/c)^2$ )
- $|t| < 0.64 (\text{GeV}/c)^2$  is a reasonable value to get a good identification between proton and pion in CAMERA and to prevent the real photon from reaching the incident muon track (domain where the BH contribution increased considerably - domain called "the ears of cat")

Note that the invisible  $\pi^0$  contributions in the 3<sup>rd</sup> and 4<sup>th</sup> columns of **Table (V.4)** are shown according different visible  $\pi^0$  yield normalisation before and after the fit. To better compare the effect of a kinematic fit on the invisible  $\pi^0$  contamination, the following table **Table (V.5)** contains their absolute numbers before and after the fit. It shows that the semi-inclusive  $\pi^0$  background is removed with an efficiency of 47%. This is justified by the wider shape of the  $\chi^2$  distribution for this sample which less suits the exclusive single photon assumption. On the other hand, the exclusive  $\pi^0$  background is much less suppressed as the high energy photon from the exclusive  $\pi^0$  decay has a kinematics extremely close to that of the DVCS photon.

phase space	type	no $\chi_{\text{red}}^2$ cut	$\chi_{\text{red}}^2 < 10$	removal ratio (%)
	semi incl. $\pi^0$	409	217	47
	excl. $\pi^0$	8760.6	8504.0	3

**Table V.5:** Effect of a reduced  $\chi^2$  cut  $\chi_{\text{red}}^2 < 10$  for invisible semi-inclusive and exclusive  $\pi^0$  production given in absolute number of events (and not renormalized to the visible  $\pi^0$  production).

## 4 Strategy of the DVCS analysis with a 160 GeV muon beam

As it was foreseen in the COMPASS II proposal and observed in the results of the 2012 pilot run [42], the COMPASS experiment using a 160 GeV muon beam allows to study the exclusive single photon muo-production in three bins of the virtual photon energy  $\nu$ :

- **at large  $\nu$**   $80 \text{ GeV} < \nu < 144 \text{ GeV}$  (small  $x_B$ ), the Bethe-Heitler contribution only should be necessary to reproduce the exclusive single photon production. The Bethe-Heitler contribution is well-known and allows us to compare the quality of the agreement between the data and the Bethe-Heitler Monte Carlo prediction, which takes into account the proper description of the spectrometer, the ECALS, and the recoil proton detector CAMERA.
- **at intermediate  $\nu$**   $32 \text{ GeV} < \nu < 80 \text{ GeV}$ , the Bethe-Heitler and DVCS should interfere significantly and will be an interesting domain to study all the Fourier coefficients of the sum and the difference of the  $\mu^+$  and  $\mu^-$  cross sections:  $c_i^{\text{DVCS}}$ ,  $s_i^{\text{DVCS}}$ ,  $c_i^{\text{I}}$ ,  $s_i^{\text{I}}$ , related to the CFFs and presented in **Eqs. (I.50)** and **(I.57)**.
- **at small  $\nu$**   $10 \text{ GeV} < \nu < 32 \text{ GeV}$  (large  $x_B$ ), the Bethe-Heitler contributions should be small enough to be subtracted, and we can study the Fourier coefficients. If we take advantage of integrating over the azimuthal angle  $\phi_{\gamma^*\gamma}$ , we are left with only the coefficient  $c_0^{\text{DVCS}}$  related to the imaginary part of the CFF  $\mathcal{H}$ . Before reaching this result, the photon contamination coming from the  $\pi^0$  decay has to be estimated and removed.

## 5 Comparison of the data with the Bethe-Heitler prediction at large $\nu$

In this section the following kinematic conditions are applied:

$$80 < \nu < 144 \text{ GeV}; \quad 1 < Q^2 < 10 \text{ (GeV}/c)^2; \quad 0.08 < |t| < 0.64 \text{ (GeV}/c)^2 \quad (\text{V.13})$$

The Bethe-Heitler is expected to dominate in the domain of large  $\nu$  (or small  $x_B$ ). The Bethe-Heitler contribution is exactly calculable in a Monte Carlo simulation and a good agreement between the data and the Bethe-Heitler in this domain will allow us to be confident in the description of the setup, also for the other domains. This consolidates our method and open the road for a reliable extraction of the DVCS cross section at small  $\nu$ . Note in this part that the Bethe-Heitler Monte Carlo and the data yields are both scaled to a flux of  $10^{12}$  muons per beam charge. The comparison has been performed for the sum of  $\mu^+$  and  $\mu^-$  yields. In addition, except for the exclusivity variables, all the quantities are displayed after the kinematic fitting procedure.

### 5.1 Quality of the Monte Carlo description

The quality of the MC description using the HEPGEN++ Bethe-Heitler generator and TGEANT can be scrutinized on the different figures **Figs. (V.11)** to **(V.16)** presenting the distributions for the exclusivity variables, for the vertex, for the LT,MT,OT Triggers, for the incident and outgoing muon, for photon and proton respectively. This comparison allows us to be confident in the description of the setup also in the other  $\nu$  domains.

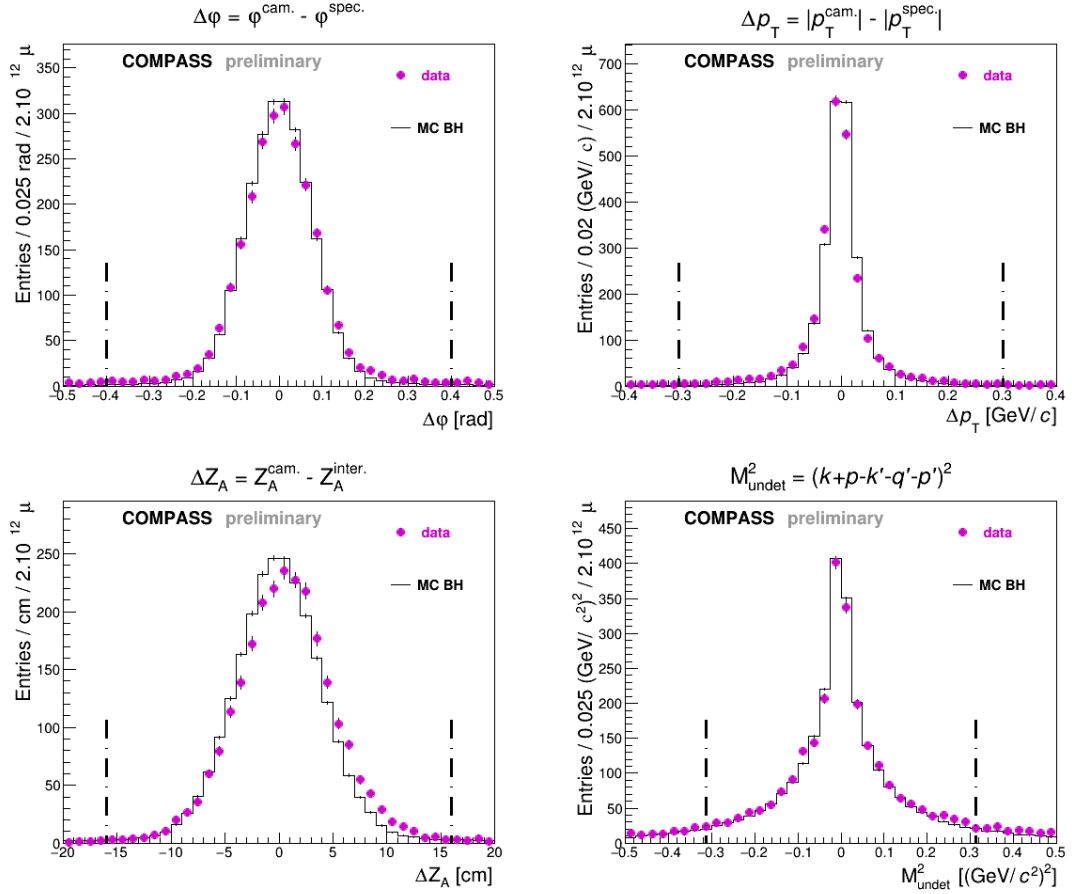


**Figure V.11:** Exclusivity variable distributions for exclusive single photon production at  $80 < \nu < 144 \text{ GeV}$ ,  $1 < Q^2 < 10 \text{ (GeV/c)}^2$ ,  $0.08 < |t| < 0.64 \text{ (GeV/c)}^2$  for the total  $\mu^+$  and  $\mu^-$  beams contribution for all the periods and comparison to the BH MC evaluated for the same muon flux. Each sample for  $\mu^+$  or  $\mu^-$  is normalized to a muon flux of  $10^{12}$ .

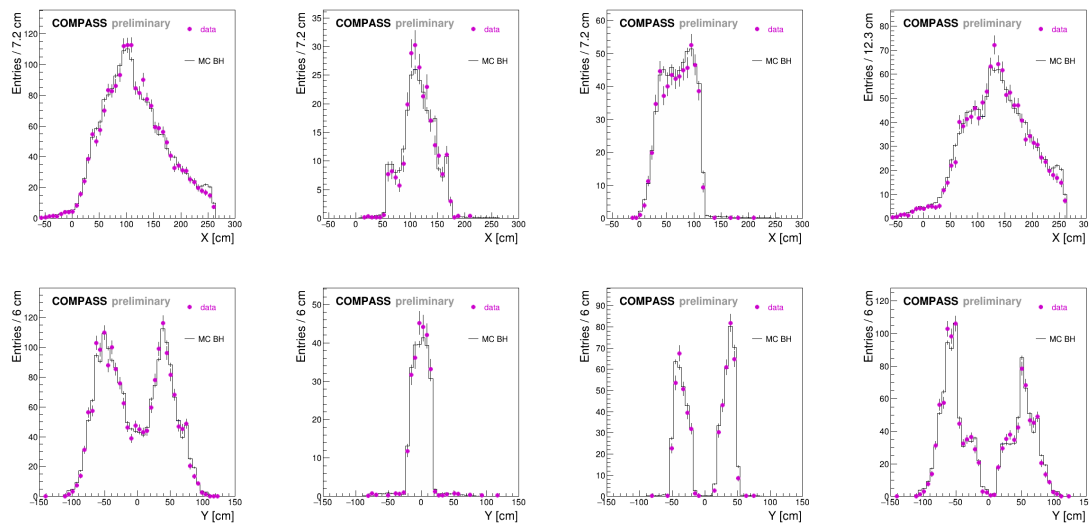


**Figure V.12:**  $X$  and  $Y$  scattered muon track positions extrapolated at  $Z=40\text{m}$  for all Triggers (on left), Ladder Trigger (LT) (on centre-left), Middle Trigger (MT) (on centre-right), Outer Trigger (OT) (on right) for the total  $\mu^+ + \mu^-$  data sample compared to the BH MC evaluated for the same muon flux at  $80 < \nu < 144 \text{ GeV}$ ,  $1 < Q^2 < 10 \text{ (GeV}/c)^2$ ,  $0.08 < |t| < 0.64 \text{ (GeV}/c)^2$ . Each sample for  $\mu^+$  or  $\mu^-$  is normalized to a muon flux of  $10^{12}$ .

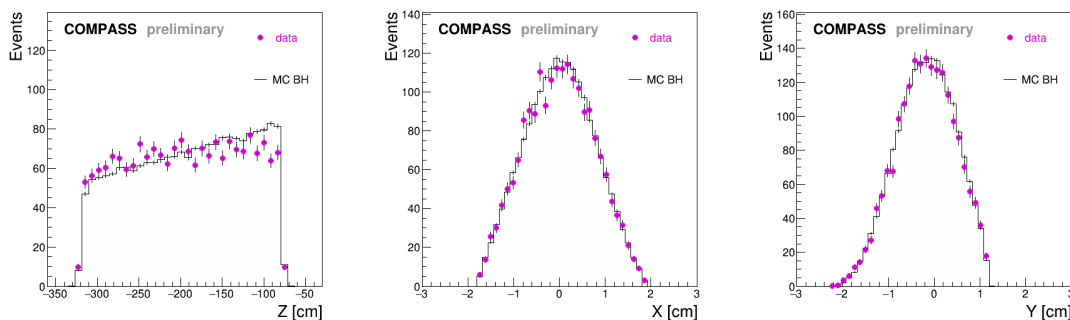


**Figure V.13:** Vertex distributions for the total  $\mu^+ + \mu^-$  data sample at  $80 < \nu < 144 \text{ GeV}$ ,  $1 < Q^2 < 10 \text{ (GeV}/c)^2$ ,  $0.08 < |t| < 0.64 \text{ (GeV}/c)^2$  for all the periods and comparison to the BH MC evaluated for the same muon flux. Each sample for  $\mu^+$  or  $\mu^-$  is normalized to a muon flux of  $10^{12}$ .

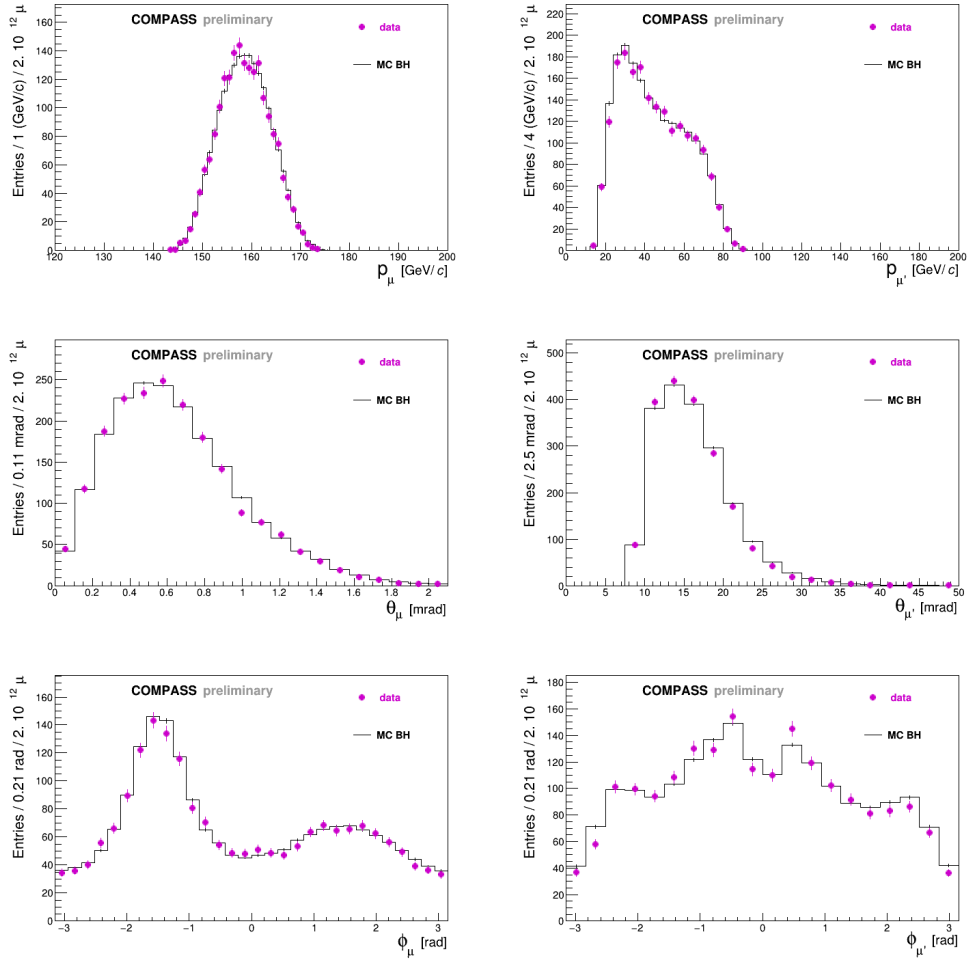


**Figure V.14:**  $P_\mu$ ,  $\theta_\mu$ ,  $\phi_\mu$  (on left) and  $P_{\mu'}$ ,  $\theta_{\mu'}$ ,  $\phi_{\mu'}$  (on right) for the muon beam and the scattered muon respectively for the total  $\mu^+ + \mu^-$  data sample and comparison to the BH MC prediction evaluated for the same muon flux at  $80 < \nu < 144$  GeV,  $1 < Q^2 < 10$  (GeV/c)<sup>2</sup>,  $0.08 < |t| < 0.64$  (GeV/c)<sup>2</sup>. Each sample for  $\mu^+$  or  $\mu^-$  is normalized to a muon flux of  $10^{12}$ .

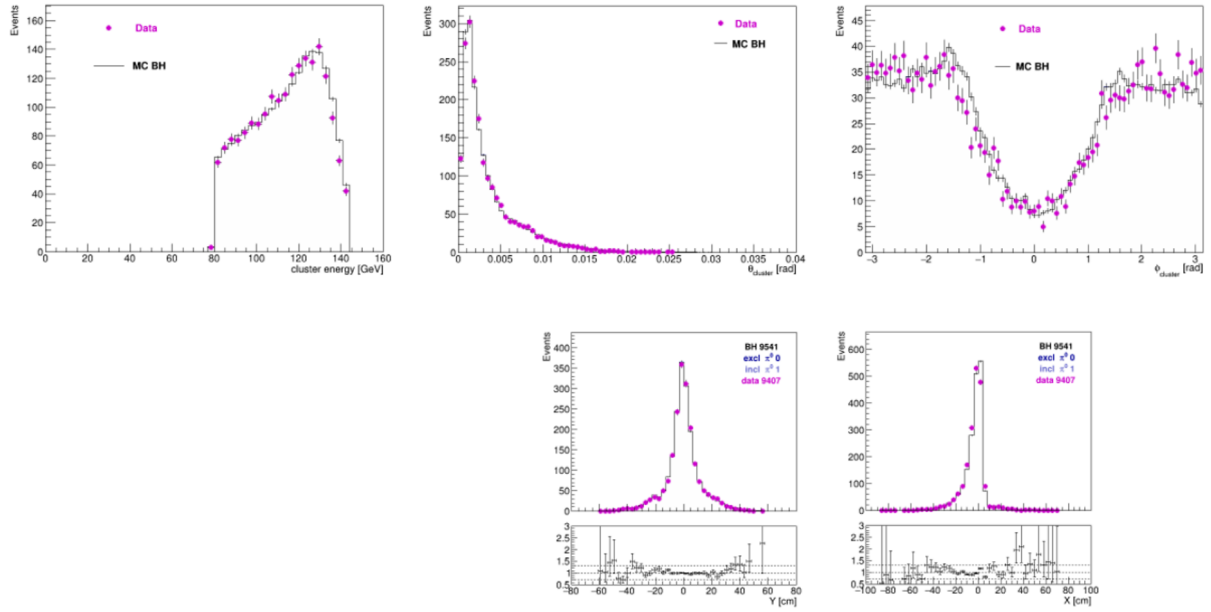


**Figure V.15:**  $E_\gamma$  given the cluster energy,  $\theta_\gamma$ ,  $\phi_\gamma$  (on top),  $X$  and  $Y$  cluster position on ECAL2 (on bottom) for the total  $\mu^+ + \mu^-$  data sample and comparison to the BH MC prediction evaluated for the same muon flux at  $80 < \nu < 144$  GeV,  $1 < Q^2 < 10$  (GeV/c)<sup>2</sup>,  $0.08 < |t| < 0.64$  (GeV/c)<sup>2</sup>. Each sample for  $\mu^+$  or  $\mu^-$  is normalized to a muon flux of  $10^{12}$ .

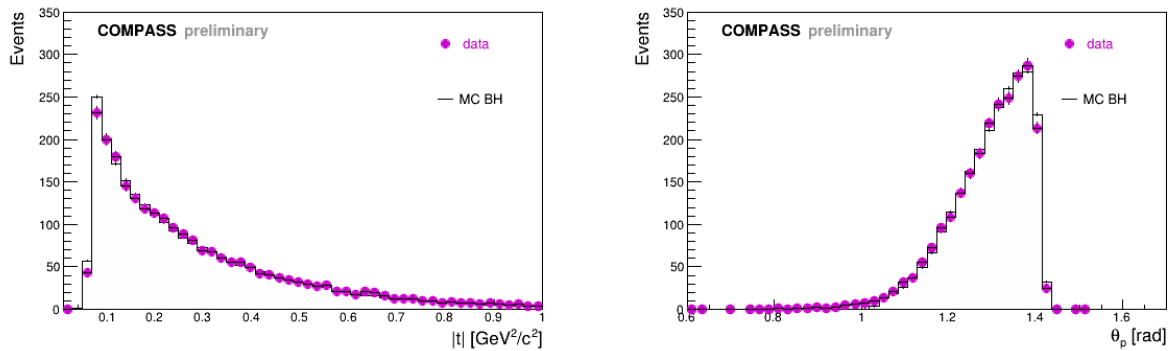


**Figure V.16:** Distribution of  $|t|$  (on left) and proton polar angle (on right) at  $80 < \nu < 144$  GeV,  $1 < Q^2 < 10$  (GeV/c)<sup>2</sup>. Each sample for  $\mu^+$  or  $\mu^-$  is normalized to a muon flux of  $10^{12}$ .

## 5.2 Quality of the agreement between the data and the Monte Carlo Bethe-Heitler prediction

**Fig. (V.17)** summarizes the statistics of events integrated over the  $\phi_{\gamma^*\gamma}$  distribution for each period and beam charge for data and for HEPGEN Bethe-Heitler Monte Carlo estimation in the 3  $\nu$  bins. All the corresponding figures are shown in **Appendix (B)**. The agreement at large  $\nu$  is rather good, of  $98.6 \pm 1\%$ . Considering the extrapolation at small  $\nu$  for the DVCS cross section extraction, the different detectors responses and the kinematic fit efficiency, a systematic error on the Bethe-Heitler yield is estimated to  $\pm 5\%$ .

	80 < nu < 144 GeV				32 < nu < 80 GeV				10 < nu < 32 GeV			
	DATA	BH MC	DATA/BH	stat. err.	DATA	BH MC	DATA/BH	stat. err.	DATA	BH MC	DATA/BH	stat. err.
P04-	691	694	0.996	0.038	248	249	0.996	0.063	117	46	2.543	0.235
P04+	832	904	0.920	0.032	314	323	0.972	0.055	174	61	2.852	0.216
P05-	627	643	0.975	0.039	274	228	1.202	0.073	109	44	2.477	0.237
P05+	704	748	0.941	0.035	270	265	1.019	0.062	122	50	2.440	0.221
P06-	679	659	1.030	0.040	259	215	1.205	0.075	103	40	2.575	0.254
P06+	806	810	0.995	0.035	289	262	1.103	0.065	133	51	2.608	0.226
P07-	880	869	1.013	0.034	272	282	0.965	0.058	132	53	2.491	0.217
P07+	916	976	0.939	0.031	323	326	0.991	0.055	143	61	2.344	0.196
P08-	872	832	1.048	0.035	305	298	1.023	0.059	166	57	2.912	0.226
P08+	946	952	0.994	0.032	366	338	1.083	0.057	210	66	3.182	0.220
P09-	734	716	1.025	0.038	254	254	1.000	0.063	135	49	2.755	0.237
P09+	737	749	0.984	0.036	240	270	0.889	0.057	145	51	2.843	0.236
<b>SUM</b>	<b>9424</b>	<b>9557</b>	<b>0.986</b>	<b>0.010</b>	<b>3414</b>	<b>3315</b>	<b>1.030</b>	<b>0.018</b>	<b>1689</b>	<b>634</b>	<b>2.664</b>	<b>0.065</b>
standard deviation over the 12 periods				0.039				0.095				0.243

**Figure V.17:** Number of events integrated over the  $\phi_{\gamma^*\gamma}$  distribution for the data or for the HEPGEN Bethe-Heitler Monte Carlo estimation for the 3  $\nu$  bins for all the periods and beam charges. Data/BH ratios are indicated with their statistical error. The standard deviation is also indicated in the last line. The yellow row gives the result for the total sample (note that the numbers indicated in the table are rounded, so that the line sum is not exactly the sum of the table values, but the *exact* sum taking into account non-rounded values).

## 6 The $\pi^0$ contamination at small $\nu$

### 6.1 The visible $\pi^0$ background

The  $\pi^0$  contamination in the single-photon events can be categorized into two cases — The *visible*  $\pi^0$  contamination, which has both of the photons from the pion decays detected, and the *invisible* one in which one of the two photons is lost. The visible  $\pi^0$  background can be observed within the selected data sample. The high energy exclusive photon candidate is combined with all the additional detected photons below the DVCS energy thresholds (4 and 5 GeV in ECAL0 and ECAL1), and above the hardware threshold of 300 MeV. The corresponding cluster is still asked to be a neutral cluster in time with the trigger time. The resulting  $M_{\gamma\gamma}$  distribution is displayed in **Fig. (V.18)**, where a clear peak around the  $\pi^0$  mass is observed. Therefore the events featuring a two photon combination close to the  $\pi^0$  mass are rejected. More precisely the exclusive single photon event selection is completed by the requirement:

$$|M_{\gamma\gamma} - M_{\pi^0}| > 20 \text{ MeV} \quad (\text{V.14})$$

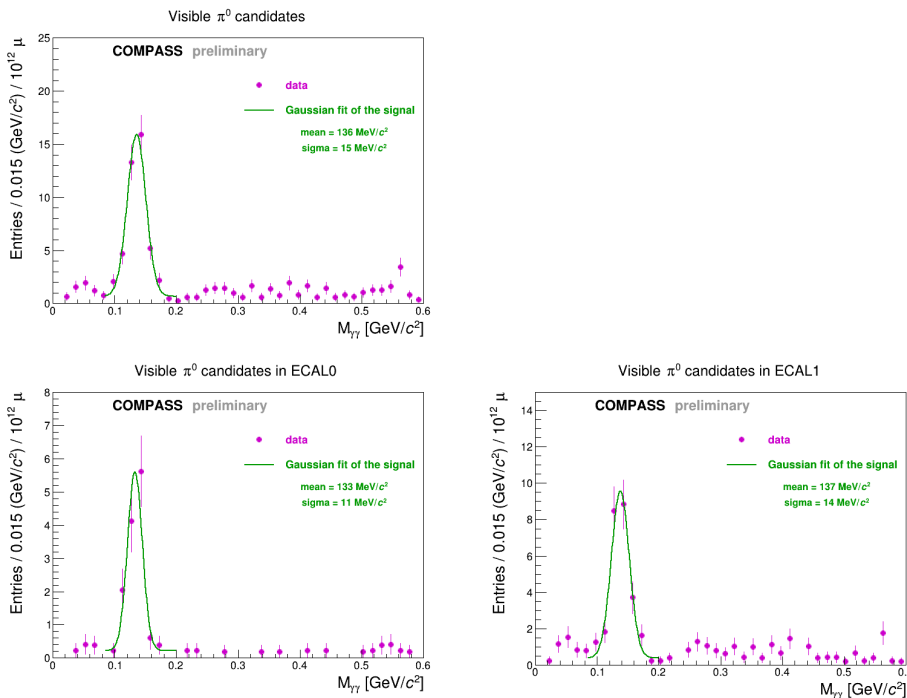


**Figure V.18:** The  $M_{\gamma\gamma}$  distributions of data formed by combining the high energy photon candidates in the selected exclusive single photon sample to the low energy ones in the same event (low energy means energy smaller than the DVCS thresholds of 4 and 5 GeV in ECAL0 and ECAL1, respectively). The plot in the top row gives the  $M_{\gamma\gamma}$  acquired with all the candidates, while the bottom plots show the ones with candidates from ECAL0 or ECAL1 respectively. Clear peaks around the  $\pi^0$  mass can be observed.

### 6.2 The invisible $\pi^0$ contamination

The invisible  $\pi^0$  contamination where one of the two photons escapes from the detection can only be deduced by Monte Carlo techniques. The sources of the invisible  $\pi^0$ s are semi-inclusive or exclusive pion production, and the LEPTO or HEPGEN- $\pi^0$  generated

events are used to reproduce them, respectively. Note that the events with an exclusive  $\pi^0$  production topology are discarded in LEPTO (using the JETSET information). Each MC, LEPTO or HEPGEN-pi0, is normalised such the number of visible  $\pi^0$ s is equal to the number of the visible  $\pi^0$ s in the real data. Thus their contribution to the invisible case can be estimated. The relative contributions from LEPTO and HEPGEN-pi0 has been studied in the determination of  $r_{\text{LEPTO}}$ , which is the fraction of the LEPTO contribution in this simple expression:

$$c_{\text{Data}}^{\pi^0} = r_{\text{LEPTO}} \cdot c_{\text{LEPTO}}^{\pi^0} + (1 - r_{\text{LEPTO}}) \cdot c_{\text{HEPGEN}-\pi^0}^{\pi^0}. \quad (\text{V.15})$$

In the equation above,  $C_{\text{Data}}^{\pi^0}$  is the count of the visible  $\pi^0$  events passing the standard cuts, and  $C_{\text{LEPTO}}^{\pi^0}$  ( $C_{\text{HEPGEN}-\pi^0}^{\pi^0}$ ) is the corresponding one from the LEPTO (HEPGEN- $\pi^0$ ) MC, normalized to  $C_{\text{Data}}^{\pi^0}$ .

### 6.3 Evaluation of the sharing ratio between exclusive and semi-inclusive productions

The extraction of  $r_{\text{LEPTO}}$  is made through fitting that minimizes the  $\chi^2$  between the distributions of the exclusivity variables of the data and the ones of the HEPGEN- $\pi^0$  and LEPTO MC weighted sum. With decent statistics of data, and the observation that the distributions of HEPGEN- $\pi^0$  behaves differently from the ones of LEPTO, a convincing fitting result can be achieved. In the case of 2012 study, supposedly due to limitation in statistics, the fitting was not performed with all cuts applied. Instead, two alternatives were adopted so that more inclusive-process backgrounds were incorporated and thus better determined by fitting:

- Release the corresponding cut on the exclusivity variable being fitted.
- Include events with higher multiplicity.

In the case of 2016 analysis, the CAMERA codes have been modified and a signal-merging feature was implemented for MC events, in order to take into account the finite time resolution of the signals from the scintillator slats of CAMERA. This feature noticeably suppresses the high multiplicity in MC events and makes the multiplicity distribution of MC more similar to the one of data. On the other hand, it has been observed that with this signal-merging treatment, the exclusivity variable distributions of high-multiplicity events from data can not be described well. This observation is consistent to the treatment in 2012 by setting a upper limit on the multiplicity of events included in the fit. Eventually, it has been decided to use the  $r_{\text{LEPTO}}$  extracted with full exclusivity cuts applied, and have it compared with the value extracted with one exclusivity cut released in order to check the consistency.

#### Data & MC used for $r_{\text{LEPTO}}$ extraction

In the analysis so far, the 2016 P07, P08 and P09 datasets of the slot7.1 production are adopted. For the MC, only the P09 slot7.1 productions of HEPGEN  $\pi^0$  and the LEPTO are used. Nevertheless, based on the other studies, the differences between periods in MC is not expected to be significant. More periods of data and the corresponding MC productions will be included in later studies. It should be addressed that in the LEPTO MC, the events with exclusive-like topology, which have one single scattered muon, proton, and  $\pi^0$  in the final state, are removed.

### Extracted $r_{\text{LEPTO}}$ from fitting

The  $r_{\text{LEPTO}}$  extraction is carried out with all the standard exclusive  $\pi^0$  cuts applied, without considering high multiplicity events (background-like) since they have quite limited statistics with the full-exclusivity conditions enforced. The cut of ECAL threshold, which is applied on the higher energy one of a photon pair, is set at the value identical to the standard DVCS event selection. That is, 4 GeV for the ECAL0 clusters, and 5 GeV for ECAL1. The ratio  $r_{\text{LEPTO}}$  is then determined by fitting the distributions of the exclusivity variables  $M_{\text{undet}}^2$ ,  $\Delta p_T$ ,  $\Delta\phi$  and  $\Delta Z$ . The fitting results are shown in **Fig. (V.19)** and the extracted  $r_{\text{LEPTO}}$  is given in **Table (V.6)**. From **Fig. (V.19)** one can observe that the peaking structure around  $\Delta Z = 0$  exists in both the HEPGEN and LETPO  $\Delta Z$  distributions. This similarity in distributions would lead to a less convincing fitting result, which also explains the difference of the fitted  $r_{\text{LEPTO}}$  between  $\Delta Z$  and the other variables. Together with the fact that there is no preference for the fitted result of a specific variable, it is suggested rather than fitting each exclusivity variable individually, to fit all the variables simultaneously, which is illustrated in the bottom row of **Fig. (V.19)**. The fitting results are summarized in **Fig. (V.20)**.

**Table V.6:** Fitting extracted  $r_{\text{LEPTO}}$ , with all exclusivity cuts applied.

	$M_{\text{undet}}^2$	$\Delta p_T$	$\Delta\phi$	$\Delta Z$	Simultaneous
$r_{\text{LEPTO}}$	$38 \pm 4\%$	$26 \pm 3\%$	$50 \pm 4\%$	$69 \pm 13\%$	$38 \pm 2\%$

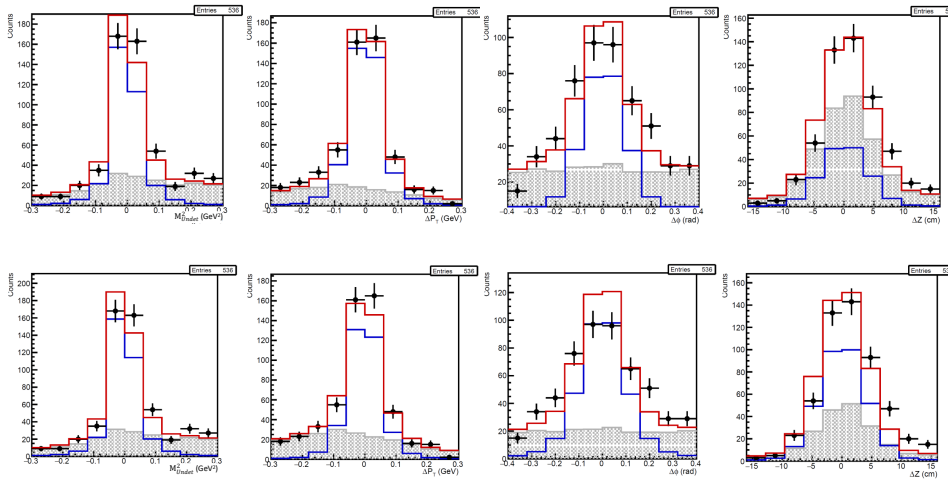


**Figure V.19:** Results of the exclusivity-variable fitting. The top row shows the results of each exclusivity variable fitted individually, while the result of simultaneous fitting of all variables is presented in the bottom row. In each plot, the data is shown as the black dots, the LEPTO is presented as the shaded grey histogram, the HEPGEN- $\pi^0$  as the blue histogram, and the sum of HEPGEN- $\pi^0$  and LEPTO as the red histogram.

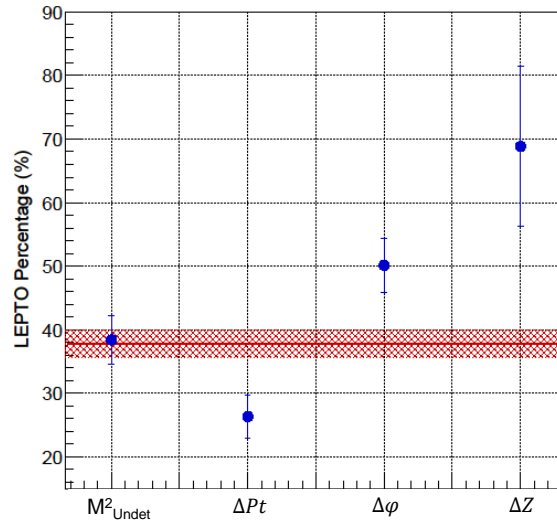


**Figure V.20:** Results of fitted  $r_{\text{LEPTO}}$ . The  $r_{\text{LEPTO}}$  extracted from the individual variable fitting is given as the blue solid dots, and the  $r_{\text{LEPTO}}$  from the simultaneous fitting is shown as the red line.

In addition to fitting the distributions with full exclusivity condition acquired, the same approach was performed for the distributions made with one of the exclusivity conditions released to test the consistency of the result with the presence of more non-exclusive background. The extracted  $r_{\text{LEPTO}}$  by simultaneous fitting of all variables in this case is  $40 \pm 2$  %, which agrees with the full-exclusivity-applied one within error. Based on the observations acquired so far, a safe estimation of  $r_{\text{LEPTO}}$  as  $40 \pm 10$  % is suggested. A demonstration of the visible  $\pi^0$  distributions of data and MCs scaled based on this suggested  $r_{\text{LEPTO}}$  value is shown in [Fig. \(V.21\)](#).

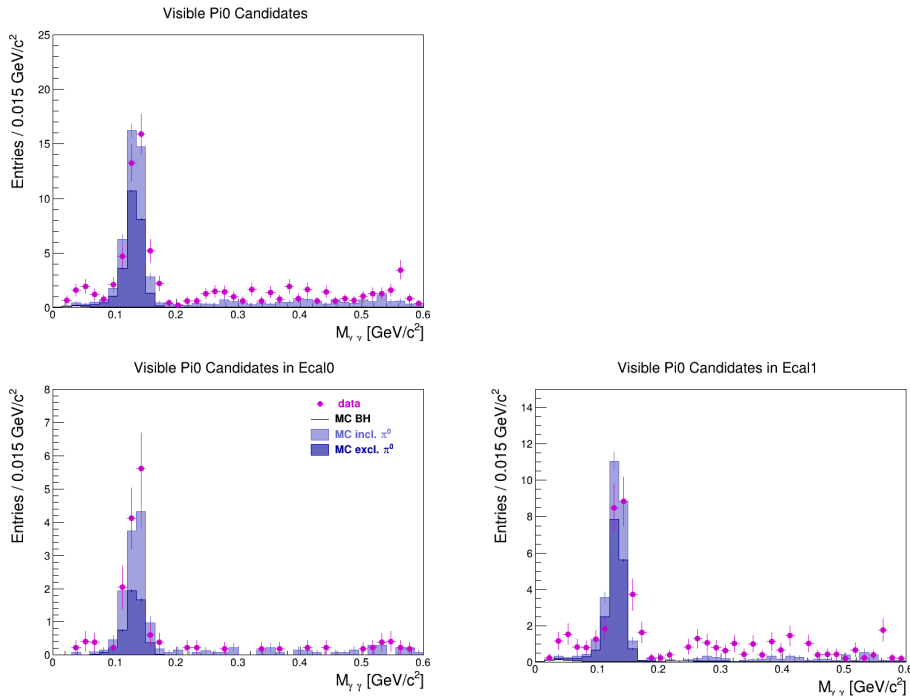


**Figure V.21:** The  $M_{\gamma\gamma}$  distributions of data, BH MC, and the MC of inclusive and exclusive  $\pi^0$ s, formed by combining the high energy photon candidates to the low energy ones in the same event. The data is given as the solid purple circles, BH MC as the black open histograms, and the inclusive or exclusive  $\pi^0$  MC as the light- or dark-blue histograms. The plot in the top row gives the  $M_{\gamma\gamma}$  acquired with all the candidates, while the bottom plots show the ones with candidates from ECAL0 or ECAL1 respectively. Clear peaks around the  $\pi^0$  mass can be observed. The inclusive (exclusive) histograms are scaled by  $r_{\text{LEPTO}}$  ( $1-r_{\text{LEPTO}}$ ), after being normalized to the  $M_{\gamma\gamma}$  of data in the 115 to 155 MeV range. Note that this plot is produced for a total sample of  $\mu^+ + \mu^-$  beams where each sample for  $\mu^+$  or  $\mu^-$  is normalized to a muon flux of  $10^{12}$ .

## 7 The DVCS contribution at small $\nu$

**Figs. (V.22)** and **(V.24)** shows clearly that the BH contribution and the  $\pi^0$  contamination are not able to reproduce the distributions at small  $\nu$ , large  $p_\mu$  and small  $E_\gamma$  with a photon detected in ECAL0 or ECAL1. This difference between the data and the different Monte Carlo contributions indicates the presence of DVCS events in this kinematic domain, which will be further extracted.

**Fig. (V.23)** shows the resulting  $|t|$ -distribution in the small  $\nu$  domain,

$$10 < \nu < 32\text{GeV}. \quad (\text{V.16})$$

The DVCS contribution is clearly visible and will be studied in the next chapter. We can note that the contribution seems rather small at large  $|t|$ .

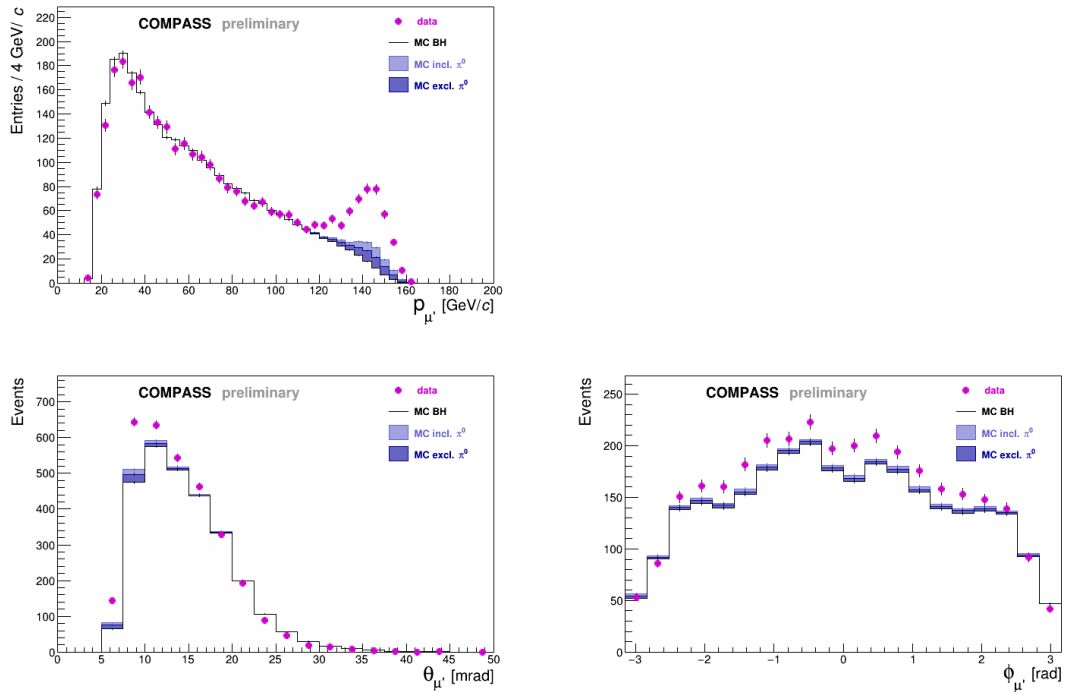


**Figure V.22:** Distributions of the outgoing muon kinematics at  $1 < Q^2 < 10$  (GeV/c) $^2$ ,  $0.05 < y < 0.9$ , for all  $\nu$  and  $0.08 < |t| < 0.64$  (GeV/c) $^2$ . Each sample for  $\mu^+$  or  $\mu^-$  is normalized to a muon flux of  $10^{12}$ .

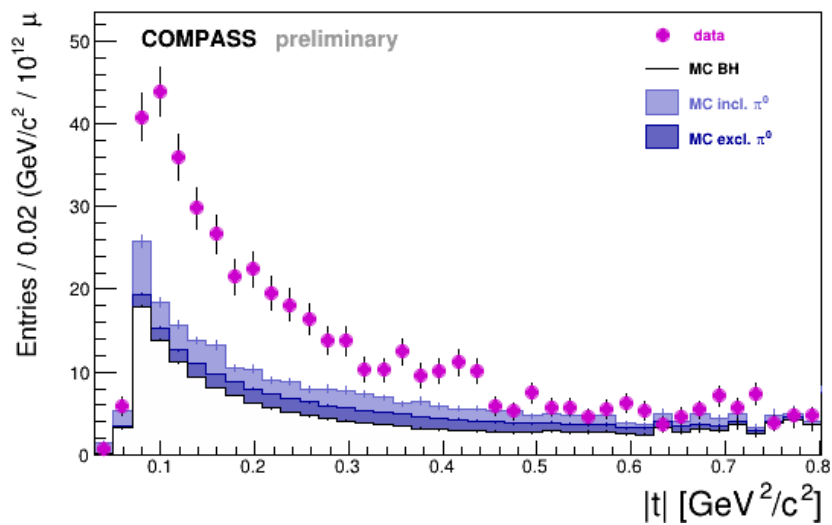


**Figure V.23:** Distribution of  $|t|$  in the small  $\nu$  domain  $10 < \nu < 32$  GeV at  $1 < Q^2 < 10$  (GeV/c) $^2$ ,  $0.05 < y < 0.9$ . Each sample for  $\mu^+$  or  $\mu^-$  is normalized to a muon flux of  $10^{12}$ .

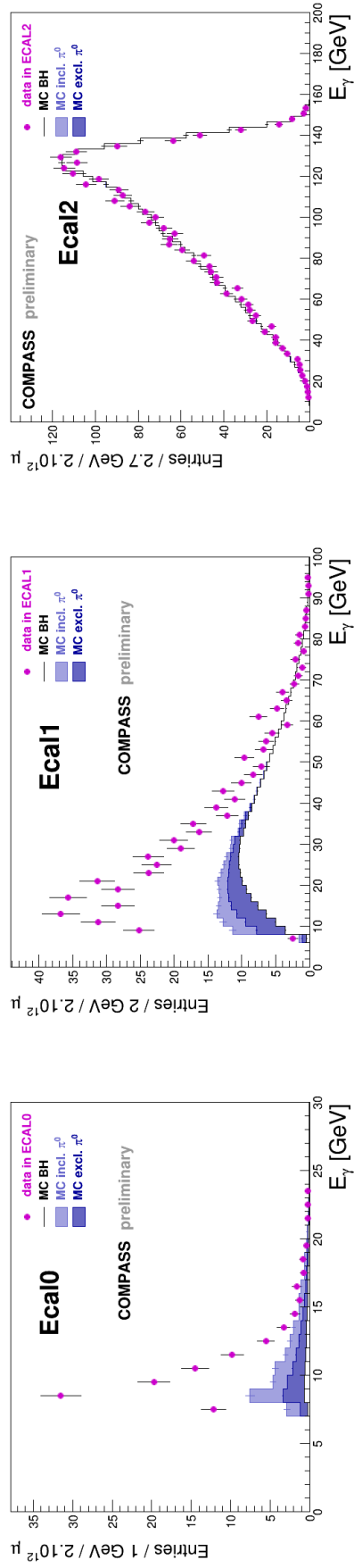


**Figure V.24:** Distributions of  $E_\gamma$  in ECAL0, ECAL1 and ECAL2 at  $1 < Q^2 < 10$  (GeV/c)<sup>2</sup>,  $0.05 < y < 0.9$ , for all  $\nu$  and  $0.08 < |t| < 0.64$  (GeV/c)<sup>2</sup>. Each sample for  $\mu^+$  or  $\mu^-$  is normalized to a muon flux of  $10^{12}$ .

## 8 Summary and $\phi_{\gamma^*\gamma}$ azimuthal distributions

The  $\phi_{\gamma^*\gamma}$  azimuthal distribution of exclusive single photon events are presented for 3 domains of  $\nu$ :

- large  $\nu$  or small  $x_B$  (called domain of BH dominance):

$$80 \text{ GeV} < \nu < 144 \text{ GeV}$$

- intermediate  $\nu$  or  $x_B$  (called domain of BH-DVCS interference):

$$32 \text{ GeV} < \nu < 80 \text{ GeV}$$

- small  $\nu$  or large  $x_B$  (called domain of significant DVCS contribution):

$$10 \text{ GeV} < \nu < 32 \text{ GeV}$$

**Fig. (V.25)** shows the exclusive single photon distributions as a function of  $\phi_{\gamma^*\gamma}$  in the three above-mentioned domains of  $\nu$  for the total periods. Note that the two beam charges contributions are summed. The distributions for each beam charge are normalized to a muon flux of  $10^{12}$ . We can compare directly the distribution of data to the distribution predicted by the Bethe-Heitler Monte Carlo (on top of which the invisible  $\pi^0$  contamination is added and evaluated by Monte Carlo simulation using the LEPTO and HEPGEN- $\pi^0$  generators (for semi-inclusive (resp. exclusive)  $\pi^0$  production). From **Fig. (V.25)** and **Table (V.7)** we can see that

- the  $\pi^0$  contamination is mainly significant in the low  $\nu$  domain
- there is a reasonably good agreement between the data and the BH contribution at large  $\nu$ . This is the basis of our analysis in order to subtract this contribution in the other  $\nu$  domains.

	Type	$80 < \nu < 144$	$32 < \nu < 80$	$10 < \nu < 32$
Absolute number of events	data	9424	3414	1689
	BH	9722.3	3315.7	634.2
	$\pi^0$	1.5	170.6	170.6
Proportion of events (in %)	data	64	24	12
	BH	71	24	5
	$\pi^0$	1	7	92

**Table V.7:** Distribution of events in the three  $\nu$  regions.

The upper plots in **Fig. (V.25)** show the data and the Bethe-Heitler and  $\pi^0$  Monte Carlo contributions. The resulting DVCS contribution from the difference of the data with the Bethe-Heitler and the  $\pi^0$  contributions is presented on the bottom plots. A fit with a constant is represented in red, where one should expect a flat contributions at small  $\nu$  on the right plot. On the left plots the visible modulations hint towards the presence of the interference term between the DVCS and the Bethe-Heitler process. Note that

there is no acceptance correction in these plots, so that the constant line fit is not exactly representative of the  $c_0$  term in the Fourier decomposition of the beam charge cross-section sum. These modulations will be studied further and the next chapter will be focused on the DVCS cross section at small  $\nu$ .

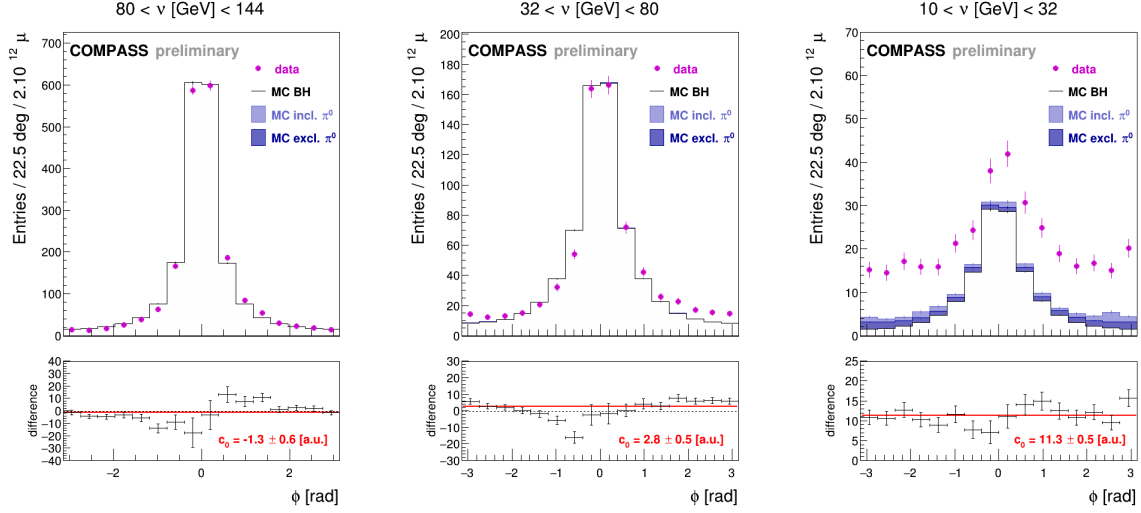


**Figure V.25:** Exclusive single photon distributions as a function of  $\phi^{\gamma^*\gamma}$  in 3 domains of  $\nu$  for the total periods. The distributions for  $\mu^+$  (in red) and  $\mu^-$  (in blue) beams have been normalised to a muon flux of  $10^{12}$ . The solid black line corresponds to the HEPGEN-BH prediction. Note that the visible  $\pi^0$  contribution has been removed. The blue bands correspond to the invisible  $\pi^0$  contamination (thanks to LEPTO (HEPGEN-pi0) MC for semi-inclusive (exclusive)  $\pi^0$  production).

The plots are produced for  $1 < Q^2 < 10$  (GeV/c) $^2$ ,  $0.05 < y < 0.9$  and  $0.08 < |t| < 0.64$  (GeV/c) $^2$ .

# CHAPTER VI

---

## DVCS CROSS SECTION EVALUATION

---

### Contents

---

<b>1</b>	<b>Method of the analysis . . . . .</b>	<b>140</b>
<b>2</b>	<b>Acceptance determination . . . . .</b>	<b>141</b>
<b>3</b>	<b>The DVCS cross section evaluation . . . . .</b>	<b>145</b>
<b>4</b>	<b>Study of the <math> t </math>-dependence of the DVCS cross section . . . . .</b>	<b>147</b>
4.1	Fitting procedure to extract the B slope . . . . .	147
4.2	Systematic studies . . . . .	149
<b>5</b>	<b>Study of the <math>\phi_{\gamma^*\gamma}</math> azimuthal dependence of the DVCS cross section</b>	<b>154</b>
<b>6</b>	<b>Interpretation, comparison to other results and prospects . . . . .</b>	<b>156</b>

---

In the previous chapter we have selected DVCS events in the virtual photon energy range from 10 to 32 GeV ( $x_B \sim 0.06$ ). Now we will determine the corresponding cross section and its  $t$ -dependence which is related to the expansion of partons in the proton probed in the sea-quark domain.

## 1 Method of the analysis

We summarize here some important points of the analysis. The goal is the measurement of the differential cross section for hard exclusive muoproduction of a single photon off an unpolarised proton target  $\mu p \rightarrow \mu' p' \gamma$  using  $\mu^+$  and  $\mu^-$  beams:

$$\frac{d^4\sigma^{\mu p}}{dQ^2 d\nu dt |d\phi_{\gamma^* \gamma}|} = d\sigma \quad (\text{VI.1})$$

where  $Q^2$  is the virtual photon virtuality,  $\nu$  the virtual photon energy in the lab system,  $t$  the total 4-momentum squared transferred between initial and final proton, and  $\phi_{\gamma^* \gamma}$  the azimuthal angle between lepton scattering plane and photon production plane.

First, we demonstrated the good quality and stability of the data for the 6 periods for both  $\mu^+$  and  $\mu^-$  beams. Secondly, we have shown the good agreement between data and Monte Carlo, which incorporates a good description of the spectrometer, the triggers, the three electromagnetic calorimeters and the recoil proton detector CAMERA.

We are considering the sum of the  $\mu^+$  and  $\mu^-$  contributions

$$\mathcal{S}_{CS,U} \equiv d\sigma^{\uparrow} + d\sigma^{\bar{\uparrow}} = 2(d\sigma^{BH} + d\sigma_{unpol}^{DVCS} - |P_\mu| d\sigma^I) \quad (\text{VI.2})$$

where  $P_\mu$  denotes the muon beam polarization. At large  $Q^2$  and small  $t$ , the azimuthal dependences of the DVCS cross section and of the interference term up to NLO and twist-3 read as follows [45]:

$$\begin{aligned} d\sigma^{DVCS} &\propto \frac{1}{y^2 Q^2} (c_0^{DVCS} + c_1^{DVCS} \cos \phi_{\gamma^* \gamma} + c_2^{DVCS} \cos 2\phi_{\gamma^* \gamma}) \\ d\sigma^I &\propto \frac{1}{x_B y^3 t P_1(\phi_{\gamma^* \gamma}) P_2(\phi_{\gamma^* \gamma})} (s_1^I \sin \phi_{\gamma^* \gamma} + s_2^I \sin 2\phi_{\gamma^* \gamma}) \end{aligned} \quad (\text{VI.3})$$

where  $P_1(\phi_{\gamma^* \gamma})$  and  $P_2(\phi_{\gamma^* \gamma})$  are the BH lepton propagators,  $y$  is the fractional energy of the virtual photon, and  $c_i^{DVCS}$  and  $s_i^I$  are related to certain combinations of Compton Form Factors (CFFs). The latter are convolutions of GPDs with functions describing the Compton interaction at the parton level. At leading order in the strong coupling constant  $\alpha_S$  and using the leading-twist approximation, in **Eq. (VI.3)** only the terms containing  $c_0^{DVCS}$  and  $s_1^I$  remain. In terms of Compton helicity amplitudes, this corresponds to the dominance of the amplitude that describes the transition from a *transversely* polarized virtual photon to a transversely polarised real photon.

We have separated our analysis in 3 domains in the virtual photon energy  $\nu$ :

- At large  $\nu$ , the exactly calculable BH contribution was the only ingredient necessary to reproduce the data.
- At small  $\nu$ , we observe a significant DVCS contribution still mixed with a BH contribution (and also a  $\pi^0$  background contribution).

After subtracting the cross section of the BH process,  $d\sigma^{BH}$ , from **Eq. (VI.2)** and integrating the remainder over  $\phi_{\gamma^* \gamma}$ , all azimuthal-dependent terms disappear and only the dominant contribution from transversely polarized virtual photons to the DVCS cross section remains. It is indicated by the subscript T:

$$\frac{d^3\sigma_T^{\mu p}}{dQ^2 d\nu dt} = \int_{-\pi}^{\pi} d\phi_{\gamma^* \gamma} (d\sigma - d\sigma^{BH}) \propto c_0^{DVCS}. \quad (\text{VI.4})$$

This cross section is converted into the cross section for virtual-photon scattering using the flux  $\Gamma(Q^2, \nu, E_\mu)$  for transverse virtual photons,

$$\frac{d\sigma^{\gamma^*p}}{d|t|} = \frac{1}{\Gamma(Q^2, \nu, E_\mu)} \frac{d^3\sigma_T^{\mu p}}{dQ^2 d\nu dt}, \quad (\text{VI.5})$$

with

$$\Gamma(Q^2, \nu, E_\mu) = \frac{\alpha_{\text{em}}(1-x_B)}{2\pi Q^2 y E_\mu} \left[ y^2 \left( 1 - \frac{2m_\mu^2}{Q^2} \right) + \frac{2}{1+Q^2/\nu^2} \left( 1 - y - \frac{Q^2}{4E_\mu^2} \right) \right], \quad (\text{VI.6})$$

for which the Hand convention [110] is used. Here,  $m_\mu$  and  $E_\mu$  denote the mass and energy of the incoming muon, respectively, and  $\alpha_{\text{em}}$  the electromagnetic fine-structure constant.

In Chapter (I) with Eqs. (I.53) to (I.55) it has been shown that the quantity  $c_0^{DVCS}$  is related at small  $x_B$  to the CFFs  $\mathcal{H}$ ,  $\tilde{\mathcal{H}}$  and  $\mathcal{E}$  as:

$$c_0^{DVCS} \propto 4(\mathcal{H}\mathcal{H}^* + \tilde{\mathcal{H}}\tilde{\mathcal{H}}^*) + \frac{t}{M^2}\mathcal{E}\mathcal{E}^*. \quad (\text{VI.7})$$

and in the  $x_B$ -domain of COMPASS,  $c_0^{DVCS}$  is dominated by the square of the imaginary part of the CFF  $\mathcal{H}$ . Thus the slope  $B$  of the  $|t|$ -dependence of the DVCS cross section or of the quantity  $c_0^{DVCS}$  can be converted into the transverse extension of partons in the proton.

## 2 Acceptance determination

In order to calculate cross sections, one need to estimate the geometrical acceptance of the apparatus as well as the inefficiencies of the event reconstruction and selection. They are computed for a fine binning in 4 dimensions

$$d\Omega = d|t|dQ^2 d\nu d\phi_{\gamma^*\gamma} \quad (\text{VI.8})$$

and are defined as the ratio of reconstructed events falling in  $d\Omega$ , called  $N_{\text{rec}}^{d\Omega}$ , to the number of generated events in  $d\Omega$ , called  $N_{\text{gen}}^{d\Omega}$ .

$$a(d\Omega) = \frac{N_{\text{rec}}^{d\Omega}}{N_{\text{gen}}^{d\Omega}} \quad (\text{VI.9})$$

In that sense the acceptance definition also takes into account the bin migration or smearing effects due to the experimental resolution. The Monte Carlo used for this acceptance study is generated by the HEPGEN++ software using the DVCS model. Therefore, the quantities  $N_{\text{gen}}^{d\Omega}$  and  $N_{\text{rec}}^{d\Omega}$  are the sum of weights of the corresponding events. **Fig. (VI.1)** displays the acceptance distribution for an extended phase space in  $Q^2$  and  $\nu$  for the lowest  $|t|$  bin,  $0.08 < |t| < 0.136(\text{GeV}/c)^2$ . In order to use only the bins with non-vanishing acceptances, a first study of the cross section is done in the following phase space:

- $1 (\text{GeV}/c)^2 < Q^2 < 5 (\text{GeV}/c)^2$
- $10 \text{ GeV} < \nu < 32 \text{ GeV}$
- $0.08 (\text{GeV}/c)^2 < |t| < 0.64 (\text{GeV}/c)^2$

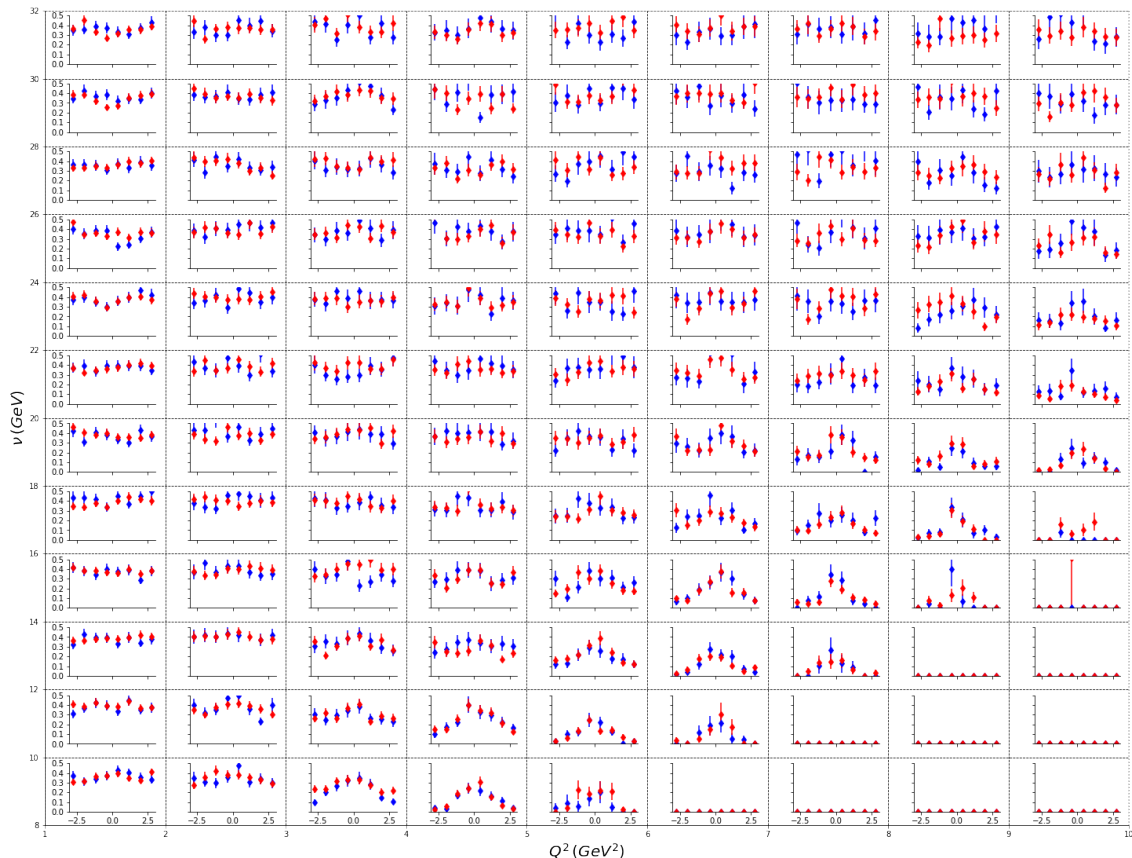


**Figure VI.1:** Acceptance for the DVCS process shown as a function of  $Q^2$ ,  $\nu$  and  $\phi_{\gamma^*\gamma}$  for  $0.08 < |t| < 0.136$  ( $\text{GeV}/c$ ) $^2$ . Each plot in a bin of  $Q^2$  and  $\nu$  shows the acceptance in 8 equidistant bins of  $\phi_{\gamma^*\gamma}$  for  $\mu^+$  (in red) and  $\mu^-$  (in blue) beams.

And to make the best use of the current Monte Carlo statistics, the following binning for the cross section determination and the acceptance computation is

- $|t|[(\text{GeV}/c)^2] : [0.08, 0.136, 0.219, 0.36, 0.64]$
- $Q^2[(\text{GeV}/c)^2] : 4$  bins of width of 1 ( $\text{GeV}/c$ ) $^2$
- $\nu[\text{GeV}] : 4$  bins of width of 5.5 ( $\text{GeV}/c$ ) $^2$
- $\phi_{\gamma^*\gamma}[\text{rad}] : 8$  bins equally spaced

The binning in  $|t|$  is chosen so that the data feature approximately the same statistics in each bin. The acceptances for these bins are presented in **Figs. (VI.2)** and **(VI.3)**.

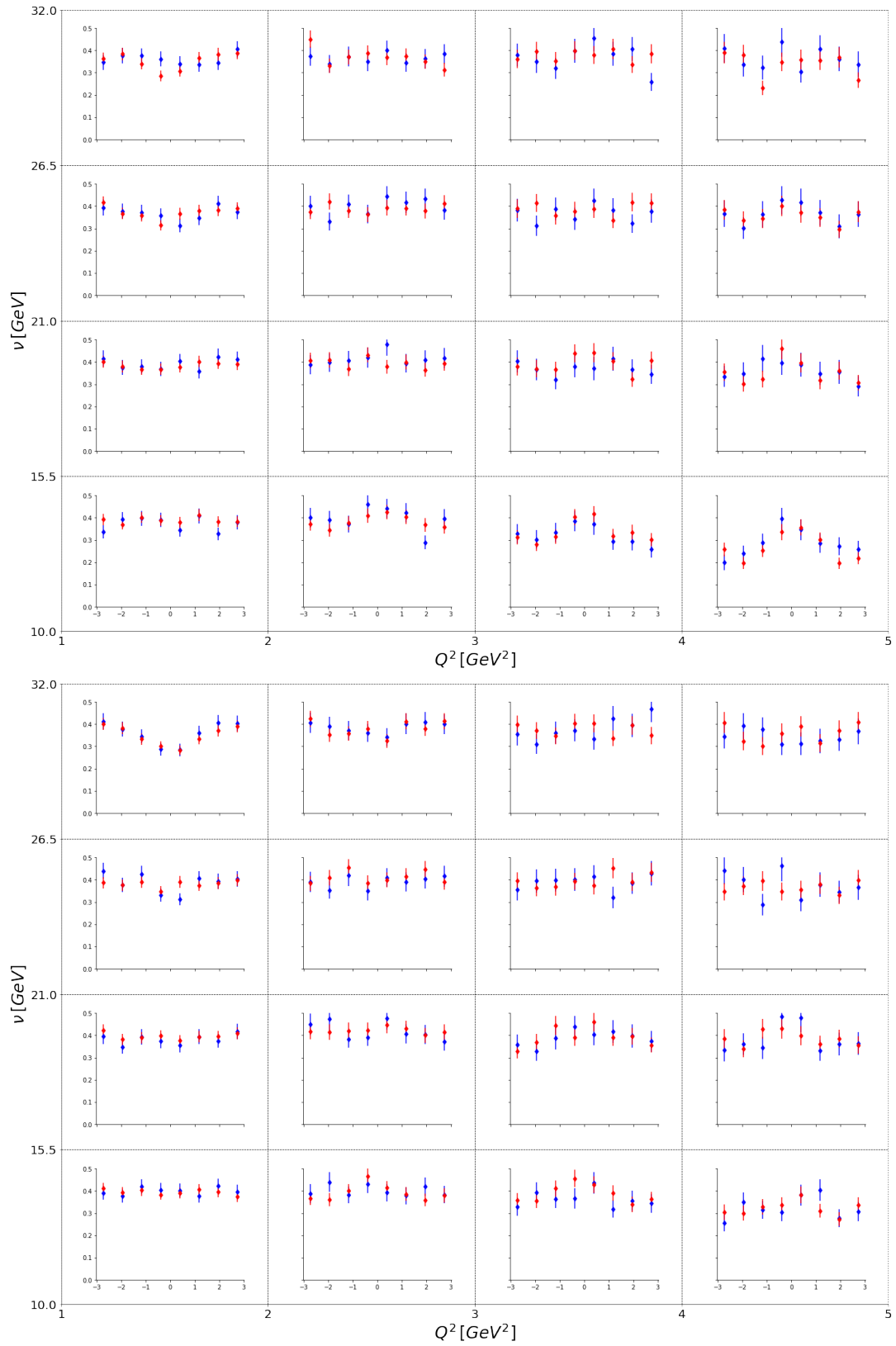


**Figure VI.2:** Acceptance for the DVCS process shown as a function of  $Q^2$ ,  $\nu$  and  $\phi_{\gamma^*\gamma}$  for  $0.08 < |t| < 0.136 (\text{GeV}/c)^2$  (upper plots) and for  $0.136 < |t| < 0.219 (\text{GeV}/c)^2$  (lower plots). Each plot in a bin of  $Q^2$  and  $\nu$  shows the acceptance in 8 equidistant bins of  $\phi_{\gamma^*\gamma}$  for  $\mu^+$  (in red) and  $\mu^-$  (in blue) beams.

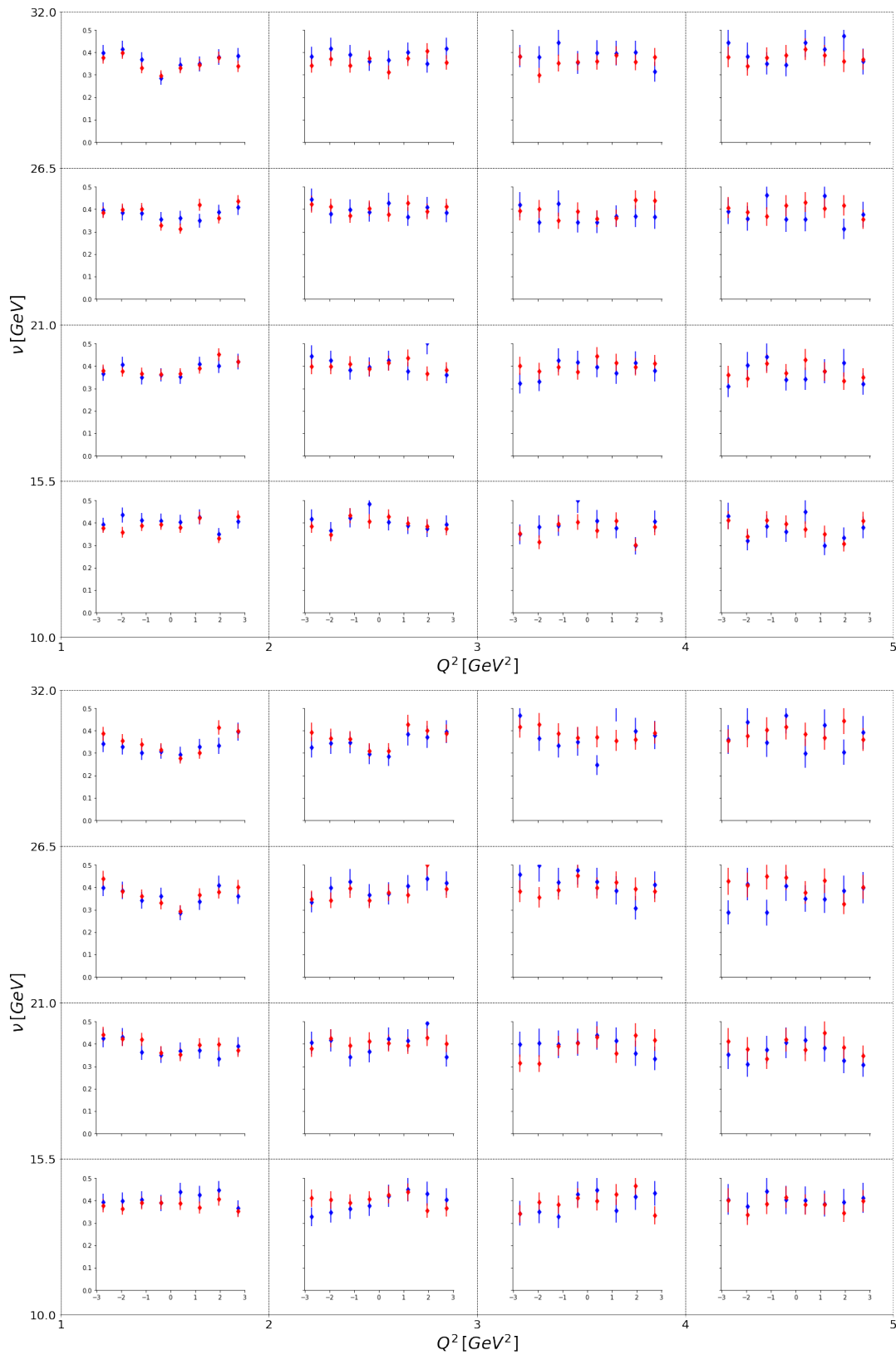


**Figure VI.3:** Acceptance for the DVCS process shown as a function of  $Q^2$ ,  $\nu$  and  $\phi_{\gamma^*\gamma}$  for  $0.219 < |t| < 0.36$  ( $\text{GeV}/c$ )<sup>2</sup> (upper plots) and for  $0.36 < |t| < 0.64$  ( $\text{GeV}/c$ )<sup>2</sup> (lower plots). Each plot in a bin of  $Q^2$  and  $\nu$  shows the acceptance in 8 equidistant bins of  $\phi_{\gamma^*\gamma}$  for  $\mu^+$  (in red) and  $\mu^-$  (in blue) beams.

### 3 The DVCS cross section evaluation

The DVCS cross section can be calculated for each beam charge (noted  $\pm$  in the following) in the bin  $\Delta\Omega_{nijk} = \Delta|t|_n\Delta\phi_i\Delta Q_j^2\Delta\nu_k$  from the data by subtracting the different Monte Carlo backgrounds <sup>1</sup>:

$$\left\langle \frac{d\sigma_{\text{DVCS}}^{\mu p \rightarrow \mu' \gamma p'}}{d\Omega} \right\rangle_{nijk}^{\pm} = \left\langle \frac{d\sigma_{\text{data}}^{\mu p \rightarrow \mu' \gamma p'}}{d\Omega} \right\rangle_{nijk}^{\pm} - \left\langle \frac{d\sigma_{\text{BH}}^{\mu p \rightarrow \mu' \gamma p'}}{d\Omega} \right\rangle_{nijk}^{\pm} - \left\langle \frac{d\sigma_{\pi^0}^{\mu p \rightarrow \mu' \gamma p'}}{d\Omega} \right\rangle_{nijk}^{\pm} \quad (\text{VI.10})$$

In order to retrieve the virtual photon-proton cross section from the measured lepton-proton cross section, we use the virtual photon flux  $\Gamma(Q^2, \nu)$  and it reads as follow:

$$\left\langle \frac{d\sigma_{\text{DVCS}}^{\gamma^* p \rightarrow \gamma p'}}{d|t|d\phi} \right\rangle_{nijk}^{\pm} = \left\langle \frac{1}{\Gamma(Q^2, \nu)} \frac{d\sigma_{\text{DVCS}}^{\mu p \rightarrow \mu' \gamma p'}}{d|t|d\phi dQ^2 d\nu} \right\rangle_{nijk}^{\pm} \quad (\text{VI.11})$$

$$\Gamma(Q^2, \nu) = \frac{\alpha_{\text{em}}(1-x_B)}{2\pi Q^2 y E_\mu} \left[ y^2 \left( 1 - \frac{2m_\mu^2}{Q^2} \right) + \frac{2}{1+Q^2/\nu^2} \left( 1 - y - \frac{Q^2}{4E_\mu^2} \right) \right] \quad (\text{VI.12})$$

By using the relation **Eq. (VI.11)** into **Eq. (VI.10)**, one obtains:

$$\begin{aligned} \left\langle \frac{d\sigma_{\text{DVCS}}^{\gamma^* p \rightarrow \gamma p'}}{d|t|d\phi dQ^2 d\nu} \right\rangle_{nijk}^{\pm} &= \left\langle \frac{1}{\Gamma(Q^2, \nu)} \frac{d\sigma_{\text{data}}^{\mu p \rightarrow \mu' \gamma p'}}{d|t|d\phi dQ^2 d\nu} \right\rangle_{nijk}^{\pm} \\ &- \left\langle \frac{1}{\Gamma(Q^2, \nu)} \frac{d\sigma_{\text{BH}}^{\mu p \rightarrow \mu' \gamma p'}}{d|t|d\phi dQ^2 d\nu} \right\rangle_{nijk}^{\pm} \\ &- \left\langle \frac{1}{\Gamma(Q^2, \nu)} \frac{d\sigma_{\pi^0}^{\mu p \rightarrow \mu' \gamma p'}}{d|t|d\phi dQ^2 d\nu} \right\rangle_{nijk}^{\pm} \end{aligned} \quad (\text{VI.13})$$

This equation can be transformed by considering the yield of each contribution and taking into account the acceptance correction. The photon flux enters the relation as a kinematic prefactor applied event by event. The proof of this transformation is done in the discrete case in [80] and results as:

$$\begin{aligned} \left\langle \frac{d\sigma_{\text{DVCS}}^{\gamma^* p \rightarrow \gamma p'}}{d|t|d\phi} \right\rangle_{nijk}^{\pm} &= \frac{1}{\mathcal{L}^\pm \Delta t_n \Delta \phi_i \Delta Q_j^2 \Delta \nu_k} \sum_{p \in \mathcal{P}} \left( a_{nijk}^{p, \pm} \right)^{-1} \left( \sum_{e=1}^{N_{nijk}^{p, \text{data}} \pm} \frac{1}{\Gamma(Q_e^2, \nu_e)} \right. \\ &\left. - c_{\text{BH}}^{p, \pm} \sum_{e=1}^{N_{nijk}^{p, \text{BH}} \pm} \frac{(w_{\text{BH}})_e}{\Gamma(Q_e^2, \nu_e)} - c_{\pi^0}^{p, \pm} \sum_{e=1}^{N_{nijk}^{p, \pi^0} \pm} \frac{(w_{\pi^0})_e}{\Gamma(Q_e^2, \nu_e)} \right) \end{aligned} \quad (\text{VI.14})$$

<sup>1</sup>to simplify the notation  $\phi = \phi_{\gamma^* \gamma}$

where the set  $\mathcal{P}$  indicates the different periods and with abbreviations <sup>2</sup>:

$$\begin{aligned}
\mathcal{L}^\pm &= \sum_{p \in \mathcal{P}} \mathcal{L}^{p\pm} \\
c_{\text{BH}}^{p\pm} &= \frac{\mathcal{L}^{p\pm}}{\mathcal{L}_{\text{BH}}^{p\pm}} \\
c_{\pi^0}^{p\pm} \sum_{e=1}^{N_{ijn}^{p,\pi^0 \pm}} \frac{(w_{\pi^0})_e}{\Gamma(Q_e^2, \nu_e)} &= c_{\pi^0}^{pH\pm} (1 - r_L) \sum_{e=1}^{N_{ijn}^{p,\pi^0 \pm}} \frac{(w_{\pi^0})_e}{\Gamma(Q_e^2, \nu_e)} + c_{\pi^0}^{pL\pm} (r_L) \sum_{e=1}^{N_{ijn}^{p,\pi^0 \pm}} \frac{1}{\Gamma(Q_e^2, \nu_e)} \\
c_{\pi^0}^{pH\pm} &= \frac{N_{\text{vis. } \pi^0}^{p,\text{data}\pm}}{N_{\text{vis. } \pi^0}^{p,\text{H}\pm}} \\
c_{\pi^0}^{pL\pm} &= \frac{N_{\text{vis. } \pi^0}^{p,\text{data}\pm}}{N_{\text{vis. } \pi^0}^{p,\text{L}\pm}}
\end{aligned} \tag{VI.15}$$

The mean cross section in each bin of  $(|t|, \phi)$  is constructed as follow:

$$\left\langle \frac{d\sigma_{\text{DVCS}}^{\gamma^* p \rightarrow \gamma p'}}{d|t|d\phi} \right\rangle_{ni}^\pm = \frac{\sum_{j,k} \left\langle \frac{d\sigma_{\text{DVCS}}^{\gamma^* p \rightarrow \gamma p'}}{d|t|d\phi} \right\rangle_{nij k}^\pm \Delta Q_j^2 \Delta \nu_k}{\sum_{j,k} \Delta Q_j^2 \Delta \nu_k} \tag{VI.16}$$

The DVCS cross section can be integrated over  $\phi$  in order to study its  $|t|$ -dependence:

$$\left\langle \frac{d\sigma_{\text{DVCS}}^{\gamma^* p \rightarrow \gamma p'}}{d|t|} \right\rangle_n^\pm = \sum_i \Delta \phi_i \left\langle \frac{d\sigma_{\text{DVCS}}^{\gamma^* p \rightarrow \gamma p'}}{d|t|d\phi} \right\rangle_{ni}^\pm \tag{VI.17}$$

The contributions of both muon beam charges are summed:

$$\left\langle \frac{d\sigma_{\text{DVCS}}^{\gamma^* p \rightarrow \gamma p'}}{d|t|} \right\rangle_n^\pm = \frac{1}{2} \left( \left\langle \frac{d\sigma_{\text{DVCS}}^{\gamma^* p \rightarrow \gamma p'}}{d|t|} \right\rangle_n^+ + \left\langle \frac{d\sigma_{\text{DVCS}}^{\gamma^* p \rightarrow \gamma p'}}{d|t|} \right\rangle_n^- \right) \tag{VI.18}$$

<sup>2</sup>BH=Bethe-Heitler, H=HEPGEN- $\pi^0$ , L=LEPTO

**Fig. (VI.4)** presents the virtual-photon proton cross-section  $d\sigma_{\text{DVCS}}^{\gamma^* p \rightarrow \gamma p'} / d|t|$  evaluated in 4  $|t|$  bins with statistical errors. The observed  $|t|$ -dependence can be well described by a single-exponential function  $e^{-B|t|}$ . The 4 data points are presented in **Table (VI.1)** and are fitted using a binned maximum-likelihood method described in the next **Section VI.4.1**. The cross section per beam charge is also given in **Table (VI.2)**

**Table VI.1:** Values of  $\langle d\sigma_{\text{DVCS}}^{\gamma^* p \rightarrow \gamma p'} / d|t| \rangle$  [nb (GeV/c) $^{-2}$ ]

$ t $ -bin	[0.08,0.136]	[0.136,0.219]	[0.219,0.36]	[0.36, 0.64]
$d\sigma/d t $	27.9	17.6	8.8	2.4
stat. error	3.1	2.0	1.1	0.5
syst. error $\uparrow$	1.2	0.8	0.5	0.4
syst. error $\downarrow$	1.3	0.8	0.5	0.4

**Table VI.2:** Values of  $\langle d\sigma_{\text{DVCS}}^{\gamma^* p \rightarrow \gamma p'} / d|t| \rangle^{\pm}$  [nb (GeV/c) $^{-2}$ ]

$ t $ -bin	[0.08,0.136]	[0.136,0.219]	[0.219,0.36]	[0.36, 0.64]
$d\sigma^+ / d t $	25.9	17.1	10.4	2.5
stat. error	4.2	2.6	1.6	0.7
$d\sigma^- / d t ^-$	30.2	18.4	7.3	2.4
stat. error	4.6	3.0	1.5	0.8

## 4 Study of the $|t|$ -dependence of the DVCS cross section

### 4.1 Fitting procedure to extract the B slope

The exponential  $|t|$ -dependance of the DVCS cross section is extracted using a binned maximum likelihood technique. The following log-likelihood function is used:

$$\log L(B) = \sum_{n=1}^4 \sigma_n \log l_n(B) \quad (\text{VI.19})$$

where:

$$l_n(B) = \sigma_{\text{tot}} \int_{t_n^{\text{min}}}^{t_n^{\text{max}}} \frac{1}{N} e^{-B|t|} dt \quad (\text{VI.20})$$

$t_n^{\text{min/max}}$  are the bin edges of the  $n^{\text{th}}$  bin in  $|t|$ , and  $\sigma_n$  is the measured cross section in the corresponding bin.

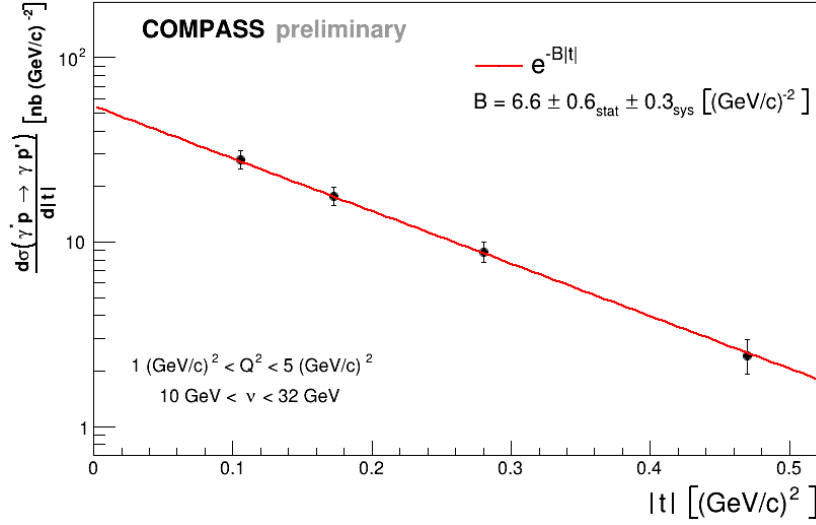


**Figure VI.4:** Virtual-photon proton cross-section  $d\sigma/d|t|$  evaluated in 4  $|t|$  bins. Only the statistical errors are reported. The observed  $|t|$ -dependence can be well described by a single-exponential function  $e^{-B|t|}$ . The 4 data points are fitted using a binned maximum-likelihood method described in [Section VI.4.1](#)

$$\sigma_n = \left\langle \frac{d\sigma_{\text{DVCS}}^{\gamma^* p \rightarrow \gamma p'}}{d|t|} \right\rangle_n \Delta t_n \quad (\text{VI.21})$$

$$\sigma_{\text{tot}} = \sum_{n=1}^4 \sigma_n$$

The normalisation term  $N$  is defined as the integral of the exponential ansatz:

$$N = \int_{0.08 \text{ GeV}^2}^{0.64 \text{ GeV}^2} e^{-B|t|} dt \quad (\text{VI.22})$$

The estimation of the error is based on the assumption of multinomial statistics. Studies have been made to show that in the case of a sum of weights (and not a sum of events, due to the photon flux prefactor event wise), a correction has to be done on the error estimation on the likelihood parameter  $B$  [80, 111]. This has been pragmatically proven by performing toy Monte Carlo tests in [80]. The final corrected variance  $V_B$  on the  $B$  parameter is:

$$V_B = V_{\sum w} \frac{1}{V_{\sum w^2}} V_{\sum w} \quad (\text{VI.23})$$

where  $V_{\sum w}$  is the variance obtained by minimising the previous log-likelihood function and  $V_{\sum w^2}$  is the variance obtained by minimising the log-likelihood under the exchange:

$$\sigma_n \rightarrow \left( \sum w^2 \right)_n$$

The quantity  $\left( \sum w^2 \right)_n$  is calculated as:

$$\left( \sum w^2 \right)_n = \frac{1}{4} \left( \left( \sum w^2 \right)_n^+ + \left( \sum w^2 \right)_n^- \right) \quad (\text{VI.24})$$

$$\begin{aligned}
\left(\sum w^2\right)_{ijn}^\pm &= \frac{1}{(\mathcal{L}^\pm \Delta t_n \Delta Q_i^2 \Delta \nu_j)^2} \sum_{p \in \mathcal{P}} \left(a_{ijn}^{p,\pm}\right)^{-2} \left( \sum_{e=1}^{N_{ijn}^{p,\text{data}\pm}} \frac{1}{\Gamma^2(Q_e^2, \nu_e)} \right. \\
&\quad \left. + \left(c_{\text{BH}}^{p\pm}\right)^2 \sum_{e=1}^{N_{ijn}^{p,\text{BH}\pm}} \frac{(w_{\text{BH}})_e^2}{\Gamma^2(Q_e^2, \nu_e)} + \left(c_{\pi^0}^{p\pm}\right)^2 \sum_{e=1}^{N_{ijn}^{p,\pi^0\pm}} \frac{(w_{\pi^0})_e^2}{\Gamma^2(Q_e^2, \nu_e)} \right) \quad (\text{VI.25})
\end{aligned}$$

$$\left(\sum w^2\right)_n^\pm = \frac{\sum_{i,j} \left(\sum w^2\right)_{ijn}^\pm (\Delta Q_i^2)^2 (\Delta \nu_j)^2}{\left(\sum_{i,j} \Delta Q_i^2 \Delta \nu_j\right)^2} \quad (\text{VI.26})$$

## 4.2 Systematic studies

### On the Bethe-Heitler contribution

As discussed in [Section VI.5](#), the agreement at large  $\nu$  between data and the Bethe-Heitler Monte Carlo prediction is  $98.6 \pm 0.01\%$ . Although the comparison of the Bethe-Heitler is done at large  $\nu$ , the BH contribution estimated by HEPGEN-BH is considered with a systematic error of 5% in the low  $\nu$  domain used for the DVCS cross section extraction.

[Fig. \(VI.5\)](#) shows the evolution of the relative difference on the  $B$  parameter and on the four different cross sections as a function of the BH prediction multiplied by a factor varying around 1. The purple points show the evolution of these differences as a function of a scaling factor applied to the BH prediction, and the green error bands display the statistical error for each evaluation. Thus it is easy to read the consequent systematic errors. A systematic error of 5% provides a relative error on  $B$  up to 2.0% down and 2.2% up. The systematic errors on the cross section in the 4  $t$ -bins are reported in [Table \(VI.3\)](#).

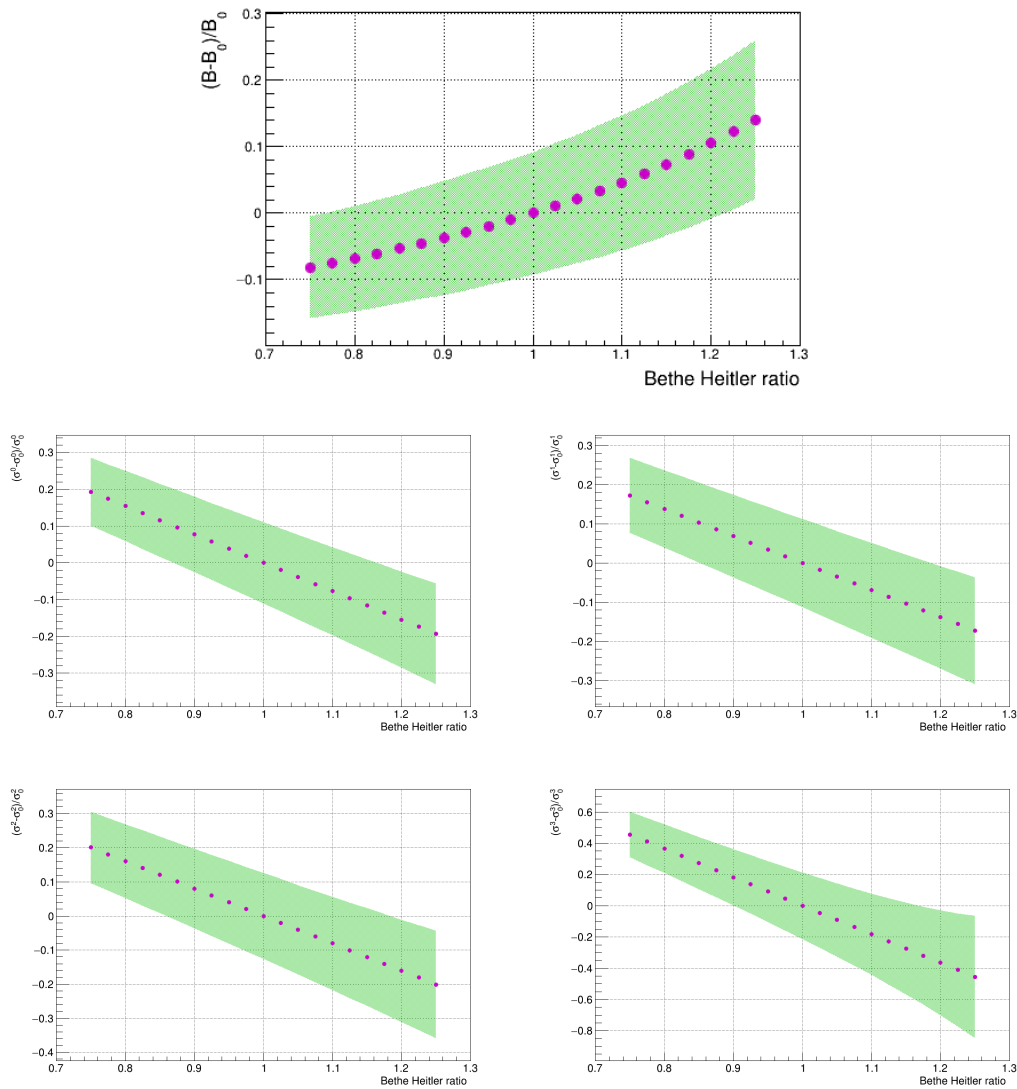


**Figure VI.5:** Relative difference on the  $B$  parameter and on the four different cross sections as a function of the BH prediction multiplied by a factor varying around 1. The purple points show the evolution of these differences as a function of a scaling factor applied to the BH prediction, and the green error bands display the statistical error for each evaluation.

### On the visible $\pi^0$ contribution

The number of invisible  $\pi^0$  is scaled on the number of visible  $\pi^0$ . This number depends on the photon energy threshold, which is chosen as low as 300 MeV. A systematic error of 20% is considered.

**Fig. (VI.6)** shows the evolution of the relative difference on the  $B$  parameter and on the four different cross sections as a function of the number of  $\pi^0$  multiplied by a factor varying around 1. A systematic error of 20% provides a relative error on  $B$  up to 4.1% down and 4.60% up. The systematic errors on the cross section in the 4  $t$ -bins are reported in Table **Table (VI.3)**.

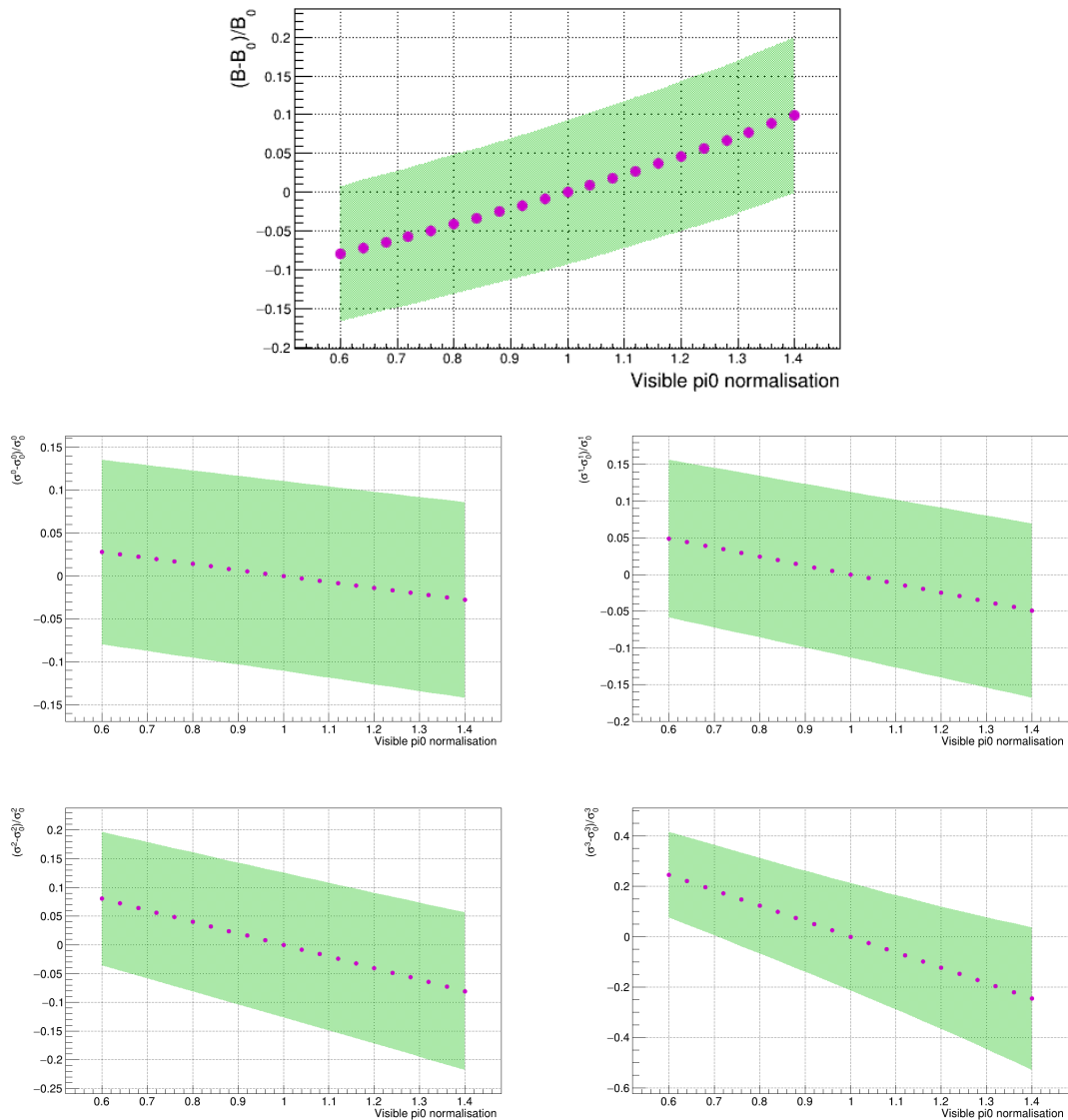


**Figure VI.6:** Relative difference on the  $B$  parameter and on the four different cross sections as a function of the number of  $\pi^0$  multiplied by a factor varying around 1. The purple points show the evolution of these differences as a function of a scaling factor applied to the BH prediction, and the green error bands display the statistical error for each evaluation.

### On the invisible $\pi^0$ contribution with the ratio $r_{\text{LEPTO}}$

In [Section VI.6.3](#) the ratio  $r_{\text{LEPTO}}$  between semi-inclusive and exclusive invisible  $\pi^0$  has been estimated to  $40 \pm 10\%$ .

[Fig. \(VI.7\)](#) shows the evolution of the relative difference on the  $B$  parameter and on the four different cross sections as a function of  $r_{\text{LEPTO}}$ . A systematic error of 10% provides a relative error on  $B$  up to 0.6% down and 0.60% up. The systematic errors on the cross section in the 4  $t$ -bins are reported in [Table \(VI.3\)](#).

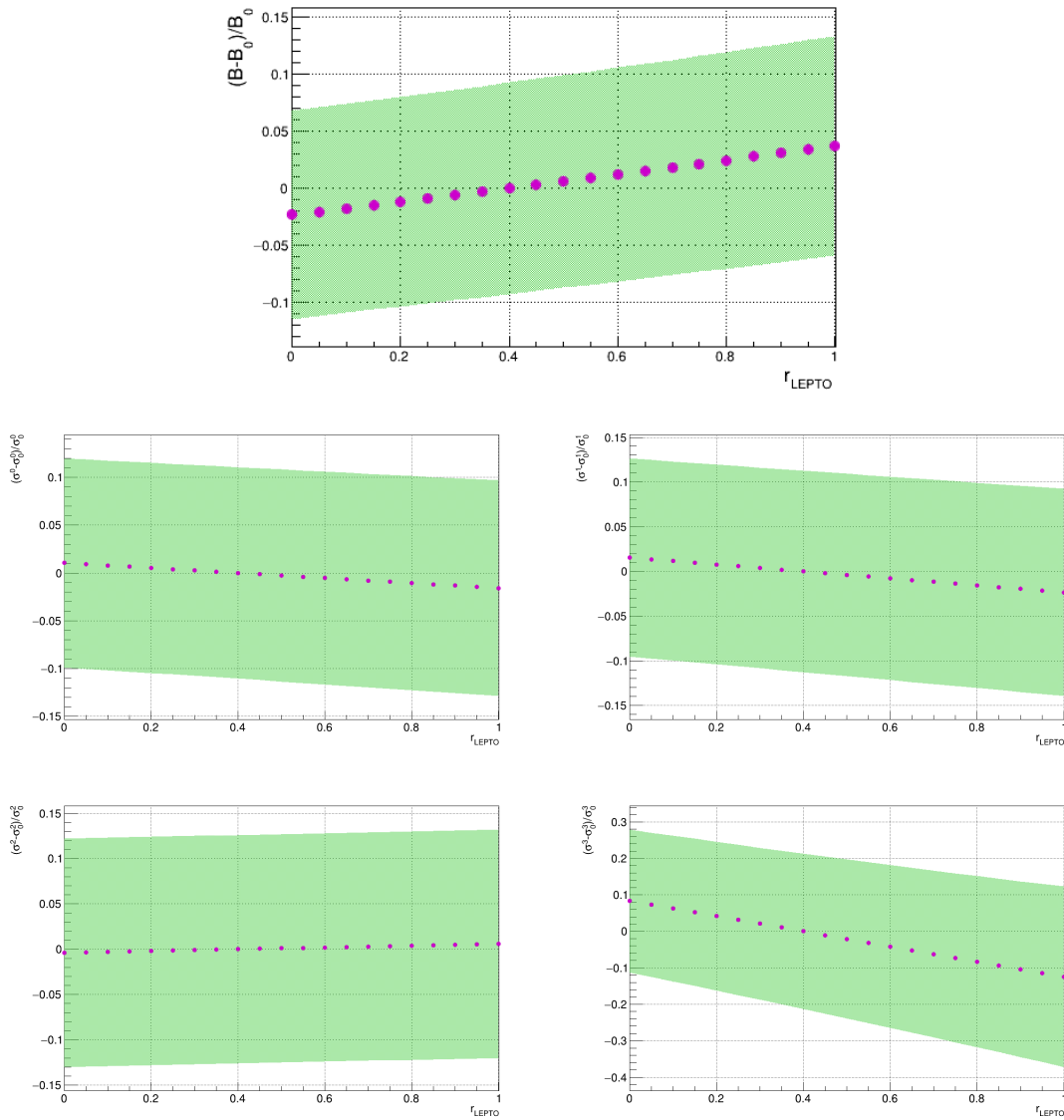


**Figure VI.7:** Relative difference on the  $B$  parameter and on the four different cross sections as a function of  $r_{\text{LEPTO}}$ . The purple points show the evolution of these differences as a function of a scaling factor applied to the BH prediction, and the green error bands display the statistical error for each evaluation.

### On the event selection using a $\chi^2$ cut in the kinematic fit

The  $\chi_{\text{red}}^2$  cut could have been enlarged up to  $\chi_{\text{red}}^2 < 14$ . **Fig. (VI.8)** shows the evolution of the relative difference on the  $B$  parameter and on the four different cross sections as a function of the cut. A new cut of 14 provides a systematic deviation on the  $B$  parameter of 1.4% down. The systematic errors on the cross section in the 4  $t$ -bins are reported in **Table (VI.3)**.

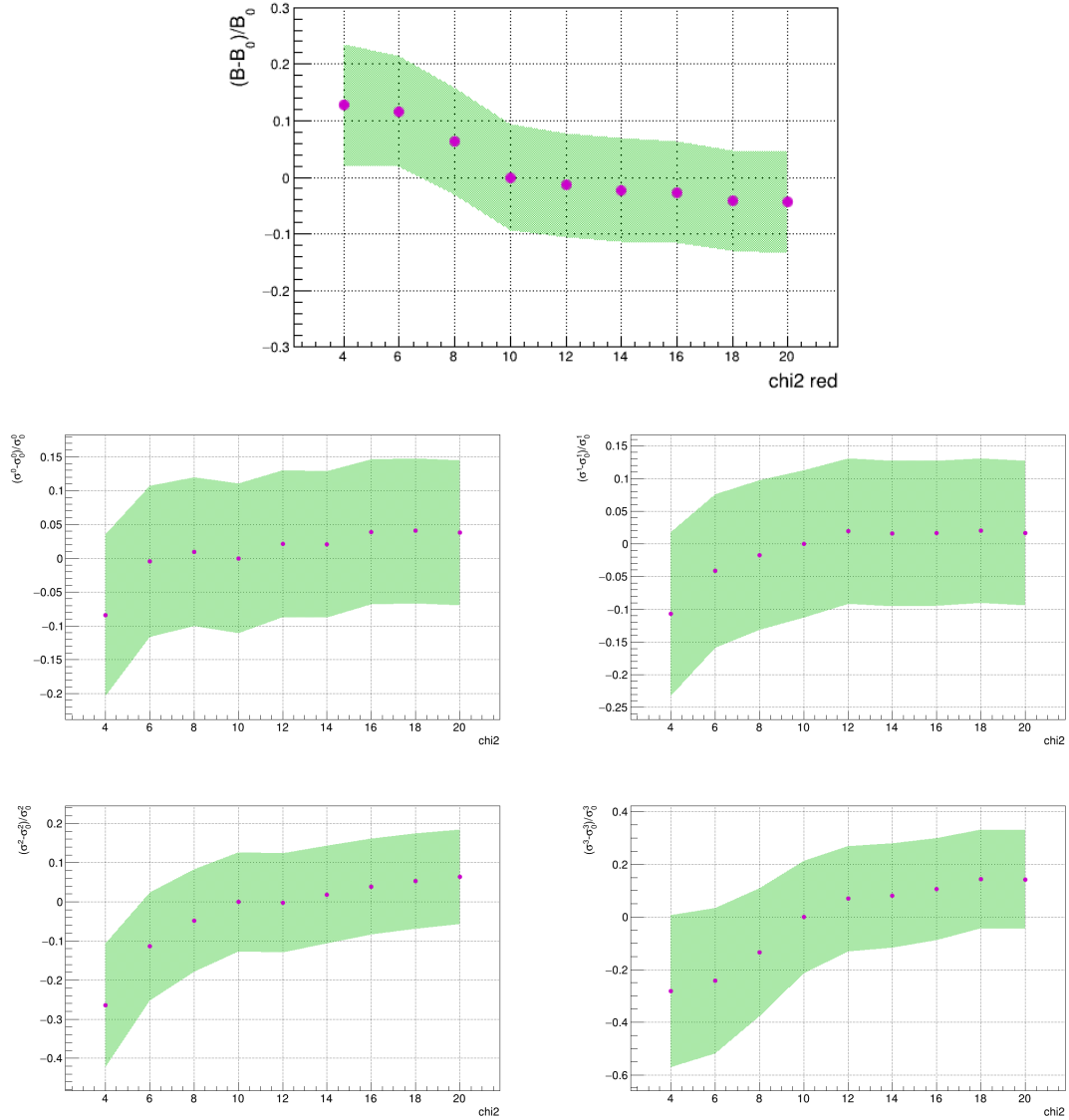


**Figure VI.8:** Relative difference on the  $B$  parameter and on the four different cross sections as a function of the  $\chi_{\text{red}}^2$  cut. The purple points show the evolution of these differences as a function of a scaling factor applied to the BH prediction, and the green error bands display the statistical error for each evaluation.

### Summary of systematic studies

**Table (VI.3)** summarizes the systematic studies on both the B-slope and the four cross section evaluations. The quadratic sum of all the systematic errors is indicated on the bottom lines. Note that the relative errors are in %. The corresponding absolute value on the cross section are indicated in **Table (VI.1)** and in **Fig. (VI.4)**. Note that additional sources of systematic errors will be added in a near future, such as radiative corrections.

		on $d\sigma_{\text{DVCS}}^{\gamma^*p \rightarrow \gamma p'} / d t $				on B
t -bin		[0.08,0.136]	[0.136,0.219]	[0.219,0.36]	[0.36, 0.64]	
BH	rel. sys. err. $\uparrow$	3.9	3.5	4.0	9.1	2.2
contrib.	rel. sys. err. $\downarrow$	3.9	3.5	4.1	9.1	2.0
Visible $\pi^0$	rel. sys. err. $\uparrow$	1.4	2.4	4.0	12.3	4.6
contrib.	rel. sys. err. $\downarrow$	1.4	2.4	4.0	12.3	4.1
$r_{\text{Lepto}}$	rel. sys. err. $\uparrow$	0.25	0.39	0.10	2.1	0.6
	rel. sys. err. $\downarrow$	0.25	0.39	0.10	2.1	0.6
$\chi_{\text{red}}^2$	rel. sys. err. $\downarrow$	2.0	1.6	1.9	8.1	1.4
$\Sigma$	rel. sys. err. $\uparrow$	4.2	4.3	5.7	15.4	5.1
	rel. sys. err. $\downarrow$	4.6	4.6	6.0	17.4	4.8

**Table VI.3:** Relative systematic errors on  $\langle d\sigma_{\text{DVCS}}^{\gamma^*p \rightarrow \gamma p'} / d|t| \rangle$  and on B given in %

## 5 Study of the $\phi_{\gamma^*\gamma}$ azimuthal dependence of the DVCS cross section

**Fig. (VI.9)** presents the  $\phi$  modulations of the virtual-photon proton cross-section  $d\sigma_{\text{DVCS}}^{\gamma^*p \rightarrow \gamma p'} / d|t| d\phi$  in four  $|t|$  bins. The red fit functions correspond to a fit of the form:

$$f(\phi) = c_0 + c_1 \cos(\phi) + c_2 \cos(2\phi) + s_1 \sin(\phi) + s_2 \sin(2\phi). \quad (\text{VI.27})$$

The result of the fit is indicated in **Table (VI.4)**. All parameters  $c_1, c_2, s_1, s_2$  are consistent with zero within 2 standard deviations. Mainly only the constant terms  $c_0$  are well determined and dominates the evolution. They are in agreement with the mean values  $\langle d\sigma_{\text{DVCS}}^{\gamma^*p \rightarrow \gamma p'} / 2\pi d|t| \rangle$  given in **Table (VI.5)** within an accuracy better than 4%. This is important in order to interpret the slope B of the  $t$ -dependence of the DVCS cross section into transverse extension of partons in the proton.

## VI.5. Study of the $\phi_{\gamma^* \gamma}$ azimuthal dependence of the DVCS cross section 155

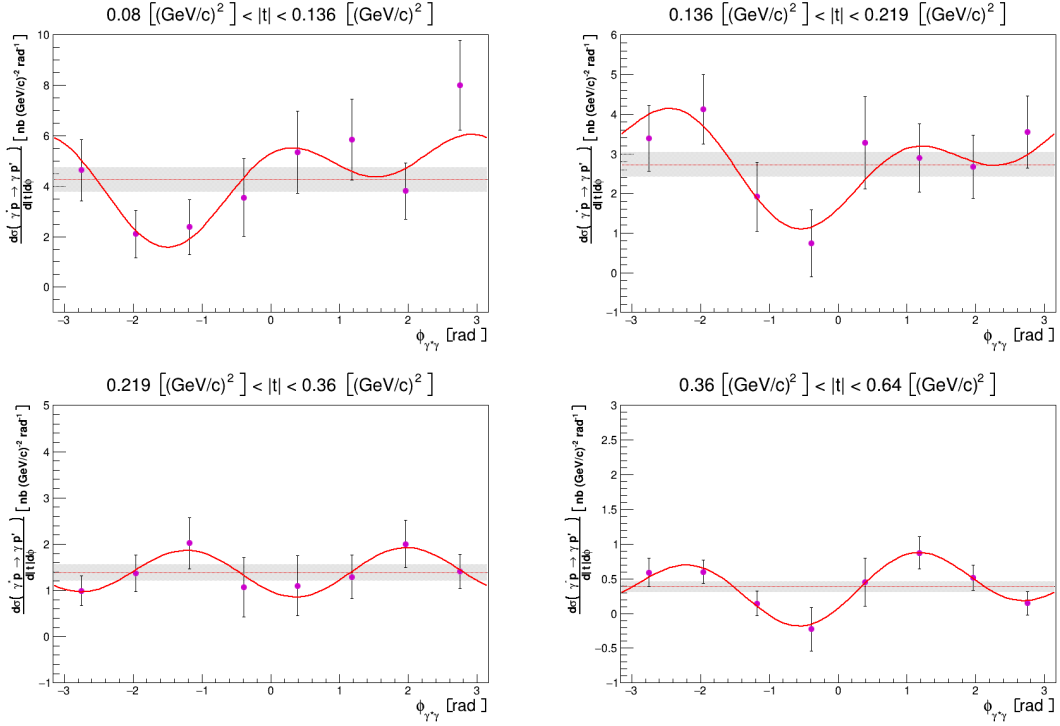


**Figure VI.9:**  $\phi$  evolution of the virtual-photon proton cross-section  $\langle d\sigma/dt|d\phi \rangle$  evaluated in 4  $|t|$  domains. Only the statistical errors are reported. The red curves correspond to a fit of Eq. (VI.27). The fitted parameters are given in Table (VI.1). The red lines and the grey bands represent the constant term  $c_0$  within its statistical error.

$ t $ -bin	[0.08,0.136]	[0.136,0.219]	[0.219,0.36]	[0.36, 0.64]
$c_0$	$4.26 \pm 0.48$	$2.73 \pm 0.31$	$1.38 \pm 0.17$	$0.38 \pm 0.08$
$c_1$	$-0.32 \pm 0.73$	$-0.94 \pm 0.45$	$-0.06 \pm 0.25$	$-0.12 \pm 0.12$
$c_2$	$1.30 \pm 0.67$	$-0.20 \pm 0.44$	$-0.35 \pm 0.24$	$-0.20 \pm 0.11$
$s_1$	$1.38 \pm 0.61$	$1.09 \pm 0.43$	$0.01 \pm 0.24$	$0.17 \pm 0.10$
$s_2$	$0.09 \pm 0.78$	$0.44 \pm 0.31$	$-0.33 \pm 0.23$	$0.33 \pm 0.10$

**Table VI.4:** Results of the fit of  $\langle d\sigma_{\text{DVCS}}^{\gamma^* p \rightarrow \gamma p'} / d|t|d\phi \rangle$  [nb (GeV/c)<sup>-2</sup> rad<sup>-1</sup>] according to Eq. (VI.27)

$ t $ -bin	[0.08,0.136]	[0.136,0.219]	[0.219,0.36]	[0.36, 0.64]
$c_0$	$4.44 \pm 0.49$	$2.80 \pm 0.32$	$1.40 \pm 0.18$	$0.38 \pm 0.08$

**Table VI.5:** Values of  $\langle d\sigma_{\text{DVCS}}^{\gamma^* p \rightarrow \gamma p'} / 2\pi d|t| \rangle$  [nb (GeV/c)<sup>-2</sup> rad<sup>-1</sup>] used in the B-slope determination.

## 6 Interpretation, comparison to other results and prospects

The present COMPASS result based on the analysis of 2/3 of the 2016 data set is obtained in the same kinematic domain as for the previous analysis of the 2012 pilot run [42]:

- $1 \text{ (GeV/c)}^2 < Q^2 < 5 \text{ (GeV/c)}^2$
- $10 \text{ GeV} < \nu < 32 \text{ GeV}$
- $0.08 \text{ (GeV/c)}^2 < |t| < 0.64 \text{ (GeV/c)}^2$

As said in Chapter (I) the slope  $B$  of the  $t$ -dependence of the DVCS cross section can be converted into the transverse extension of partons in the proton assuming:

- the dominance of the imaginary part of the CFF  $\mathcal{H}$  (i.e. GPD H at  $x = \xi$ ) given by  $c_0^{DVCS}$ ,
- a negligible effect of non-zero value of the skewness  $\xi \simeq x_B/2 \simeq 0.03$  in the COMPASS domain.

$$\langle b_{\perp}^2(x = \xi \simeq x_B/2) \rangle \approx 2B \quad (\text{VI.28})$$

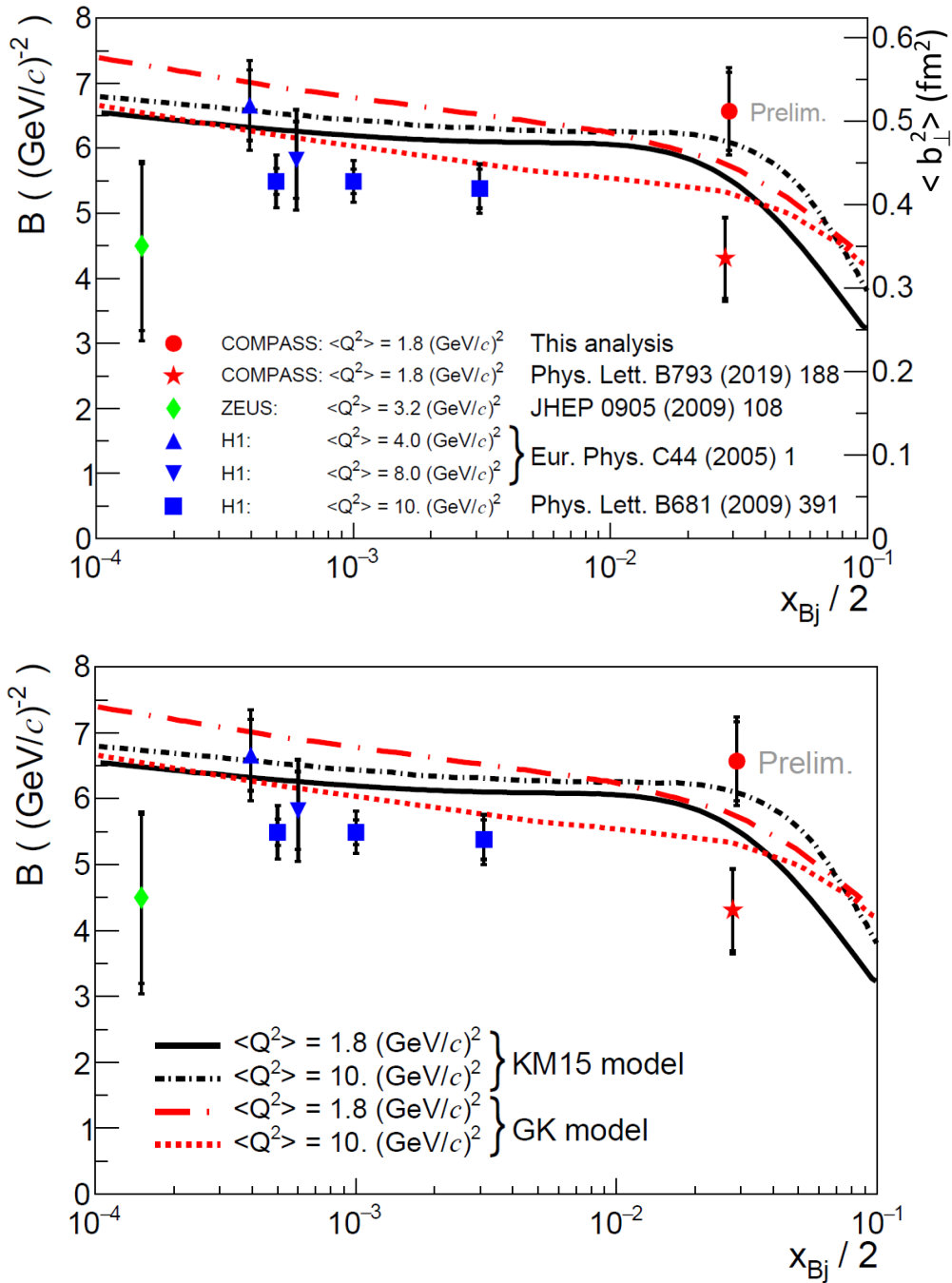
$$\langle b_{\perp}^2 \rangle \approx 0.53 \pm 0.05 \pm 0.03 \text{ fm}^2 \text{ at } x_B/2 \simeq 0.03 \quad (\text{VI.29})$$

Fig. (VI.10) presents the slope  $B$  for our result together with the previous COMPASS result and those from earlier high-energy experiments that used the same method. The equivalent average squared transverse extension of partons in the proton  $\langle b_{\perp}^2 \rangle$  is also indicated.

Note that the results from HERA collider experiments H1 [65, 66] and ZEUS [67] which investigate values of  $x_B/2$  smaller than  $10^{-2}$  were obtained at higher values of  $Q^2$  as compared to that of COMPASS. The predictions of 2 models GK [50, 51, 52] and KM15 [48, 49] are also indicated as well as the  $Q^2$  evolution between 1.8 and 10  $(\text{GeV/c})^2$ .

There is a 3 sigma difference between our result and the one published using the 2012 pilot run data. Our new value of the  $t$ -slope parameter  $B$  was obtained with a more advanced analysis method than that of the previous analysis. The situation will be clarified by analysing the full statistics including the remaining 2016 data and the full 2017 data set, which is 3 times larger than the 2016 analysed data set. A deeper investigation of all systematics (related to  $\pi^0$  contamination, to the different cuts, to radiative corrections) has still to be done.

The further goal is to use the complete set of data up to  $Q^2 = 10 \text{ (GeV/c)}^2$  and to provide results at 3  $x_B$  values.



**Figure VI.10:** On Top: Results from COMPASS and previous measurements by H1 [65, 66] and ZEUS [67] on the  $t$ -slope parameter  $B$ , or equivalently the average squared transverse extension of partons in the proton,  $\langle r_{\perp}^2 \rangle$ , as probed by DVCS at the proton longitudinal momentum fraction  $x_B/2$  (see text). Inner error bars represent statistical and outer ones the quadratic sum of statistical and systematic uncertainties. (b) Same results compared to the predictions of the GK [50, 51, 52] and KM15 [48, 49] models.



---

## SUMMARY AND CONCLUSION

---

Generalised Partons Distributions will help to unravel the proton structure conundrum. As of today, most of the information is obtained by Deeply Virtual Compton Scattering, Time-like Compton Scattering and Hard Exclusive Meson production measurements, giving access to Compton Form Factors which are convolutions of GPDs with a specific kernel.

The GPD program started in the COMPASS collaboration in 2012. With the use of high energy polarized positive and negative muon beams, COMPASS can bring information to the imaginary and real parts of the CFF  $\mathcal{H}$  playing with the sum or difference of DVCS cross sections obtained with the two beam charges. Before the new collider EIC is operational, COMPASS is a natural bridge between the gluon domain probed by the experiments held at HERA and the valence quark region studied at JLab.

The DVCS cross section measurement at COMPASS consists of the detection of all the final state particles thanks to the forward spectrometer and the recoil proton detector CAMERA. The large coverage in  $x_B$  and  $Q^2$  is insured by the hodoscope muon triggers. The different steps for a reliable measurement are presented through this thesis:

- The qualification of the electromagnetic calorimeters ECAL0, ECAL1 and ECAL2 has been realized thanks to large efforts for the best energy and timing calibrations.
- The recoil proton detector, CAMERA, allows a good selection of exclusive events and a good determination of the 4-momentum transfer  $t$  when it is small. Therefore the calibration of the CAMERA detector is a crucial point. In addition, the CAMERA Monte Carlo simulation has been updated to reproduce more accurately the real data within the background. This resulted in the improvement and refurbishment of the "Saclay" CAMERA code which is now the official reconstruction software of the CAMERA detector used in the COMPASS Collaboration.
- The selection of the exclusive single photon events relies on the redundancy of the measurement between CAMERA and the forward spectrometer. A kinematically constrained fit has been applied to improve the determination of each observable, notably the 4-momentum transfer  $t$  over its complete range. In particular, a software has been developed and shared in the COMPASS collaboration in order to setup and apply a kinematic fit on the DVCS or any HEMP topology (such as exclusive  $\pi^0$  and  $J/\Psi$ ).
- In the small  $x_B$  domain of COMPASS, a detailed and systematic comparison of the data with the well-known Bethe-Heitler process has been investigated. The Bethe-Heitler is expected to be the only contribution in this  $x_B$  domain, and the agreement of  $98.6 \pm 1\%$  is reached. This confirms also the luminosity determination and the proper description of the different detectors and hodoscope triggers involved.
- In the large  $x_B$  domain, the Bethe-Heitler contribution is subtracted from the data as well as the  $\pi^0$  contamination. The remaining contribution represents that of the

DVCS and the interference terms.

- The DVCS cross section has been measured. Its  $\phi_{\gamma^*\gamma}$  azimuthal angle and  $|t|$ -dependencies are studied. The  $t$ -evolution associated to the square of the imaginary part of the CFF  $\mathcal{H}$  has provided a transverse extension of the partons probed in the proton,  $\langle b_{\perp}^2 \rangle \approx 0.53 \pm 0.05 \pm 0.03 \text{ fm}^2$  at  $x_B/2 \simeq 0.03$

For future plans it is expected to expand the analysis such as increasing the range in  $Q^2$  up to  $10 (\text{GeV}/c)^2$  and providing 3 bins in  $x_B$  to see the evolution of  $\langle b_{\perp}^2 \rangle$  as function of  $x_B$ . In addition, studies can be extended to the other  $x_B$  domains where the modulations in  $\phi_{\gamma^*\gamma}$  are significant due to the interference contribution, to determine all the Fourier coefficients. Moreover, the statistics provided by the complete 2016-2017 data set should allow us to study the beam charge and polarisation cross section difference dominated by the real part of the Compton Form Factor  $\mathcal{H}$ . The good agreement between the  $\mu+$  and  $\mu-$  cross sections integrated over the  $\phi_{\gamma^*\gamma}$  azimuthal angle seems already promising.

## APPENDIX A

---

### CAMERA description and calibrations

---

Note that the following tables are done directly with the values obtained and used for the CAMERA software (the 3 digits given after the coma could have been suppressed).

# 1 Azimuthal calibrations

## 1.1 Fit results for ring B

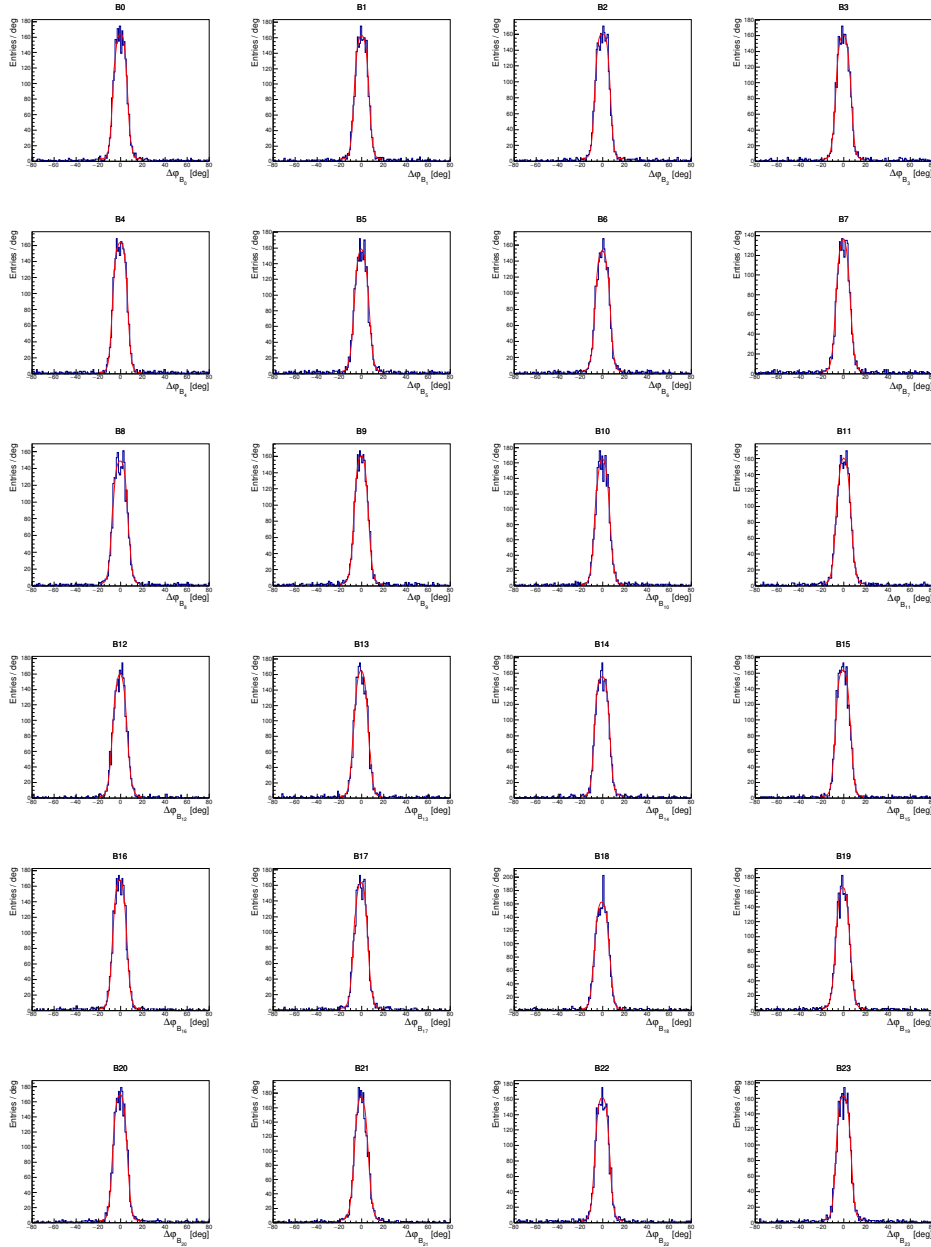


Figure A.1: Azimuthal calibration results for all sectors of CAMERA ring B

scintillator	0	1	2	3	4	5	6	7	8	9	10	11
$\varphi_B$ [rad]	2.22	1.962	1.696	1.43	1.171	0.912	0.649	0.383	0.124	-0.138	-0.398	-0.657
$\sigma_B$ [rad]	0.118	0.119	0.125	0.123	0.121	0.119	0.122	0.112	0.128	0.116	0.121	0.12
scintillator	12	13	14	15	16	17	18	19	20	21	22	23
$\varphi_B$ [rad]	-0.927	-1.189	-1.45	-1.716	-1.979	-2.239	-2.501	-2.766	-3.02	3.002	2.741	2.482
$\sigma_B$ [rad]	0.116	0.12	0.125	0.124	0.115	0.116	0.123	0.115	0.118	0.111	0.119	0.121

Table A.1: Azimuthal calibration values for all sectors of Camera ring B

## 1.2 Fit results for ring A

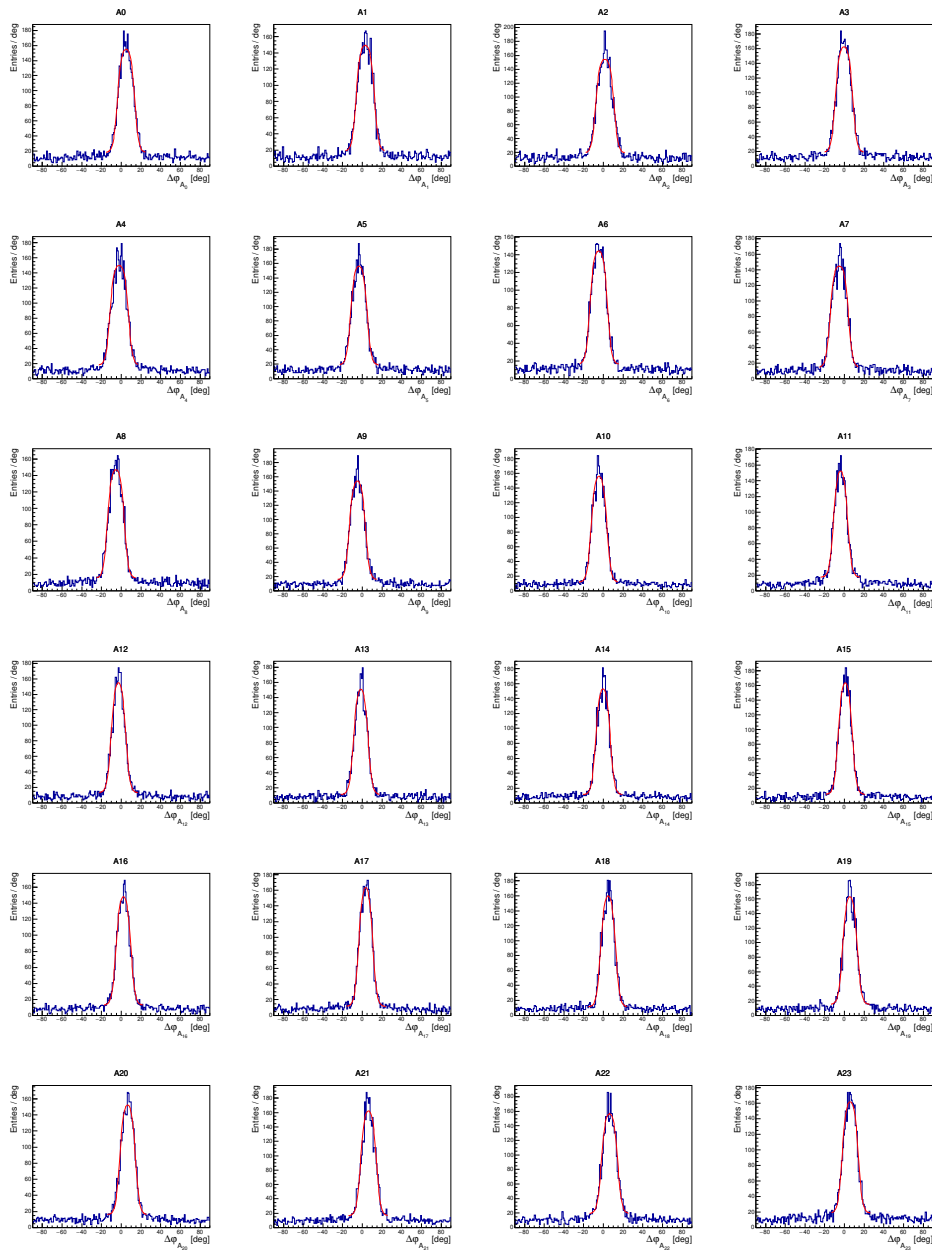


Figure A.2: Azimuthal calibration results for all sectors of CAMERA ring A

scintillator	0	1	2	3	4	5	6	7	8	9	10	11
$\varphi_A$ [rad]	2.179	1.885	1.597	1.301	1.01	0.725	0.441	0.17	-0.095	-0.35	-0.601	-0.854
$\sigma_A$ [rad]	0.154	0.163	0.163	0.155	0.165	0.148	0.157	0.164	0.152	0.146	0.142	0.127
scintillator	12	13	14	15	16	17	18	19	20	21	22	23
$\varphi_A$ [rad]	-1.096	-1.336	-1.578	-1.818	-2.056	-2.296	-2.534	-2.782	-3.029	2.989	2.727	2.458
$\sigma_A$ [rad]	0.13	0.13	0.131	0.127	0.133	0.125	0.134	0.131	0.14	0.141	0.145	0.144

**Table A.2:** Azimuthal calibration values for all sectors of Camera ring A

## 2 Radial tomography

As explained in [Section A.2.3](#), one can derive the effective center and the new radii in the laboratory frame using a perfect circle assumption of nominal radius  $r_{\text{nom}}$ .

### 2.1 Derivation of the effective center

One can use the fit of the azimuthal deviations with the function

$$F(\varphi) := p_0 + p_1 \sin(p_2 \cdot \varphi + p_3) \quad (\text{A.1})$$

$\vec{r}_C = (r_C, \varphi_C)$  be the effective center coordinates. For the ring A, the fit parameters are provided by:

$$\begin{aligned} p_0 &= 0.0105 & \pm 0.00123 \\ p_1 &= -0.0104 & \pm 0.000972 \\ p_2 &= 0.979 & \pm 0.00101 \\ p_3 &= 1.71 & \pm 0.00753 \end{aligned}$$

Note that in the perfect circle assumption, one needs to have  $p_2 = 1$  and  $p_0 = 0$ . From the values above, this will be considered. We remind that the function  $F(\varphi)$  shows the angular deviations of the points in a circle not centered around 0. Using [Fig. \(A.3\)](#) we can evaluate the function  $F(\varphi)$  in the two following particular cases:

- For  $\varphi = \varphi_C$ , no deviation is expected. Therefore  $F(\varphi = \varphi_C) = 0$  which leads to  $\varphi_C = -p_3$ .
- For  $\varphi = \varphi_C + \frac{\pi}{2}$ , we expect a maximal deviation. Therefore  $F(\varphi = \varphi_C + \frac{\pi}{2}) = p_1$ . Using [Fig. \(A.3\)](#) and the nominal radius of the ring, one gets:  $r_C = r^{\text{nom}} \cdot \tan |p_1|$

In fine,

$$\begin{pmatrix} r_C \\ \varphi_C \end{pmatrix} = \begin{pmatrix} r^{\text{nom}} \cdot \tan |p_1| \\ -p_3 \end{pmatrix}$$

The azimuthal angle of the tracks detected in CAMERA are based on the forward spectrometer measurement in addition to a kinematically constrained fit at the vertex position. Therefore in order to place the CAMERA scintillators in the laboratory frame, a correction of this angle from the vertex to the origin is implemented using the following relations:

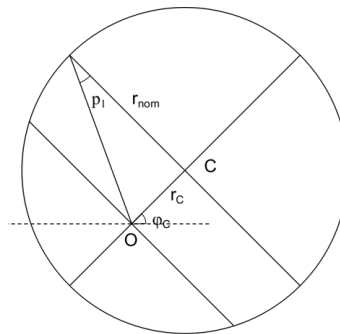
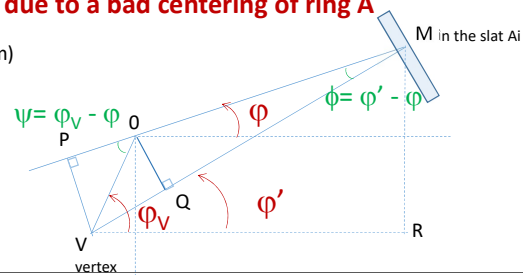


**Figure A.3:** Transverse sketch of CAMERA. The point  $O$  is the origin of the laboratory and  $C$  the centre of the ring A.

**Corrections due to the vertex and due to a bad centering of ring A**

In the plane  $x, y$  ( $\perp$  to  $z$  direction of beam)



- 1-  $\phi_v$  is known ;  $R_v = OV$  is known  
 $\phi'$  is determined thanks to the spectro and exclusive rho  
 + Hypothese to start  $OM = R_A$
- 2- with all the phi of the 24 sectors,  
 with Hypothese Ring A is a circle  
 we can determine the new position  $OM$  of each slat =  $R_{Ai}$

Evaluation of  $OQ$   
 $OQ = OV \sin(\phi_v - \phi') = OM \sin(\phi' - \phi)$

$$\phi = \phi' - \text{asin}(\sin(\phi_v - \phi') R_v / R_A)$$

Evaluation of  $MR$       $MR = R_{Ai} \sin \phi + R_v \sin \phi_v = VM \sin \phi'$   
 Hypo  $VM \approx PM = R_{Ai} + R_v \cos(\phi_v - \phi)$       $\rightarrow \phi' = \text{asin} [ (R_{Ai} \sin \phi + R_v \sin \phi_v) / (R_{Ai} + R_v \cos(\phi_v - \phi)) ]$

$\phi'$  proton with respect to the vertex =  $(\phi'$  for A +  $\phi'$  for B) / 2     (The impact on  $\phi'$  for B is  $\ll$ )

**Figure A.4:** Azimuthal corrections due to the vertex position and due to a bad centering of ring A.

## 2.2 Derivation of the effective radii in the laboratory frame

We can use the polar equation of a circle. It can be obtained from the Cartesian one for instance as

$$\begin{aligned} r(\varphi)^2 - 2r(\varphi)r_C \cos(\varphi - \varphi_C) + |\vec{r}_C|^2 &= r_{\text{nom}}^2 \\ \Leftrightarrow r(\varphi)^2 + r(\varphi)p + q &= 0 \end{aligned}$$

using the following definitions

$$\begin{cases} \vec{v} := \begin{pmatrix} 1 \\ \varphi \end{pmatrix} \\ p := -2\vec{v} \cdot \vec{r}_C \\ q := |\vec{r}_C|^2 - r_{\text{nom}}^2 \end{cases}$$

Thus, solving the second degree polynomial one retrieves **Eq. (IV.16d)**.

$$r = -p/2 + \sqrt{p^2/4 - q}$$

### 3 Longitudinal calibrations

#### 3.1 Fit results for ring B

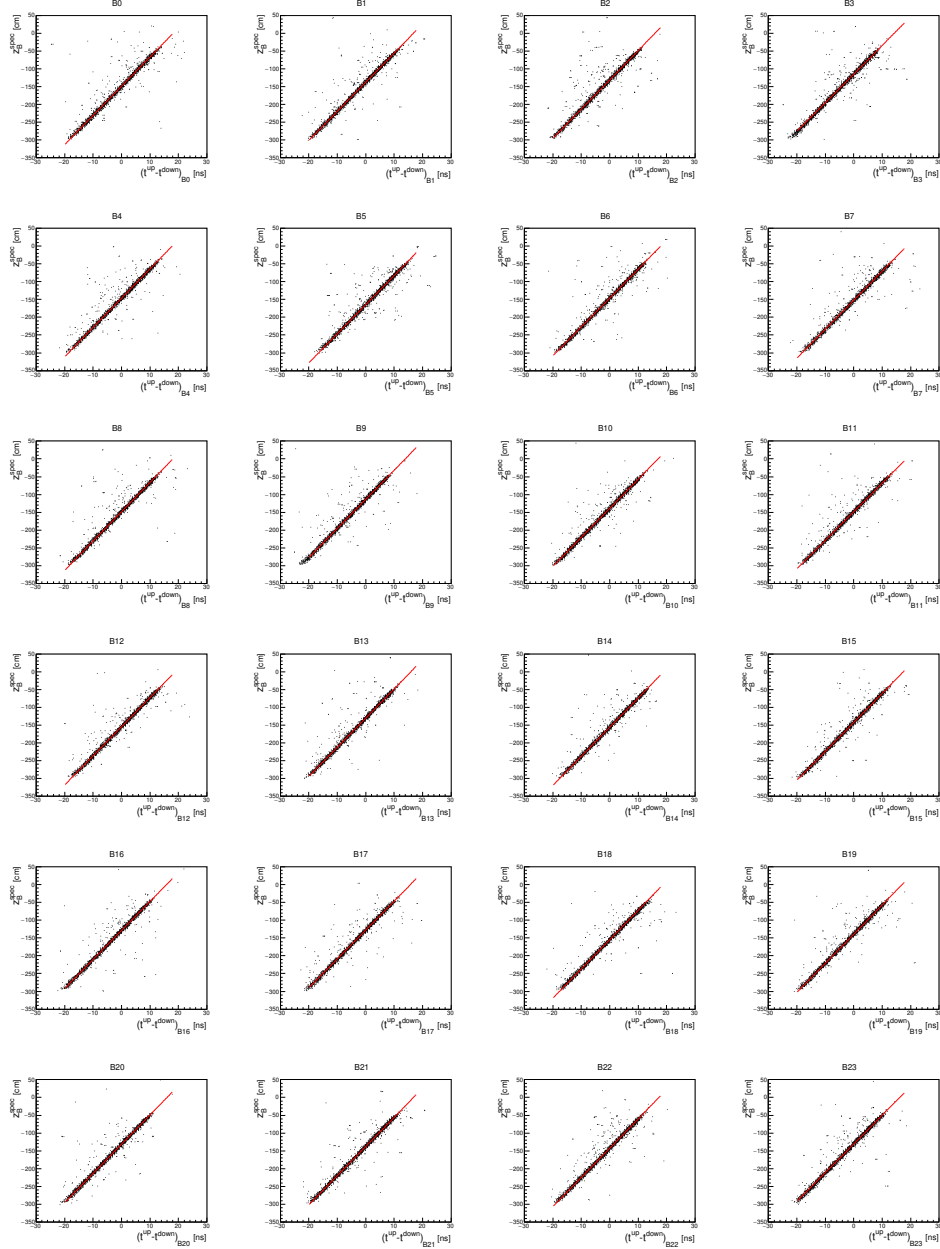
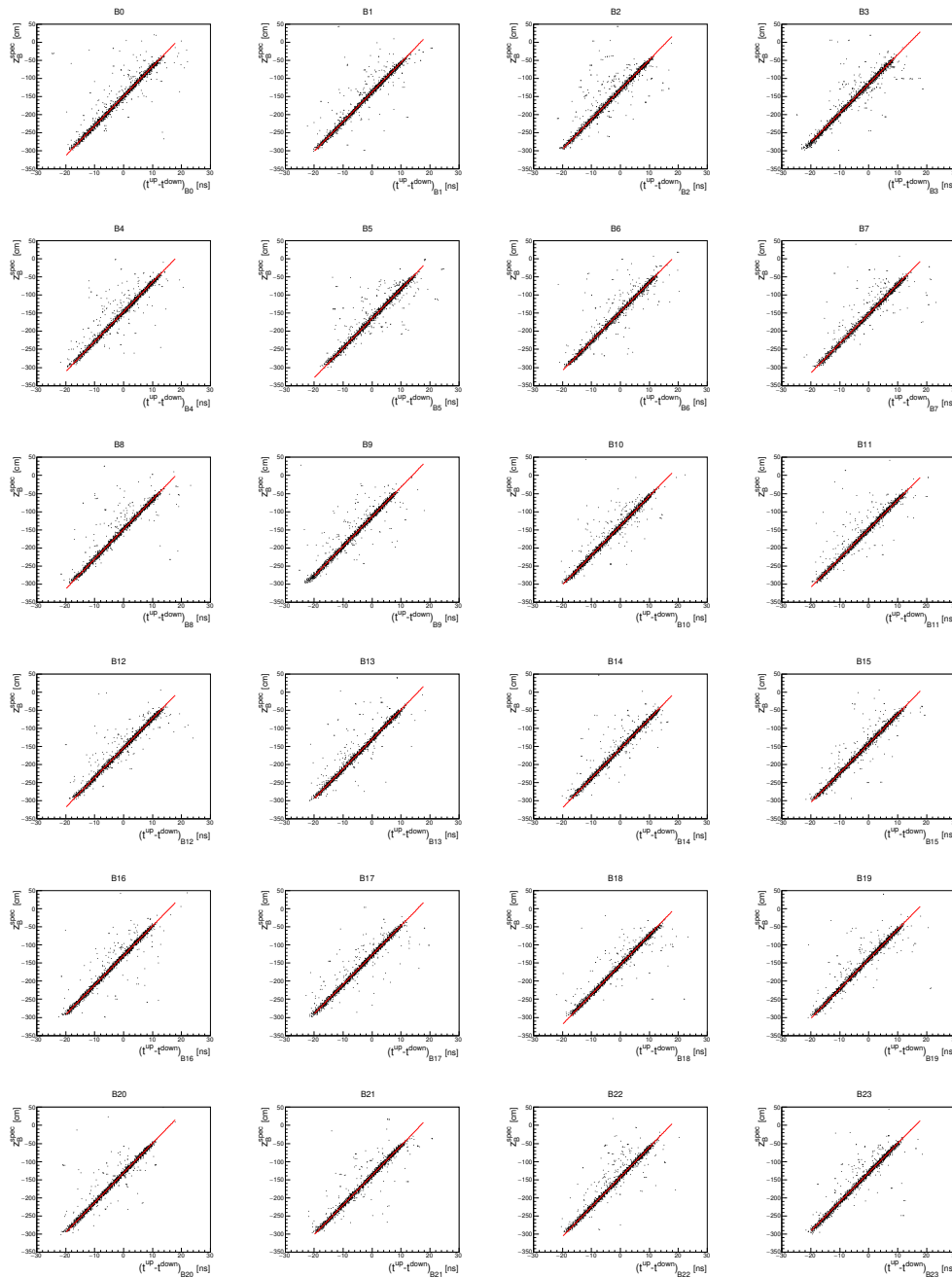


Figure A.5: Longitudinal calibration results for all sectors of CAMERA ring B

scintillator	0	1	2	3	4	5	6	7	8	9	10	11
$v_B/2[\text{cm ns}^{-1}]$	8.213	8.195	8.22	8.045	8.236	8.2	8.129	8.156	8.238	8.188	8.158	8.034
$C_B[\text{cm}]$	-148.738	-137.86	-131.03	-114.727	-146.268	-164.7	-146.079	-151.94	-148.233	-113.785	-138.694	-148.031
scintillator	12	13	14	15	16	17	18	19	20	21	22	23
$v_B/2[\text{cm ns}^{-1}]$	8.19	8.206	8.201	8.141	8.161	8.125	8.245	8.191	8.219	8.202	8.226	8.064
$C_B[\text{cm}]$	-154.169	-130.375	-155.602	-142.076	-128.686	-127.848	-154.439	-139.05	-131.059	-137.919	-142.556	-130.407

Table A.3: Longitudinal calibration values for all sectors of Camera ring B

### 3.2 Fit results for ring A



**Figure A.6:** Longitudinal calibration results for all sectors of CAMERA ring A

scintillator	0	1	2	3	4	5	6	7	8	9	10	11
$v_B/2[\text{cm ns}^{-1}]$	8.152	8.086	8.338	8.164	8.337	8.278	8.371	8.143	8.366	8.198	8.324	8.219
$C_B[\text{cm}]$	-156.238	-161.085	-155.3	-155.432	-149.005	-145.385	-155.926	-150.07	-137.801	-150.465	-143.216	-159.18
scintillator	12	13	14	15	16	17	18	19	20	21	22	23
$v_B/2[\text{cm ns}^{-1}]$	7.929	8.336	8.287	8.41	8.153	8.151	8.212	7.92	8.086	8.165	8.159	8.087
$C_B[\text{cm}]$	-130.456	-141.941	-150.488	-133.349	-149.695	-161.761	-163.285	-145.512	-132.403	-150.521	-143.192	-144.993

**Table A.4:** Longitudinal calibration values for all sectors of Camera ring B

## 4 Time of flight calibrations

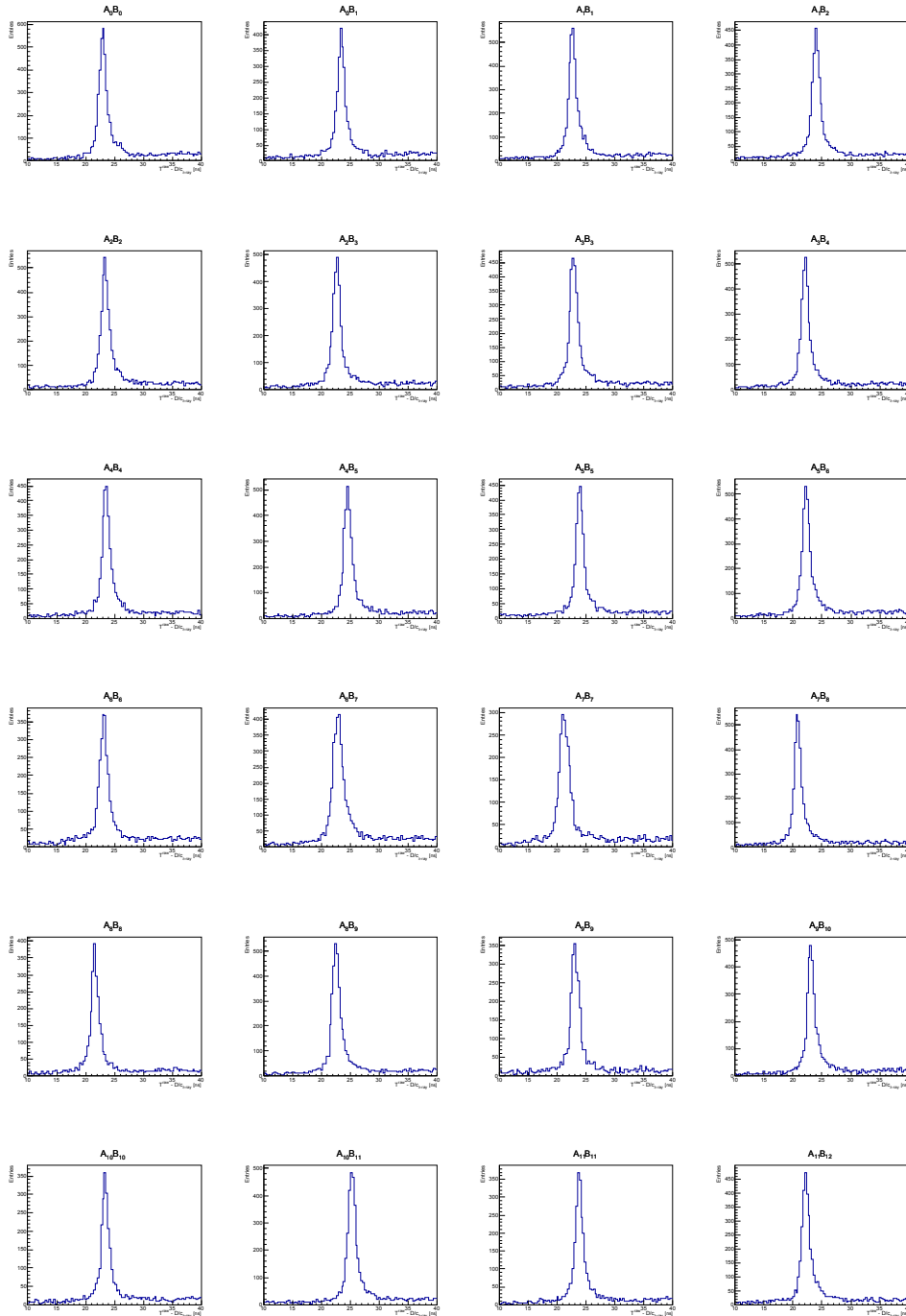


**Figure A.7:** Projection of the correlation between the time of flight and the distance of flight recorded in CAMERA. The calibration is obtained by the central value (part 1)

pair	$A_0B_0$	$A_0B_1$	$A_1B_1$	$A_1B_2$	$A_2B_2$	$A_2B_3$	$A_3B_3$	$A_3B_4$	$A_4B_4$	$A_4B_5$	$A_5B_5$	$A_5B_6$
$C_{AB}[\text{ns}]$	22.952	23.411	22.625	23.973	23.368	22.646	22.823	22.093	23.486	24.530	23.932	22.260
pair	$A_6B_6$	$A_6B_7$	$A_7B_7$	$A_7B_8$	$A_8B_8$	$A_8B_9$	$A_9B_9$	$A_9B_{10}$	$A_{10}B_{10}$	$A_{10}B_{11}$	$A_{11}B_{11}$	$A_{11}B_{12}$
$C_{AB}[\text{ns}]$	23.115	22.820	21.168	20.777	21.596	22.487	23.105	23.071	23.386	25.224	23.819	22.210

**Table A.5:** Longitudinal calibration values for all sectors of Camera ring B (part 1)

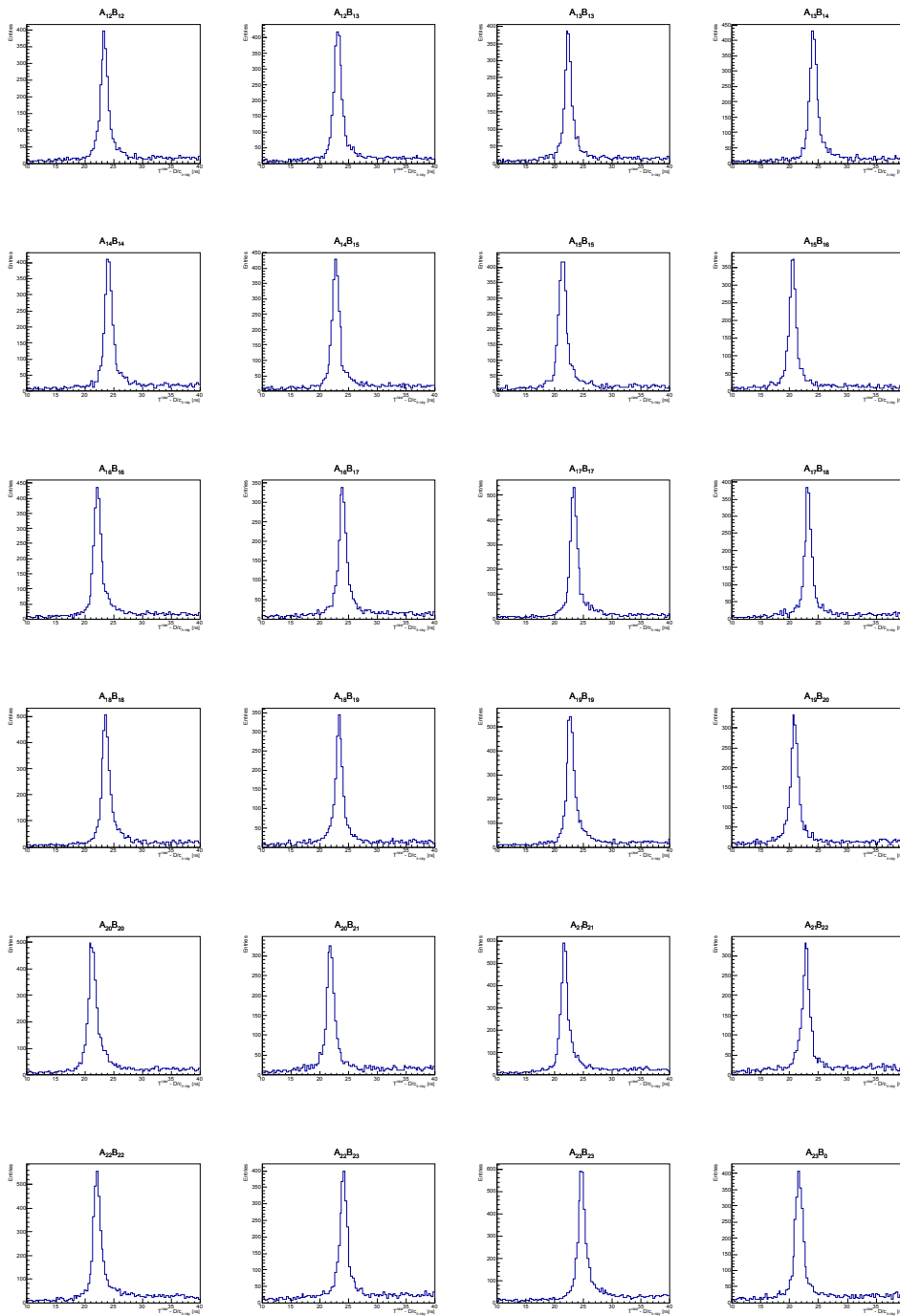


**Figure A.8:** Projection of the correlation between the time of flight and the distance of flight recorded in CAMERA. The calibration is obtained by the central value (part 2)

pair	$A_{12}B_{12}$	$A_{12}B_{13}$	$A_{13}B_{13}$	$A_{13}B_{14}$	$A_{14}B_{14}$	$A_{14}B_{15}$	$A_{15}B_{15}$	$A_{15}B_{16}$	$A_{16}B_{16}$	$A_{16}B_{17}$	$A_{17}B_{17}$	$A_{17}B_{18}$
$C_{AB}$ [ns]	23.401	23.139	22.300	24.101	24.110	22.791	21.315	21.526	22.205	23.983	23.344	23.191
pair	$A_{18}B_{18}$	$A_{18}B_{19}$	$A_{19}B_{19}$	$A_{19}B_{20}$	$A_{20}B_{20}$	$A_{20}B_{21}$	$A_{21}B_{21}$	$A_{21}B_{22}$	$A_{22}B_{22}$	$A_{22}B_{23}$	$A_{23}B_{23}$	$A_{23}B_0$
$C_{AB}$ [ns]	23.609	23.370	22.735	20.846	21.253	21.837	21.682	22.845	22.147	24.163	24.725	21.619

**Table A.6:** Longitudinal calibration values for all sectors of Camera ring B (part 2)

## APPENDIX B

---

Additional content: Bethe-Heitler comparison per period and  
beam charge

---

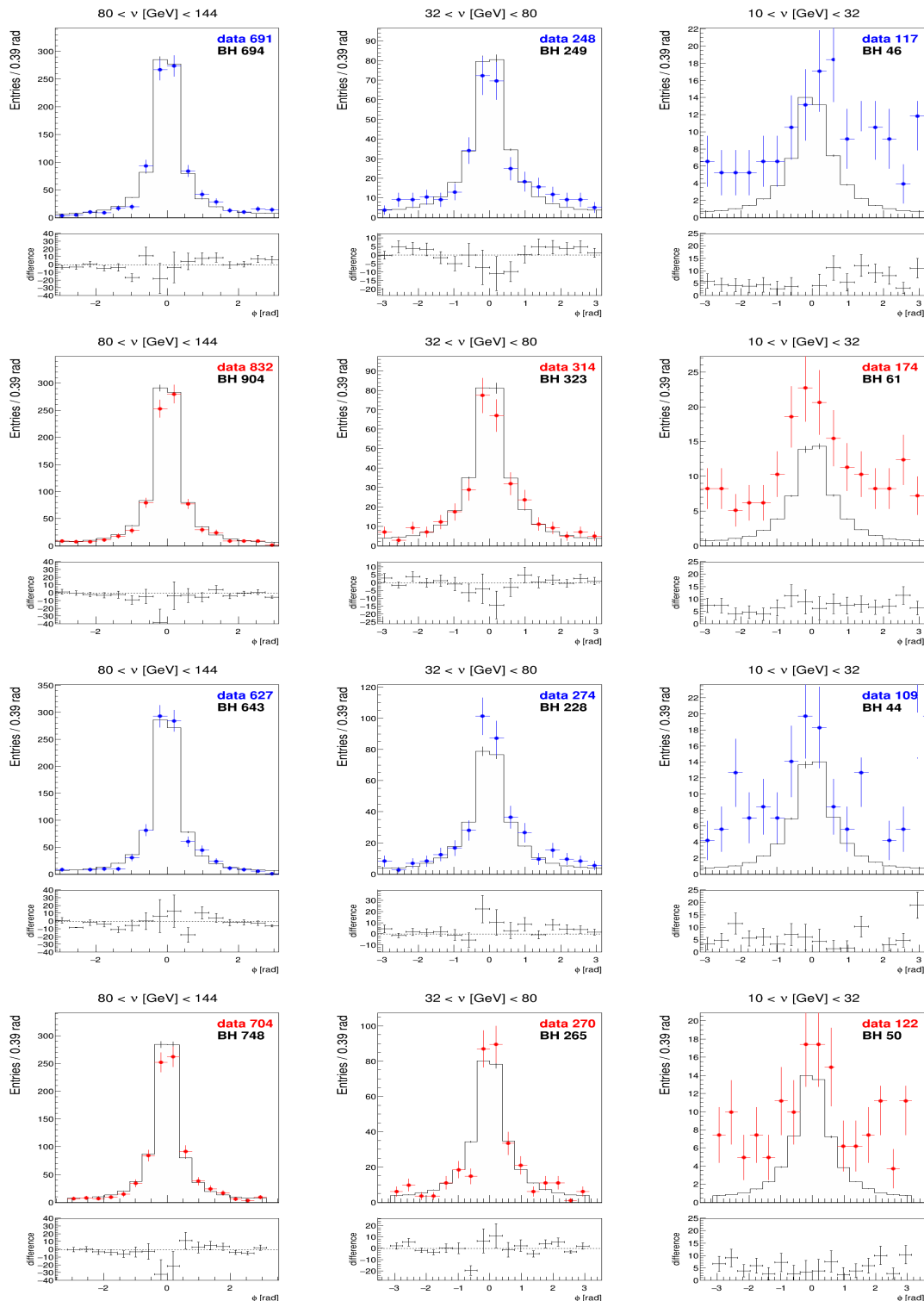


**Figure B.1:** Exclusive single photon distributions as a function of  $\phi^{\gamma^* \gamma}$  in 3 domains of  $\nu$  for the periods P04 on top and P05 on bottom. The distributions for  $\mu^+$  (in red) and  $\mu^-$  (in blue) beams have been normalised to a muon flux of  $10^{12}$ . The number indicated on each plot correspond to the number of real entries. The solid black line corresponds to the HEPGEN-BH prediction. Note that the visible  $\pi^0$  contribution has been removed. The plots are produced for  $1 < Q^2 < 10$  (GeV/c) $^2$ ,  $0.05 < y < 0.9$  and  $0.08 < |t| < 0.64$  (GeV/c) $^2$ .

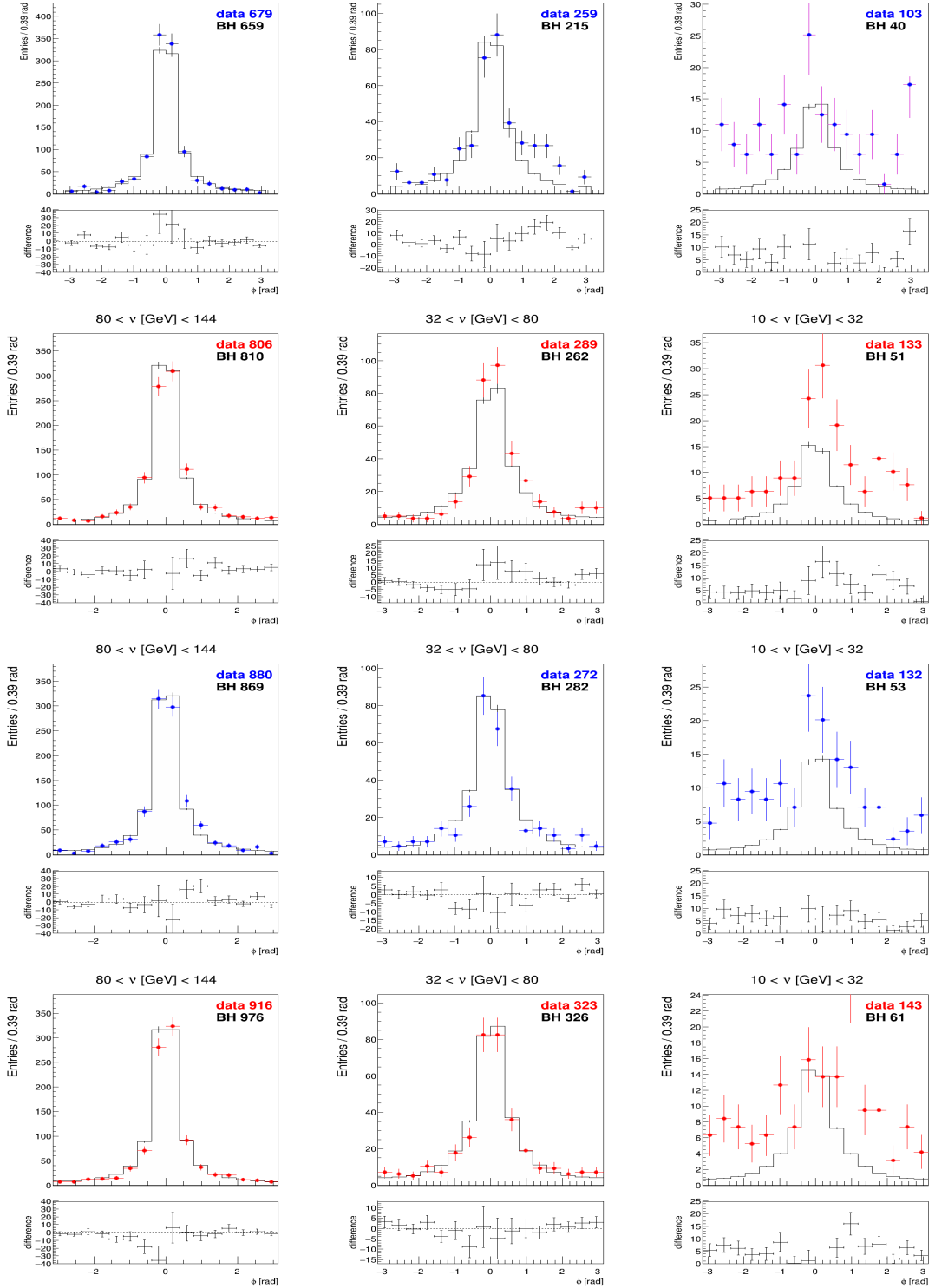


**Figure B.2:** Exclusive single photon distributions as a function of  $\phi^{\gamma^* \gamma}$  in 3 domains of  $\nu$  for the periods P06 on top and P07 on bottom. The distributions for  $\mu^+$  (in red) and  $\mu^-$  (in blue) beams have been normalised to a muon flux of  $10^{12}$ . The number indicated on each plot correspond to the number of real entries. The solid black line corresponds to the HEPGEN-BH prediction. Note that the visible  $\pi^0$  contribution has been removed.

The plots are produced for  $1 < Q^2 < 10$  (GeV/c) $^2$ ,  $0.05 < y < 0.9$  and  $0.08 < |t| < 0.64$  (GeV/c) $^2$ .

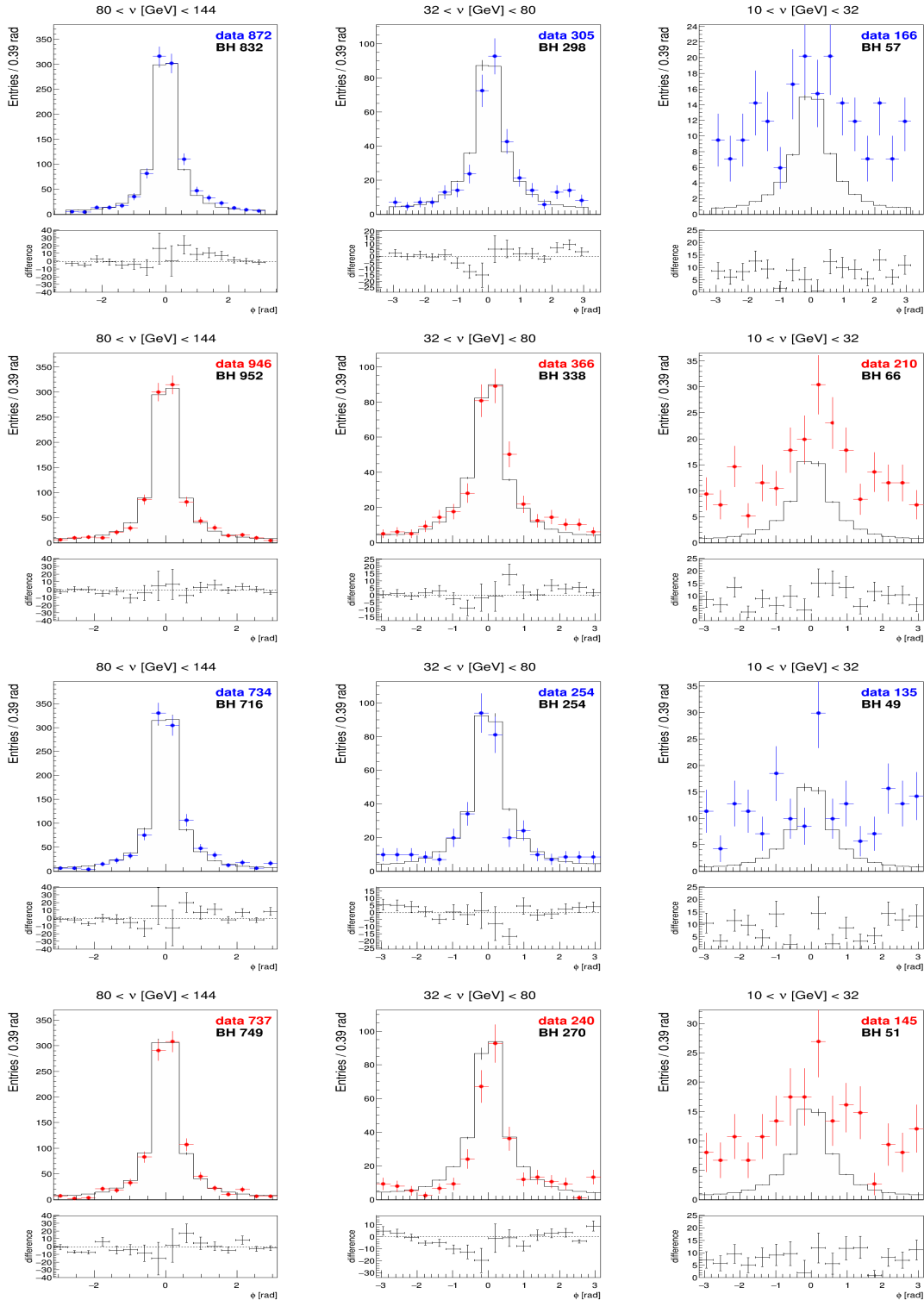


**Figure B.3:** Exclusive single photon distributions as a function of  $\phi^{\gamma^* \gamma}$  in 3 domains of  $\nu$  for the periods P08 on top and P09 on bottom. The distributions for  $\mu^+$  (in red) and  $\mu^-$  (in blue) beams have been normalised to a muon flux of  $10^{12}$ . The numbers indicated on each plot correspond to the number of real entries. The solid black line corresponds to the HEPGEN-BH prediction. Note that the visible  $\pi^0$  contribution has been removed.

The plots are produced for  $1 < Q^2 < 10$  ( $\text{GeV}/c^2$ ),  $0.05 < y < 0.9$  and  $0.08 < |t| < 0.64$  ( $\text{GeV}/c^2$ ).

## APPENDIX C

---

### Optimized kinematical generation

---

## 1 Position of the problem

HEPGEN++ is a weighted Monte Carlo generator which associate to each event a weight proportional to the cross section of the process seeked. Due to the variety of processes available in HEPGEN and its very versatile use, the generation of kinematical variables has not been adapted for each process but factorised before computing the event weight. It consists in a uniform kinematical generation over the phase space  $(\nu, Q^2, \phi_{\gamma^*\gamma})$  with a decreasing exponential generation over  $t'$  (due to the expected Regge ansatz for exclusive processes) to optimise the event generation at most.

In order to define the event weights using the cross section  $d\sigma$ , a crucial point of HEPGEN is to be able to retrieve a uniform distribution over the full phase space in  $(\nu, Q^2, t', \phi_{\gamma^*\gamma})$ . This is trivial in the case of  $(\nu, Q^2, \phi_{\gamma^*\gamma})$  due to their uniform generation. For  $t'$ , the inverse cumulative function is computed analytically. The last point is analytically possible for only a very few types of distributions (for instance it is impossible for Gaussian distributions). With these ingredients, we can define the event weight as:

$$w_{\text{event}} = d\sigma_{\text{event}} \times Pf_{\text{event}}$$

where the label "event" stands for a fixed kinematical distribution  $(\nu, Q^2, t', \phi_{\gamma^*\gamma})$ , and  $Pf_{\text{event}}$  is the phase factor which retrieves a uniform distribution over  $t'$ . Note that in the case of the Bethe-Heitler PAM, a Jacobian (VGG-Moutarde) is added to the phase factor to switch between the  $(\nu, Q^2)$  representation to  $(x_B, Q^2)$ .

## 2 The VEGAS algorithm

Different solutions have been considered for generating the kinematical variables based on the evolution of the cross section. A first approach consists in developping a Markov Chain Monte Carlo (MCMC) software to generate variables according to a given distribution. A toy MCMC has been implemented using the Metropolis-Hastings algorithm and showed accurate results. In addition, it is less prone to the curse of dimensionality. However the precariousness of the implementation was not reliable enough, and a way more advanced solution has been considered. The VEGAS algorithm developed by G.P Lepage [107] is a very advanced preferential sampling algorithm, perfectly suited to this study. It consists in an iterative generation of variable which converges towards an optimised sampling of the distribution one wants to reproduce. The official implementation provided by G. P. Lepage is in Cython, and a simple illustration can be found in **Fig. (C.1)**

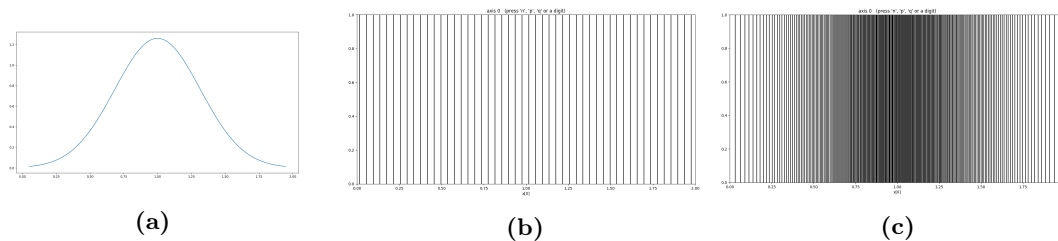


**Figure C.1:** (a): Gaussian distribution.

(b): Uniform sampling of the Gaussian distribution.

(c): Preferential sampling of the Gaussian distribution given by the VEGAS algorithm.

In cases the distribution varies too much and the initial sampling is not performed on a high enough number of events, the preferential sampling algorithm might generate variables only in the regions where the distribution is very peaked. To avoid this extreme case, and be able to have a uniform number of variables in different phase space regions, one can use a method called stratified sampling. It consists in applying the very same preferential sampling algorithm with the same amount of event generated, but on different sub-spaces separately. This is very useful in the case of very peaked distributions where the migration of points is very high. This solution is proposed in VEGAS.

This preferential sampling algorithm has been applied in the case of the Bethe-Heitler cross section distribution. **Fig. (C.2a)** shows the Bethe-Heitler function in a phase space which exhibits the "ears of cats" region. Note that the drop in the singularity is due to the presence of the muon mass in the formula, and is much more pronounced for muons than for electrons. The red curve shows the result of the preferential sampling after applying the phase factor. It is *essential* to retrieve a uniform distribution at this step due to the philosophy of HEPGEN. A fit with a constant function is applied on **Fig. (C.2b)**, and the  $p$ -value is shown in **Fig. (C.2c)**. The excellent  $p$ -value obtained is the proof that the VEGAS algorithm is able to generate variables based on the shape of a distribution, *and* is able to retrieve the initial uniform generation to define the phase factor within HEPGEN.

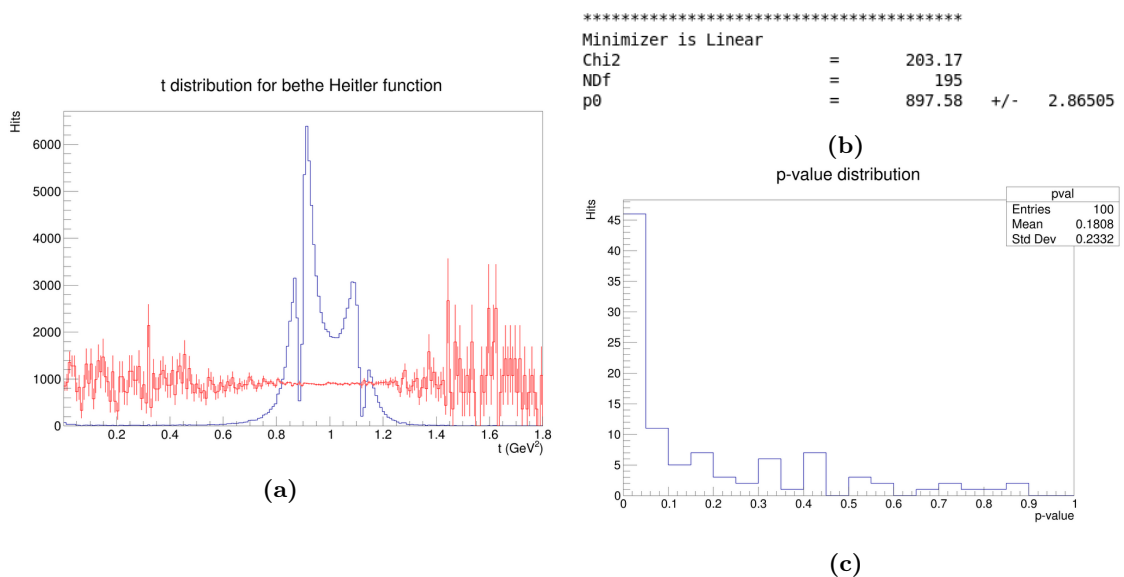


**Figure C.2: Left:** Bethe-Heitler cross section in blue as function of  $|t|$ . The red curve indicates the result of a jacobian transformation from the Bethe-Heitler distribution to a uniform distribution, as required in HEPGEN through the quantity named phase factor.

**Right:** Result of a fit of the red curve with a constant line on top, with the underlying p-value distribution on the bottom. The very low p-value indicates a strong statistical confidency on the fit.



### Introduction

Les Distributions des Partons Généralisées (GPDs) permettent de décrire la dynamique des partons au sein du nucléon. Ces fonctions sont accessibles expérimentalement grâce à l'étude de processus exclusifs. La relation entre les GPDs et les observables de la réaction exclusive est néanmoins indirecte et se fait au travers de fonctions intégrales appelées Facteurs de Forme Compton dans le cas de la Diffusion Compton Virtuelle (ou Deep Inelastic Virtual Compton Scattering noté DVCS) étudiée dans cette thèse. La réaction précisément étudiée est  $\mu p \rightarrow \mu p \gamma$  où le photon virtuel, échangé lors de la diffusion d'un muon sur un proton, interagit avec un parton au sein de ce proton pour créer un photon réel. Le parton actif réintègre le proton et l'état final de la réaction est constitué du photon réel, du proton de recul et du muon diffusé.

### L'expérience COMPASS au CERN

L'expérience DVCS est réalisée à COMPASS au CERN. Elle utilise les faisceaux de muons issus des protons extraits du SPS au CERN. Les muons naturellement polarisés de 160 GeV sous deux configurations : muons chargés positivement et polarisés négativement, ou muons chargés négativement et polarisés positivement. Ces muons interagissent avec une cible d'hydrogène liquide de plus de 2,5m de long, et l'état final est reconstruit grâce au spectromètre COMPASS d'une longueur avoisinant les 50m (**Fig. (C.3)**). En particulier dans le cas du processus DVCS, les muons incidents et diffusés sont analysés par divers plans de détections sur une large couverture angulaire et cinématique. Le photon réel de l'état final est intercepté par 3 calorimètres électromagnétiques (ECAL0,1,2) couvrant différentes acceptances angulaires et le proton de recul est reconstruit grâce à un détecteur de temps de vol placé autour de la cible (CAMERA). Une prise de données a été faite en 2016 et 2017. Cette thèse se concentre principalement sur les résultats des données prises en 2016 mais le travail de calibration s'étend aussi à l'année 2017.

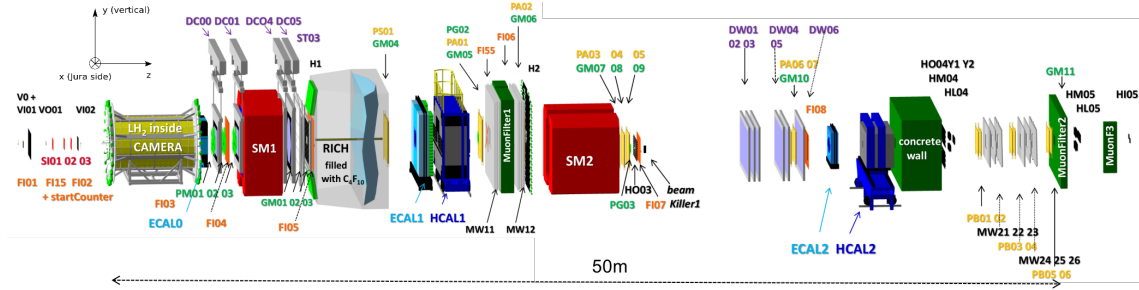


Figure C.3: Vue schématique de l'expérience COMPASS pour la prise de données 2016-2017 [76]

## Qualité des données

La première étape de l'analyse du processus DVCS nécessite d'étudier la qualité (stabilité, efficacité...) de détection des différentes particules concernées, ainsi que la bonne fidélité des simulations Monte Carlo. En particulier, les réponses temporelles et énergétiques des 6000 cellules des calorimètres électromagnétiques sont calibrées. Diverses paramétrisations et corrections sont appliquées à la fois dans les données et les simulations Monte Carlo, expliquées en détail dans le corps de la thèse.

## Ajustement cinématique et calibrations de CAMERA

L'expérience COMPASS permet de détecter toutes les particules impliquées dans le processus exclusif DVCS. Si l'on ajoute les lois de conservation cinématique de la réaction, les observables du DVCS sont sur-contraintes. Cette propriété est utilisée afin de redéterminer les observables avec des résolutions optimales grâce à un ajustement cinématique. On peut noter que le problème reste encore sur-contraint même sans la détection du proton de recul. Cela est utilisé afin de calibrer le détecteur de proton de recul CAMERA. Les observables du proton mesurées directement par CAMERA sont comparées à celles déduites de la mesure des observables des autres particules détectées dans le spectromètre COMPASS. Pour cela, le processus de production de méson  $\rho^0$  est utilisé ( $\mu p \rightarrow \mu p \rho^0$ ) car il donne accès à une statistique importante tout en présentant une cinématique proche de celle du DVCS. De plus ce processus permet de ne pas dépendre des calorimètres électromagnétiques nécessaires dans la mesure DVCS car les pions chargés issus de la désintégration du méson  $\rho^0 \rightarrow \pi^+ \pi^-$  sont détectés dans les trajectographes du spectromètre. Les figures **Figs. (C.4)** and **(C.5)** montrent le résultat des calibrations azimuthales et longitudinales du détecteur CAMERA pour 2 des 48 secteurs angulaires. Une calibration du temps de vol a aussi été effectuée. L'étude a été approfondie dans le cas des simulations Monte Carlo, où les détails précis de la géométrie du détecteur CAMERA sont pris en compte ainsi que les efficacités de détection dans les scintillateurs, guides de lumière et photomultiplicateurs qui composent le détecteur.

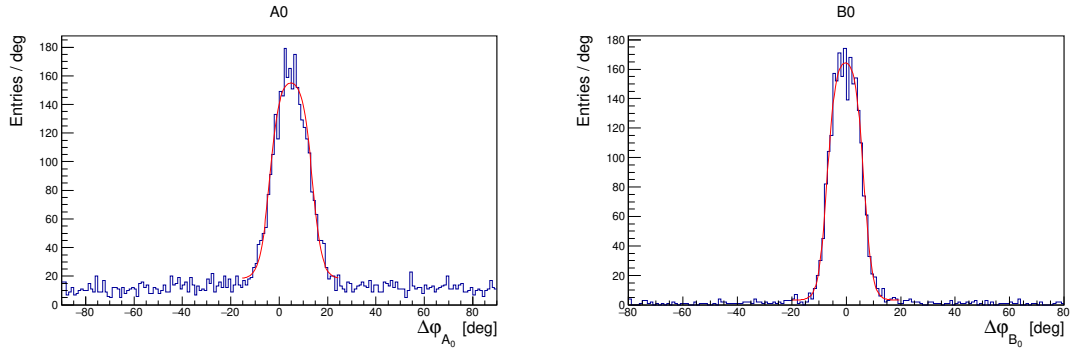


**Figure C.4:** Distributions azimuthale des protons pour les secteurs  $A_0$  et  $B_0$  de CAMERA ramenées à leur position angulaire nominale. Une courbe d'ajustement est indiquée en rouge définie à l'aide d'une sigmoïde symétrique dont le paramètre de translation est extrait.

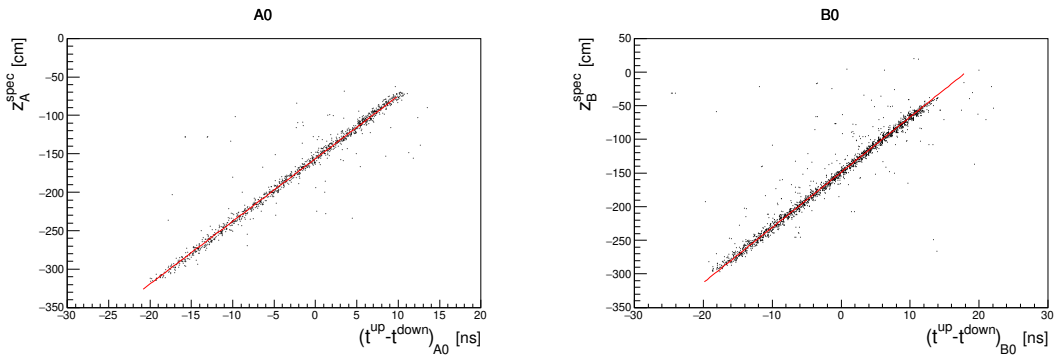


**Figure C.5:** Estimation de la position longitudinale du proton dans les scintillateur  $A_0$  et  $B_0$  à l'aide du spectromètre et de l'ajustement cinématique en fonction de la différence en temps mesurée par les photomultiplicateurs *upstream* et *downstream*. La courbe rouge indique un ajustement affine dont les calibrations longitudinales de CAMERA sont extraites.

## Sélection des événements pour de la réaction exclusive DVCS

La sélection des événement impose les critères suivants (et détaillés dans le corps de la thèse) :

- un point d'interaction situé dans le volume de la cible d'hydrogène
- une bonne qualité de reconstruction des muons incident et diffusé
- un photon réel détecté dans l'un des calorimètres électromagnétiques au dessus des seuils respectivement de 4, 5 et 10 GeV dans ECAL0, 1 et 2.
- un proton de recul détecté dans CAMERA avec une vitesse telle que  $0.1 < \beta < 0.9$ .

Les seuils énergétiques pour le photon réel correspondent au domaine cinématique analysé et prennent en compte les résolutions des calorimètres à l'aide de simulation Monte Carlo.

Si l'on suppose l'exclusivité de la réaction DVCS, la cinématique du proton de recul est soit mesurée par le détecteur de proton de recul ou soit déterminée par les lois de conservations de la réaction et la détection des autres particules dans le spectromètre. Cette corrélation est utilisée dans la sélection des événements DVCS par des coupures sur des observables géométriques et en impulsion du proton de recul comme indiqué dans la figure **Fig. (C.6)**. Les définitions de ces variables sont détaillées dans la thèse.

En plus de cette sélection, un ajustement cinématique est effectué afin de réévaluer les observables et leur résolution optimale. Le  $\chi^2$  obtenu donne un indicateur quantitatif de proximité (une distance) pour un événement à la signature attendue du DVCS et permet de purifier encore la sélection.

Les événements ayant une signature exclusive avec un photon unique dans l'état final ne correspondent pas forcément au processus DVCS. En effet, le DVCS et le processus Bethe-Heitler (BH) partagent strictement le même état final, mais le photon réel du BH est émis par les leptons incident ou diffusé et non pas par un parton au sein du proton. Les deux processus BH et DVCS interfèrent. Suivant l'énergie du photon virtuel ( $\nu = E_\mu - E_{\mu'}$ ) la contribution du BH change significativement. L'analyse est divisée en 3 domaines d'étude:

domaine 1 :  $80 < \nu < 144$  GeV

domaine 2 :  $32 < \nu < 80$  GeV

domaine 3 :  $10 < \nu < 32$  GeV

On s'attend à avoir une dominance totale du BH dans le domaine 1. Les distributions azimuthales des événements sélectionnés sont présentées sur la figure **Fig. (C.8)**.  $\phi$  ou  $\phi_{\gamma^*\gamma}$  est l'angle entre le plan leptonique des muons et le plan hadronique contenant les photon et proton. L'accord entre les données et la simulation Monte Carlo du Bethe-Heitler dans le domaine 1 est remarquable. Une étude systématique des 6 périodes de prise de données pour les deux états de charges des muons permet de conclure à un accord à global de  $98.6 \pm 1\%$ . Ce bon accord permet d'avoir confiance dans l'évaluation des contributions BH dans les 2 autres domaines d'énergie du photon virtuel.

Les événements sélectionnés sont également pollués par des événements de production du méson  $\pi^0$  où seul un photon de décroissance est sélectionné par les critères DVCS. Soit le second photon n'est pas sélectionné car son énergie est comprise entre le seuil de détection des photons dans les calorimètres et le seuil minimal imposé au photon DVCS et ce genre d'événement  $\pi^0$  peut être "visible" en reconstruisant la masse invariante de

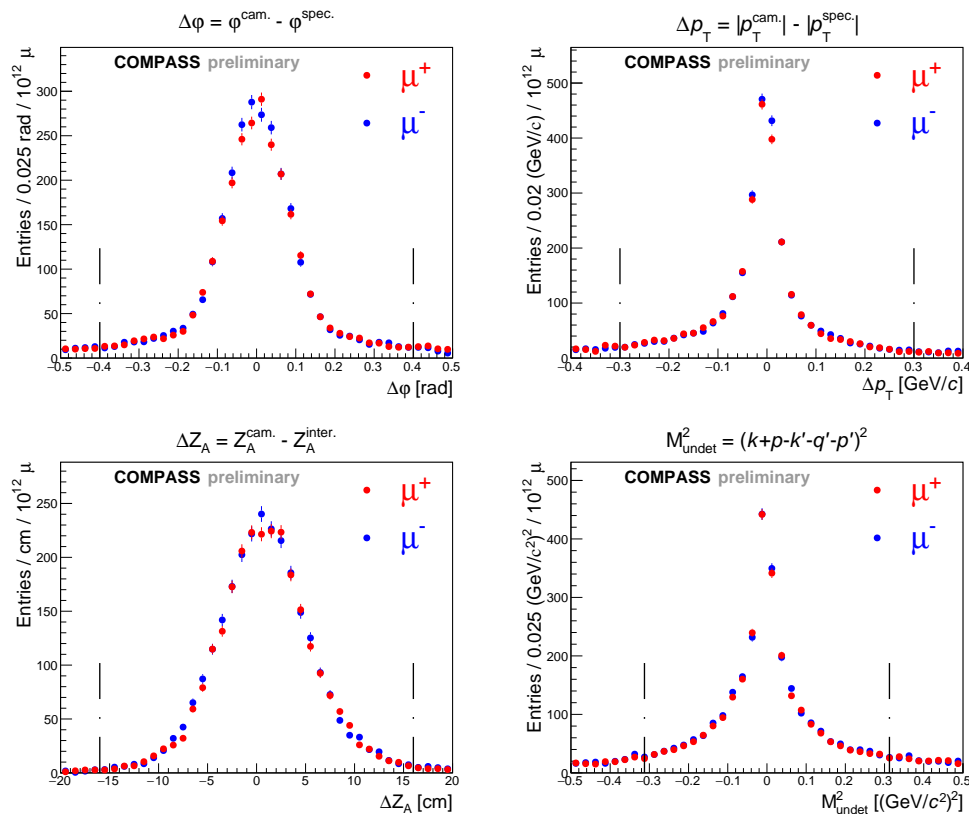


**Figure C.6:** Variables d'exclusivités pour la sélection du DVCS. La statistique des 6 périodes de prise de données est séparée suivant la charge du muon : muon chargé positivement (en rouge) et muon chargé négativement (en bleu). Les deux jeux de données sont normalisés à un même flux de  $10^{12}$  muons. Les limites noires indiquent les coupures appliquées, et chaque figure est montrée en coupant sur les trois autres variables d'exclusivité. Les figures sont produites dans l'espace de phase suivant:  $1 < Q^2 < 10$   $(\text{GeV}/c)^2$ ,  $0.05 < y < 0.9$  et  $0.08 < |t| < 0.64$   $(\text{GeV}/c)^2$ .

ce second photon avec chaque photon candidat au DVCS (voir la figure **Fig. (C.7)** où un pic est observé autour de la masse du  $\pi^0$ ). Une coupure est appliquée autour de la masse du  $\pi^0$  et permet d'enlever ces évènements de la sélection DVCS. Soit le second photon n'est pas détecté car son énergie est trop faible, ou il est en dehors de l'acceptance ou il est absorbé dans les matériaux traversés. Cette contribution est estimée par une simulation Monté Carlo à partir de génération d'évènements exclusifs ou semi-exclusifs de  $\pi^0$ . Le partage entre ces deux populations exclusives ou semi-exclusives est étudié en comparant des distributions d'évènements réels ou simulés et la normalisation de la somme de ces deux contributions est effectuée sur le nombre total de  $\pi^0$  visibles détectés dans les données comme indiqué dans la figure **Fig. (C.7)**.

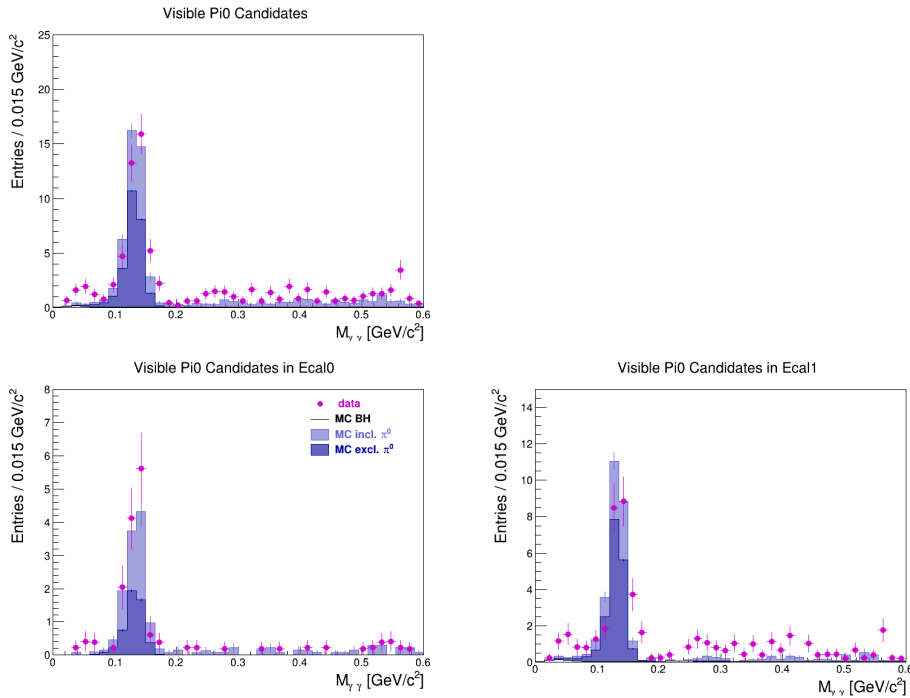


**Figure C.7:** Distribution de la masse des deux photons pour les données et les différentes contributions Monte Carlo (Bethe-Heitler, production inclusive et exclusive de  $\pi^0$ ).

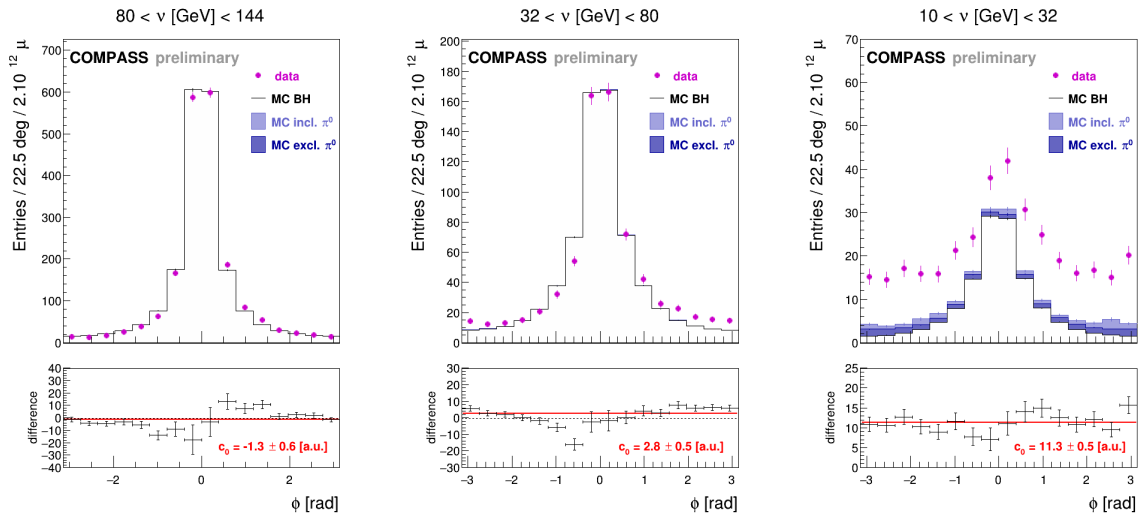


**Figure C.8:** Distribution azimuthale des événements exclusifs avec un seul photon détecté dans trois domaines d'énergie du photon virtuel  $\nu$ . Les points violets indiquent la somme des données  $\mu^+$  et  $\mu^-$  pour un même flux de muons et l'histogramme noir montre la contribution Monte Carlo du Bethe-Heitler. La contribution des  $\pi^0$  visibles est soustraite des données. La contribution des  $\pi^0$  invisibles est indiquée par les zones bleues. Les histogrammes en dessous de la figure montrent la différence des données avec la somme des contributions Monte Carlo (BH+ $\pi^0$ ). Le domaine de petite énergie domaine 3 :  $10 < \nu < 32$  GeV montre une différence significative entre les données et les contributions BH+ $\pi^0$ . Cette différence permet de mesurer la contribution DVCS dans ce domaine.

## Calcul de la section efficace DVCS et conclusions

La section efficace du DVCS ainsi que son interférence avec le Bethe-Heitler peuvent être décomposées en séries de Fourier. Les coefficients résultants dépendent des Facteur de

Forme Compton qui font intervenir les GPDs. Grâce à la sélection des évènements faite précédemment, une mesure expérimentale de ces coefficients de Fourier est possible, donnant un accès aux Facteurs de Forme Compton. Il est essentiel de noter que dans le cas de l'expérience COMPASS, les deux états de charge et polarisation des muons ( $\mu^-$  polarisés positivement et  $\mu^+$  polarisés négativement), permettent d'obtenir les coefficients de Fourier des différents termes de la section efficace de manière non ambiguë par la somme ou la différence des sections efficaces des réactions obtenues soit avec un muon  $\mu^+$  soit avec un muon  $\mu^-$ . Dans le domaine cinématique couvert par l'expérience COMPASS, la somme des sections efficaces permet d'être sensible à la partie imaginaire du Facteur de Forme  $\mathcal{H}$ , et la différence à sa partie réelle.

L'analyse effectuée dans cette thèse concerne la somme des sections efficaces après soustraction de la contribution du Bethe-Heitler et des évènements  $\pi^0$ . Le terme d'interférence entre le DVCS et le Bethe-Heitler est annulé par intégration sur l'angle azimuthal  $\phi_{\gamma^*\gamma}$  afin de ne laisser que le terme de Fourier  $c_0^{\text{DVCS}}$ . La section efficace DVCS est étudiée en fonction du transfert en impulsion  $t$  au proton de recul et une loi exponentielle décroissante est observée (voir la figure Fig. (C.9)). La caractéristique de l'exponentielle permet d'accéder à la distribution transverse des partons dans le proton dans le domaine cinématique de COMPASS (domaine des quarks de la mer). La mesure (voir la figure Fig. (C.10)) est comparée à la mesure préliminaire faite lors de la prise de données en 2012 et aux données obtenues à HERA. Une étude des erreurs systématiques a aussi été effectuée.

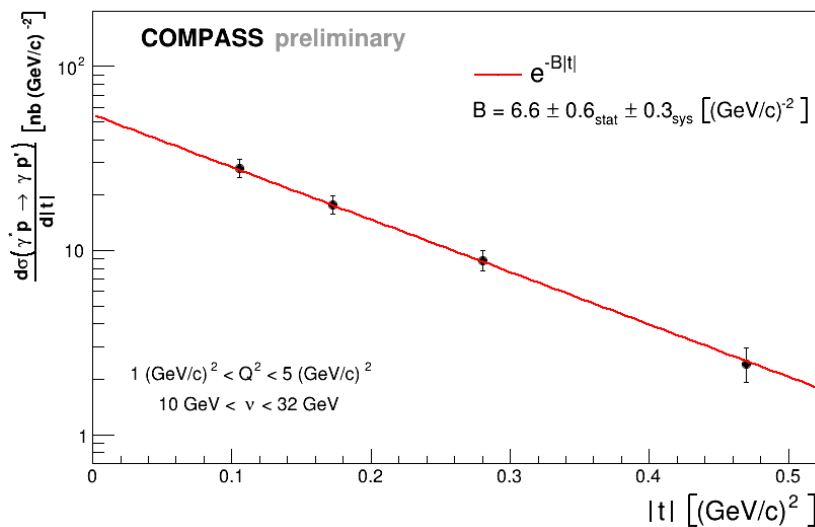


**Figure C.9:** Section efficace différentielle du processus DVCS ( $\gamma * p \rightarrow \gamma p$ )  $d\sigma/d|t|$  évaluée dans 4 régions en transfert  $|t|$ . Les barres d'erreurs systématiques ne sont pas indiquées sur la figure. La courbe rouge est obtenue par méthode du maximum de vraisemblance échantillonné décrite dans le corps de la thèse.

L'extraction des différents coefficients de Fourier devrait se poursuivre en cumulant aussi la longue prise de données faite en 2017 pour augmenter la statistique (par un facteur supérieur à 3). Cette étude sera étendue à une plus grande couverture cinématique en  $Q^2$  et en  $x_B$ . Les histogrammes présents en dessous de la figure Fig. (C.8) montrent la soustraction du Bethe-Heitler aux données. La forme sinusoïdale indique la possibilité d'extraire les termes issus de l'interférence entre le DVCS et le Bethe-Heitler à plus petit  $x_B$  qui sont sensibles à d'autres coefficients de Fourier (comme  $s_1^T$ ). Finalement, la statistique complète des données 2016-2017 va permettre l'étude de la différence des sections efficaces des réactions obtenues soit avec un muon  $\mu^+$  soit avec un muon  $\mu^-$ , afin d'accéder à la

partie réelle des Facteurs de Forme Compton, encore aujourd'hui peu contrainte.

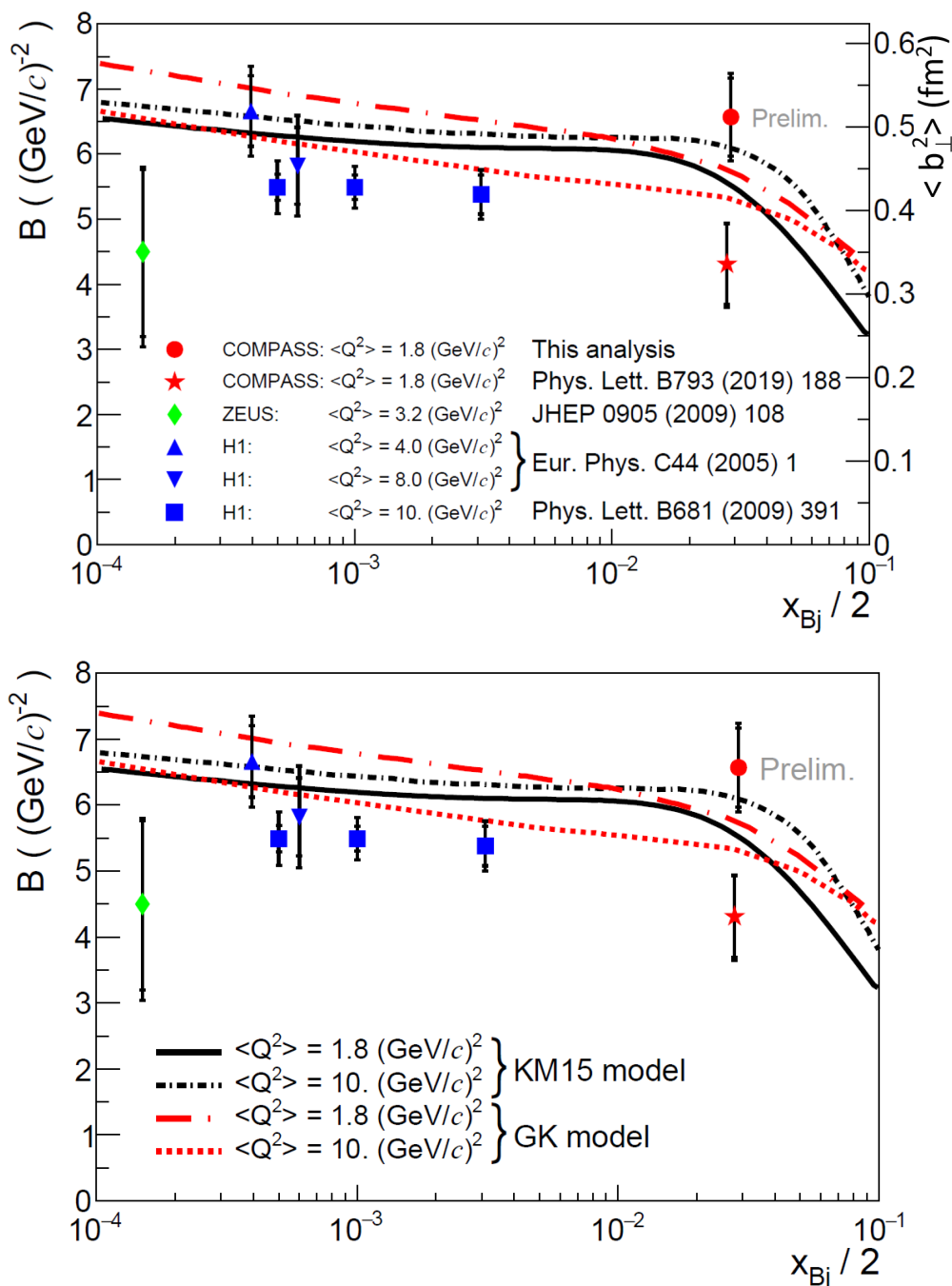


**Figure C.10:** En haut: Résultats de COMPASS et des mesures précédentes effectuées par H1, ZEUS à HERA pour le paramètre  $B$  de la pente en  $|t|$ . Une correspondance est effectuée pour la moyenne du carré de l'extension transverse des partons au sein du proton. Les barres d'erreur intérieures indiquent l'erreur statistique, et les barres d'erreur extérieures la somme quadratique des erreurs statistiques et systématiques. En bas: Les mêmes résultats comparés aux modèles théoriques de Goloskokov et Kroll (GK) [50, 51, 52] et Kumericki Müller (KM15) [48, 49].

---

## Bibliography

---

- [1] M. Diehl. “Generalized parton distributions”. In: *Physics Reports* 388.2-4 (Dec. 2003), pp. 41–277. ISSN: 0370-1573. DOI: [10.1016/j.physrep.2003.08.002](https://doi.org/10.1016/j.physrep.2003.08.002). URL: <http://dx.doi.org/10.1016/j.physrep.2003.08.002>.
- [2] Cédric Mezrag. “Generalised Parton Distributions : from phenomenological approaches to Dyson-Schwinger equations”. 2015PA112144. PhD thesis. 2015. URL: <http://www.theses.fr/2015PA112144/document>.
- [3] Nabil Chouika. “Generalized Parton Distributions and their covariant extension : towards nucleon tomography”. Theses. Université Paris-Saclay, Sept. 2018. URL: <https://tel.archives-ouvertes.fr/tel-01925746>.
- [4] Hervé Moutarde. *Peut-on entendre la forme du proton ?* 2019. URL: [http://irfu.cea.fr/Phocea/Vie\\_des\\_labos/Ast/ast.php?t=fait\\_marquant&id\\_ast=4643](http://irfu.cea.fr/Phocea/Vie_des_labos/Ast/ast.php?t=fait_marquant&id_ast=4643).
- [5] Mark Kac. “Can One Hear the Shape of a Drum?” In: *The American Mathematical Monthly* 73.4P2 (1966), pp. 1–23. DOI: [10.1080/00029890.1966.11970915](https://doi.org/10.1080/00029890.1966.11970915). eprint: <https://doi.org/10.1080/00029890.1966.11970915>. URL: [https://www.maa.org/sites/default/files/pdf/upload\\_library/22/Ford/MarkKac.pdf](https://www.maa.org/sites/default/files/pdf/upload_library/22/Ford/MarkKac.pdf).
- [6] Carolyn Gordon, David L. Webb, and Scott Wolpert. “One cannot hear the shape of a drum”. In: *Bull. Amer. Math. Soc* (1992), pp. 134–138.
- [7] Laurent Schwartz. *Théorie des distributions*. Hermann, Paris, 1966.
- [8] Maciej Zworski. “Semiclassical analysis”. In: vol. 138. 2012. Chap. 1–3. DOI: <http://dx.doi.org/10.1090/gsm/138>.
- [9] E. Wigner. “On the Quantum Correction For Thermodynamic Equilibrium”. In: *Phys. Rev.* 40 (5 June 1932), pp. 749–759. DOI: [10.1103/PhysRev.40.749](https://doi.org/10.1103/PhysRev.40.749). URL: <https://link.aps.org/doi/10.1103/PhysRev.40.749>.
- [10] Cosmas K Zachos, David B Fairlie, and Thomas L Curtright. *Quantum Mechanics in Phase Space*. World Scientific, 2005. DOI: [10.1142/5287](https://doi.org/10.1142/5287). URL: [https://www.academia.edu/20832064/Quantum\\_Mechanics\\_in\\_Phase\\_Space\\_An\\_Overview\\_with\\_Selected\\_Papers\\_World\\_Scientific\\_](https://www.academia.edu/20832064/Quantum_Mechanics_in_Phase_Space_An_Overview_with_Selected_Papers_World_Scientific_).
- [11] C. Lorcé and B. Pasquini. “Quark Wigner distributions and orbital angular momentum”. In: *Phys. Rev. D* 84 (1 July 2011), p. 014015. DOI: [10.1103/PhysRevD.84.014015](https://doi.org/10.1103/PhysRevD.84.014015). URL: <https://link.aps.org/doi/10.1103/PhysRevD.84.014015>.
- [12] D. Müller et al. “Wave Functions, Evolution Equations and Evolution Kernels from Light-Ray Operators of QCD”. In: *Fortschritte der Physik/Progress of Physics* 42.2 (1994), pp. 101–141. ISSN: 1521-3979. DOI: [10.1002/prop.2190420202](https://doi.org/10.1002/prop.2190420202). URL: <http://dx.doi.org/10.1002/prop.2190420202>.
- [13] Xiangdong Ji. “Gauge-Invariant Decomposition of Nucleon Spin”. In: *Physical Review Letters* 78.4 (Jan. 1997), pp. 610–613. ISSN: 1079-7114. DOI: [10.1103/physrevlett.78.610](https://doi.org/10.1103/physrevlett.78.610). URL: <http://dx.doi.org/10.1103/PhysRevLett.78.610>.

- [14] Xiangdong Ji. “Deeply virtual Compton scattering”. In: *Physical Review D* 55.11 (June 1997), pp. 7114–7125. ISSN: 1089-4918. DOI: [10.1103/physrevd.55.7114](https://doi.org/10.1103/physrevd.55.7114). URL: <http://dx.doi.org/10.1103/PhysRevD.55.7114>.
- [15] A.V Radyushkin. “Scaling limit of deeply virtual compton scattering”. In: *Physics Letters B* 380.3-4 (July 1996), pp. 417–425. ISSN: 0370-2693. DOI: [10.1016/0370-2693\(96\)00528-x](https://doi.org/10.1016/0370-2693(96)00528-x). URL: [http://dx.doi.org/10.1016/0370-2693\(96\)00528-X](http://dx.doi.org/10.1016/0370-2693(96)00528-X).
- [16] A. V. Radyushkin. “Nonforward parton distributions”. In: *Physical Review D* 56.9 (Nov. 1997), pp. 5524–5557. ISSN: 1089-4918. DOI: [10.1103/physrevd.56.5524](https://doi.org/10.1103/physrevd.56.5524). URL: <http://dx.doi.org/10.1103/PhysRevD.56.5524>.
- [17] Professor E. Rutherford F.R.S. “LXXIX. The scattering of  $\alpha$  and  $\beta$  particles by matter and the structure of the atom”. In: *The London, Edinburgh, and Dublin Philosophical Magazine and Journal of Science* 21.125 (1911), pp. 669–688. DOI: [10.1080/14786440508637080](https://doi.org/10.1080/14786440508637080). eprint: <https://doi.org/10.1080/14786440508637080>. URL: <https://doi.org/10.1080/14786440508637080>.
- [18] Robert Hofstadter. “Electron Scattering and Nuclear Structure”. In: *Rev. Mod. Phys.* 28 (3 July 1956), pp. 214–254. DOI: [10.1103/RevModPhys.28.214](https://doi.org/10.1103/RevModPhys.28.214). URL: <https://link.aps.org/doi/10.1103/RevModPhys.28.214>.
- [19] R. Hofstadter. “International Congress on Nuclear Sizes and Density Distributions Held at Stanford University, December 17-19, 1957”. In: *Rev. Mod. Phys.* 30 (2 Apr. 1958), pp. 412–413. DOI: [10.1103/RevModPhys.30.412](https://doi.org/10.1103/RevModPhys.30.412). URL: <https://link.aps.org/doi/10.1103/RevModPhys.30.412>.
- [20] M. N. Rosenbluth. “High Energy Elastic Scattering of Electrons on Protons”. In: *Phys. Rev.* 79 (4 Aug. 1950), pp. 615–619. DOI: [10.1103/PhysRev.79.615](https://doi.org/10.1103/PhysRev.79.615). URL: <https://link.aps.org/doi/10.1103/PhysRev.79.615>.
- [21] J. C. Bernauer et al. “Electric and magnetic form factors of the proton”. In: *Phys. Rev. C* 90 (1 July 2014), p. 015206. DOI: [10.1103/PhysRevC.90.015206](https://doi.org/10.1103/PhysRevC.90.015206). URL: <https://link.aps.org/doi/10.1103/PhysRevC.90.015206>.
- [22] Peter J. Mohr, David B. Newell, and Barry N. Taylor. “CODATA recommended values of the fundamental physical constants: 2014”. In: *Rev. Mod. Phys.* 88 (3 Sept. 2016), p. 035009. DOI: [10.1103/RevModPhys.88.035009](https://doi.org/10.1103/RevModPhys.88.035009). URL: <https://link.aps.org/doi/10.1103/RevModPhys.88.035009>.
- [23] Randolph Pohl et al. “The size of the proton”. In: *Nature* 466 (2010), pp. 213–216. DOI: [10.1038/nature09250](https://doi.org/10.1038/nature09250).
- [24] W. Xiong et al. “A small proton charge radius from an electron-proton scattering experiment”. In: *Nature* 575 (2019), pp. 147–150. DOI: [10.1038/s41586-019-1721-2](https://doi.org/10.1038/s41586-019-1721-2).
- [25] J. M. Alarcón, D. W. Higinbotham, and C. Weiss. “Precise determination of the proton magnetic radius from electron scattering data”. In: *Phys. Rev. C* 102.3 (2020), p. 035203. DOI: [10.1103/PhysRevC.102.035203](https://doi.org/10.1103/PhysRevC.102.035203). arXiv: [2002.05167 \[hep-ph\]](https://arxiv.org/abs/2002.05167).
- [26] Zhu-Fang Cui et al. “Pauli Radius of the Proton”. In: *Chin. Phys. Lett.* 38.12 (2021), p. 121401. DOI: [10.1088/0256-307X/38/12/121401](https://doi.org/10.1088/0256-307X/38/12/121401). arXiv: [2109.08768 \[hep-ph\]](https://arxiv.org/abs/2109.08768).
- [27] Murray Gell-Mann. “Symmetries of Baryons and Mesons”. In: *Phys. Rev.* 125 (3 Feb. 1962), pp. 1067–1084. DOI: [10.1103/PhysRev.125.1067](https://doi.org/10.1103/PhysRev.125.1067). URL: <https://link.aps.org/doi/10.1103/PhysRev.125.1067>.

- [28] M. Gell-Mann. “A schematic model of baryons and mesons”. In: *Physics Letters* 8.3 (1964), pp. 214–215. ISSN: 0031-9163. DOI: [https://doi.org/10.1016/S0031-9163\(64\)92001-3](https://doi.org/10.1016/S0031-9163(64)92001-3). URL: <https://www.sciencedirect.com/science/article/pii/S0031916364920013>.
- [29] Richard P. Feynman. “Very High-Energy Collisions of Hadrons”. In: *Phys. Rev. Lett.* 23 (24 Dec. 1969), pp. 1415–1417. DOI: [10.1103/PhysRevLett.23.1415](https://doi.org/10.1103/PhysRevLett.23.1415). URL: <https://link.aps.org/doi/10.1103/PhysRevLett.23.1415>.
- [30] J. D. Bjorken and Emmanuel A. Paschos. “Inelastic Electron Proton and gamma Proton Scattering, and the Structure of the Nucleon”. In: *Phys. Rev.* 185 (1969), pp. 1975–1982. DOI: [10.1103/PhysRev.185.1975](https://doi.org/10.1103/PhysRev.185.1975).
- [31] Elliott D. Bloom et al. “High-Energy Inelastic e p Scattering at 6-Degrees and 10-Degrees”. In: *Phys. Rev. Lett.* 23 (1969), pp. 930–934. DOI: [10.1103/PhysRevLett.23.930](https://doi.org/10.1103/PhysRevLett.23.930).
- [32] Martin Breidenbach et al. “Observed behavior of highly inelastic electron-proton scattering”. In: *Phys. Rev. Lett.* 23 (1969), pp. 935–939. DOI: [10.1103/PhysRevLett.23.935](https://doi.org/10.1103/PhysRevLett.23.935).
- [33] P.A. Zyla et al. “Review of Particle Physics”. In: *PTEP* 2020.8 (2020), p. 083C01. DOI: [10.1093/ptep/ptaa104](https://doi.org/10.1093/ptep/ptaa104). URL: <https://pdg.lbl.gov/2021/reviews/rpp2020-rev-structure-functions.pdf>.
- [34] Xiangdong Ji. “Gauge-Invariant Decomposition of Nucleon Spin”. In: *Phys. Rev. Lett.* 78 (4 Jan. 1997), pp. 610–613. DOI: [10.1103/PhysRevLett.78.610](https://doi.org/10.1103/PhysRevLett.78.610). URL: <https://link.aps.org/doi/10.1103/PhysRevLett.78.610>.
- [35] M. Burkardt. “Impact Parameter Dependent Parton Distributions and Off-Forward Parton Distributions for  $\xi \rightarrow 0$ ”. In: *Physical Review D* 62 (2000). DOI: [10.1103/PhysRevD.62.071503](https://doi.org/10.1103/PhysRevD.62.071503), [10.1103/PhysRevD.66.119903](https://doi.org/10.1103/PhysRevD.66.119903). URL: [hep-ph/0005108v2](https://arxiv.org/abs/hep-ph/0005108v2).
- [36] M. Burkardt. “Impact parameter space interpretation for Generalized Parton Distributions”. In: *International Journal of Modern Physics A* 18.02 (Jan. 2003), pp. 173–207. ISSN: 1793-656X. DOI: [10.1142/s0217751x03012370](https://doi.org/10.1142/s0217751x03012370). arXiv: [hep-ph/0207047v3](https://arxiv.org/abs/hep-ph/0207047v3) [hep-ph].
- [37] Matthias Burkardt. “Generalized parton distributions for large  $x$ ”. In: *Physics Letters B* 595.1-4 (Aug. 2004), pp. 245–249. ISSN: 0370-2693. DOI: [10.1016/j.physletb.2004.05.070](https://doi.org/10.1016/j.physletb.2004.05.070). URL: <http://dx.doi.org/10.1016/j.physletb.2004.05.070>.
- [38] Hyun-Chul Kim, Peter Schweitzer, and Ulugbek Yakhshiev. “Energy–momentum tensor form factors of the nucleon in nuclear matter”. In: *Physics Letters B* 718.2 (Dec. 2012), pp. 625–631. ISSN: 0370-2693. DOI: [10.1016/j.physletb.2012.10.055](https://doi.org/10.1016/j.physletb.2012.10.055). URL: <http://dx.doi.org/10.1016/j.physletb.2012.10.055>.
- [39] K. Goeke, M.V. Polyakov, and M. Vanderhaeghen. “Hard exclusive reactions and the structure of hadrons”. In: *Progress in Particle and Nuclear Physics* 47.2 (Jan. 2001), pp. 401–515. ISSN: 0146-6410. DOI: [10.1016/s0146-6410\(01\)00158-2](https://doi.org/10.1016/s0146-6410(01)00158-2). URL: [http://dx.doi.org/10.1016/S0146-6410\(01\)00158-2](http://dx.doi.org/10.1016/S0146-6410(01)00158-2).
- [40] M. V. Polyakov and C. Weiss. “Skewed and double distributions in the pion and the nucleon”. In: *Physical Review D* 60.11 (Nov. 1999). ISSN: 1089-4918. DOI: [10.1103/PhysRevD.60.114017](https://doi.org/10.1103/PhysRevD.60.114017). URL: <http://dx.doi.org/10.1103/PhysRevD.60.114017>.
- [41] Laurent Mossé. “Etude de la diffusion Compton virtuelle en régime profondément inélastique pour le dispositif expérimental COMPASS”. PhD thesis. 2002.

- [42] R. Akhunzjanov et al. “Transverse extension of partons in the proton probed in the sea-quark range by measuring the DVCS cross section”. In: *Physics Letters B* 793 (June 2019), pp. 188–194. ISSN: 0370-2693. DOI: [10.1016/j.physletb.2019.04.038](https://doi.org/10.1016/j.physletb.2019.04.038). URL: <https://arxiv.org/abs/1802.02739>.
- [43] Nicole d’Hose, Silvia Niccolai, and Armine Rostomyan. “Experimental overview of Deeply Virtual Compton Scattering”. In: *The European Physical Journal A* 52.6 (June 2016), p. 151. ISSN: 1434-601X. DOI: [10.1140/epja/i2016-16151-9](https://doi.org/10.1140/epja/i2016-16151-9). URL: <https://doi.org/10.1140/epja/i2016-16151-9>.
- [44] Alessandro Bacchetta et al. “Single-spin asymmetries: The Trento conventions”. In: *Physical Review D* 70.11 (Dec. 2004). ISSN: 1550-2368. DOI: [10.1103/physrevd.70.117504](https://doi.org/10.1103/physrevd.70.117504). URL: <http://dx.doi.org/10.1103/PhysRevD.70.117504>.
- [45] A.V. Belitsky, D. Müller, and A. Kirchner. “Theory of deeply virtual Compton scattering on the nucleon”. In: *Nuclear Physics B* 629.1-3 (May 2002), pp. 323–392. ISSN: 0550-3213. DOI: [10.1016/S0550-3213\(02\)00144-X](https://doi.org/10.1016/S0550-3213(02)00144-X). URL: [http://dx.doi.org/10.1016/S0550-3213\(02\)00144-X](http://dx.doi.org/10.1016/S0550-3213(02)00144-X).
- [46] V. Bertone et al. “Deconvolution problem of deeply virtual Compton scattering”. In: *Physical Review D* 103.11 (June 2021). ISSN: 2470-0029. DOI: [10.1103/physrevd.103.114019](https://doi.org/10.1103/physrevd.103.114019). URL: <http://dx.doi.org/10.1103/PhysRevD.103.114019>.
- [47] COMPASS Collaboration and F. Gautheron. “COMPASS-II Proposal”. In: (). URL: [https://wwwcompass.cern.ch/compass/proposal/compass-II\\_proposal/compass-II\\_proposal.pdf](https://wwwcompass.cern.ch/compass/proposal/compass-II_proposal/compass-II_proposal.pdf).
- [48] Krešimir Kumerički and Dieter Müller. “Deeply virtual Compton scattering at small  $x$  and the access to the GPD  $H$ ”. In: *Nuclear Physics B* 841.1-2 (Dec. 2010), pp. 1–58. ISSN: 0550-3213. DOI: [10.1016/j.nuclphysb.2010.07.015](https://doi.org/10.1016/j.nuclphysb.2010.07.015). URL: <http://dx.doi.org/10.1016/j.nuclphysb.2010.07.015>.
- [49] Krešimir Kumerički and Dieter Müller. “Description and interpretation of DVCS measurements”. In: *EPJ Web of Conferences* 112 (Dec. 2015). DOI: [10.1051/epjconf/201611201012](https://doi.org/10.1051/epjconf/201611201012). URL: [https://www.epj-conferences.org/articles/epjconf/abs/2016/07/epjconf\\_poetic2016\\_01012/epjconf\\_poetic2016\\_01012.html](https://www.epj-conferences.org/articles/epjconf/abs/2016/07/epjconf_poetic2016_01012/epjconf_poetic2016_01012.html).
- [50] S. V. Goloskokov and P. Kroll. “Vector-meson electroproduction at small Bjorken- $x$  and generalized parton distributions”. In: *The European Physical Journal C* 42.3 (Aug. 2005), pp. 281–301. ISSN: 1434-6052. DOI: [10.1140/epjc/s2005-02298-5](https://doi.org/10.1140/epjc/s2005-02298-5). URL: <http://dx.doi.org/10.1140/epjc/s2005-02298-5>.
- [51] S.V. Goloskokov and P. Kroll. “The role of the quark and gluon GPDs in hard vector-meson electroproduction”. In: *The European Physical Journal C* 53.3 (Nov. 2007), pp. 367–384. ISSN: 1434-6052. DOI: [10.1140/epjc/s10052-007-0466-5](https://doi.org/10.1140/epjc/s10052-007-0466-5). URL: <http://dx.doi.org/10.1140/epjc/s10052-007-0466-5>.
- [52] S. V. Goloskokov and P. Kroll. “An attempt to understand exclusive  $\pi^+$  electroproduction”. In: *The European Physical Journal C* 65.1-2 (Nov. 2009). ISSN: 1434-6052. DOI: [10.1140/epjc/s10052-009-1178-9](https://doi.org/10.1140/epjc/s10052-009-1178-9). URL: <http://dx.doi.org/10.1140/epjc/s10052-009-1178-9>.
- [53] A. Airapetian et al. “Measurement of double-spin asymmetries associated with deeply virtual Compton scattering on a transversely polarized hydrogen target”. In: *Physics Letters B* 704.1-2 (Oct. 2011), pp. 15–23. ISSN: 0370-2693. DOI: [10.1016/j.physletb.2011.08.067](https://doi.org/10.1016/j.physletb.2011.08.067). URL: <http://dx.doi.org/10.1016/j.physletb.2011.08.067>.

- [54] A. Airapetian et al. “Beam-helicity and beam-charge asymmetries associated with deeply virtual Compton scattering on the unpolarised proton”. In: *Journal of High Energy Physics* 2012.7 (July 2012). ISSN: 1029-8479. DOI: [10.1007/jhep07\(2012\)032](https://doi.org/10.1007/jhep07(2012)032). URL: [http://dx.doi.org/10.1007/JHEP07\(2012\)032](http://dx.doi.org/10.1007/JHEP07(2012)032).
- [55] A. Airapetian et al. “Beam-helicity asymmetry arising from deeply virtual Compton scattering measured with kinematically complete event reconstruction”. In: *Journal of High Energy Physics* 2012.10 (Oct. 2012). ISSN: 1029-8479. DOI: [10.1007/jhep10\(2012\)042](https://doi.org/10.1007/jhep10(2012)042). URL: [http://dx.doi.org/10.1007/JHEP10\(2012\)042](http://dx.doi.org/10.1007/JHEP10(2012)042).
- [56] C. Muñoz Camacho et al. “Scaling Tests of the Cross Section for Deeply Virtual Compton Scattering”. In: *Phys. Rev. Lett.* 97 (26 Dec. 2006), p. 262002. DOI: [10.1103/PhysRevLett.97.262002](https://doi.org/10.1103/PhysRevLett.97.262002). URL: <https://link.aps.org/doi/10.1103/PhysRevLett.97.262002>.
- [57] M. Defurne et al. “E00-110 experiment at Jefferson Lab Hall A: Deeply virtual Compton scattering off the proton at 6 GeV”. In: *Phys. Rev. C* 92 (5 Nov. 2015), p. 055202. DOI: [10.1103/PhysRevC.92.055202](https://doi.org/10.1103/PhysRevC.92.055202). URL: <https://link.aps.org/doi/10.1103/PhysRevC.92.055202>.
- [58] M. Defurne et al. “A Glimpse of Gluons through Deeply Virtual Compton Scattering on the Proton”. In: *Nature Communications* 8 (Nov. 2017). DOI: [10.1038/s41467-017-01819-3](https://doi.org/10.1038/s41467-017-01819-3). URL: <https://www.nature.com/articles/s41467-017-01819-3#citeas>.
- [59] F. X. Girod et al. “Measurement of Deeply Virtual Compton Scattering Beam-Spin Asymmetries”. In: *Phys. Rev. Lett.* 100 (16 Apr. 2008), p. 162002. DOI: [10.1103/PhysRevLett.100.162002](https://doi.org/10.1103/PhysRevLett.100.162002). URL: <https://link.aps.org/doi/10.1103/PhysRevLett.100.162002>.
- [60] E. Seder et al. “Longitudinal Target-Spin Asymmetries for Deeply Virtual Compton Scattering”. In: *Physical Review Letters* 114.3 (Jan. 2015). ISSN: 1079-7114. DOI: [10.1103/physrevlett.114.032001](https://doi.org/10.1103/physrevlett.114.032001). URL: <http://dx.doi.org/10.1103/PhysRevLett.114.032001>.
- [61] S. Pisano et al. “Single and double spin asymmetries for deeply virtual Compton scattering measured with CLAS and a longitudinally polarized proton target”. In: *Physical Review D* 91.5 (Mar. 2015). ISSN: 1550-2368. DOI: [10.1103/physrevd.91.052014](https://doi.org/10.1103/physrevd.91.052014). URL: <http://dx.doi.org/10.1103/PhysRevD.91.052014>.
- [62] H. S. Jo et al. “Cross Sections for the Exclusive Photon Electroproduction on the Proton and Generalized Parton Distributions”. In: *Physical Review Letters* 115.21 (Nov. 2015). ISSN: 1079-7114. DOI: [10.1103/physrevlett.115.212003](https://doi.org/10.1103/physrevlett.115.212003). URL: <http://dx.doi.org/10.1103/PhysRevLett.115.212003>.
- [63] R. Dupré, M. Guidal, and M. Vanderhaeghen. “Tomographic image of the proton”. In: *Physical Review D* 95.1 (Jan. 2017). ISSN: 2470-0029. DOI: [10.1103/physrevd.95.011501](https://doi.org/10.1103/physrevd.95.011501). URL: <http://dx.doi.org/10.1103/PhysRevD.95.011501>.
- [64] R. Dupré et al. In: *The European Physical Journal A* 53 (2017).
- [65] “Measurement of deeply virtual Compton scattering at HERA”. In: *The European Physical Journal C* 44.1 (Sept. 2005), pp. 1–11. ISSN: 1434-6052. DOI: [10.1140/epjc/s2005-02345-3](https://doi.org/10.1140/epjc/s2005-02345-3). URL: <http://dx.doi.org/10.1140/epjc/s2005-02345-3>.
- [66] F.D. Aaron et al. “Deeply Virtual Compton Scattering and its Beam Charge Asymmetry in  $e^\pm p$  Collisions at HERA”. In: *Physics Letters B* 681.5 (Nov. 2009), pp. 391–399. ISSN: 0370-2693. DOI: [10.1016/j.physletb.2009.10.035](https://doi.org/10.1016/j.physletb.2009.10.035). URL: <http://dx.doi.org/10.1016/j.physletb.2009.10.035>.

- [67] ZEUS collaboration. “A measurement of the  $Q^2, W$  and  $t$  dependences of deeply virtual Compton scattering at HERA”. In: *Journal of High Energy Physics* 2009.05 (May 2009), pp. 108–108. ISSN: 1029-8479. DOI: [10.1088/1126-6708/2009/05/108](https://doi.org/10.1088/1126-6708/2009/05/108). URL: <http://dx.doi.org/10.1088/1126-6708/2009/05/108>.
- [68] L. Favart et al. “Deeply Virtual Meson Production on the nucleon”. In: *Eur. Phys. J. A* 52.6 (2016), p. 158. DOI: [10.1140/epja/i2016-16158-2](https://doi.org/10.1140/epja/i2016-16158-2). arXiv: [1511.04535](https://arxiv.org/abs/1511.04535) [hep-ph].
- [69] P. Kroll, H. Moutarde, and F. Sabatié. “From hard exclusive meson electroproduction to deeply virtual Compton scattering”. In: *The European Physical Journal C* 73.1 (Jan. 2013). ISSN: 1434-6052. DOI: [10.1140/epjc/s10052-013-2278-0](https://doi.org/10.1140/epjc/s10052-013-2278-0). URL: <http://dx.doi.org/10.1140/epjc/s10052-013-2278-0>.
- [70] Brandon Kriesten et al. *Parametrization of Quark and Gluon Generalized Parton Distributions in a Dynamical Framework*. 2021. arXiv: [2101.01826](https://arxiv.org/abs/2101.01826) [hep-ph]. URL: <https://arxiv.org/abs/2101.01826>.
- [71] P. Abbon et al. “The COMPASS experiment at CERN”. In: *Nuclear Instruments and Methods in Physics Research, Section A: Accelerators, Spectrometers, Detectors and Associated Equipment* 577.3 (July 2007), pp. 455–518. ISSN: 01689002. DOI: [10.1016/j.nima.2007.03.026](https://doi.org/10.1016/j.nima.2007.03.026).
- [72] P. Abbon et al. “The COMPASS setup for physics with hadron beams”. In: *Nuclear Instruments and Methods in Physics Research Section A: Accelerators, Spectrometers, Detectors and Associated Equipment* 779 (Apr. 2015), pp. 69–115. ISSN: 0168-9002. DOI: [10.1016/j.nima.2015.01.035](https://doi.org/10.1016/j.nima.2015.01.035). URL: <https://arxiv.org/abs/hep-ex/0703049>.
- [73] Nicolas Du Fresne Von Hohenesche. “Measurement of Hadron Multiplicities in Deep Inelastic Muon-Nucleon Scattering”. PhD thesis. Johannes Gutenberg-Universität Mainz, Nov. 2015. URL: [https://wwwcompass.cern.ch/compass/publications/theses/2016\\_phd\\_fresne.pdf](https://wwwcompass.cern.ch/compass/publications/theses/2016_phd_fresne.pdf).
- [74] E. Bielert et al. “A 2.5m long liquid hydrogen target for COMPASS”. In: *Nuclear Instruments & Methods in Physics Research Section A: Accelerators, Spectrometers, Detectors and Associated Equipment*. 746 (2014), pp. 20–25. DOI: <https://doi.org/10.1016/j.nima.2014.01.067>.
- [75] Antoine Vidon. “Probing the proton structure through deep virtual Compton Scattering at COMPASS, CERN”. PhD thesis. Université Paris-Saclay, Oct. 2019.
- [76] Nicole D’Hose. URL: [https://wwwcompass.cern.ch/compass/gpd/meetings/201606\\_23juin\\_CM/dHose\\_20160623\\_CM.pdf](https://wwwcompass.cern.ch/compass/gpd/meetings/201606_23juin_CM/dHose_20160623_CM.pdf).
- [77] Nicolas Pierre. “Multiplicities of hadrons in deep-inelastic scattering of muons on nucleons at COMPASS”. PhD thesis. Johannes Gutenberg-Universität Mainz and Université Paris-Saclay, June 2019. URL: <https://tel.archives-ouvertes.fr/tel-02283265/document>.
- [78] Sergei Gerassimov. *Physics Analysis Software Tools*. URL: <http://ges.home.cern.ch/%20ges/phast>.
- [79] A. Ferrero. “Nucleon Structure with TMDs and GPDs”. PhD thesis. May 2017.
- [80] Philipp Jörg. “Deeply Virtual Compton Scattering at CERN - What is the Size of the Proton ?” PhD thesis. Fakultät für Mathematik und Physik Albert-Ludwigs-Universität Freiburg, Feb. 2017.

- [81] Florian Herrmann. “Development and verification of a high performance electronic readout framework for high energy physics”. MA thesis. Fakultät für Mathematik und Physik Albert-Ludwigs-Universität Freiburg, Aug. 2011. URL: [https://wwwcompass.cern.ch/compass/publications/theses/2011\\_phd\\_herrmann.pdf](https://wwwcompass.cern.ch/compass/publications/theses/2011_phd_herrmann.pdf).
- [82] Robert Schäfer. “Charakterisierung eines Detektors zum Nachweis von Rückstoßprotonen am COMPASS Experiment”. MA thesis. Fakultät für Mathematik und Physik Albert-Ludwigs-Universität Freiburg, Sept. 2013. URL: [https://cds.cern.ch/record/2005748/files/schaefer\\_diplom\\_2013.pdf](https://cds.cern.ch/record/2005748/files/schaefer_diplom_2013.pdf).
- [83] C. Bernet et al. “The COMPASS trigger system for muon scattering”. In: *Nuclear Instruments and Methods in Physics Research, Section A: Accelerators, Spectrometers, Detectors and Associated Equipment* 550.1-2 (Sept. 2005), pp. 217–240. ISSN: 01689002. DOI: [10.1016/j.nima.2005.05.043](https://doi.org/10.1016/j.nima.2005.05.043).
- [84] Johannes Giarra. *Determination of the hodoscope and trigger efficiencies in 2016*. June 2021. URL: <https://wwwcompass.cern.ch/compass/notes/2021-1/2021-1.pdf>.
- [85] Matthias Gorzelli. “Cross-section measurement of exclusive  $\pi^0$  muoproduction and firmware design for an FPGA-based detector readout”. PhD thesis. Fakultät für Mathematik und Physik Albert-Ludwigs-Universität Freiburg, Mar. 2018.
- [86] Sebastian Schopferer. “An FPGA-based trigger processor for a measurement of deeply virtual compton scattering at the COMPASS-II experiment”. MA thesis. Fakultät für Mathematik und Physik Albert-Ludwigs-Universität Freiburg, Oct. 2013. URL: <https://freidok.uni-freiburg.de/data/9274>.
- [87] R. Frühwirth. “Application of Kalman filtering to track and vertex fitting”. In: *Nuclear Instruments & Methods in Physics Research Section A: Accelerators, Spectrometers, Detectors and Associated Equipment* (1987). DOI: [https://doi.org/10.1016/0168-9002\(87\)90887-4](https://doi.org/10.1016/0168-9002(87)90887-4).
- [88] Rene Brun and Fons Rademakers. “ROOT - An Object Oriented Data Analysis Framework”. In: *Nuclear Instruments and Methods in Physics Research, Section A: Accelerators, Spectrometers, Detectors and Associated Equipment* 389.1-2 (Apr. 1997), pp. 81–86. DOI: [https://doi.org/10.1016/S0168-9002\(97\)00048-X](https://doi.org/10.1016/S0168-9002(97)00048-X). URL: <https://root.cern.ch/>.
- [89] Johannes Giarra. *Analysis of the spill profile and the muon flux in 2016*. Feb. 2021. URL: <https://wwwcompass.cern.ch/compass/notes/2021-2/2021-2.pdf>.
- [90] N. du Fresne et al. *Flux determination for 2009 DVCS data*. 2012.
- [91] J. Veit B. Barth. *Trigger related issues for the DVCS runs 2016/2017*. Feb. 2018. URL: <https://wwwcompass.cern.ch/compass/notes/2018-2/2018-2.pdf>.
- [92] Tobias Christian Szameitat. “New Geant4-based Monte Carlo Software for the COMPASS-II Experiment at CERN”. PhD thesis. Fakultät für Mathematik und Physik Albert-Ludwigs-Universität Freiburg, Dec. 2016.
- [93] Marlene Gertsner. Analysis meeting. 2020.
- [94] B. Adeva et al. “Spin asymmetries  $A(1)$  and structure functions  $g_1$  of the proton and the deuteron from polarized high-energy muon scattering”. In: *Phys. Rev. D* 58 (1998), p. 112001. DOI: [10.1103/PhysRevD.58.112001](https://doi.org/10.1103/PhysRevD.58.112001).
- [95] Eric Fuchey. private communication. 2015.
- [96] Po-Ju Lin. private communication. 2019.
- [97] Sergei Gerassimov. private communication. May 2020.

- [98] G. Grindhammer and S. Peters. *The Parameterized Simulation of Electromagnetic Showers in Homogeneous and Sampling Calorimeters*. 2000. arXiv: [hep-ex/0001020](https://arxiv.org/abs/hep-ex/0001020) [[hep-ex](#)].
- [99] R.K.Bock et al. “Formulae and methods in experimental data evaluation with Emphasis on High Energy Physics”. In: vol. Vol. 3: Articles on Statistical and Numerical Methods. European Physical Society (Computational Physics Group), Dec. 1983. Chap. I, pp. I23–I30.
- [100] Sandro Scherrers. “Extraction of the exclusive  $J/\Psi$  photoproduction cross section at COMPASS, CERN”. MA thesis. Fakultät für Mathematik und Physik Albert-Ludwigs-Universität Freiburg, Sept. 2019.
- [101] A. Sandacz and P. Sznajder. *HEPGEN - generator for hard exclusive leptoproduction*. 2012. arXiv: [1207.0333](https://arxiv.org/abs/1207.0333) [[hep-ph](#)].
- [102] Christopher Ralp Regali. “Exclusive event generation for the COMPASS-II experiment at CERN and improvements for the Monte-Carlo chain”. PhD thesis. Fakultät für Mathematik und Physik Albert-Ludwigs-Universität Freiburg, Oct. 2016. URL: [doi:10.6094/UNIFR/11449](https://doi.org/10.6094/UNIFR/11449).
- [103] P. A. M. Guichon. private communication. 2015.
- [104] L. L. Frankfurt, A. Freund, and M. Strikman. “Diffractive exclusive photon production in DIS at DESY HERA”. In: *Phys. Rev. D* 58 (11 Oct. 1998), p. 114001. DOI: [10.1103/PhysRevD.58.114001](https://doi.org/10.1103/PhysRevD.58.114001). URL: <https://link.aps.org/doi/10.1103/PhysRevD.58.114001>.
- [105] L.L Frankfurt, A Freund, and M Strikman. “Deeply virtual compton scattering at HERA – A probe of asymptotia”. In: *Physics Letters B* 460.3 (1999), pp. 417–424. ISSN: 0370-2693. DOI: [https://doi.org/10.1016/S0370-2693\(99\)00803-5](https://doi.org/10.1016/S0370-2693(99)00803-5). URL: <https://www.sciencedirect.com/science/article/pii/S0370269399008035>.
- [106] S.V. Goloskokov and P. Kroll. “Transversity in hard exclusive electroproduction of pseudoscalar mesons”. In: (). DOI: <https://doi.org/10.1140/epja/i2011-11112-6>.
- [107] G. Peter Lepage. “Adaptive multidimensional integration: vegas enhanced”. In: *Journal of Computational Physics* 439 (Aug. 2021), p. 110386. ISSN: 0021-9991. DOI: [10.1016/j.jcp.2021.110386](https://doi.org/10.1016/j.jcp.2021.110386). URL: <http://dx.doi.org/10.1016/j.jcp.2021.110386>.
- [108] G Peter Lepage. “A new algorithm for adaptive multidimensional integration”. In: *Journal of Computational Physics* 27.2 (1978), pp. 192–203. ISSN: 0021-9991. DOI: [https://doi.org/10.1016/0021-9991\(78\)90004-9](https://doi.org/10.1016/0021-9991(78)90004-9). URL: <https://www.sciencedirect.com/science/article/pii/0021999178900049>.
- [109] Brian Ventura. *Internship report*. 2018.
- [110] L. N. Hand. “Experimental Investigation of Pion Electroproduction”. In: *Phys. Rev.* 129 (4 Feb. 1963), pp. 1834–1846. DOI: [10.1103/PhysRev.129.1834](https://doi.org/10.1103/PhysRev.129.1834). URL: <https://link.aps.org/doi/10.1103/PhysRev.129.1834>.
- [111] Christoph Langenbruch. *Parameter uncertainties in weighted unbinned maximum likelihood fits*. 2019. arXiv: [1911.01303](https://arxiv.org/abs/1911.01303) [[physics.data-an](#)].



**Titre:** Etude de la diffusion Compton profondément virtuelle dans l'expérience COMPASS au CERN  
**Mots clés:** Diffusion Compton, Structure interne du nucléon, Distributions de partons Généralisées, COMPASS

**Résumé:** Les protons et neutrons sont les constituants principaux de la matière visible de l'univers, mais restent néanmoins encore aujourd'hui une énigme dans la physique moderne. Ces composants de la matière sont en réalité constitués de particules élémentaires appelés quarks et gluons (regroupés sous le terme générique de partons), dont la dynamique et les interactions sont orchestrées par la chromodynamique quantique (QCD). Cependant aux énergies proches de la masse du proton, les méthodes perturbatives usuelles ne peuvent être employées, et la dynamique des partons est par conséquent régie par des fonctions de structure appelées distributions de partons généralisées (GPDs). Ces fonctions modélisent en particulier la position transverse et le moment longitudinal des quarks et gluons ainsi que les corrélations associées. Les GPDs peuvent être étudiées au travers de la diffusion Compton profondément virtuelle (DVCS) : il s'agit d'un processus exclusif où le proton est sondé au moyen d'un photon virtuel, pour produire dans l'état final un photon réel tout en laissant le proton intact. Ce processus est notamment étudié dans le cadre

de l'expérience COMPASS au CERN, où un faisceau de muons polarisés à 160 GeV interagit sur une cible d'hydrogène liquide. Aussi toutes les particules présentes au sein du processus sont détectées : le système de guidage magnétique avant la cible permet de mesurer le muon incident, tandis que le muon diffracté et le photon sont détecté au sein du spectromètre COMPASS et dans les trois calorimètres électromagnétiques. Le proton de recul est quant à lui mesuré à l'aide d'un détecteur de temps de vol placé autour de la cible. Cette thèse présente les résultats actuels de l'analyse du processus DVCS au sein de l'expérience COMPASS sur les données collectées en 2016 et 2017. Après une introduction sur la théorie des GPDs et leur lien avec le processus DVCS, le contexte expérimental du sujet sera traité. En particulier l'accent sera mis sur la calibration du détecteur de temps de vol et des calorimètres électromagnétiques, ainsi que sur une technique d'optimisation permettant l'ajustement cinématique des observables mesurées. Une comparaison détaillée des données sera faite avec une simulation Monte Carlo afin de permettre l'extraction de la section efficace DVCS, dont les résultats seront présentés discutés.

**Title:** Study of Deeply Virtual Compton Scattering at COMPASS at CERN

**Keywords:** Deeply Virtual Compton Scattering, Internal structure of the nucleon, Generalised Partons Distributions, COMPASS

**Abstract:** Although protons and neutrons are known to be the main constituents of the visible matter in the universe, they still remain nowadays a conundrum in modern physics. These constituents of matter are actually made out of quarks and gluons (gathered under the denomination of partons), and are governed by the laws of quantum chromodynamics (QCD). Nevertheless at energies close to the proton mass, the usual perturbative methods cannot be used, and the partons dynamics is therefore orchestrated by structure functions called Generalised Partons Distributions (GPDs). These functions provide information on the longitudinal momentum and transverse position of quarks and gluons, including their correlations. GPDs can be studied through the Deeply Virtual Compton Scattering process (DVCS), where the proton is probed by a virtual photon, in order to produce a real photon in the final state and a recoil of the proton remaining intact. In particular, this process is studied in the COMPASS experiment at CERN, where a polarised muon beam of 160 GeV interacts on a

liquid hydrogen target. All the involved particles are detected in this process: the magnetic guidance system before the target allows to measure the incident muon, while the diffracted muon and the photon are detected in the forward spectrometer and the three electromagnetic calorimeters. The recoiled proton is detected in a time of flight detector placed around the target. This thesis shows the most recent results on the DVCS analysis in the COMPASS experiment, based on the 2016 and 2017 data taking. After the introduction of GPDs and their link with the DVCS process, the experimental situation will be depicted. In particular, the emphasis will be put on the calibrations of the time of flight detector and the electromagnetic calorimeters. In addition, an optimisation procedure called kinematic fitting will be detailed in order to improve the measured resolutions on the observables. A detail comparison between the data and a Monte Carlo simulation will be performed in the purpose of accessing the DVCS cross section. The results will be finally shown and discussed.

